

**THE BEHAVIOUR OF SHORT FATIGUE CRACKS  
IN A  $\beta$ -PROCESSED TITANIUM ALLOY.**

**BY**

**PHILIP JOHN HASTINGS**

**Thesis submitted to the University of Nottingham  
for the degree of Doctor of Philosophy  
August 1989.**



## **IMAGING SERVICES NORTH**

Boston Spa, Wetherby  
West Yorkshire, LS23 7BQ  
[www.bl.uk](http://www.bl.uk)

**BEST COPY AVAILABLE.**

**VARIABLE PRINT QUALITY**

## ABSTRACT

An investigation has been made into the behaviour of short fatigue cracks in the  $\beta$ -processed titanium alloy, Ti65s.

The effect on the material of a number of different variables was studied, particularly microstructure, as well as stress level, specimen design and specimen size.

Initiation of cracks was found to occur at similar microstructural features in smooth specimens, regardless of  $\alpha$ -platelet morphology. Cracks initiated from slip bands across small bundles of  $\alpha$ -platelets, despite the presence of longer, more intense slip bands across  $\alpha$ -colonies.  $\alpha$ -platelet morphology was found to have a significant effect on short crack propagation rates when crack length was of the order of, or less than, the  $\alpha$ -colony size - the more aligned the  $\alpha$ -platelets, the greater the short crack propagation rates at equivalent  $\Delta K$ s. Increasing the prior  $\beta$ -grain size (and hence the  $\alpha$ -colony size) led to higher short crack propagation rates at equivalent  $\Delta K$ s.

Specimen design appeared to have an effect on short crack growth rates - a uniaxial tension specimen design gave slightly higher growth rates than a four point bend specimen design. Variation in specimen size had no effect on short crack growth rates for the same microstructural condition, but a larger specimen size was found to reduce the scatter in specimen lives observed in smaller specimens. Short crack growth rates were apparently insensitive to stress level when compared at the same nominal  $\Delta K$  values. Crack shape was found to vary considerably at crack depths below approximately 0.75mm. At crack depths greater

than this value, cracks took an approximately semi-circular form.

In keeping with many recent studies of short crack behaviour, short cracks were found to grow faster than long cracks at the same nominal  $\Delta K$ s and at  $\Delta K$ s below the long crack threshold value,  $\Delta K_{th}$ .

A case study was carried out to determine the behaviour of short cracks in a cheese forged from an ingot slice of IMI685. Crack growth behaviour was found to be the same as that of Ti65s, but initiation behaviour was affected by the presence of pores in the IMI685, leading to a significant reduction in fatigue life.

## CONTENTS

CHAPTER 1	INTRODUCTION	1
CHAPTER 2	MATERIALS	4
2.1	OCCURRENCE AND EXTRACTION OF TITANIUM . . . . .	4
2.1.1	Raw Materials . . . . .	4
2.1.2	Extraction Technology . . . . .	4
2.2	PROCESSING OF TITANIUM . . . . .	5
2.2.1	Ingot Production . . . . .	5
2.3	STRUCTURE AND PROPERTIES OF TITANIUM ALLOYS . . . . .	6
2.3.1	Microstructure . . . . .	6
2.3.1.1	Alloying Additions . . . . .	8
2.3.2	Structure And Properties Of Ti65s . . . . .	9
2.3.3	$\beta$ Heat Treatment Of Ti65s . . . . .	9
2.4	DEFORMATION MECHANISMS . . . . .	10
2.4.1	Hexagonal Metals . . . . .	10
2.4.2	Titanium . . . . .	11
2.5	SUMMARY . . . . .	13
2.6	BIBLIOGRAPHY FOR CHAPTER 2 . . . . .	14
CHAPTER 3	LITERATURE REVIEW	16
3.1	LONG CRACKS . . . . .	16
3.1.1	Introduction . . . . .	16
3.1.2	Near-Threshold Regime . . . . .	17
3.1.3	Paris Regime . . . . .	19
3.1.4	Regime C - Final Failure . . . . .	20
3.1.5	Long Crack Growth In Titanium And Its Alloys . . . . .	20
3.1.5.1	$\alpha$ -Titanium . . . . .	20
3.1.5.2	Titanium Alloys . . . . .	21
3.1.5.2.1	$\alpha+\beta$ Processed Microstructures . . . . .	21
3.1.5.2.2	$\beta$ -Processed Microstructures . . . . .	22
3.1.5.2.3	Comparisons Of $\alpha+\beta$ - And $\beta$ -processed Conditions Within The Same Alloys . . . . .	26
3.1.5.3	Dwell Effects In Titanium Alloys . . . . .	27
3.1.5.4	Summary Of Long Fatigue Crack Behaviour In Titanium Alloys . . . . .	32
3.2	SHORT CRACK BEHAVIOUR . . . . .	34
3.2.1	Introduction . . . . .	34
3.2.2	Reasons For Breakdown In Similitude . . . . .	36
3.2.2.1	Inconsistencies In Mechanical Similitude . . . . .	36
3.2.2.2	Inconsistencies In Microstructural Similitude . . . . .	38
3.2.2.3	Crack Shape And Three-Dimensional Problems . . . . .	38
3.2.3	Initiation Processes . . . . .	39
3.2.3.1	General Initiation Processes . . . . .	39
3.2.3.2	Surface Finish Effects . . . . .	40
3.2.3.3	Short Crack Growth Experiments Involving 'Artificial' Initiation . . . . .	41

3.2.4	Initiation Behaviour In Commercial Purity Titanium . . . . .	44
3.2.5	Initiation Behaviour In $\beta$ -Processed Titanium Alloys . . . . .	44
3.2.5.1	Subsurface Initiation . . . . .	46
3.2.6	Microstructural Effects . . . . .	47
3.2.7	Short Crack Growth Arrest . . . . .	52
3.2.8	Observations On Short Crack Growth Behaviour In Titanium Alloys . . . . .	53
3.2.8.1	Primary $\alpha$ Microstructures . . . . .	54
3.2.8.2	$\beta$ - And $\alpha+\beta$ -processed Microstructures . . . . .	54
3.2.8.3	Summary Of Short Crack Growth Behaviour In Titanium Alloys . . . . .	56
3.2.9	Observations On Short Crack Behaviour In Other Engineering Alloys . . . . .	57
3.2.10	Short Crack Closure/thresholds . . . . .	59
3.2.11	Effect Of Texture . . . . .	61
3.2.12	Effect Of Environment - 'Chemically' Short Cracks	62
3.2.13	Modified Driving Force Parameters For Short Cracks . . . . .	64
 CHAPTER 4            EXPERIMENTAL TECHNIQUES		 66
4.1	HEAT TREATMENTS . . . . .	66
4.1.1	As-received Microstructure . . . . .	66
4.1.2	Aligned Structure . . . . .	67
4.1.3	Coarse Grain Microstructures . . . . .	67
4.1.3.1	Coarse Grain Basketweave Structure . . . . .	67
4.1.3.2	Coarse Grain Aligned Structure . . . . .	68
4.1.4	IMI685 Microstructure . . . . .	68
4.2	SHORT CRACK EXPERIMENTS . . . . .	68
4.2.1	Specimen Preparation . . . . .	68
4.2.2	Four Point Bend Testing . . . . .	69
4.2.2.1	Specimen Size Effects . . . . .	70
4.2.2.2	Low Stress Tests . . . . .	71
4.2.3	Uniaxial Tension Tests . . . . .	71
4.2.4	The Replicating Technique . . . . .	71
4.3	LONG CRACK EXPERIMENTS . . . . .	72
4.4	TENSILE TESTING . . . . .	72
4.5	METALLOGRAPHIC TECHNIQUES . . . . .	73
4.5.1	Preparation For Examination Of Microstructure . . . . .	73
4.5.2	Preparation For Macro-examination Techniques . . . . .	73
4.5.3	Sectioning Techniques . . . . .	73
4.5.4	Crack Shape Measurement . . . . .	74
4.5.4.1	The Crack Face Oxidation Technique . . . . .	74
4.5.4.2	The Crack Sectioning Technique . . . . .	75
4.6	MICROSCOPY . . . . .	75
 CHAPTER 5            TREATMENT OF EXPERIMENTAL SHORT CRACK DATA		 77
5.1	INTRODUCTION . . . . .	77
5.2	FACILITIES WITHIN THE COMPUTER MODEL . . . . .	77
5.2.1	Crack Length Versus Number Of Cycles . . . . .	77



7.3.2	Discussion . . . . .	108
7.4	COMPARISON OF SHORT CRACK DATA WITH LONG CRACK DATA . . . . .	110
7.4.1	Results . . . . .	110
7.4.2	Discussion . . . . .	111
7.5	A CASE STUDY IN IMI685 . . . . .	113
7.5.1	Introduction . . . . .	113
7.5.2	Results . . . . .	114
7.5.3	Discussion . . . . .	115
7.5.3.1	Possible Causes Of The Porosity . . . . .	115
7.5.3.2	Consequences . . . . .	116
7.6	SUMMARY . . . . .	119
CHAPTER 8	CONCLUSIONS	121
CHAPTER 9	FURTHER WORK	123
REFERENCES		126
ACKNOWLEDGEMENTS		136
APPENDIX 1		137

## CHAPTER 1

### INTRODUCTION

Titanium alloys have played an important part in the development of aeroengines in recent years for two main reasons. First and foremost is their superior strength to weight ratio over other alloys in the temperature range concerned. This is illustrated in Fig.1.1. In addition to this they possess excellent corrosion resistance and are therefore ideal materials in the hostile environment of the aeroengine.

Since their introduction into the aeroengine industry in the mid 1950s, their use has grown to an extent so that they now make up approximately 30% of the weight of most modern engines, such as the Rolls-Royce RB211 shown in Fig.1.2. In this particular engine titanium alloys are used for the front fan and for the majority of discs and blades in the compressor section of the engine where temperatures reach 550°C. The  $\alpha/\beta$  alloy IMI318 is used for the fan blades and cooler parts of the compressor whereas near- $\alpha$  alloys such as Ti65s are used for the hotter parts where high temperature creep resistance is required. Under current operating conditions the service lives of Ti65s compressor discs are limited by their low temperature fatigue performance. Fig.1.3 shows a schematic

phase diagram for a titanium alloy to illustrate the terms  $\alpha/\beta$  and near- $\alpha$ .

Components made from Ti65s are  $\beta$ -processed. In the  $\beta$ -processing route components are forged at high temperatures in the  $\beta$  phase field, where the alloy has a body centred cubic structure, and then quenched to produce a transformation to the hexagonal phase,  $\alpha$ , with an aligned or basketweave morphology. The prior  $\beta$ -grain size, which determines the maximum size of the colonies of aligned  $\alpha$ -platelets, is coarse, when compared with the microstructures of  $\alpha/\beta$  titanium alloys, or those produced by other processing routes. Average  $\beta$ -grain sizes are commonly of the order of 1mm, with occasional grains considerably larger.

The two areas of interest to Rolls-Royce involve the development of quality acceptance standards for Ti65s components and the prediction of safe fatigue lives, using fracture mechanics, of these components in service.

The quality acceptance issue arises from the possibility of isolated grains or groups of grains in a component which are significantly larger than average. It is important to know how these large grains are likely to affect the fatigue behaviour of the component so that an acceptance standard can be set which says, for example, that isolated grains up to twice the average grain diameter are tolerable and will not affect component integrity. Such a criterion would need to be based on an understanding of how the presence of these grains affects fatigue life, derived from the results of tests to determine the effect of grain size on fatigue crack initiation and growth in Ti65s.

The other area of direct interest to Rolls-Royce arises from attempts to predict safe component lives, via the integration of conventional fatigue crack propagation data, in the form of crack growth rate  $da/dN$  vs. alternating stress intensity  $\Delta K$  curves. This technique is successfully used to predict the behavior of components made from other alloys with finer grain sizes, but it has been shown to overestimate crack propagation lives in  $\beta$ -processed titanium alloys such as Ti65s, unless very conservative assumptions are made regarding initial crack sizes.

The solution to these problems could be closely linked to an understanding of fatigue crack initiation and the propagation of short fatigue cracks in this alloy. It is this understanding that the project is designed to provide.



## **IMAGING SERVICES NORTH**

Boston Spa, Wetherby  
West Yorkshire, LS23 7BQ  
[www.bl.uk](http://www.bl.uk)

# **MISSING PRINT**

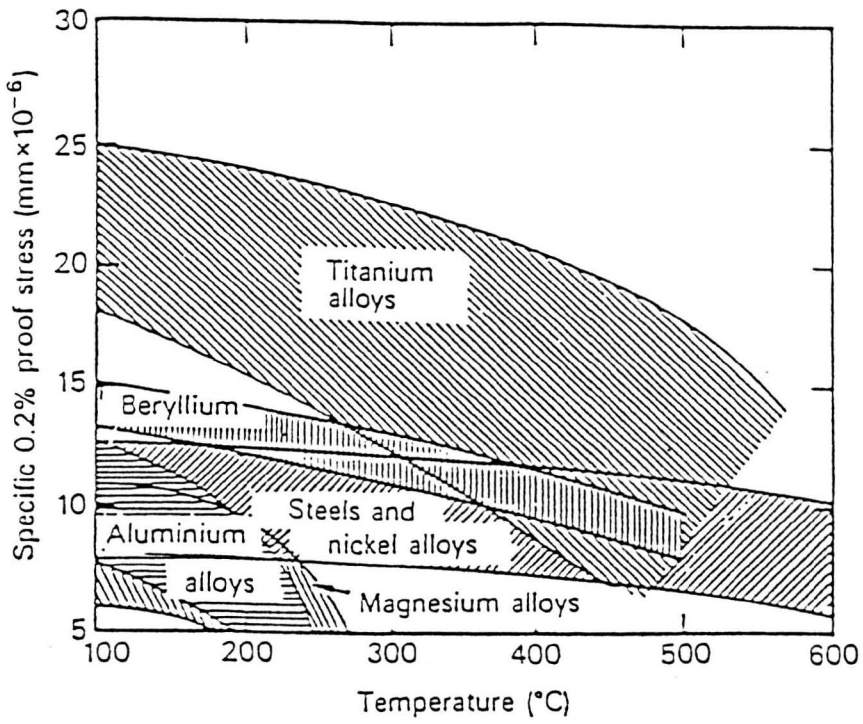


Fig.1.1 Relationship of specific 0.2% proof stress (ratio of proof stress to relative density) with temperature for light alloys, steels and nickel alloys.

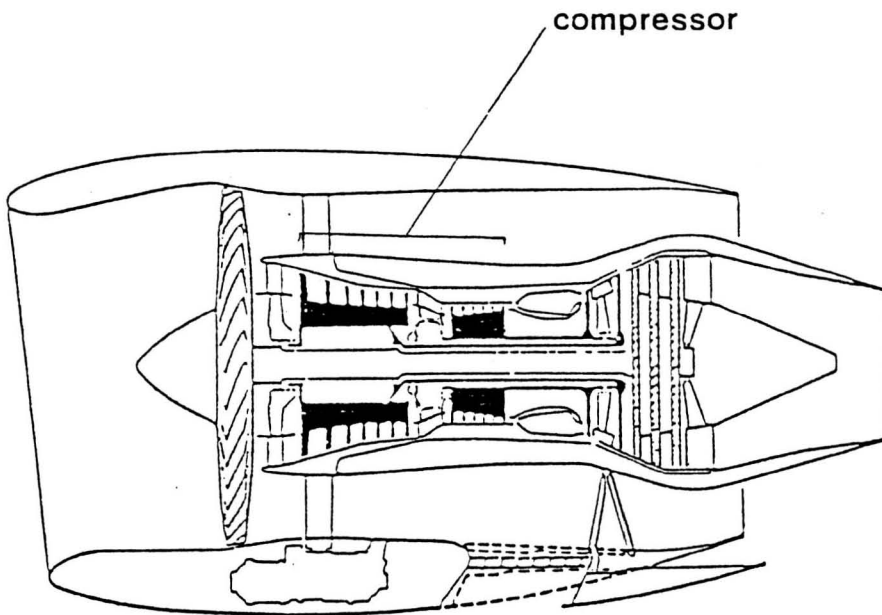


Fig.1.2 Schematic diagram of Rolls-Royce RB211 three shaft turbofan engine.

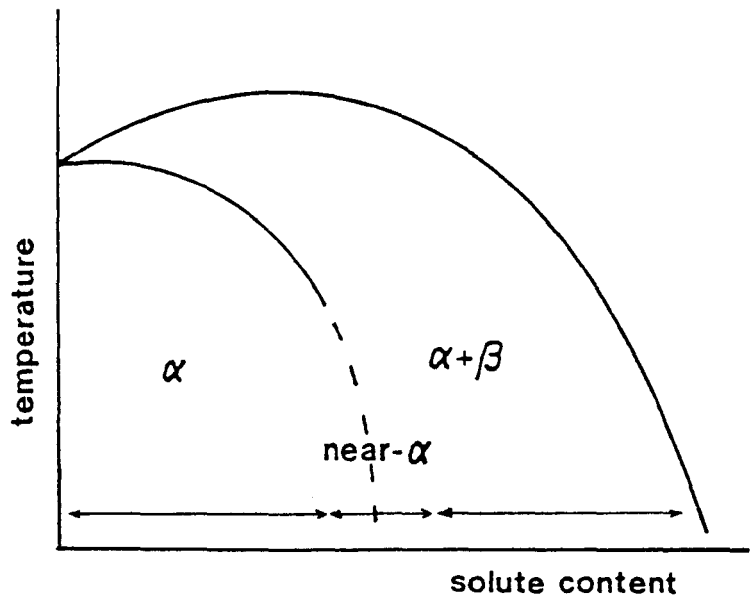


Fig.1.3 Schematic phase diagram for titanium alloys.

## CHAPTER 2

### MATERIALS

#### 2.1 OCCURRENCE AND EXTRACTION OF TITANIUM

##### 2.1.1 Raw Materials

It is not often realised that, although the titanium industry is relatively small, titanium is in fact the fourth most abundant metal in the earth's crust. It occurs mainly in the form of Ilmenite (50-60%  $\text{TiO}_2$ ) and Rutile (95%  $\text{TiO}_2$ ), while other titanium-containing minerals are Anatase ( $\text{TiO}_2$ ), Brookite ( $\text{TiO}_2$ ) and Perovskite ( $\text{CaTiO}_3$ ). Ilmenite is the most common mineral, but most of the metal produced in the West comes from Rutile.

##### 2.1.2 Extraction Technology

Since a direct oxide reduction route is not practical for titanium, the foundations of an acceptable extraction route had to wait until the advent of halide processing. Dr.W.J.Kroll probably made the most important contribution to this in the 1930's, when he successfully reduced titanium tetrachloride ( $\text{TiCl}_4$ ) with magnesium to produce titanium 'sponge', although titanium tetrachloride had been reduced by sodium very much earlier. Sodium

and magnesium reduction of titanium tetrachloride are still the basis of the routes used today.

The Kroll route involves the reduction of titanium tetrachloride by magnesium in argon under carefully controlled conditions to prevent contamination of the titanium product. The reaction product is a mixture of titanium, magnesium chloride ( $MgCl_2$ ) and excess magnesium. Originally, the reaction product was machined out under controlled atmosphere and leached in dilute hydrochloric acid, but this gave 'dirty' sponge from residual magnesium and magnesium chloride. Distillation is now used, which involves distilling off surplus magnesium and magnesium chloride in vacuo. The disadvantage of this is that during distillation the metal sinters together and has to be subsequently crushed before melting.

The only significant modification of the Kroll process has been to use sodium instead of magnesium. This is known as the Hunter process. Sodium reduced titanium is more easily separated by crushing and continuous leaching than magnesium reduced material and, in contrast to the coke-like Kroll sponge, the product is granular. This makes it more easily compacted to electrodes for melting and in addition to this advantage, granules are also better suited to mixing and alloy blending before electrode manufacture, especially for complex alloys.

## 2.2 PROCESSING OF TITANIUM

### 2.2.1 Ingot Production

Difficulties associated with melting titanium in conventional refractories necessitate the procedure of consumable electrode arc melting in vacuum (see Fig.2.1). After appropriate blending, the raw materials are dry pressed to form compacts which are welded together in a plasma welding chamber to produce a consumable electrode for melting. The electrode is then melted inside a water or liquid sodium-potassium eutectic cooled copper crucible to form the ingot. Unlike conventional crucible melting, only a relatively small volume of metal is molten at one time. Therefore the extent of mixing is very limited and the homogeneity of the final ingot depends on the homogeneity of the compacted electrode.

One of the problems which can occur when producing alloys is 'drop-in', whereby a non-molten lump of metal falls from the electrode and remains solid in the molten pool of titanium alloy. If the electrode material has not been mixed sufficiently this can lead to segregation, which may in turn lead to reductions in integrity of final components. A double melting process will reduce the chance of segregation via drop-in, but to ensure still further ingot quality, a triple melting process is now normally employed. The alloys IMI685 and Ti65s are related in this way, the only difference between them being that IMI685 undergoes a double melting process, whereas Ti65s undergoes a triple melting process.

## 2.3 STRUCTURE AND PROPERTIES OF TITANIUM ALLOYS

### 2.3.1 Microstructure

Titanium exists in two structural forms: up to 882°C it exists in the close packed hexagonal form,  $\alpha$ , and above this temperature it exists in the body centred cubic form,  $\beta$ .

The addition of alloying elements, as well as strengthening titanium, can affect the  $\alpha$ - $\beta$  transition and therefore preferentially stabilise one or other of the two phases. As a result of this there are many possible combinations of composition, structure and heat treatment, giving rise to a wide range of alloys, from fully- $\alpha$  to fully- $\beta$  in character and possessing widely differing properties. Basic types of phase diagrams for titanium alloys are shown in Fig.2.2 and typical schematic microstructures obtainable from heat treatments on  $\alpha$ -base alloys are shown in Fig.2.3. Structure (a) consists of equiaxed primary  $\alpha$  grains, typical of commercial purity (CP) titanium, e.g. Ti125. Structure (b) is an  $\alpha$ + $\beta$  structure as a result of solution treating in the  $\alpha$ + $\beta$  phase field. The resulting microstructure is one of regions of primary  $\alpha$  surrounded by transformed  $\beta$  in the form of  $\alpha$ -platelets. This is typical of the  $\alpha$ / $\beta$  alloy Ti-6Al-4V (IMI318). Structures (c) and (d) have undergone  $\beta$  heat treatments, i.e. solution treatment in the  $\beta$  phase field. Structure (c) is one of basketweave  $\alpha$ -platelets, resulting from a fast cooling rate from the solution treatment temperature, and structure (d) is one of colonies of aligned  $\alpha$ -platelets, resulting from a slow cooling rate from the solution treatment temperature. Structures (c) and (d) are typical of near- $\alpha$  alloys such as IMI685. These differences in platelet

morphology can have a substantial effect on the subsequent mechanical behaviour of the alloy. This is illustrated by a plot showing the effect of cooling rate from the solution treatment temperature on the creep properties of IMI685, shown in Fig.2.4. Optimum creep resistance is associated with a 'fast furnace cool', giving a platelet morphology somewhere between aligned and basketweave.

#### 2.3.1.1 Alloying Additions -

The most important  $\alpha$ -stabilising elements are aluminium and oxygen, the most important  $\beta$ -stabilising elements are molybdenum, iron and vanadium. Examples of binary phase diagrams for an  $\alpha$ - and a  $\beta$ -stabilising element are shown in Fig.2.5. In the titanium-aluminium phase diagram (Fig.2.5a) the  $\alpha$  phase field is very prominent, whereas in the titanium-molybdenum phase diagram (Fig.2.5b),  $\beta$  is the equilibrium structure for compositions greater than 15% Mo and the  $\alpha$  phase field is almost non-existent. In addition to  $\alpha$ - and  $\beta$ -stabilising elements there are 'neutral' elements, zirconium and tin, which are in fact weak  $\alpha$ -stabilisers. These are solid solution strengtheners. Table 2.1 lists the influence of some of the more common alloying additions on phase stability.

In both  $\alpha$  and  $\beta$  alloys, there is a practical limit to the amount of stabilising elements that can be added to titanium. In  $\alpha$  alloys, embrittlement occurs due to ordering if the 'aluminium equivalent' exceeds about 9%. Ordering within the  $\alpha$  phase occurs due to the formation of  $Ti_3(Al,Sn)$ , an ordered (DO<sub>19</sub> structure) coherent phase which possesses extremely limited ductility below

600°C and influences planar slip in  $\alpha$ -titanium. The aluminium equivalent, in weight percent, is given as:

$$\text{Al} + \text{Sn}/3 + \text{Zr}/6 + 10(\text{O}+\text{C}+2\text{N}) = \text{Al equivalent} \quad (2.1)$$

The addition of  $\beta$ -stabilising elements is limited due to embrittlement caused by the precipitation of intermetallic phases such as  $\text{TiCr}_2$  and the  $\omega$  phase. (The  $\omega$  phase forms as homogeneously nucleated, coherent precipitates, probably possessing a hexagonal structure.)

Titanium alloy development in the U.K. aeroengine industry has centred on achieving high temperature creep resistance. In this area  $\beta$  alloys were found to be greatly inferior to  $\alpha$  alloys, so development has centred around alloys based on the  $\alpha$  phase.

### 2.3.2 Structure And Properties Of Ti65s

Ti65s is a near- $\alpha$  alloy, whose nominal composition and typical mechanical properties are given in Table 2.2. The main alloying addition is that of aluminium, an  $\alpha$ -stabiliser. The  $\beta$ -stabilizing element molybdenum is added in a relatively small quantity to limit the amount of  $\beta$ -phase present and therefore improve creep resistance. Zirconium is added to give solid solution strengthening of the  $\alpha$ -phase along with silicon. In near- $\alpha$  alloys, above 500°C, some silicide precipitation occurs in the form of  $(\text{Ti},\text{Zr})_5\text{Si}_3$ . This increases creep resistance by dispersion strengthening, as does spheroidising of the thin film of  $\beta$  phase surrounding the  $\alpha$ -platelets. To gain maximum benefit from the silicon additions and to reduce the amount of  $\beta$  phase present after solution treatment the alloy is solution treated in

the  $\beta$  phase field. This leads to improved creep resistance but can have a detrimental effect on fatigue resistance.

### 2.3.3 $\beta$ Heat Treatment Of Ti65s

The material is solution treated in the  $\beta$  phase field to give equiaxed  $\beta$ -grains with a grain size dependent on both time and temperature above the  $\beta$  transus. After the solution treatment the material is cooled to room temperature to form colonies of  $\alpha$  platelets within the prior  $\beta$ -grains. The degree of alignment of the  $\alpha$ -platelets is controlled by the cooling rate; a fast cooling rate will produce a basketweave Widmanstatten structure (Fig.2.3c), whereas a slow cooling rate such as a furnace cool results in a structure of aligned  $\alpha$ -platelets (Fig.2.3d). The cooling rate from the  $\beta$  phase field also affects the  $\beta$ - $\alpha$  transformation. A very fast cooling rate produces hexagonal martensitic  $\alpha'$  which can be subsequently tempered. The final stage of the treatment is tempering of the material at 550°C for 24 hours. This reduces quenching stresses and causes any  $\alpha'$  present to transform to  $\alpha$ . Any  $\beta$  phase which may be present at the  $\alpha$ -platelet boundaries as a thin film, is partly broken up and spheroidized. In Ti65s, there is virtually no  $\beta$  phase present in the final microstructure.

Heat treatments used and the microstructures studied for this report will be discussed in Chapter 4.

## 2.4 DEFORMATION MECHANISMS

### 2.4.1 Hexagonal Metals

The important parameter in the plastic deformation of hexagonal metals is the  $c/a$  ratio. This can vary considerably around 1.633, the value for an ideally close packed lattice of hard spheres. Zinc and cadmium show  $c/a$  ratios as high as 1.856 and 1.886 respectively, while in beryllium the value is as low as 1.567. The changes in crystal geometry dictate which of the crystal planes are the most closely packed, which then influence the slip behaviour of the material during plastic deformation. Fig.2.6 shows the hexagonal close packed unit cell along with the important crystal planes. In an ideal close packed hexagonal structure the closest packed plane will be the basal plane (0001). The parameter  $c$  is the distance between the first and third layer of atoms while the parameter  $a$  is the distance between atoms along the basal plane in any of the 'close packed' directions  $\langle 11\bar{2}0 \rangle$ . As the  $c/a$  value is altered from the ideal value, the relative close packing of the crystal planes will vary.

Table 2.3 shows the relative packing densities along with ease of operation of slip planes for four different hexagonal close packed metals including titanium, assuming the basal plane packing density to be unity. The data for titanium shows that for pure titanium the prism plane and not the basal plane is the one on which slip most readily occurs. It should be noted that the packing densities for the prism and pyramidal planes in Table 2.3 have been calculated assuming the atoms at the  $c/2$  position in the lattice to be involved. This has the effect of producing 'corrugated' slip planes, as illustrated in Fig.2.7.

#### 2.4.2 Titanium

The crystallography of slip in pure titanium is heavily influenced by the concentration of interstitial impurity atoms, especially oxygen and nitrogen. Crystals with an interstitial content of less than 0.01wt% - corresponding to a c/a ratio of 1.587 - tend to deform primarily on the prism planes, although some basal slip does occur. With less pure metal, containing 0.1wt% interstitial impurities, slip has been observed to occur on the  $\{10\bar{1}1\}$  pyramidal planes. Table 2.4 shows some critical resolved shear stresses for different slip planes and different interstitial impurity concentrations in titanium crystals. In the more pure metal the critical resolved shear stress  $\tau_0$  for prismatic slip is well below that for basal slip but there is not such a marked difference in the less pure metal. This is thought to be due to the greater effect of interstitial oxygen atoms on the movement of dislocations along  $\{10\bar{1}0\}$  prism planes, than on dislocations moving on  $\{10\bar{1}1\}$  pyramidal planes.

In general, problems associated with the limited availability of slip systems for deformation in hcp titanium can be practically avoided by deforming the metal in the  $\beta$ -phase field, where the metal is bcc in form. The limited number of slip systems available in hcp titanium and the fact that all slip directions are within the basal plane, means that twinning plays an important role during the deformation of hcp titanium. Twinning planes in hcp titanium are the  $\{10\bar{1}2\}$ ,  $\{11\bar{2}1\}$ ,  $\{11\bar{2}2\}$  and  $\{11\bar{2}3\}$  planes, but twinning is most frequently observed on the  $\{10\bar{1}2\}$  and  $\{11\bar{2}1\}$  planes. Grain orientation has a strong effect on the likelihood of twinning. It has been observed that, when the basal plane is more

nearly parallel to the stress axis, deformation occurs almost entirely by slip, whereas a basal plane orientation more nearly perpendicular to the stress axis results in deformation predominantly by twinning, after an initial extension due to basal plane slip.

## 2.5 SUMMARY

It is clear that the chemical and physical aspects of titanium involve a good deal of complexity. At the same time, they offer a good deal of versatility, so that a wide range of properties are available from alloying and heat treatment of titanium. It is worth remembering also that a constant dilemma for the materials scientist is that of compromise. Improvement of a relevant material property for a certain application is usually at the expense of one or more other properties. This is illustrated for the case of near- $\alpha$  alloys by Fig.2.8, where  $\beta$  heat treatment leads to an increase in creep strength over  $\alpha+\beta$  heat treatment, but also leads to inferior low cycle fatigue lives.

## 2.6 BIBLIOGRAPHY FOR CHAPTER 2

1) **I.J.Polmear**

Light Alloys - Metallurgy of the Light Metals, Edward Arnold, 1981.

2) **P.A.Blenkinsop, D.F.Neal, R.E.Goosey**

Titanium and Titanium Alloys, Plenum Press, 1976, p2003.

3) **A.D.McQuillan, M.K.Mcquillan**

Metallurgy of the Rarer Metals 4 - Titanium, Butterworths, 1956.

4) **R.W.K.Honeycombe**

The Plastic Deformation of Metals, Edward Arnold, 1968.

5) **P.A.Blenkinsop**

Developments in High Temperature Alloys, Titanium Science and Technology, Vol.4, 1984, p2323.

6) **C.Ramachandra, V.Singh**

Scripta Metallurgica, vol.21 (1987), p.633.

7) **P.Hallam, K.Parker, P.J.Postans**

'Forging and Properties of Aerospace Materials', (proc. conf.), The Metals Society, London, U.K. (1977), p.217.

8) **G.Sridhar, V.V.Kutumbarao, D.S.Sarma**

Met. Trans. A, vol.18A (1987), p.877.

9) **J.E.Coyne**

'Forging and Properties of Aerospace Materials', (proc. conf.), The Metals Society, London, U.K. (1977), p.234.

10) T.W.Farthing

'The Metallurgy of Light Alloys' (proc. conf.), The Institution of Metallurgists (1983), p.252.

11) M.W.Kearns

'The Metallurgy of Light Alloys' (proc. conf.), The Institution of Metallurgists (1983), p.105.

---

Publications listed in this bibliography are referenced using round brackets, e.g. (4). These publications are only referred to in the figures for this chapter.

Table 2.1 Influence of some of the more common alloying elements on the phase stability of titanium alloys (11).

$\alpha$ stabilisers	Al C O N							
$\beta$ stabilisers	$\beta$ eutectoid						$\beta$ isomorphous	
	Fe	Mn	Co	Ni	Cr	W	Mo	V Nb Ta
Neutral additions	Sn Zr							

Table 2.2a Nominal composition of Ti65s (wt.%).

Al	Zr	Mo	Si	Fe	Hf	Ti
6.0	5.0	0.5	0.25	0.2	100ppm	bal.

Table 2.2b Typical mechanical properties of Ti65s.

UTS(MPa)	0.2% proof stress(MPa)	elongation(%)
1020	900	12

Table 2.3 Relative packing densities along with ease of operation of slip planes for four different hexagonal close packed metals (4).

Metal	c/a	Packing densities			Observed slip planes in order of ease of operation		
		(0001)	{10 $\bar{1}$ 0}	{10 $\bar{1}$ 1}			
Cadmium	1.886	1.000	0.918	0.816	(0001)	(1 $\bar{1}$ 00)	(10 $\bar{1}$ 1)
Zinc	1.856	1.000	0.933	0.846	(0001)	(1 $\bar{1}$ 00)	( $\bar{1}$ $\bar{1}$ 22)
Magnesium	1.624	1.000	1.066	0.940	(0001)	(10 $\bar{1}$ 1)	(1 $\bar{1}$ 00)
Titanium	1.587	1.000	1.092	0.959	(1 $\bar{1}$ 00)	(0001)	( $\bar{1}$ 011)

Table 2.4 Critical resolved shear stresses for different slip planes and different interstitial impurity concentrations in titanium crystals (4).

Slip plane	$\tau_0$ , g/mm <sup>2</sup>	
	0.01% O and N	0.1% O and N
{1 $\bar{1}$ 00}	1400	9190
{0001}	6300	10900
{10 $\bar{1}$ 1}	--	9900

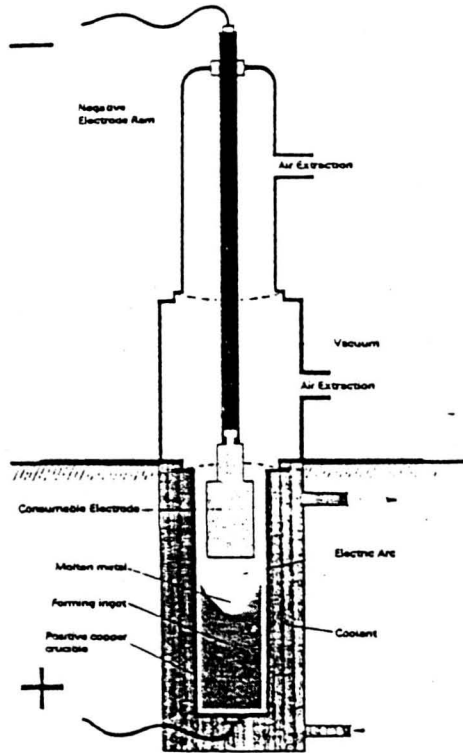


Fig.2.1 Vacuum arc melting furnace for titanium (10).

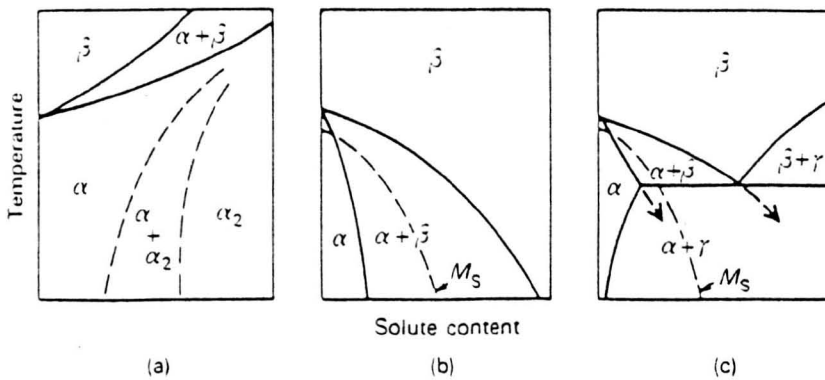


Fig.2.2 Basic types of phase diagrams for titanium alloys (1). The dotted phase boundaries in (a) refer specifically to the Ti-Al system. The dotted lines in (b) and (c) show the martensite start ( $M_s$ ) temperatures. Alloying elements favouring the different types of phase diagram are: a) Al, O, N, C, Ga; b) Mo, V, W, Ta; c) Cu, Mn, Cr, Fe, Ni, Co, H.

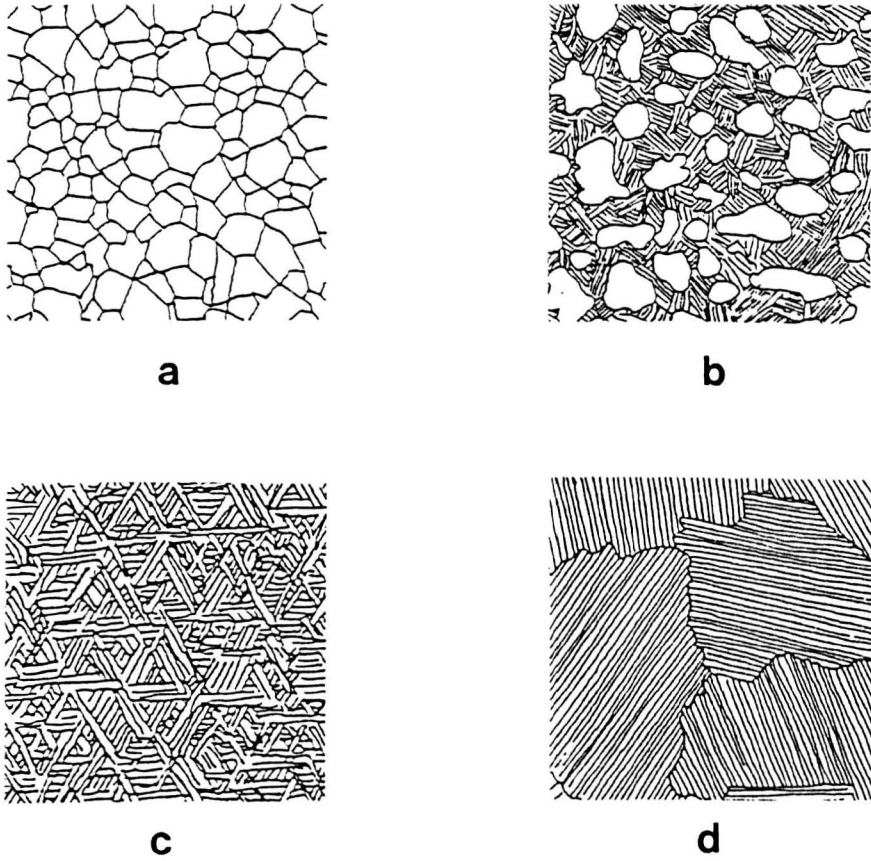


Fig.2.3 Typical schematic microstructures obtainable from heat treatments on  $\alpha$ -base alloys: a) equiaxed primary  $\alpha$  structure, b)  $\alpha+\beta$ -processed structure, c)  $\beta$ -processed structure (fast cooling rate from  $\beta$  solution treatment temperature), d)  $\beta$ -processed structure (slow cooling rate from  $\beta$  solution treatment temperature).

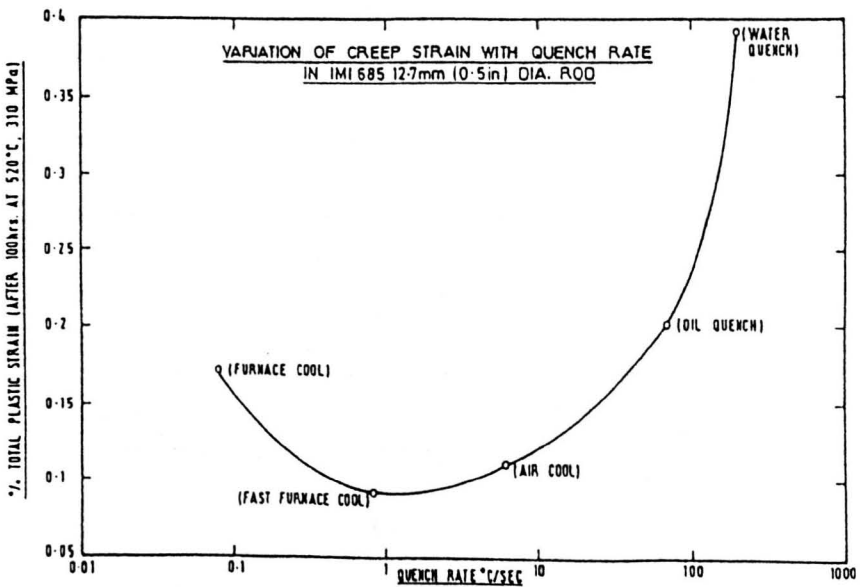
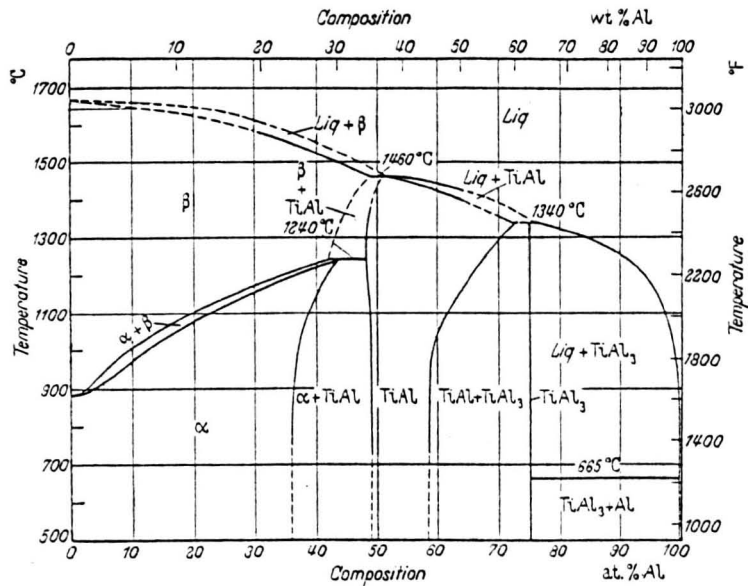
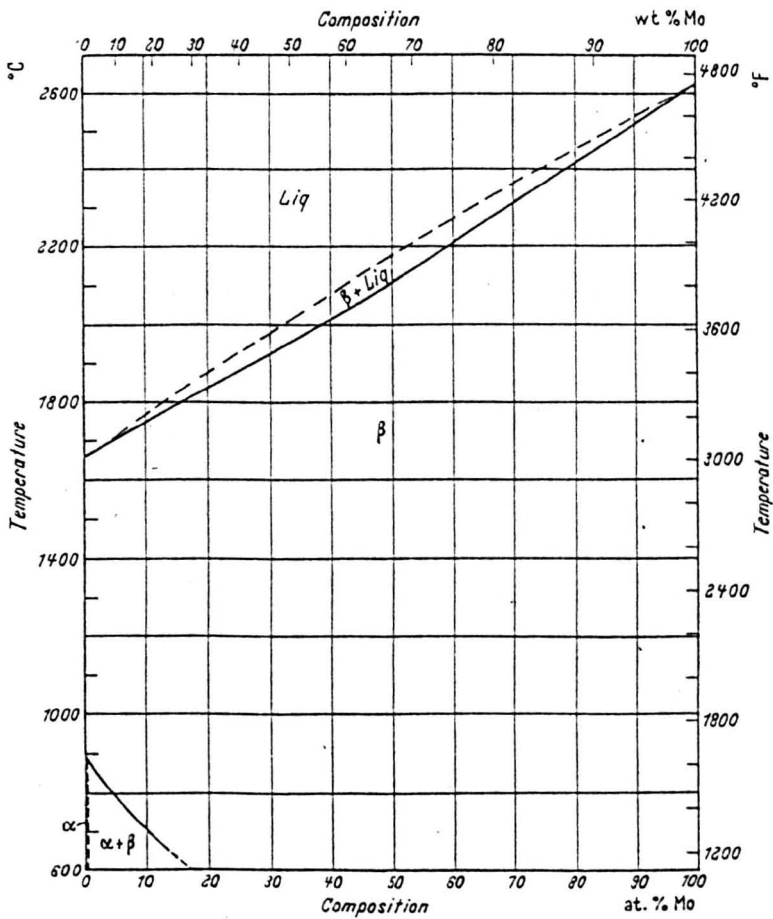


Fig.2.4 Effect of cooling rate after solution treatment on the creep properties of IMI685 (5).



a



b

Fig.2.5 Binary phase diagrams for a) the titanium-aluminium system and b) the titanium-molybdenum system (3).

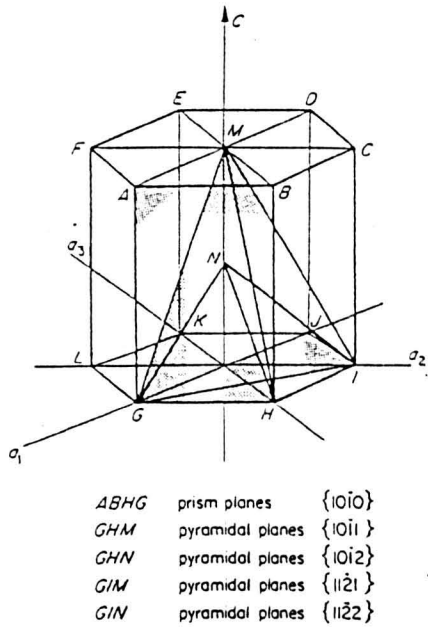


Fig.2.6 The hexagonal close packed unit cell, along with important crystal planes (4).

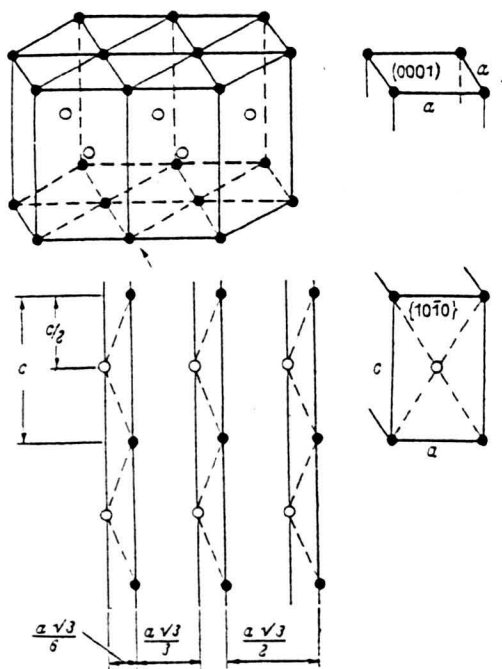


Fig.2.7 Crystal structure of  $\alpha$ -titanium illustrating the arrangement of atoms in 'corrugated' configuration (3).

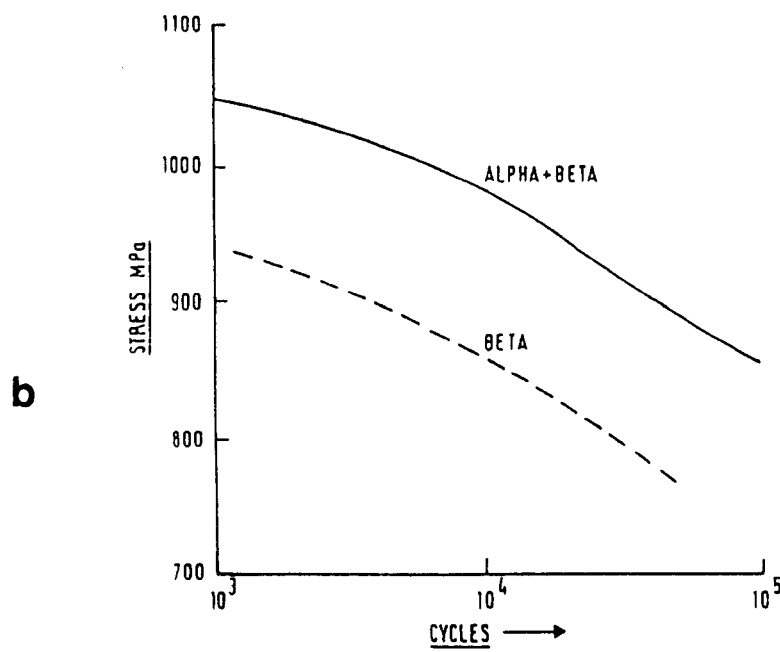
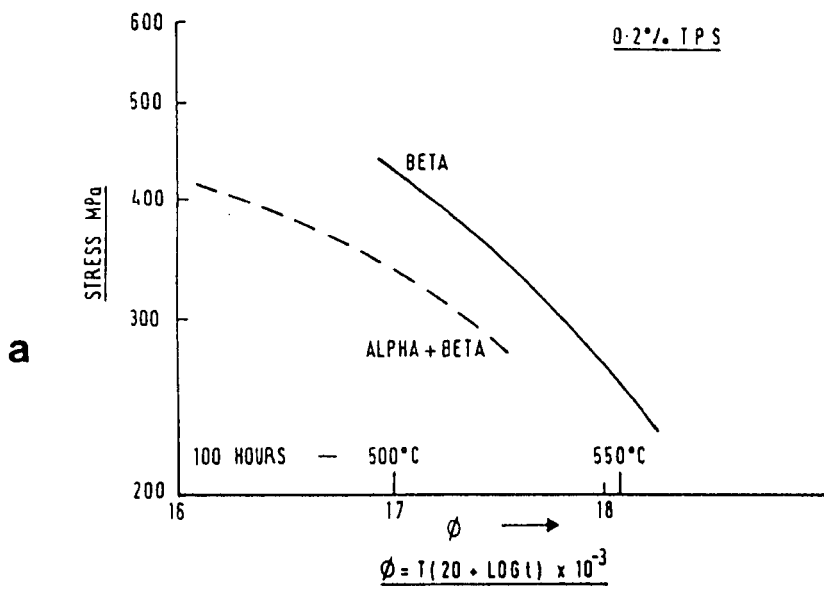


Fig.2.8 Comparison of creep strengths (a) and low cycle fatigue lives (b) for  $\alpha+\beta$  and  $\beta$  heat treatments in a near- $\alpha$  alloy (5).

CHAPTER 3  
LITERATURE REVIEW

3.1 LONG CRACKS

3.1.1 Introduction

The understanding of fatigue crack growth is important when applied to modern aircraft engines, as there is an increasing need to design components which are comparatively light and capable of operating at both high temperatures and stresses, whilst ensuring that an appropriate factor of safety is included. This is especially important in the case of turbine and compressor discs, because the kinetic energy which these acquire during service means that they cannot be contained within the engine casing if they fail.

A fracture mechanics approach is employed to model fatigue behaviour of components in service using long crack data from laboratory tests on specimens of the same material as the relevant component. The long crack data can be plotted in the form of a crack growth rate ( $da/dN$ ) vs. alternating stress intensity range ( $\Delta K$ ) curve. The general form of the curve is shown in Fig.3.1. Prediction of component fatigue life is then carried out using a

'defect-tolerant' approach. This assumes there will be a defect present in the material which is the same size as the smallest detectable NDI dimension. The number of stress cycles for a defect of this size to grow to failure can then be determined by integrating the long crack curve. The defect tolerant approach is shown schematically in Fig.3.2. The basic form of the  $da/dN$  curve for long cracks can be divided into three distinct regions - the near threshold regime, the Paris regime and the final failure regime in which the maximum stress intensity at the crack tip approaches the fracture toughness of the material.

### 3.1.2 Near-Threshold Regime

The near-threshold regime is of particular interest, as the majority of the fatigue life of a component which possesses a crack will be spent with the crack in this regime. Near-threshold crack growth is found to be strongly dependent on microstructure, mean stress (e.g.[3-6]) and environment (e.g.[5-7]).

One of the most important features of crack behaviour in this regime is the phenomenon of crack closure. The concept of crack closure was first described by Elber [8] for crack growth at high stress intensities. The phenomenon arises from contact of the fracture surfaces in the wake of the advancing crack tip. This leads to the possibility of the crack being effectively closed at positive loads above the minimum load during the stress cycle. This decreases the stress intensity range  $\Delta K$  and affects the reverse or cyclic plastic zone at the tip of the crack. Hence the driving force for crack growth is reduced. Ritchie and Suresh [9,10] suggested several models for closure: roughness induced

closure, plasticity induced closure (Elber's concept) and debris induced closure (eg. oxide, corrosion deposits). The parameters  $K_{max}$ ,  $K_{min}$ ,  $K_{cl}$ ,  $\Delta K$  and  $\Delta K_{eff}$  are illustrated in Fig.3.3, along with schematics of the simple closure mechanisms.

A more recent modification is that of crack shielding, as described by Ritchie and Yu [11], who proposed mechanisms of extrinsic and intrinsic toughening. Intrinsic toughening is achieved by increasing the inherent microstructural resistance eg. coarsening particle spacings, or increasing ductility. Extrinsic toughening is due to crack tip shielding - crack extension is impeded by mechanical, microstructural and environmental factors which locally reduce the crack driving force.

Different micromechanisms for crack tip shielding, shown in Fig.3.4a, are: a) crack deflection and meandering, b) inelastic or dilated zones surrounding the wake of the crack ('zone shielding'), c) wedging, bridging and/or sliding between crack surfaces ('contact shielding'), d) combined zone and contact shielding. The effects of crack tip shielding mechanisms on crack driving force,  $K$ , can be seen in Fig.3.4b.

The direct implications of shielding for crack propagation are to reduce crack propagation rate because of the lower local driving force and to cause behaviour dependent on crack length, as the shielding mechanisms are active in the wake of the crack. In a monotonic loading situation this leads to R-curve toughness behaviour, where the driving force to sustain cracking will increase with increasing crack length (until steady state). This is paralleled in fatigue by increasing threshold with crack length. Therefore shielding can be used to explain the effects of

microstructure, load ratio R, mean stress and environment. Microstructural effects are related to crack deflection and, indirectly, to crack face roughness. Reductions in load ratio are associated with greater amounts of contact shielding and zone shielding due to crack wake plasticity. Environmental factors are associated with corrosion debris or oxide induced closure and wedging and bridging due to fluid pressure induced closure.

### 3.1.3 Paris Regime

The Paris regime - region B in Fig.3.1 - is so called because the equation to describe crack growth behaviour in this region was derived by Paris [12]. In this region crack growth behaviour can be described by the following relationship

$$\frac{da}{dN} = C.\Delta K^m \quad (3.1)$$

where C and m are constants. On a log-log plot this behaviour is represented by a straight line of slope m which intersects the growth rate axis at log.C. Typical m values for titanium alloys are between m=2 and m=8 [13,14].

In the Paris region the influences of microstructure, mean stress and dilute environment on fatigue crack growth are minimal, and continuum mechanisms are in operation. This type of growth is often characterised by the appearance of striations on the fracture surface. These striations are formed by a plastic blunting process. If this process was entirely plastic then we would expect a value for m of 2, but in most cases, as can be seen above, m values in titanium alloys are substantially higher than

this. This suggests that Paris regime crack growth in titanium alloys is only partially plastic in character.

#### 3.1.4 Regime C - Final Failure

In addition to fatigue mechanisms, in this region static mode mechanisms are in operation, ie. those mechanisms which are characteristic of monotonic, rather than cyclic, stress conditions, such as cleavage, intergranular and fibrous crack growth. Microstructure, mean stress and specimen thickness have a large effect on crack behaviour in this region.

#### 3.1.5 Long Crack Growth In Titanium And Its Alloys

This section considers general observations and conclusions from studies on long fatigue crack growth behaviour in titanium alloys.

##### 3.1.5.1 $\alpha$ -titanium -

Robinson and Beevers [15] drew the following conclusions from long crack tests on  $\alpha$ -titanium. Decreasing load ratio  $R$ , increasing grain size and increasing interstitial alloying content all produced significant reductions in fatigue crack propagation rates in air at  $\Delta K$  values between 4 and 20  $\text{MNm}^{-3/2}$ . The fatigue fracture process involved the formation of faceted regions (mainly  $\Delta K$  controlled) and their interconnection by localised plastic tearing (mainly  $K_{\text{max}}$  controlled). Grain orientation control of the fracture path was visible in all specimens, especially at low  $\Delta K$  values. This occurred when the extent of reversed plasticity at the crack tip was of the order of, or less than the grain size.

Walker and Beevers [16] conducted further experiments to study the closure behaviour of CP titanium. It was deduced that crack closure was caused by deviations in the crack path associated with transgranular growth. Crack growth rate data at different R ratios were brought together to show a singular dependence on the empirically derived parameter  $\Delta\theta$ .  $\Delta\theta$  was defined as being roughly the change in the angle subtended by the crack faces, but was actually calculated by normalising the change in crack mouth opening displacement, CMOD, with respect to the distance of the transducer armature from the crack tip in their experimental set-up (shown in Fig.3.5). When no closure occurred  $\Delta\theta$  was directly proportional to  $\Delta K$  and it was suggested that in the presence of closure the measured value of  $\Delta\theta$  reflected the effective stress intensity amplitude  $\Delta K_{eff}$ .

#### 3.1.5.2 Titanium Alloys -

Whilst the microstructure of CP titanium is quite simple (ie. equiaxed grains), those of  $\alpha$ ,  $\alpha+\beta$  and  $\beta$  titanium alloys are a good deal more complex. Long crack behaviour in some of these alloys, especially Ti-6Al-4V (IMI318), is now considered.

##### 3.1.5.2.1 $\alpha+\beta$ Processed Microstructures -

Irving and Beevers [5,17] found with  $\alpha+\beta$  processed Ti-6Al-4V that microstructural changes strongly affected  $da/dN$  in the threshold region. The microstructures considered were  $\alpha$  with a small quantity of discontinuous  $\beta$  in the boundaries,  $\alpha$  plus transformed  $\beta$ ,  $\alpha$  plus tempered martensite and a  $\beta$ -annealed microstructure. Crooker and Krause, however, found no strong

microstructural effects [18]. Rosenfield [13] pointed out that this situation was compounded because such a region of very low growth rates was likely to be where experimental errors were greatest. Irving and Beevers showed that microstructural variations could produce variations in crack growth rate by a factor between 3 and 10 when testing at  $R=0.35$ . Above a critical  $\Delta K$  value of  $10-12\text{MNm}^{-3/2}$  the effects disappeared and growth became structure insensitive. This value of  $\Delta K$  corresponded for all the microstructures with the cyclic plastic zone size being equal to the  $\alpha$ -grain size of the microstructure in question. They described the process in terms of a two stage model for structure sensitive crack growth. These conclusions were also drawn from their work on  $\alpha$ -titanium [15] (section 1.2.1.1).

Yuen et al [19] studied Stage II fatigue crack propagation in Ti-6Al-4V which had been forged in the  $\alpha+\beta$  phase field (giving a microstructure consisting of primary  $\alpha$  + transformed  $\beta$ ). From observations on fracture surfaces they found that Stage II fatigue crack propagation underwent a transition in appearance from 'cyclic cleavage' (corresponding to Stage I, crystallographic growth) to striations at a  $\Delta K_{\text{eff}}$  of approximately  $13\text{MNm}^{-3/2}$ . This was when the cyclic plastic zone size was approximately equal to the  $\alpha$ -grain size, believed to correspond with a change from primarily single to multiple slip within the individual grains at the crack tip.

#### 3.1.5.2.2 $\beta$ -Processed Microstructures -

Yoder, Cooley and Crooker [14] looked at the behaviour of a

number of different microstructural variants of Ti-6Al-4V and Ti-8Al-1Mo-1V, which had all been given a  $\beta$  heat treatment but with different resultant Widmanstätten colony sizes. The growth rate plot for each alloy exhibited a bi-linear form with a distinct transition evident at a value  $\Delta K_t$ , such that both mean packet size and cyclic plastic zone size were equal. Exponents (values of  $m$  in the Paris equation) were calculated in both the hypotransitional region ( $\Delta K$ s less than  $\Delta K_t$ ) and the hypertransitional region ( $\Delta K$ s greater than  $\Delta K_t$ ). Exponents in the hypertransitional region varied inversely with the degree of clustering of packet sizes about the mean value. This was attributed to a remnant of structure-sensitive growth which occurred in the nominally structure-insensitive hypertransitional region. Hypotransitional exponents were significantly larger than hypertransitional exponents, owing to crystallographic bifurcation of the Widmanstätten packets in the structure sensitive, hypotransitional region. The larger colonies permit larger bifurcations which serve to reduce the effective  $\Delta K$ , increase crack path tortuosity and thus decrease  $da/dN$ . Their results are summarised in Fig.3.6.

In a later report [20] by the same authors it was noted that increasing load ratio had little effect on the influence of mean Widmanstätten packet size on crack growth rates in  $\alpha+\beta$  titanium alloys. In addition to this, and quite significantly, there appeared to be no load ratio 'saturation' effects over the range of  $R$  values from 0.1 to 0.7. This conflicted with reports from other authors [15,17,21] who noted that  $da/dN$  vs.  $\Delta K$  curves tended to coincide above an  $R$  of 0.35.

It was discovered by Chesnutt and Wert [22] that the fatigue crack propagation behaviour of  $\beta$ -processed microstructures in Ti-6Al-4V was dependent on load ratio. The three structures studied were  $\beta$ -forged,  $\beta$ -annealed and  $\beta$ -quenched. The  $\beta$ -quenched condition exhibited the fastest growth rates at both high and low load ratios. Their results, shown in Fig.3.7, showed that the  $\beta$ -forged condition was the most crack propagation resistant at a low load ratio ( $R=0.1$ ). The  $\beta$ -annealed condition, consisting of aligned platelets but with smaller colony size than the  $\beta$ -forged, showed the greatest propagation resistance of the three conditions at a high load ratio ( $R=0.75$ ).

Yoder and Eylon linked the kind of behaviour that had been seen in  $\beta$ -processed titanium alloys with the very sound argument [23] for colony size being thought of as an effective grain size. Intense shear bands, slip lines and slip related cracks had been seen in many cases to extend across a colony, seemingly uninhibited by the  $\alpha/\beta$  interfaces. Such behaviour is consistent with the fact that a colony of similarly aligned  $\alpha$ -platelets which transform from the  $\beta$  phase according to the Burgers relation [24,25] is of a single orientation [26,27]. The Burgers orientation relationship is

$$\begin{aligned} & \{110\}\beta \parallel (0001)\alpha \\ & \langle 111 \rangle\beta \parallel \langle 11\bar{2}0 \rangle\alpha \end{aligned}$$

Moreover, the yield strength has been found to depend on colony size in a way similar to a Petch-type relationship [28].

Postans and Jeal [29] compared basketweave and aligned  $\alpha$ -platelet morphologies in  $\beta$ -processed IMI685. Extensive crack branching was observed, typical of transformed  $\beta$  microstructures, occurring when two potential crack paths presented to the crack tip were equally favourable. They found that growth rates in the aligned structure were in fact lower than in the basketweave structure. They suggested that this was due to either the increased stopping power of a large colony boundary in the aligned structure, because of potentially larger grain boundary misorientations, or to the coarse aligned structure causing large deviations in the crack path and thus increasing the total crack length. This would be particularly important near threshold where a greater degree of crack deflection would lead to an increase in roughness-induced closure.

Eylon and Hall [30] found that fatigue lives were longer for basketweave structures than for aligned structures in IMI685. At first sight, this would appear to contradict the results of Postans and Jeal, but the results of Eylon and Hall were from S-N tests, involving both initiation and propagation, whilst those of Postans and Jeal were from fatigue crack propagation tests, involving no initiation stage. Eylon and Hall deduced from fractographic examination that crack propagation processes were dominated by crack growth related to intense shear across the colonies. A decrease in colony size (of which the extreme would be basketweave microstructure) reduced the slip band length and inhibited fatigue crack initiation by limiting the size of the shear-related initial crack. The result was a higher LCF life.

Hicks et al [31] studied near-threshold fatigue crack growth behaviour in IMI685. Their conclusions were that fatigue crack growth rates and  $\Delta K_{th}$  in IMI685 were influenced by microstructure, test environment and load ratio. The mean stress effect on fatigue crack growth rate and  $\Delta K_{th}$  could be directly attributed to the occurrence and magnitude of closure. The extent of closure varied with crack length and microstructure, reflecting crack path tortuosity and number of closure points. Relatively high  $\Delta K_{th\text{eff}}$  values in IMI685 were considered to be related to the dominant transgranular crack path and the occurrence of crack branching.

Plumbridge and Stanley [32] came up with a somewhat surprising observation from LCF experiments on IMI829, namely that the microstructural variations between the aligned and basketweave states in the  $\beta$ -processed microstructure had no effect on endurance and cyclic stress response, either at room temperature or 600°C. This may be explained by the fact that the 'basketweave' condition contained 75% of basketweave  $\alpha$  with the rest in a fairly aligned state. Intense slip across an  $\alpha$  colony is normally associated with the aligned platelet morphology, so it was suggested by the authors that the 'basketweave' condition contained a sufficient number of large aligned colonies to be able to accommodate the plasticity in a planar manner.

#### 3.1.5.2.3 Comparisons Of $\alpha+\beta$ - And $\beta$ -processed Conditions Within The Same Alloys -

Chesnutt and Wert [22] studied Ti-6Al-4V plate in several different microstructural conditions, these being recrystallisation annealed (RA),  $\beta$ -annealed (BA) and solution

treated and overaged (STOA). They observed the following rankings for near threshold growth: STOA - fastest growth rate and smallest  $\Delta K_{th}$ , RA - intermediate growth rate and  $\Delta K_{th}$ , BA - slowest growth rate and largest  $\Delta K_{th}$ . The controlling microstructural features were: RA - mean linear intercept distance through  $\alpha$  particles, BA - Widmanstätten  $\alpha$ -colony size, STOA - mean linear intercept distance through  $\beta$  phase.

Peters et al [33] looked at the fatigue crack growth behaviour of Ti-6Al-4V in two microstructural forms, fine equiaxed, an  $\alpha+\beta$  - heat treated condition, and coarse lamellar, a  $\beta$ -heat treated condition. They found that, even at a high R ratio of 0.8, crack growth rates for the coarse lamellar structure were substantially lower than for the fine equiaxed, therefore eliminating closure as a factor and showing that the differences were likely to be due primarily to microstructure. Similar results were found for Ti-8Al-1Mo-1V [20]. In their study, Peters et al made some interesting observations by using quantitative methods to describe the differences between the two conditions in terms of actual crack paths on a microscopic scale and the 'effective' stress intensity,  $\Delta K_{1eff}$ , acting in the macroscopic crack plane (ie. normal to the applied stress direction). In terms of a 'fracture surface creation rate' and an 'effective' stress intensity, it was found that the high R ratio data (where no closure effects were present) for the two microstructural conditions could be brought together.

### 3.1.5.3 Dwell Effects In Titanium Alloys -

A substantial amount of work has been carried out by various authors into the effects of using a trapezoidal waveform for applied stress in laboratory fatigue tests. The logic behind this is that the loading pattern resembles more closely the actual loading pattern experienced by components in service: a load is applied at take-off, which will be reduced somewhat during cruising and removed on landing. The period during which the load is held at a constant level is normally termed the hold time or dwell time.

From the work carried out on the effect of dwell periods it has become clear that the application of a dwell period to the stress cycle during fatigue can reduce fatigue lives.

Ryder et al [34] conducted fatigue crack propagation experiments on IMI685 to determine the effect of microstructure, dwell time, temperature and environment. They found that a 5 minute hold time at maximum load markedly increased the slope of the  $da/dN$  vs.  $\Delta K$  curve relative to baseline data at 10Hz and  $R=0$ . The effect of dwell time was found to decrease with increasing temperature above 150°C.

Postans and Jeal [29] also studied dwell behaviour of IMI685 in fatigue crack propagation tests at room temperature with  $R=0.1$  and 0.25Hz for the baseline test conditions. It was found that for an aligned  $\alpha$ -platelet microstructure there was a large increase in crack growth rate in response to a 5 minute dwell at maximum load. For a Widmanstätten microstructure in the same alloy, however, no dwell effect was observed. This was thought to be related to

intense basal plane shear across colonies of aligned  $\alpha$ -platelets being easier than across colonies of basketweave platelets. Introducing a hold on load resulted in cracks having an increased tendency to move through  $\alpha$ -colonies on basal planes rather than other slip planes, both in aligned and basketweave structures, but the effect was amplified by the nature of the platelet alignment in the aligned  $\alpha$  structure.

A mechanism was proposed for crack propagation with dwell on load involving preferential diffusion of interstitial hydrogen to the basal slip plane (this being the hydride habit plane in Ti-6Al alloys [35]). By doing this the interstitial strain energy of the hydrogen is reduced along with the strain energy of the slip band. Dislocation cross slip out of the basal plane is now rendered energetically unfavourable and narrow highly strained slip bands form ahead of the crack tip and subsequently crack. The fracture surface produced by this slip band cracking, i.e. flat but containing some evidence of small scale ductility, corresponded well to the facets observed experimentally by the authors. To qualify this observation, they stated that some slip band cracking will occur on favourable slip systems without dwell but the introduction of dwell periods greatly increases this phenomenon. In the case of a basketweave structure, however, slip bands could only cross a few platelets before encountering a substantial change in crystallographic orientation.

In IMI685, the amount of retained  $\beta$  present at  $\alpha$ -platelet boundaries is only 1-2%. It then follows by considering the above mechanism, that for  $\beta$ -processed microstructures in higher strength alloys, containing 6-8% retained  $\beta$  at platelet boundaries (e.g.

Ti-6Al-4V), there is not such a marked dwell effect. This is because in the higher strength alloys the preferential crack path is along  $\alpha$ -platelet boundaries and any slip through  $\alpha$ -platelets, is halted by the layer of retained  $\beta$  at the platelet boundaries.

One interesting point that they did notice was that among all the LCF specimens tested only those which experienced the dwell time showed subsurface crack initiation sites, which were believed to be directly associated with the life reduction. This could be related to migration of hydrogen to regions of triaxiality, assuming the migration of hydrogen to be a time-dependent process. Other reasons for subsurface initiation could include residual stresses at the specimen surface, or simply the coarse nature of the microstructure decreasing the chances of finding a suitably oriented region of microstructure at the surface. If either of these were true however, then subsurface initiation would have been observed in the non-dwell specimens as well.

Eylon and Hall [30] obtained results from testing IMI685 which conflict with those of Postans and Jeal. In fatigue crack propagation tests, a 5 minute dwell period with a cyclic load running at 0.1Hz gave no apparent change in growth rate data compared to tests run at the same frequency without a dwell period in the range of  $\Delta K=20-60\text{MNm}^{-3/2}$ . This was despite the fact that the microstructural condition studied was essentially the same (i.e. aligned  $\alpha$ -platelets). A significant dwell effect was seen in LCF tests however, suggesting that initiation-related processes were involved and that time dependent changes occurring in intense slip bands reduced the resistance to fatigue initiation. In the LCF tests, some subsurface crack origins were noticed, which

propagated into pan-shaped cleavage-like fracture regions with small pores in the middle. These were not seen by Postans and Jeal but this is unlikely to account for the difference in responses from the fatigue crack propagation tests.

Similar results to those of refs. [29] and [30] were reported by Evans and Gostelow [36], who studied IMI685 with an aligned  $\alpha$  platelet microstructure. In LCF tests at room temperature the introduction of a dwell time reduced the number of cycles to failure by a factor of about 16 (see Fig.3.8). In both [29] and [36] it was mentioned that the cleavage-like facets around the crack origins in the dwell tests were of a similar size to the  $\alpha$  colony size. Evans and Gostelow concluded that the LCF dwell on load behaviour was directly dependent on the static creep properties of the alloy. Again, a model for dwell sensitivity and facet formation was proposed which was dependent on a combined creep/hydrogen locking mechanism (provided the texture is such that growth occurs predominantly on the basal plane).

It was found by Evans [37], while looking at the dwell behaviour of IMI685, that on strain dominated fracture surfaces the facets were inclined at a high angle (typically  $45^\circ$ ) to the stress axis. Hack and Leverant [38] reported similarly inclined features in their studies. Evans concluded that failures from creep and cyclic dwell testing of IMI685 at room temperature with aligned and basketweave microstructures could be subdivided into two groups. Firstly, failures in basketweave material at all stresses considered and aligned material at high stress were characterised by high rates of strain accumulation and facets on the fracture surface inclined at a high angle to the stress axis.

Secondly, in aligned material at low stress, the failures were characterised by low strain accumulation and facets perpendicular to the stress axis. The occurrence of two failure types could be explained by a model for time dependent deformation that invoked stress redistribution on a microscopic scale [39].

The effect of different loading patterns in dwell tests at 650°C was studied by Plumbridge on IMI829 [40]. Patterns studied were compressive dwell, tensile dwell and balanced dwell. Minimum lifetimes resulted from compressive only or balanced dwell cycling, such waveforms also producing the highest number of surface initiated cracks. Under those conditions it was argued that mean stress effects dominated over microstructural damage except in the balanced dwell situation where environment became most influential. The dominant failure mode was extremely sensitive to the test conditions and it was suggested that microstructural damage could easily assume an important role resulting in a transition to 'tensile-dwell sensitivity' either under fatigue or creep domination.

#### 3.1.5.4 Summary Of Long Fatigue Crack Behaviour In Titanium Alloys -

It is clear from the above survey of the published literature that variations in microstructure can produce large differences in fatigue crack behaviour in titanium alloys at low  $\Delta K$ s where crack growth is structure-sensitive. The behaviour is characterised by the planar nature of slip in titanium and the lower number of operative slip systems in hexagonal structures compared to cubic structures.

In the case of  $\alpha$ -titanium, increasing grain size decreases crack growth rate. In  $\alpha+\beta$  microstructures the dominant microstructural feature is the primary  $\alpha$ -grain size, and in both  $\alpha$  and  $\alpha+\beta$  microstructures, a transition from structure sensitive to structure-insensitive growth occurs when the cyclic plastic zone size is approximately equal in magnitude to the  $\alpha$ -grain size.

For the case of  $\beta$ -processed microstructures, while a basketweave platelet morphology produces higher crack growth rates than an aligned platelet morphology, initiation is more difficult. As a result, basketweave structures show longer LCF lives. Platelet colony size is the dominant microstructural feature in the aligned microstructures - a transition from structure-sensitive to nominally structure-insensitive crack growth is seen when cyclic plastic zone size is equal in magnitude to the colony size.  $\beta$ -processed microstructures show lower fatigue crack growth rates than  $\alpha+\beta$  processed microstructures.

Due to the highly faceted fracture surfaces produced by fatigue crack growth in titanium alloys, roughness induced closure plays an important part in the process. This explains the influence of load ratio  $R$ , i.e. decreasing  $R$  generally leads to a decrease in crack growth rates. In addition the large crack path deviations and crack bifurcations, associated in particular with the  $\beta$ -processed microstructures, serve to reduce the effective driving force and increase the closure contribution.

Dwell effects in  $\beta$ -processed microstructures are confined mainly to aligned platelet morphologies, where intense basal plane shear across  $\alpha$ -colonies - the mechanism associated with these dwell effects - is relatively easy. Although this review has

concentrated on dwell effects in  $\beta$ -processed alloys, it is interesting to note that in  $\alpha+\beta$  microstructures, dwell sensitivity is strongest in microstructures containing a high proportion of primary  $\alpha$  phase [41], again where intense basal plane shear is relatively easy.

A summary of long fatigue crack growth behaviour in titanium alloys is shown in schematic form in Fig.3.9.

## 3.2 SHORT CRACK BEHAVIOUR

### 3.2.1 Introduction

Ever since the work of Pearson [42] in the middle 70's, the apparently anomalous behaviour of 'short' fatigue cracks has been the subject of much contention.

Many researchers carrying out work on short cracks have found that they will grow at stress intensities below the long crack threshold  $\Delta K_{th}$  and, in addition, near threshold short crack growth rates can be substantially higher than those for long cracks at corresponding  $\Delta K$ s. By way of illustration, some typical short crack data along with the corresponding long crack data, are shown in Fig.3.10.

Since lifing procedures are carried out using data obtained from laboratory tests on long crack specimens, there is some concern that these predictions may be non-conservative. Pickard et al [43] studied specimen design for lifing procedures. Corner crack specimens were found to give results in good agreement with spin pit tests on actual discs. Perhaps the most important point they raised, however, was concerned with short crack behaviour -

they stressed that caution should be exercised when applying long crack data to component lifing procedures where crack size was of the order of, or less than, the microstructural unit size. This is particularly pertinent when dealing with materials used in aeroengine components. These materials are normally very 'clean', i.e. free from defects, so it is possible that a substantial proportion of the component fatigue life may be spent with crack lengths in the short crack regime. Other instances of short crack behaviour may occur in highly stressed, short fatigue life components or in thin sections [44].

Before going any further, it is useful to define the term 'short crack'. Short cracks have been defined to varying degrees by different authors [9,10,44-52], but there are essentially four definitions:

- 1) Microstructurally short - cracks which are of a similar size with respect to the dominant microstructural unit size (eg. grain size)
- 2) Mechanically short - cracks which are small with respect to the scale of local plasticity
- 3) Physically short - cracks which have length less than or equal to 1mm (this is a somewhat arbitrary definition and is related to both 1) and 2))
- 4) Chemically short - cracks which grow faster than expected due to environmental effects. These cracks can be large, e.g. a few mm.

The two most important definitions, certainly for the purposes of this study, are numbers 1) and 2).

Many authors, eg. Tanaka [49], have linked the short crack problem to a breakdown in similitude. The 'similitude concept' [9,10] states that for two different sized cracks subjected to equal stress intensity values (under small scale yielding) in a given material/microstructure/environment system, crack tip plastic zones will be equal in size and stress and strain distributions along the borders of these zones will be identical. This would be expected to give equal amounts of crack extension.

Leis et al [48] summarised similitude conditions as follows:

- 1) small  $r_p$  with respect to all length dimensions (including crack front length)
  - 2) small  $r_p$  with respect to distance over which the 1st term of the stress field solution is dominant
  - 3) equal  $K_{max}$  and  $\Delta K$
  - 4) equal closure fields
- } or equal  $K_{max}$  and  $K_{eff}$
- 5) long crack front with respect to metallurgical features
  - 6) dominate singularity (continuum behaviour)
  - 7) stable crack shape (no initiation transient)
  - 8) same material (and crack orientation)
  - 9) same environment, including temperature field.

### 3.2.2 Reasons For Breakdown In Similitude

#### 3.2.2.1 Inconsistencies In Mechanical Similitude -

Certainly there seems to be a failure in mechanical similitude for the case of short cracks as defined earlier. Therefore it could be argued that the use of linear elastic fracture mechanics (LEFM) and the parameter  $\Delta K$  associated with it,

loses its meaning.

It is generally accepted that plastic zone size should be 1/50th of the total crack length to satisfy LEFM requirements, although in the case of fatigue, where cyclic plastic zone size is more important, the monotonic plastic zone size  $r_p$  could be much bigger while the cyclic plastic zone size  $r_p^c$  would still be sufficiently small. For most short crack studies where stresses close to yield are used, especially in the case of smooth specimen testing,  $r_p$  and  $r_p^c$  exceed the size predicted by LEFM.

If the J integral [53] as adapted to fatigue [54] is used instead of K as a mechanical similitude parameter, requirement 1) will be somewhat relaxed but all the other requirements would remain in force. So it is easy to see why there are problems with the similitude concept with respect to the small crack problem. If significant unloading is involved, the use of the J integral becomes even more uncertain [55,56].

It has been suggested [48] that failure to correlate the behaviour of short cracks with that of long cracks may be due to the way in which LEFM is implemented, rather than to some inherent deficiency in the theory. For example,  $\Delta K$  has long been used for short cracks where closure is a factor, even though it is well accepted that  $\Delta K$  alone is inadequate for long cracks (e.g. [8]). For this reason it cannot be conclusively stated that the failure to consolidate short crack data is due solely to the limited applicability of LEFM. It is clear, however, that there are examples in the literature where the underlying assumptions of LEFM have been violated, such as large scale plasticity at crack tips in smooth specimens and at notch roots ([57] and [58])

respectively).

### 3.2.2.2 Inconsistencies In Microstructural Similitude -

There is also a breakdown in 'microstructural similitude' in the short crack regime. When a crack is of the order of the microstructural unit size, plastic deformation near the crack tip is greatly influenced by the local material microstructure and the assumption of a macroscopic continuum is no longer valid. For short through cracks, of a similar geometrical nature to long cracks, microstructural effects are averaged out over the whole of the crack front. As a result, crack growth through weak parts of the microstructure will be countered by other unfavourable orientations elsewhere along the crack front. For thumbnail cracks, initiated from 'point' defects or from smooth surfaces, there is no such averaging out or continuum effect.

It is possible to rectify the breakdown in mechanical similitude by using a modified driving force parameter. The effect of non-continuum behaviour, however, cannot be rectified.

### 3.2.2.3 Crack Shape And Three-dimensional Problems -

Crack shape is perhaps one of the main differences in character between long and short cracks. Whilst short cracks of a two dimensional nature, i.e. short through cracks, are reasonably easy to deal with, the added complexity of modifying driving force parameters to account for subsurface crack shape for thumbnail-type short cracks presents a problem. Several authors have reported a good deal of scatter in experimentally determined  $c/a$  ratios [59-62], especially in the early stages of growth.

Since subsurface crack behaviour cannot be monitored directly during testing, using existing techniques, this is another potential source of discrepancy.

Pineau [63] highlighted the three-dimensional problem of short cracks by studying large, three-dimensional cracks. From these studies a number of aspects often associated with short cracks, such as anomalously high fatigue crack growth rates and crack arrest phenomena, were observed.

### 3.2.3 Initiation Processes

#### 3.2.3.1 General Initiation Processes -

Crack initiation from a smooth surface can take place in several different ways. This can be from defects such as inclusions, grain boundary triple points or, if sufficiently high stress levels are involved, by the formation of persistent slip bands due to slip on various crystallographic planes. Mughrabi [64] was one of many to suggest that crack initiation at grain boundaries was due to the incompatible deformation between surface grains. For the case of subsurface initiation, plastic deformation processes are altered by the fact that there is no free surface to interact with.

Miller argued that initiation of short cracks was, to all intents and purposes, immediate [47,65]. The argument ran as follows. Metal surfaces, however smooth, contain micronotches which can be microstructural inhomogenities, such as a triple point of grain boundaries or inclusions, or notch-like equivalent features such as machining marks. Even the best prepared

engineering surfaces have micronotches to a depth of 2-3 $\mu$ m and, in fact, fatigue cracks of 3 $\mu$ m in length or less have been observed [66,67]. Therefore engineers can consider the fatigue lifetime to consist of growth from an initial defect size  $a_0$  of the order of 2-3 $\mu$ m to a final crack size  $a_f$ . In fact, a good approximation would be to assume  $a_0$  to be zero since growth from 0 to 3 $\mu$ m makes little difference to the overall lifetime.

This argument calls in to question the definition of a crack, i.e. when does a defect actually become a crack. There are without doubt cases where it takes many cycles before defects/cracks actually start to propagate, presumably because dislocation pile-ups which in turn form cracks take a finite number of cycles to form themselves.

Another point made by Miller is that initiation of a crack from a grain boundary triple point or inclusion does not preclude it from propagating transgranularly. Hence the differences between transgranular and intergranular initiation may not be as distinctive or as critical as previously supposed.

### 3.2.3.2 Surface Finish Effects -

Very little recent work has been carried out on this particular aspect of material behaviour. Suhr [68] made a useful study on the effect of surface finish on the high cycle fatigue properties of a low alloy steel, in the absence of any surface residual stresses. In this particular study it was shown that critical surface flaw sizes involved an interaction between surface roughness, inclusion size and inclusion orientation. Wilson et al. [69] concluded from work on Ti-6Al-4V plate that

fatigue strength was dependent on residual stresses caused by machining operations and, in the case of severely ground surfaces, to the presence of microcracks. Earlier work [70-73] had indicated that grinding generally produced residual tensile stresses near to the surface and milling or turning produced residual compressive stresses near the surface.

Usami [74] derived an empirical expression relating the critical surface roughness,  $a_c$ , with cyclic yield stress and monotonic yield stress in steels. The parameter  $a_c$  was defined as the limiting defect size below which the fatigue limit for a plain specimen was no longer affected.

Miller pointed out that in order for surface finish effects to be of benefit in terms of improving fatigue life, the quality of a surface should be such as to provide surface irregularities less than the size of the dominant microstructural barrier, so that the crack arrest period is operative [47].

### 3.2.3.3 Short Crack Growth Experiments Involving 'Artificial' Initiation -

A number of workers have studied the growth of short fatigue cracks from a variety of types of notches. One advantage of this approach is that the actual propagation portion of fatigue life can be studied in greater detail as the whereabouts of the crack are known from the very start of the test. The obvious disadvantage of this is that no information can be gained about 'natural' initiation behaviour, as from a smooth specimen test. An argument for forced initiation tests is that the notches used in the specimens may be a close approximation in some cases to

defects in components.

One type of short crack test involves a very shallow macronotch, e.g. [75,76], normally on axial fatigue specimens, so that cracks will initiate in a certain area rather like in a smooth specimen four point bend test. Because the actual notch effect is so small ( $K_t$  normally about 1.03) and not on a microstructural scale, cracks can be considered to be naturally initiated rather than artificially so.

Below is a brief review of the various experimental techniques used to initiate short cracks artificially.

Several workers [11,77-83] have used the method of precracking a V-notched long crack specimen and then grinding down from the specimen top surface until only the tip of the precrack remains, of length in the physically short crack regime. Romaniv et al [78] used this method on rectangular V-notch specimens of mild steel, aluminium alloy Al-Mg-Mn and austenitic 0.45C steel to obtain short through cracks of initial length 0.25-2.0mm. Ritchie and co-workers [11,77] used the same technique in analysing crack tip shielding in aluminium alloy 2124 by machining off the major portion of CT specimens containing long cracks arrested at  $\Delta K_{th}$ . The resulting samples were then machined into SEN bend specimens with through thickness crack lengths between 50 and 400 $\mu$ m. Short crack growth rate and closure data can then be readily obtained using this type of technique. Kendall et al [79] used the technique on low strength and high strength steels and included a specimen stress-relief of 650°C for 1 hour in a vacuum furnace prior to testing.

James and Knott [82] pointed out the possible nature of stress history effects and showed that, in an alloy steel, even when stress relief was attempted, a much higher value of the transition crack length from short to long crack behaviour would be deduced from these short through cracks, than from surface cracks of more common form. It was suggested that incomplete stress relief, leaving residual closure stresses, may have been involved. Similar results were obtained by Breat et al [81] and in an aluminium alloy by Zeghloul and Petit [83].

Hussey et al [80] introduced a rather novel variation on the V-notched specimen method by drilling a hole immediately behind the tip of a precrack in a CT specimen, thus producing a physically short through crack at a blunt notch, similar to what one might find in an engineering component.

Another method used to artificially initiate short cracks is to introduce micro-pits onto the specimen surface by electro-discharge-machining (EDM). Examples of this can be found in refs. [84-86]. At first sight this may appear to be an ideal method because there is no mechanical damage in the material surrounding the pit. Therefore there are unlikely to be residual stresses involved which might influence the early stages of growth of a crack initiating from such a defect. It has been suggested however that micro-residual stresses do exist around EDM pits [86] and also, that the chemical composition around an EDM pit will also be affected [84]. A sensible way around this problem is not to include initial crack extension from the micropit in any subsequent analyses. Nevertheless, an EDM pit is a good representation of defects such as shrinkage cavities, or brittle

inclusions with a low degree of matrix cohesion, eg. nodular cast iron, found in engineering situations.

On the whole the methods of artificial initiation of short cracks were found to give satisfactory results. Short through cracks tend to show higher growth rates than long cracks due to reduced closure effects, while microstructural effects are averaged out over the whole crack front, in similar fashion to long cracks. Short surface cracks tend to show higher growth rates than long cracks due to microstructural, plasticity and reduced closure effects.

#### 3.2.4 Initiation Behaviour In Commercial Purity Titanium

Work in this area was performed by Takao and Nisitani [87] on specimens of CP titanium containing shallow notches with root radii of 1mm and 0.1mm. Cracks were seen to initiate along slip bands within grains at notch roots. It was suggested that these slip bands could contain several microcracks which would join up to form a crack along the whole length of the prior slip band. During the initiation process the slip bands within the grains did not increase in size once microcracks had started to form. Thus fatigue cracks were not considered to form at a point within the grain, but along the area of the slip band contained by the grain. These characteristics were also observed on unnotched specimens.

#### 3.2.5 Initiation Behaviour In $\beta$ -Processed Titanium Alloys

Although some of the following experimental observations were made from LCF studies on titanium alloys (cf. section 3.2.1.2), the fact that the observations were made from natural initiation

brings that feature of behaviour, at least, into the microstructurally short crack category.

Initiation of cracks in  $\beta$ -processed IMI685 was found by Eylon and Hall [30] to be governed by shear across  $\alpha$ -colonies leading to the formation of intense slip bands. Initiation was promoted by the presence of large colonies of similarly oriented  $\alpha$ -platelets, and cracking occurred on or parallel to these intense slip bands. The introduction of smaller colony size and a basketweave structure was found to inhibit fatigue crack initiation.

Bolingbroke [88], working on  $\beta$ -annealed IMI318 with a basketweave microstructure, found initiation to occur within regions of grain boundary  $\alpha$  even though intense slip bands appeared across prior  $\beta$ -grains much earlier in the fatigue life of his specimens. This would agree with the findings of Eylon and Hall, that a basketweave structure inhibits the initiation of cracks from intense slip bands, although it appears to contradict their observation of initiation in slip bands across large colonies.

Funkenbusch and Coffin [89] studied the  $\alpha+\beta$  titanium alloy Ti-17 in several different microstructural states. In microstructures containing Widmanstätten  $\alpha$ -platelets (i.e.  $\beta$ -processed) multiple crack nucleation occurred in the first 3-5% of specimen life, via the formation of extrusions, along  $\alpha$ -platelet boundaries. This contrasts with the findings discussed above but this could be explained by the much greater presence of the  $\beta$ -phase at the  $\alpha$ -platelet boundaries in this material as it contains more  $\beta$ -stabilising elements. In common with the above two studies, slip bands were occasionally observed crossing groups of

$\alpha$ -platelets.

### 3.2.5.1 Subsurface Initiation -

Several authors [30,36,90] have written about the occurrence of subsurface initiation in titanium alloys. As Ruppen et al [90] pointed out, since fatigue crack initiation is generally considered to be a surface related phenomenon, a subsurface cracking mechanism is of great interest. In their study, they observed subsurface initiation from smooth hourglass fatigue specimens of Ti-6Al-4V with a Widmanstatten structure. Initiation sites took the form of cleavage-type facets but no defects were detected within these facets. Their discussion suggests mechanisms for subsurface initiation. These mechanisms are dealt with in detail in ref. [90] but essentially, they involved slip primarily on prism planes being blocked at  $\alpha/\beta$  interfaces. The piled-up dislocations induced slip in the  $\beta$  phase under cyclic loading, leading to Cottrell cleavage knife type initiation. Fig.3.11 illustrates the initiation mechanism. The mechanism relies on prism slip being the dominant mode, since there will be a higher probability of finding a suitably oriented colony at locations other than the surface. It was suggested that at high stresses, surface initiation may also be important if compatible slip between  $\alpha$  and  $\beta$  phases can occur along pyramidal planes. For near- $\alpha$  alloys, the mechanisms proposed by Ruppen et al. are unlikely to operate, since there would be much less  $\beta$  phase present.

Eylon and Hall [30] found subsurface crack initiation to be associated with 'cleavage rosettes' containing small pores of approximately 10 $\mu$ m in size (cf. section 3.1.5.3). It was believed that the defects were associated with porosity inherited from the original ingot and not completely healed during subsequent ingot breakdown procedures. This hypothesis was supported by radiographic evidence correlating the occurrence of the cleavage rosettes to areas of the forgings which had received very little deformation.

Such observations had originally been made by Rolls-Royce Aeroengine Division and Lockheed Aircraft personnel in 1972/73 related to RB211 fan disc failures. It should be pointed out that these cleavage rosettes containing pores were, in the main, associated with dwell tests. Eylon and Hall concluded that the dwell time effect on fatigue crack initiation appeared to be related to time dependent changes occurring in the intense slip bands which reduced the resistance to fatigue crack initiation.

Evans and Gostelow [36] found, from the examination of both LCF dwell and non-dwell test specimen fracture surfaces, that cracks initiated in many instances from subsurface origins. Cleavage or quasi-cleavage type facets were again observed at crack origins. In several dwell specimens crack initiation occurred at a number of sites. Other possible reasons for subsurface initiation are discussed in section 3.2.1.2.

### 3.2.6 Microstructural Effects

Perhaps the best way of illustrating the possible effects of microstructure on fatigue crack growth rate is to plot stress range necessary to cause fatigue failure versus crack length. This was carried out and reported by Kitagawa and Takahashi [91] in 1976 and their diagram can be seen in Fig.3.12a. At zero crack length the stress range is equal to the endurance limit. For long cracks the threshold stress intensity range is independent of crack length, leading to a straight line of slope  $-1/2$  on a logarithmic plot. This is because stress intensity is proportional to the square root of crack length.

The two lines representing the endurance limit or constant stress condition and the threshold condition can be extrapolated to meet at a crack length defined by El Haddad et al. [92] as  $l_0$ . If short cracks were to follow this pattern of behaviour then specimens or components containing no cracks would be just as likely to fail as specimens or components containing cracks of length  $l_0$ . Thus it would be sensible to assume that smooth specimens fatigued above the endurance limit would initiate and grow cracks up to length  $l_0$  very quickly.

Experimental data obtained from short cracks (eg. Kitagawa and Takahashi [93]) tend to lie on a curve between the two straight line regions, joining with the lines at crack lengths  $l_1$  and  $l_2$  on the endurance and threshold lines respectively. This deviation is hardly surprising as LEFM starts to break down as the stress range reaches that of the endurance limit. The value  $l_1$ , and not  $l_0$ , is the limiting value below which crack length has no further significance, as all crack lengths below  $l_1$  have the same

limiting stress range. Between lengths of  $l_1$  and  $l_2$  cracks would be expected to grow more quickly and to have a lower  $\Delta K_{th}$  value than cracks of length greater than  $l_2$ .

The Kitagawa - Takahashi plot has since been re-analysed and extended by M.W.Brown [94] to the form shown in Fig.3.12b to include contours of crack speed and fatigue fracture modes. An examination of Fig.3.12b reveals why cracks can grow at stress levels below the threshold value,  $\Delta K_{th}$ , determined from LEFM type tests, and below the fatigue limit stress level. It is also evident from Brown's diagram that whilst LEFM type cracks only increase in speed as crack length increases, at stress levels above the fatigue limit cracks can initially retard and then accelerate. In addition, at stress levels just below the fatigue limit cracks eventually stop propagating.

More general modifications to the Kitagawa - Takahashi plot were made by Miller [46,47] as shown in Fig.3.12c and C.W.Brown and King [44] (Fig.3.12d). These both serve to distinguish the different regimes of short cracks. Fig.3.12c shows additional lines of crack length equal to  $d_1$ ,  $d_2$  and  $d_3$  representing the size of microstructural units such as inclusions, precipitation spacing, grains or distances between phases. So cracks with lengths up to  $d_3$  would be termed microstructurally short cracks. At crack lengths beyond the microstructurally short regime, ie. crack length  $a > d_3$ , crack growth behaviour might be expected to be represented by a continuum mechanics approach, but Miller argued that, since these cracks are still physically small and require high stress levels for propagation, this would involve some macro-plasticity, particularly at higher growth rates and hence an

elastic-plastic fracture mechanics (EPFM) approach should be used. These cracks would be termed physically short cracks.

Taylor [95] defined  $l_2$  as being less than or equal to  $10d$ ,  $d$  being the microstructural unit size. He later went on to propose a simple predictive model for determining the length  $l_2$ , this being the critical crack length below which anomalous short crack behaviour is observed [96]. He cited five distinct reasons for this anomalous short crack behaviour and these are listed below:

- 1) microstructure
- 2) closure
- 3) K-estimation errors
- 4) crack deflection
- 5) constraint

It was then shown that the microstructure and deflection arguments could be related to an  $l_2=10d$  prediction ( $d$  being microstructural unit size) while the closure, K-estimation and constraint arguments could be related to an  $l_2=10r_p^C$  prediction ( $r_p^C$  being the cyclic plastic zone size). Whichever of these two quantities was largest would define  $l_2$  and hence the boundary of the anomalous crack growth behaviour. Comparison of this hypothesis with experimental data gave a good agreement for a range of materials.

To be able to use this prediction with some degree of confidence for design purposes would obviously be of considerable use, but it is likely that most designers would want this to be backed up with experimental information from the particular material in question.

Lankford and co-workers [45,50,97] have shown that growth rates for short cracks and long cracks generally converge when the cyclic plastic zone size,  $r_p^c$  is equal to the material grain size. This is illustrated by results shown in Fig.3.13.

Brown and King [44] compared single crystal data as a means of removing microstructural effects from short crack growth but expressed reservations about whether short crack behaviour is actually possible in single crystal material. They argued that the complete absence of grain boundaries means that the relevant microstructural dimension then becomes either the inter precipitate spacing or, going to the extreme, the magnitude of the Burger's vector. These would still be present, in a polycrystalline material and it could be argued that studying crack behaviour in single crystals is a useful model for very early growth of a short crack within the first grain. The authors did point out that in the single crystal case, where the 'microstructural features' are clearly so much smaller than the crack length, fatigue crack growth may well be adequately described by LEFM for all reasonably low stress levels.

Another interesting point in their paper was their plot of fatigue crack growth rates in single crystals versus the crack opening displacement range,  $\Delta\delta$ , shown in Fig.3.14. Plotting the data in this way had the effect of bringing the data from the different materials into a fairly narrow band, with the notable exception of the data for Ti-4Al, this being the only hexagonal material of those discussed. They speculated that this could be associated with the limited distribution of slip systems in hexagonal materials and a greater accumulation of localised strain

on the loading part of the cycle (an observation made by Affeldt and Gerold [98]).

### 3.2.7 Short Crack Growth Arrest

Several explanations have been forwarded for the reduction in short crack growth rates approaching grain boundaries. Growth rate minima have been explained in terms of development of a 'mature' plastic zone in the next grain [99], blockage of crack tip slip bands by the grain boundary [100] and the change in crystallographic orientation across a grain boundary causing crack deflection, leading to a reduction in the effective stress intensity [101].

Miller discussed crack growth arrest [47] by considering a Stage I surface fatigue crack in an equiaxed grain structure, where the major barrier is associated with the grain boundaries. There are obviously different variations on this situation, such as different types of barriers and different types of defects. The model, shown in Fig.3.15, assumes that the initial surface crack will grow in the largest surface grain having the most favourably inclined slip system. Once this crack has reached its grain boundary it is confronted by several smaller grains, none of which is as favourably oriented as the first grain (labelled X).

The crack now has a line stress concentration along new slip systems that present themselves at different inclinations and have potential crack growth directions which are different to the initial crack plane and crack growth direction (Fig.3.15b). It is likely therefore that the crack may continue propagating in only one of the surrounding grains, which is most favourably situated,

of the largest possible size and having the least constraint, probably along the surface ie into grain Y of Fig.3.15a. Grain Z is now almost surrounded by cracked grains and so this grain is likely to be the next to succumb, and so on. Each grain beyond the initial crack will not sense the full crack length as given in the crack growth law equation, but a length substantially smaller and less effective in terms of a singularity condition.

At some point, for the case of a tensile applied bulk stress, the crack will deviate from Stage I type growth, i.e. crystallographic, to Stage II type growth. At the end of the apparent crack arrest period the crack front may be macroscopically Stage II although microscopically it may contain several Stage I type crystallographic facets having various three-dimensional inclinations. The crack will now cease to be dominated by the material microstructure and a continuum mechanics approach will be appropriate.

James and Morris [102] looked at the problem of preferential short crack growth in large grains. They examined the possibility of greater cyclic softening in the larger grains making a significant contribution to crack tip opening displacement. It was noted that for grains four to five times the mean grain size the local yield strength may fall to 30% of the bulk value, which means that the degree of plasticity will be greater than for a smaller grain. Therefore it is evident that the largest grain within a material can dictate the fatigue resistance in the case of plain specimens.

### 3.2.8 Observations On Short Crack Growth Behaviour In Titanium Alloys

#### 3.2.8.1 Primary $\alpha$ Microstructures -

Gerdes et al [103] and later, Wagner et al [62] found that smaller grains offered a greater fatigue resistance in a primary  $\alpha$  microstructure of Ti-8.6Al, with crack arrest at grain boundaries, an effect opposite to that seen for long cracks. Grain boundary resistance was greater for the crack front propagating down into the specimen than along the surface, so giving a non-uniform crack shape as the crack developed. This highlights the importance of three-dimensional considerations in short crack growth. It was also found that although short crack growth was faster than long crack growth for the same nominal  $\Delta K$ , growth rate data of surface cracks at low stress ratios approached those of through cracks at high stress ratios, suggesting that crack closure effects were much less significant for the small cracks.

In commercial purity titanium it was noted also [87] that growth across grain boundaries was relatively difficult compared to bcc and fcc structures because of a smaller number of slip systems operating in the titanium.

#### 3.2.8.2 $\beta$ - And $\alpha+\beta$ -Processed Microstructures -

Brown and Hicks looked at the effect of a very coarse prior  $\beta$ -grain size in IMI685 [104]. Within these coarse prior  $\beta$ -grains were colonies of aligned  $\alpha$ -platelets. The authors noticed short crack propagation rates up to four times higher than long crack propagation rates, the greatest values being associated with

crystallographic growth. Crack arrest was observed both at grain and colony boundaries, and dwell at maximum load during cycling caused a decrease in growth rate over the range investigated. This was the opposite of observations made on the effect of dwell on long crack growth (section 3.2.1.2).

Hicks, Howland and Brown [105] went on to study the other common  $\beta$ -processed alloy, IMI829, and were in agreement with the general consensus that short crack growth rates were higher than basic long crack growth rates when crack length was of the order of the microstructural unit size. When looking at IMI829 with a basketweave platelet morphology, however, they found short crack growth rates to be similar to those for long cracks, suggesting this was because the crack tip sampled a wide variety of platelet orientations. By implication it seems that the dominant microstructural dimension in the basketweave structure was the  $\alpha$ -platelet width. Similar results were obtained by Goddard [76], who found little evidence of a short crack effect in IMI550 in  $\alpha+\beta$ -processed and basketweave  $\beta$ -processed conditions.

Studies on  $\alpha+\beta$  Ti-6Al-4V (IMI318) made by Brown and Taylor [106] showed there to be little effect of  $\alpha$ -grain size on short crack propagation rates at high stresses, although for long cracks an increase in  $\alpha$ -grain size caused a decrease in growth rate. The idea of closure was again invoked here, the authors suggesting that a larger  $\alpha$ -grain size lead to a rougher fracture surface and hence a greater amount of closure. The results did show the existence of a short crack effect however.

Bolingbroke and King [88], working on IMI318 and IMI550 looked at the effect of different microstructures produced by different processing/heat treatment routes. A number of interesting observations were made, including the observation that in IMI318 short cracks in a  $\beta$ -processed microstructure consisting of aligned platelets showed growth rates up to an order of magnitude faster than those in an  $\alpha+\beta$ -processed microstructure. Also, in  $\alpha+\beta$  microstructures, a finer transformed  $\beta$  produced by a fast cooling rate impeded crack growth more effectively than coarser transformed  $\beta$  produced by a slow cooling rate. It was shown that there were different barriers to short crack growth in  $\alpha+\beta$  and  $\beta$  titanium alloys, these being either phase boundaries - particularly when the crack was growing from the softer primary  $\alpha$  into harder regions of transformed  $\beta$  - or simply changes in microstructural orientation. Two phase structures in steels also produce similar situations of cracks initiating in the softer phase (in this case ferrite) and subsequent growth being impeded by a harder phase (pearlite or martensite) [60,107-109].

### 3.2.8.3 Summary Of Short Crack Growth Behaviour In Titanium Alloys -

Short crack growth behaviour in titanium alloys seems to show effects quite the opposite of those seen in long cracks. For example, an increase in grain or colony size tends to lead to an increase in short crack growth rate. In addition, a  $\beta$ -processed microstructure consisting of aligned platelets gives faster short crack growth rates than an  $\alpha+\beta$  processed microstructure. This is attributable in large part to the absence of roughness induced closure effects and also to the colonies of  $\alpha$ -platelets acting as

if they were primary  $\alpha$ -grains, allowing easy slip across a whole colony [23]. In the case of basketweave structures, the dominant microstructural dimension seems to be the  $\alpha$ -platelet or needle size, so there is very little microstructurally short crack behaviour. General trends in short crack behaviour in titanium alloys are shown in diagram form in Fig.3.16.

### 3.2.9 Observations On Short Crack Behaviour In Other Engineering Alloys

Whilst it is not the purpose of this review to cover the work performed on short cracks in other engineering alloys in detail, there are several observations to be made by way of a summary of this particular topic. Examples of work done on steels can be found in refs. [61,63,78,79,85,86,110-118], for aluminium alloys in refs. [11,42,63,77,78,94,113,114,119-126] and for nickel-base alloys in refs. [80,84,114,127,128]. Useful reviews of experimental data for several different alloys can be found in refs. [44,97,129].

The trend for short crack behaviour in most engineering alloys is that short cracks grow faster than long cracks at the same nominal  $\Delta K$  values and that short crack growth occurs below the long crack threshold value,  $\Delta K_{th}$ . The effect of grain size is seen to be the reverse of that observed with long crack behaviour, i.e. for short cracks an increase in grain size will tend to increase crack growth rates while for long cracks an increase in grain size will tend to decrease crack growth rates. Fig.3.17 shows the schematic effect of grain size on short crack growth rate, along with the corresponding growth minima associated with

grain boundary arrest. In reality crack growth rates show more than one arrest, for example, the data shown in Fig.3.18 from a magnesium 'model' alloy [130].

Data has been published which showed an apparent reversal in, or an apparent absence of, the short crack effect, as reviewed by Lankford [97]. The materials in question were quenched and tempered steels [131-133] and a nickel-base superalloy IN100 [134]. In all of these studies, although the scale of local plasticity was small when compared to crack length, the plastic zone size  $r_p$  seemed to be in excess of the most relevant microstructural dimension, which suggests that one might not expect to see a substantial short crack effect anyway. This observation was further reinforced by the findings of Ritchie and Yu [11] from work on an aluminium alloy. In their experiments, through cracks of length 200-400 $\mu\text{m}$  exhibited a short crack effect, even though plastic zone sizes were only approximately 20 $\mu\text{m}$  in size. The pancake grains in the aluminium alloy were roughly 350 $\mu\text{m}$  in diameter and 50 $\mu\text{m}$  thick. Therefore, again  $r_p$  was less than the microstructural unit size and the short crack effect was observed without violating LEFM conditions.

Brown and Hicks compared both short and long crack growth in titanium alloys, nickel-base alloys and aluminium alloys [129]. They noticed that short crack growth rates showed slightly less dependence on alloy type than those for long cracks, but there was a trend in terms of crystal structure. From the materials they studied it could be seen that, as a general trend, f.c.c. structures exhibited the slowest growth and c.p.h. structures the fastest. Although a crack tip opening criterion was suggested to

unify the data, the two titanium alloys studied would still have shown disparate growth rates.

### 3.2.10 Short Crack Closure/thresholds

One important question concerning crack growth thresholds is the contribution of an intrinsic, material-related crack growth threshold in the absence of any closure effects, closure being associated normally with long crack threshold behaviour. Short crack thresholds have certainly been observed by a number of authors, eg. [128,135,136].

McCarver and Ritchie [4-53] studied the effect of crack size on  $\Delta K_{th}$  in a nickel-base superalloy, Rene 95. They found that measured  $\Delta K_{th}$  values at a low R value (0.1) for physically short cracks (0.01-0.2mm) were 60% smaller than corresponding threshold values for long cracks (25mm). The short crack threshold did correspond, however, with the long crack threshold at a high R value of 0.8, where the cracks remained open over the whole of the load cycle. This showed that the absence of closure in long cracks will give a  $\Delta K_{th}$  value  $\Delta K_{(eff)th}$  in line with that for physically short cracks. This finding, along with many others (eg. [11,63,112,137]) strongly supports the theory that one of the main reasons for discrepancies between short and long crack growth behaviour is the absence of closure in short cracks. Although an explanation for the short crack thresholds was not forwarded by the authors of this particular report, theories have been postulated, such as Ritchie's 'crack tip shielding' theory, involving intrinsic and extrinsic toughening [11] (see earlier). Morris and James cited blockage of growth by grain boundaries and

closure due to crack tip plasticity as being two important mechanisms for a short crack threshold [135]. Examples of  $da/dN$  vs.  $\Delta K_{eff}$  data compared with short crack data are shown in Fig.3.19.

Only a limited number of studies have been made in order to measure directly the extent of crack closure, rather than just an intrinsic threshold, in short cracks, involving experimental techniques of varying intricacy. Techniques include a back face strain measurement technique [11], an interferometric technique [138,139] and a much simpler technique involving the relative mismatch of a line scribed across a surface crack [85].

The interferometric technique involves the measurement of the displacement between two microhardness pits introduced either side of a short surface crack. One question that ought to be raised concerning this method is whether the plasticity generated by the indents affects the behaviour of the crack, especially as in some cases the crack-to-indent distance has been of the order of the material grain size.

Newman and Beevers [137] discussed thresholds for single and multigrained short cracks in a nickel-base superalloy AP1. Short cracks did not display any evidence of closure up to 250 $\mu$ m length. Multigrained short cracks did show a threshold  $\Delta K_{th(mg)}$  which was similar to the long crack  $\Delta K_{(eff)th}$ . Although it was proposed that short crack growth in this case was unaffected by crack closure, an intrinsic threshold was still evident. The single grain cracks showed a lower intrinsic resistance to crack growth than the multigrained cracks, attributed to the ease of slip within one grain compared to the difficulty of accomodating slip in

differently oriented grains along a multigrained crack front.

There are problems associated with incorporating closure effects within an overall unifying model for crack growth. The point is that there are a large number of variables affecting the extent of closure, these being crack length, stress-strain rate, microstructure, stress range, crack growth mode, mean stress and the position of closure measurement along the crack front. This renders closure almost impossible to quantify in simple terms, especially since each variable may change in importance as a crack propagates.

#### 3.2.11 Effect Of Texture

Both physical and crystallographic texture have been observed for short crack behaviour in aluminium alloys [140] and titanium alloys [106]. It has been suggested [44] that texture may be most important in planar slip materials, especially in hexagonal titanium alloys where fatigue crack propagation tends to occur along the basal plane. Control of the basal plane orientation can force the crack to grow at large angles to the Mode I propagation direction and produce large changes in crack path orientation from grain to grain. In the long crack situation, such growth behaviour would presumably result in an increased fracture surface roughness and hence an increased contribution from roughness induced closure.

For hexagonal materials, crystallographic texture is likely to be the dominant factor, due to a lower number of operative slip systems than cubic materials. The anisotropy effects found in aluminium alloys [140] may well rely more on the physical

texturing of aligned inclusions and irregularly shaped grains, than on crystallographic texture.

### 3.2.12 Effect Of Environment - 'Chemically' Short Cracks

Although titanium alloys have good corrosion resistance, certain combinations of stress, temperature and time have been shown to accelerate failure by a hot salt stress corrosion (HSSC) mechanism [141].

Winstone and Weaver [142] looked at the effect of a hot salt (NaCl) environment on the fatigue and creep behaviour of three titanium alloys, IMI679 ( $\alpha+\beta$  processed), IMI685 and IMI829 (both  $\beta$ -processed). The temperatures used were those approximating to the maximum temperature capabilities of the alloys, namely 450°C, 500°C and 600°C respectively. Although fatigue crack propagation rates were not affected, it was found that both creep and fatigue lives were greatly reduced, as shown in Fig.3.20. It was thought that the failures occurring as a direct result of accelerated crack initiation which produced cleavage-like facets. The size of these facets was related directly to the grain size and therefore the coarse grained,  $\beta$  heat treated alloys were found to be more susceptible to HSSC than the  $\alpha+\beta$  processed IMI679.

Sinigaglia et al [143] also looked at HSSC in titanium alloys and outlined the four basic processes involved, these being corrosion of the metallic substrate, generation of nascent hydrogen, hydrogen embrittlement of the metallic substrate and initiation and propagation of cracks. They found a very high susceptibility to HSSC, this susceptibility increasing with tensile stress. Although Winstone and Weaver did not study

specifically the stress dependence of HSSC they did find a low stress dependence of life in their tests, this clearly being due to the hot salt environment. Sinigaglia et al proposed a model whereby the electrochemical reaction at the tip of the cracks produced nascent hydrogen, which was absorbed in the region of triaxial stress at the tip of the crack causing localised embrittlement. This led to discontinuous crack propagation and brittle fracture.

It is interesting to note that HSSC failures have not been observed in current gas turbine components, when laboratory data clearly shows its existence. Several explanations for this apparent anomaly have been advanced [142]. One of these is that the engine operating cycle is not sufficiently aggressive in terms of peak stress and temperature to promote HSSC, or at least not for the process to be taken past its critical point.

Therefore there is no guarantee that future engines with different operating cycles will not suffer from this problem. Another possibility is that HSSC does occur in service but the stresses are too low to allow the cracks to grow beyond the surface grain. One would still expect to see cracks up to 1mm in length in a  $\beta$ -processed alloy, the sort of defect size that can be detected by NDI, yet none have been seen in engine-run components. A third possibility is that the salt concentration in service is not sufficiently high to promote HSSC.

With there being chemical reactions involved in this sort of process, one might expect to see an effect of frequency on crack growth rates. Such an effect was reported by Wei [144] who found, in a Ti6Al4V alloy tested in 0.6M NaCl solution, that crack growth

rates increased with decreasing frequency, up to a maximum depending on  $\Delta K$  and then decreased to rates comparable to those observed in vacuum, or other inert environments. The critical frequency range seemed to be between 0.1Hz and 10Hz, a range which may be relevant in laboratory testing but would not coincide with the high frequency of rotating engine parts, or the low frequency of the actual aircraft flight cycles.

### 3.2.13 Modified Driving Force Parameters For Short Cracks

A number of workers have tried to find a suitable characterising parameter for the driving force for short crack growth, the most useful being those which can be measured globally yet describe local conditions at the crack tip. Table 3.1 shows certain approaches which can be used when dealing with short crack behaviour, yet it seems that there is no universal parameter which can be used with any confidence.

For mechanically small cracks, where local plasticity is of similar magnitude to crack length, EPFM solutions have been proposed through the use of  $\Delta J$  and  $\Delta S$  (strain energy density). It is important to note that, while  $J$  is certainly an adequate description of excessive plasticity ahead of the crack tip, it cannot account for wake plasticity behind the crack tip, which is the cause of crack closure effects. The use of  $\Delta K_{eff}$  may be suitable for physically short cracks and cracks emanating from notches. The treatment of microstructurally short cracks presents a much harder problem, as initial cracking tends to occur preferentially from weak spots in the microstructure and there is no continuum situation. In this situation a probabilistic approach

(e.g. [145]) may be more satisfactory than any of the characterising parameters already mentioned.

Table 3.1 Classes of short fatigue cracks [158].

Type of short crack	Dimension	Mechanism responsible	Potential solution
Mechanically short	$a \ll r_y$	excessive (active) plasticity	use of $\Delta J$ , $\Delta S$ and CTOD
Microstructurally short	$a \ll d$ $2c \ll 5-10d$	crack tip shielding enhanced $\Delta \epsilon_p$ crack shape	probabilistic approach
Physically short	$a \ll 1\text{mm}$	crack tip shielding (crack closure)	use of $\Delta K_{eff}$
Chemically short	up to $\sqrt{10}\text{mm}^*$	local crack tip environment	

$r_y$  is plastic zone size or plastic field of notch

$d$  is critical microstructural dimension, e.g. grain size

$a$  is crack depth

$2c$  is surface crack length

\*critical size is a function of frequency and reaction kinetics

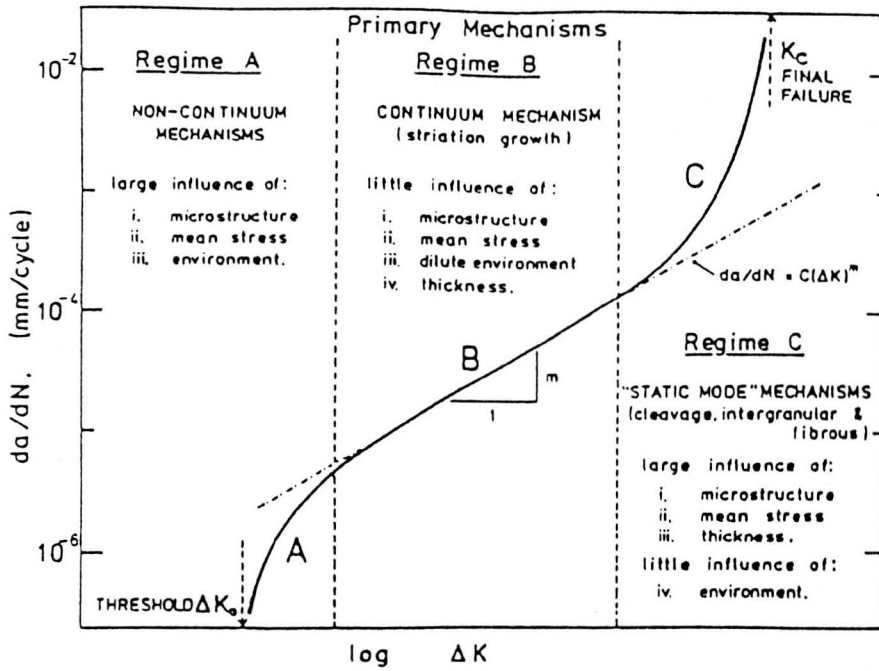


Fig.3.1 General form of crack growth rate  $da/dN$  versus alternating stress intensity range  $\Delta K$  curve for long fatigue cracks [1].

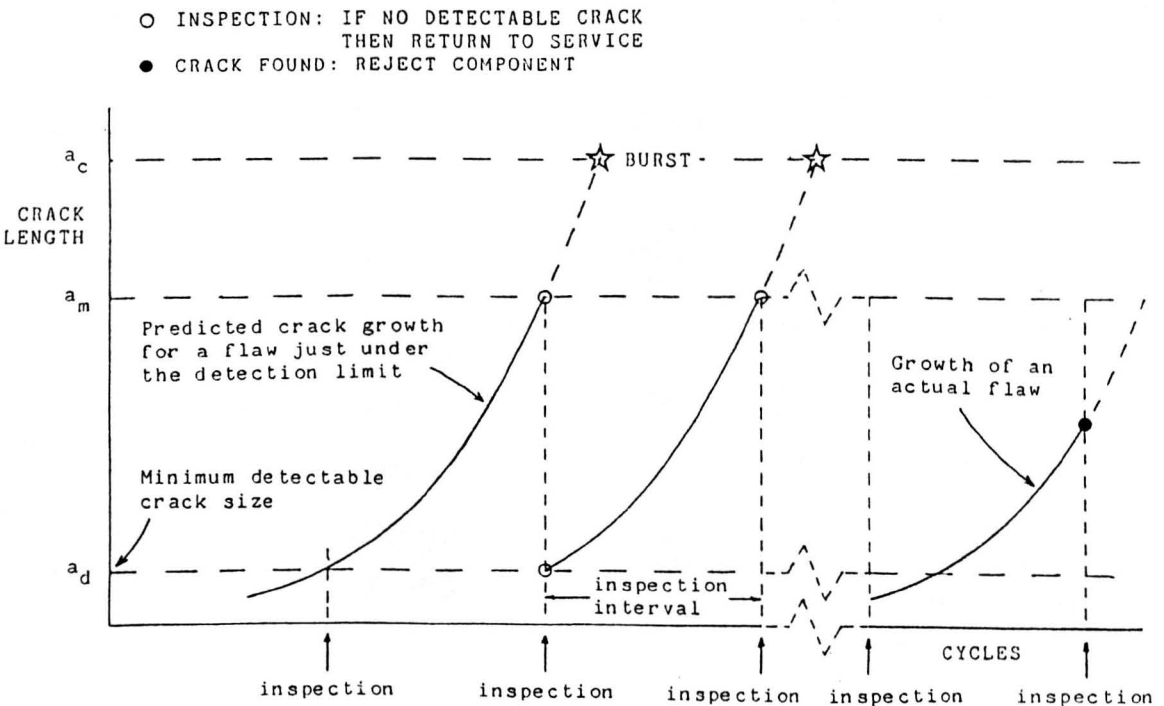


Fig.3.2 The philosophy of the defect tolerant approach for components in service [2].

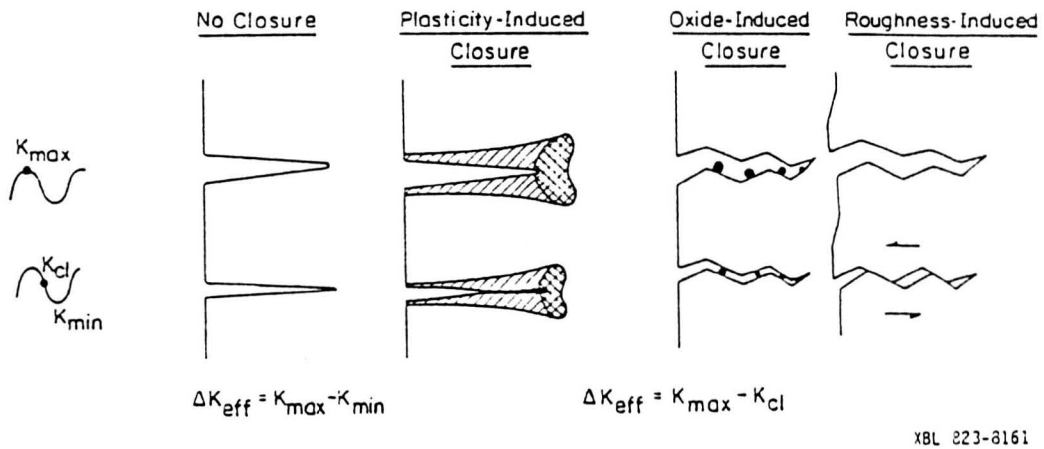


Fig.3.3 Explanation of the parameters  $K_{max}$ ,  $K_{min}$ ,  $K_{cl}$ ,  $\Delta K$  and  $\Delta K_{eff}$  along with the simple closure mechanisms [10].

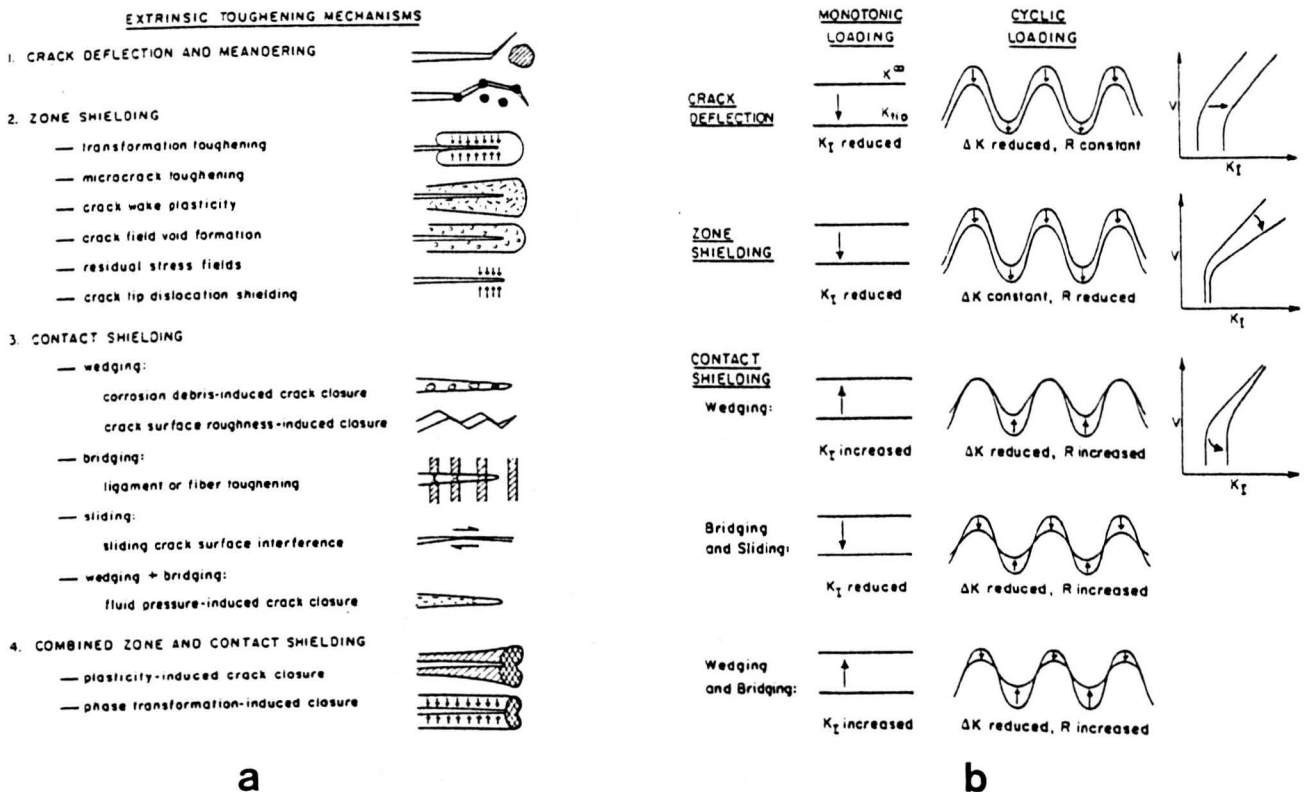
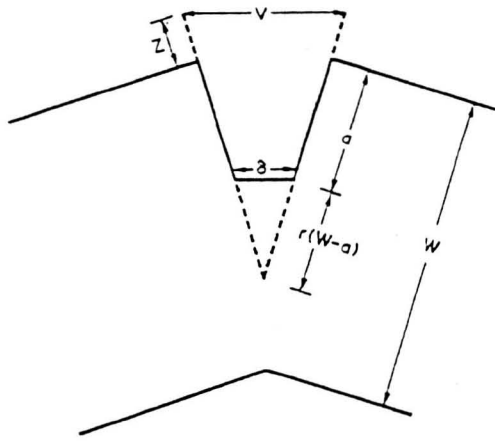


Fig.3.4 a) Different micromechanisms for crack tip shielding and b) the effects of crack tip shielding mechanisms on crack driving force,  $K$  [11].



$$\Delta\theta = \frac{\Delta V}{a+z}$$

Fig.3.5 Experimental set-up of Walker and Beevers [16], showing how their parameter  $\Delta\theta$  was calculated.

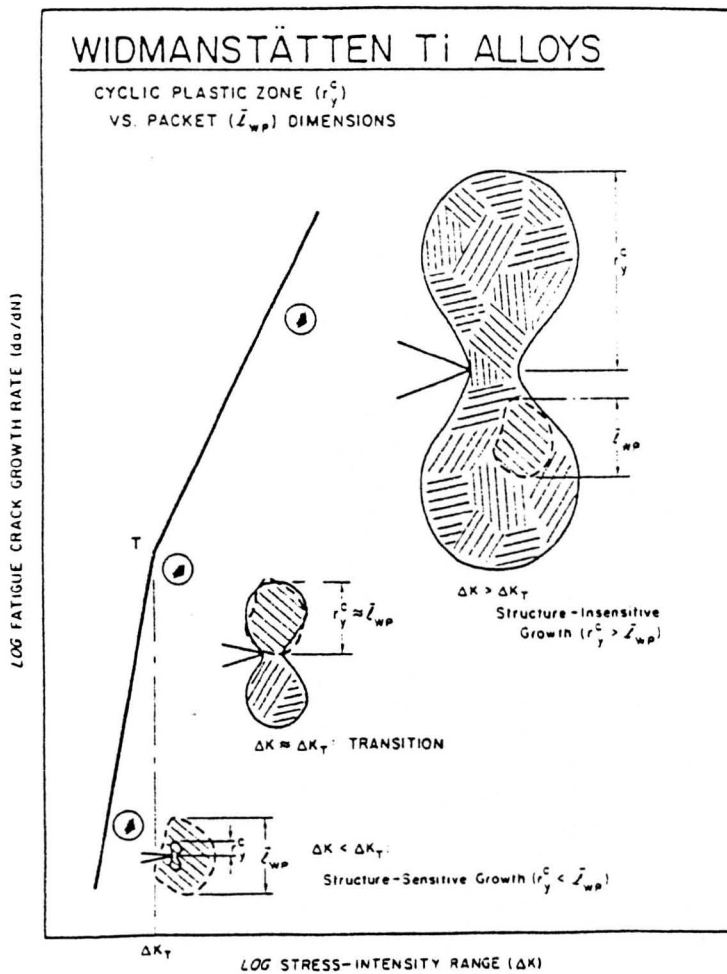


Fig.3.6 Influence of cyclic plastic zone size, relative to mean colony or packet size, upon the development of bilinear form of fatigue crack growth behaviour in a titanium alloy, as observed by Yoder, Cooley and Crooker [14].

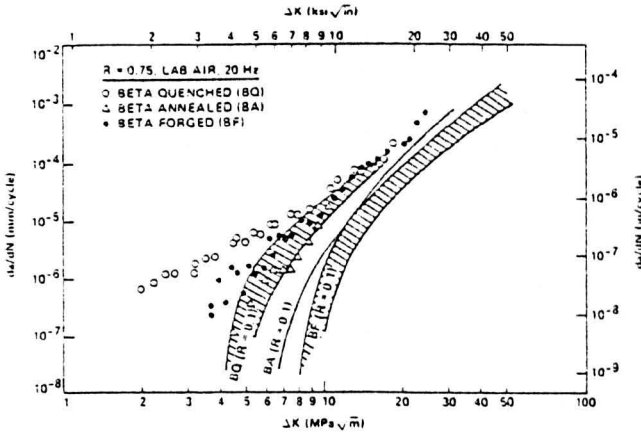


Fig.3.7 Effect of  $\beta$ -heat treatment and load ratio on fatigue crack propagation behaviour in Ti-6Al-4V, as observed by Chesnutt and Wert [22].

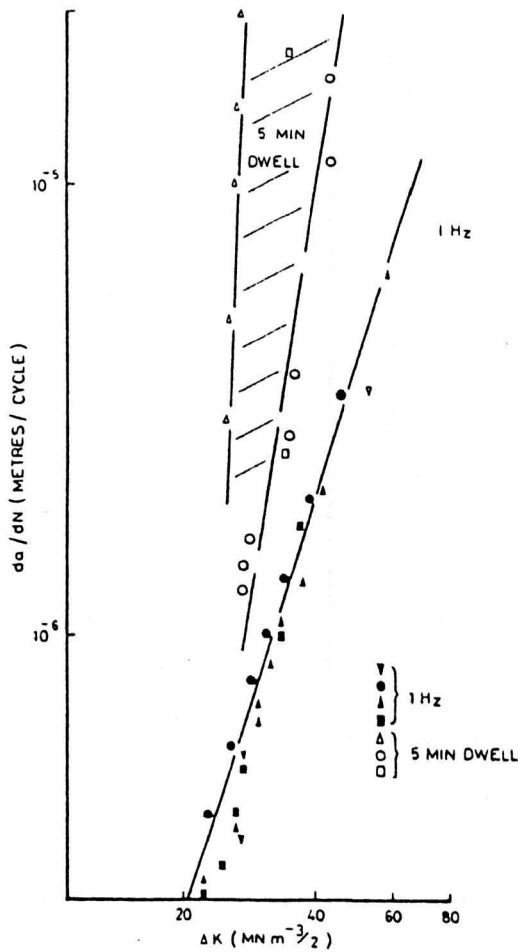


Fig.3.8 Results of Evans and Gostelow [36], showing the effect of dwell periods on the LCF behaviour of IMI685.

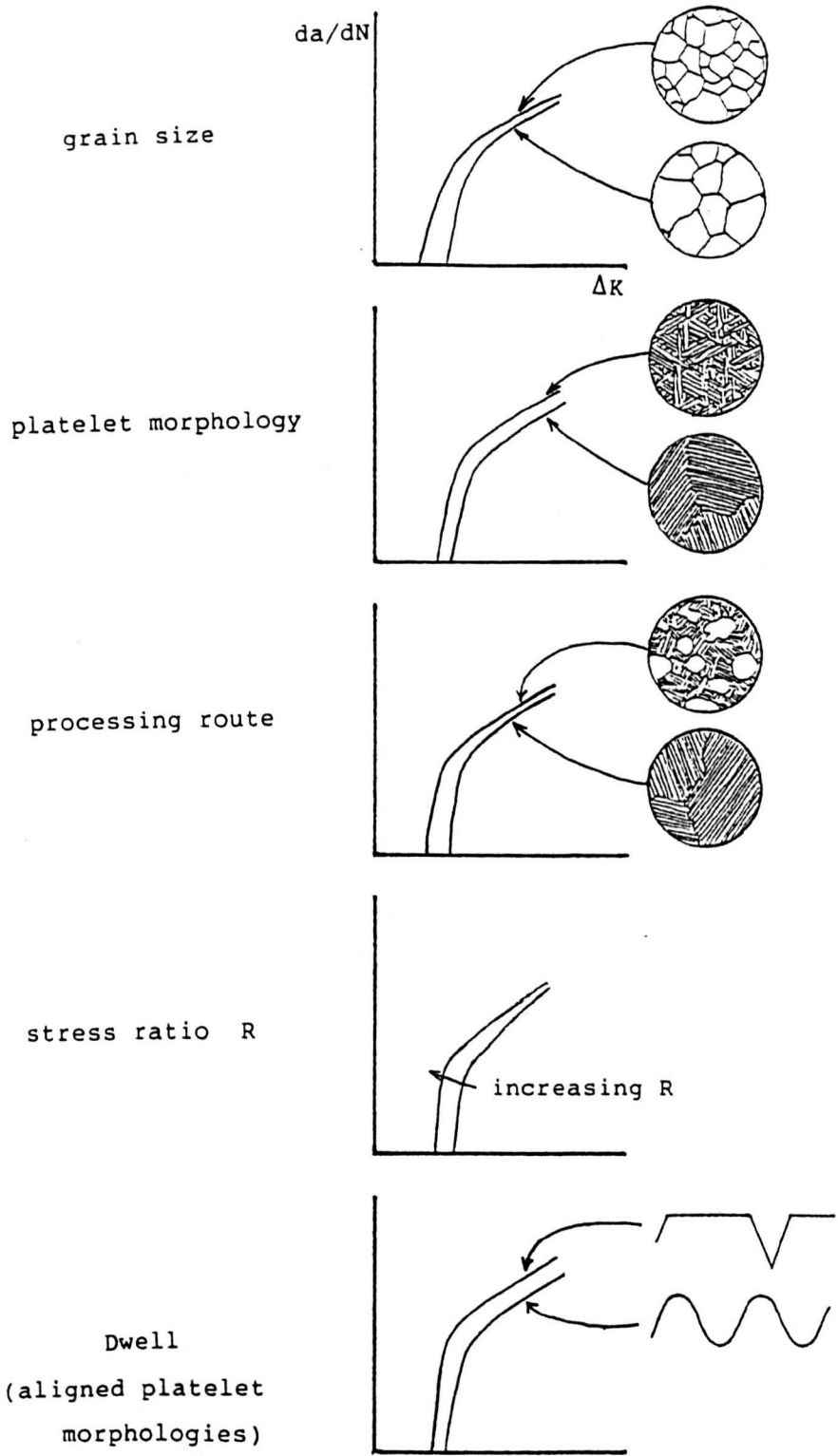


Fig.3.9 Summary diagram of long fatigue crack growth behaviour in titanium alloys.

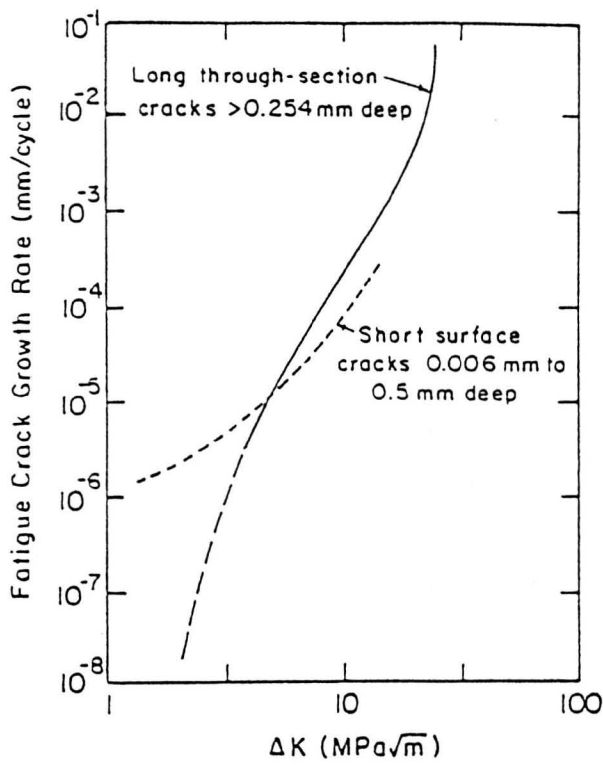
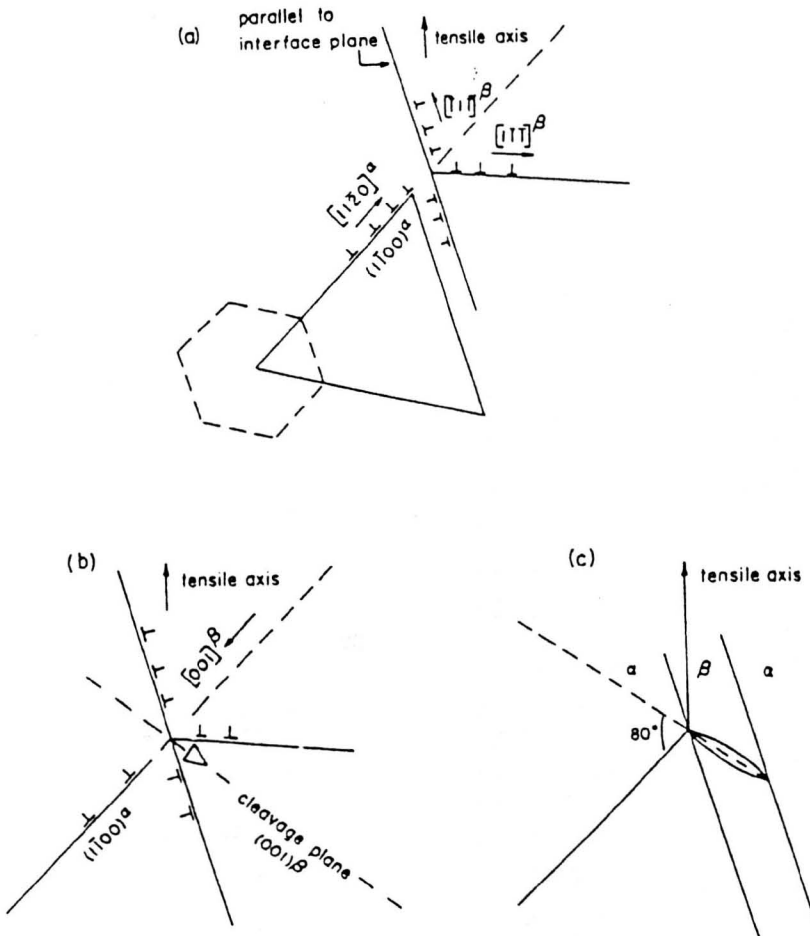
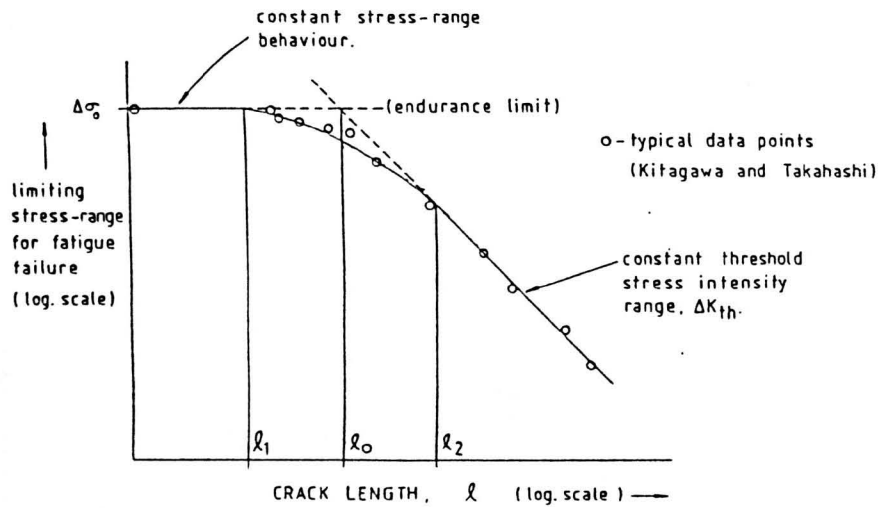


Fig.3.10 Comparison of typical short crack data with corresponding long crack data [42].

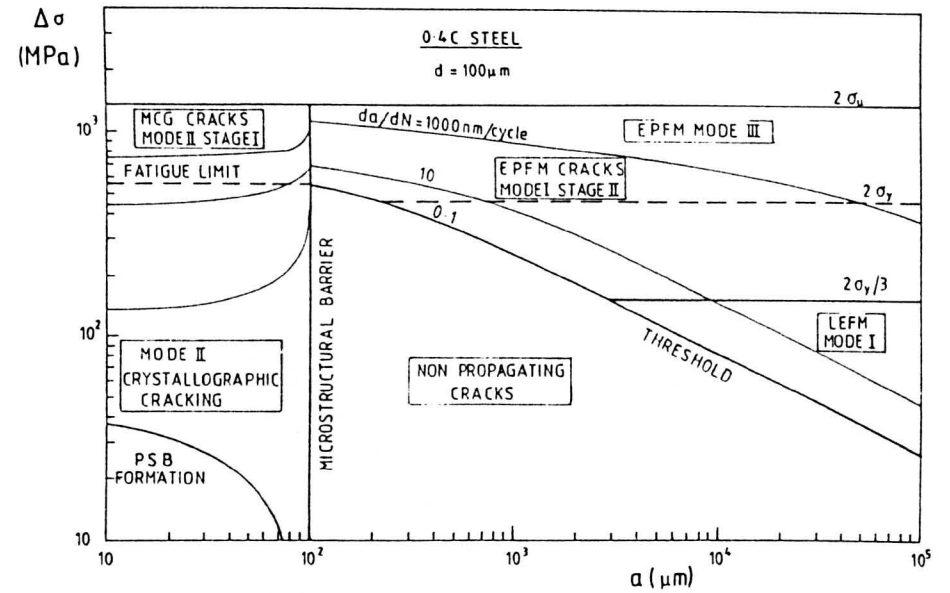


Proposed model for crack initiation in  $\beta$  due to cyclic loading. (a) On loading, slip in  $\alpha$  is accommodated by slip on two planes of different Burgers vectors in  $\beta$ . (b) On reversal of loading, dislocations in  $\beta$  coalesce to give a  $[001]$  displacement and initiate a crack on a  $(001)$  of  $\beta$ . (c) Crack grows across  $\beta$ . Projection of  $(001)$   $\beta$  plane into  $\alpha$ -phase is at  $80^\circ$  deg to initial prism slip plane in  $\alpha$ .

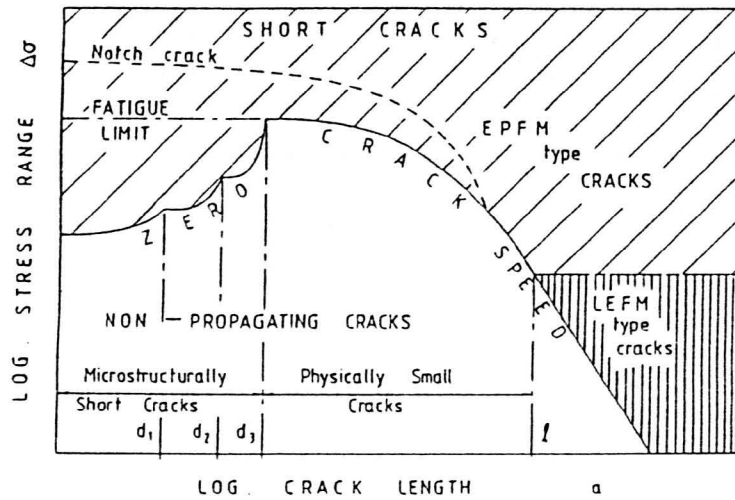
Fig.3.11 Model proposed by Ruppen et al [90] for subsurface initiation.



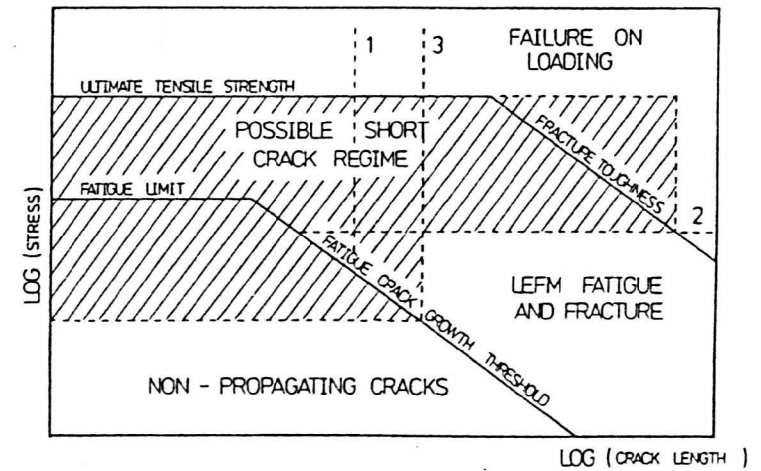
a



b



c



d

Fig.3.12 Kitagawa-Takahashi plot of stress range necessary to cause fatigue failure versus crack length [91] (a) and modifications made by M.W.Brown [94] (b), Miller [46] (c), and C.W.Brown and King [44] (d).

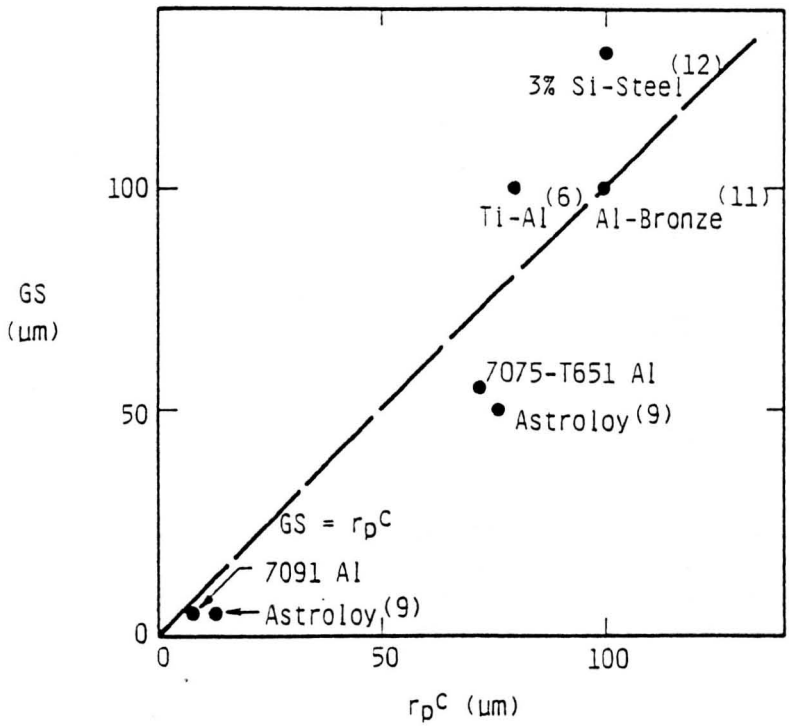


Fig.3.13 Convergence of short crack and long crack data when cyclic plastic zone size ( $r_p^C$ ) is equal to grain size (GS) [50].

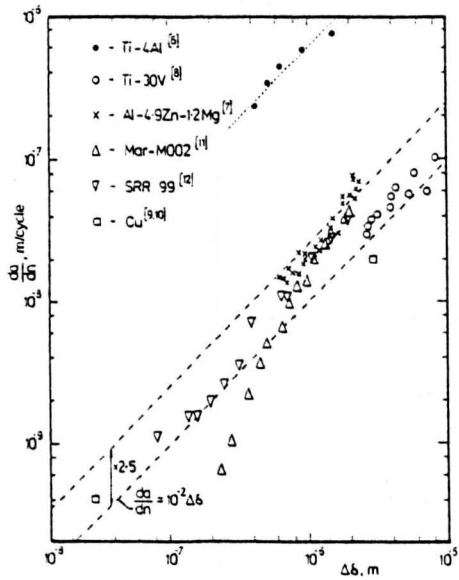


Fig.3.14 Plot of fatigue crack growth rates in single crystals versus crack opening displacement,  $\Delta \delta$  [44].

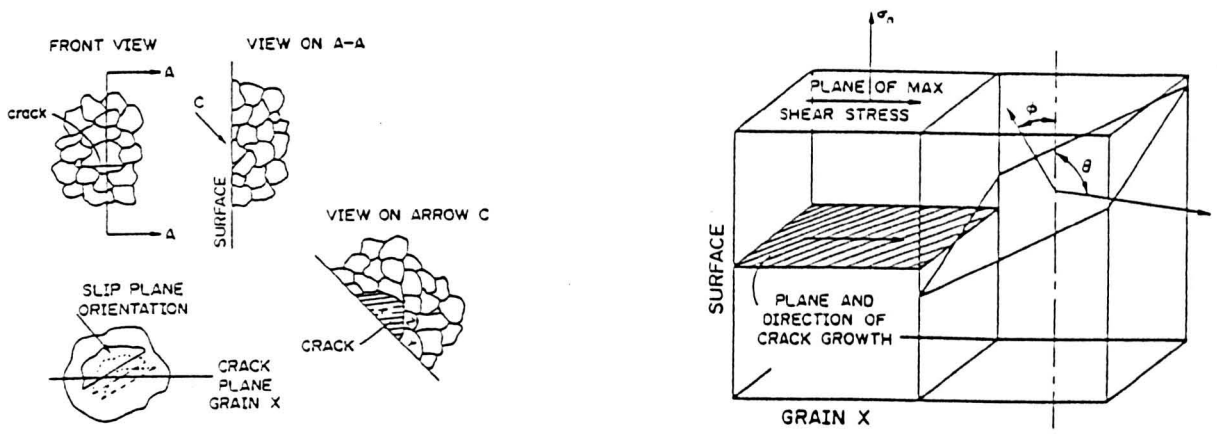


Fig.3.15 Miller's model for crack growth arrest [47]: a) a surface grain and its three-dimensional relationship with surrounding grains, b) the orientation of a crack plane (normal  $\phi$ ) and crack growth direction ( $\theta$ ) with respect to the initial crack in grain X.

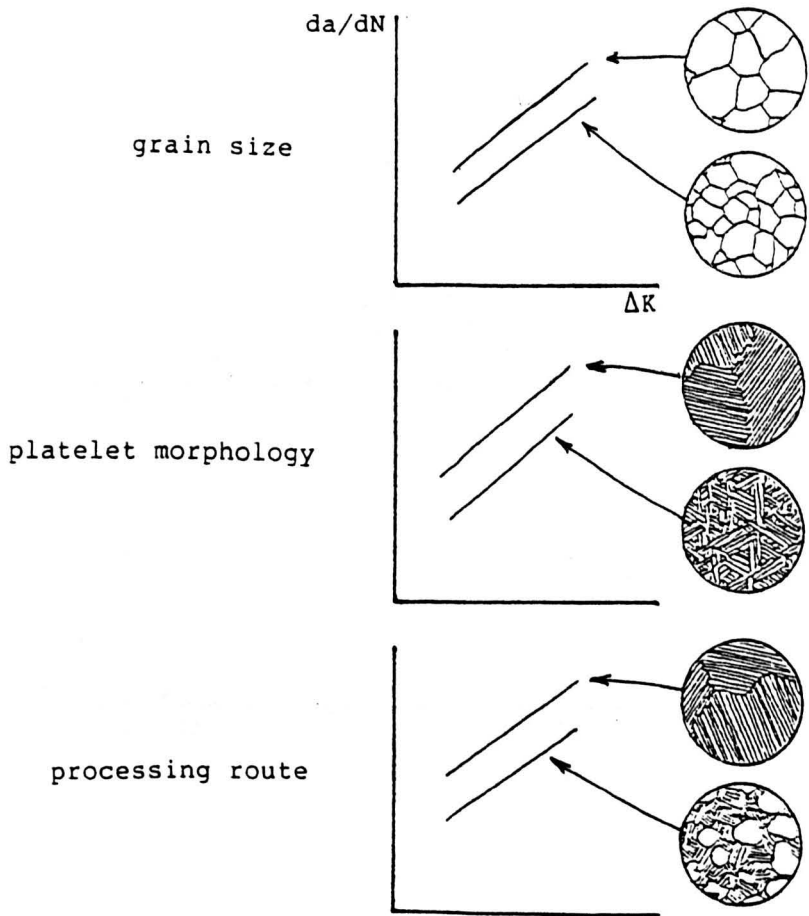


Fig.3.16 Summary of general trends in short crack behaviour seen in titanium alloys.

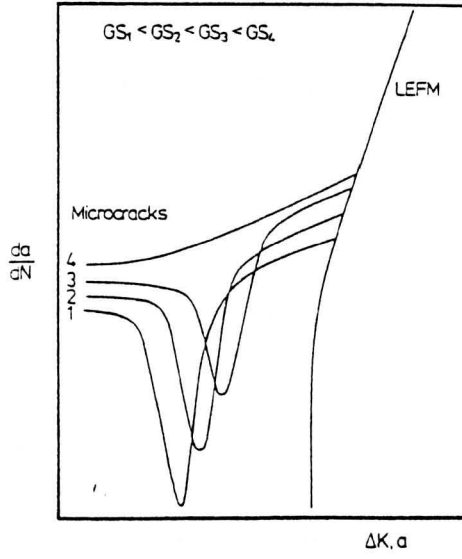


Fig.3.17 Schematic effect of grain size on short crack growth rate [44].

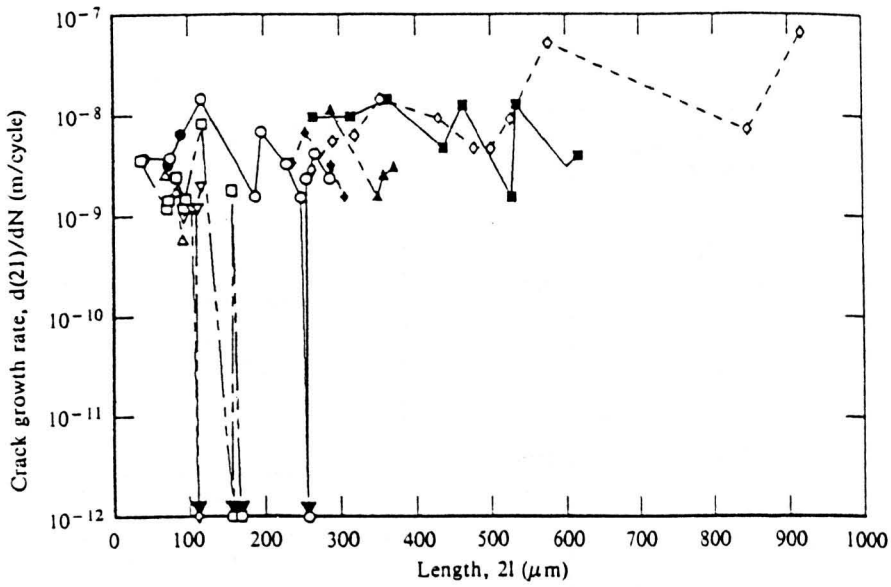


Fig.3.18 Experimental short crack growth rate data for pure magnesium, showing several crack tip arrests [130].

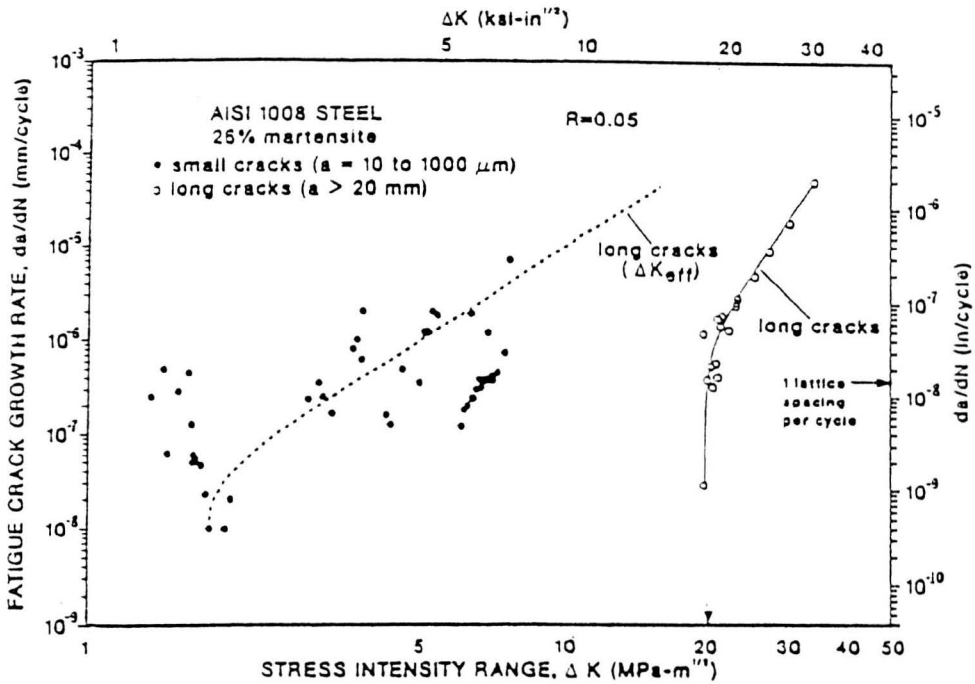


Fig.3.19 Example of  $da/dN$  vs.  $\Delta K_{eff}$  and  $\Delta K$  data for long cracks compared with the corresponding short crack data [118], showing how long crack data can be brought into line with short crack data when analysed in terms of  $\Delta K_{eff}$ .

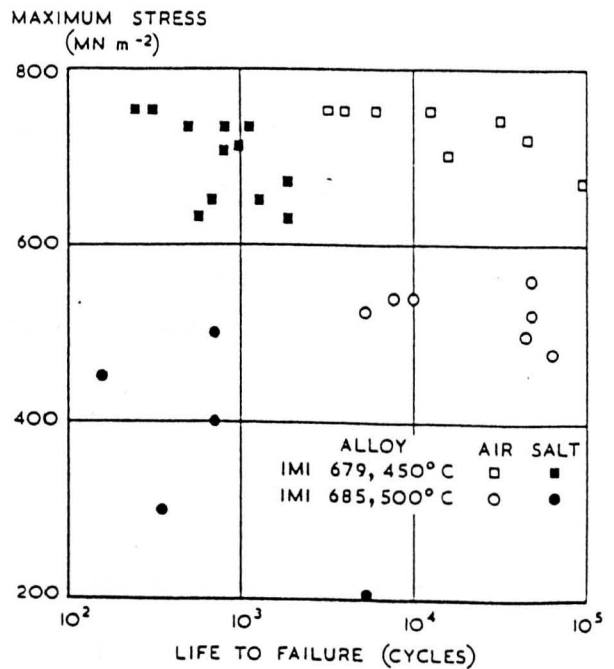
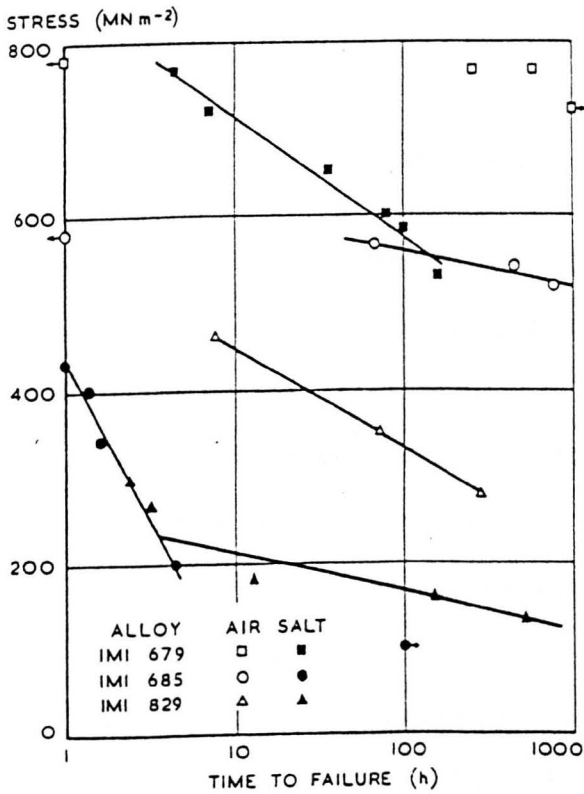


Fig.3.20 Effect of environment on creep and fatigue properties of three titanium alloys, IMI679, IMI685 and IMI829 [142].

CHAPTER 4  
EXPERIMENTAL TECHNIQUES

4.1 HEAT TREATMENTS

Several microstructures were studied for this report, four from the alloy Ti65s and one from the alloy IMI685. The heat treatments and the resulting structures are described below. All structures were given a  $\beta$ -heat treatment i.e. solution treated in the  $\beta$  phase field.

4.1.1 As-received Microstructure

The as-received microstructure was that of an as-forged and part-machined Ti65s compressor disc which had undergone the following heat treatment:

- 1) solution treat at 1050°C for 24hrs. in vacuum
- 2) forced air cool
- 3) temper/age at 550°C for 24hrs.
- 4) air cool.

The resultant microstructure is one of Widmanstätten (basketweave)  $\alpha$ -platelets within prior  $\beta$ -grains (see Fig.4.1a). This structure will be referred to as the AR structure.

#### 4.1.2 Aligned Structure

The heat treatment was carried out on specimen blanks of Ti65s which were subsequently machined to give the required specimen design.

- 1) solution treat at 1050°C for 24hrs. in vacuum
- 2) furnace cool in vacuum
- 3) temper/age at 550°C for 24hrs.
- 4) air cool

The resultant microstructure is one of colonies of aligned  $\alpha$ -platelets within prior  $\beta$ -grains (see Fig.4.1b). This structure will be referred to as the A structure.

#### 4.1.3 Coarse Grain Microstructures

The heat treatments were carried out on specimen blanks of Ti65s and were solution treated at 1250°C to give much coarser structures than the as-received (AR) and aligned (A) microstructures.

##### 4.1.3.1 Coarse Grain Basketweave Structure -

- 1) solution treat at 1250°C for 24hrs. in vacuum
- 2) air cool
- 3) temper/age at 550°C for 24 hrs.
- 4) air cool.

The resultant structure is one of Widmanstätten  $\alpha$ -platelets within very large prior  $\beta$ -grains (see Fig.4.1c). This microstructure will be referred to as the CGB structure.

#### 4.1.3.2 Coarse Grain Aligned Structure -

- 1) solution treat at 1250°C for 24hrs. in vacuum
- 2) furnace cool in vacuum
- 3) temper/age at 550°C for 24 hrs.
- 4) air cool.

The resultant microstructure is one of large colonies of aligned  $\alpha$ -platelets within very large prior  $\beta$ -grains (see Fig.4.1d). This microstructure will be referred to as the CGA structure.

#### 4.1.4 IMI685 Microstructure

Specimens were machined from an IMI685 cheese which had been fully heat treated so that its microstructure was similar to the AR structure (Fig.4.1a).

Metallographic dimensions for the different microstructural conditions are given in Table 4.1.

### 4.2 SHORT CRACK EXPERIMENTS

#### 4.2.1 Specimen Preparation

Two types of specimen were used for investigations of short crack behaviour. These were a square section bar, for use in four point bend testing, and an hour-glass-shaped specimen for use in uniaxial tension testing. The two specimen designs are shown in Appendix 1. Both types of specimen were prepared in a similar way. In order to be able to monitor clearly the behaviour of cracks as they travelled through various microstructures the specimens required a smooth surface finish. This was achieved by taking the previously heat treated specimens and grinding them on

successively finer grades of silicon carbide paper then polishing with 9 $\mu$ m diamond paste. Specimens were then lacquered ready for electropolishing, leaving the particular area to be tested unlacquered.

It is important to leave an area larger than that which will be subjected to the maximum stress during testing, in order that no initiation occurs on electropolishing steps. The reason for electropolishing, rather than mechanical polishing, was to relieve any residual stresses on the specimen surface caused by the grinding and mechanical polishing operations. Specimens were electropolished in a solution of 94% acetic acid and 6% perchloric acid at approximately 50V and a temperature of around 13°C for 3-4 minutes. This gave a current density of around 4000A/m<sup>2</sup>, this being the most important variable in the process. Following electropolishing, the electropolished region was etched in an aqueous solution of 2% hydroflouric acid (40%) and 10% nitric acid (Kroll's reagent) to reveal the top surface microstructure and hence facilitate the monitoring of crack interaction with the microstructure. Examples of four point bend specimens and a uniaxial tension specimen, after preparation and prior to testing, are shown in Fig.4.2.

#### 4.2.2 Four Point Bend Testing

Four point bend tests were carried out on all the microstructural conditions mentioned above. For the AR condition, the effects of specimen size and stress range were also studied.

The standard smooth specimen four point bend tests were carried out in the following way. Square section specimens were tested in four point bend using a Mayes closed loop servohydraulic testing machine in laboratory air at 20°C. The rig configuration and test parameters are shown in Fig.4.3 All tests were carried out at a stress ratio ( $\sigma_{\min}/\sigma_{\max}$ ) of 0.1 and a frequency of 10Hz. Several different maximum top surface stresses were used, between 800 and 900MPa. Maximum stress levels were calculated using the equation:

$$\sigma_{max} = \frac{3P_{max}d}{th^2} \quad (4.1)$$

where  $\sigma_{max}$  is the maximum top surface stress,  $P_{max}$  is the maximum load on the specimen,  $d$  is the distance between the inner rollers,  $t$  is the specimen width and  $h$  is the specimen thickness (see Fig.4.3).

Monitoring of crack length was carried out using a replication technique. Tests were interrupted at various intervals, generally between 1000 and 10000 cycles, depending on whether there was a crack present, and acetate replicas of the maximum stress region were taken at mean load.

#### 4.2.2.1 Specimen Size Effects -

Two different specimen sizes were used, to see whether the behaviour of the inherently coarse microstructure of the Ti65s would be more predictable, especially in terms of initiation, with a larger specimen size. It was also intended to observe if the stress intensity solutions would be affected in any way.

Dimensions for the two different specimen sizes were 10x10x70mm<sup>3</sup> and 17x17x90mm<sup>3</sup>.

#### 4.2.2.2 Low Stress Tests -

Low stress tests were carried out to determine whether there were any stress effects during testing. These tests were started at high stress (850MPa) in order to initiate a crack. As soon as a crack had been detected the load was removed and the specimen stress relieved in a vacuum furnace for 6 hours at 550°C. After heat treatment the test was restarted at a lower maximum stress and the testing carried out in the normal way. The maximum stresses for the low stress tests were in the range 400MPa to 500MPa

#### 4.2.3 Uniaxial Tension Tests

Specimens were prepared the same way as for the four point bend tests except that the whole of the notched section on all four sides was electropolished. Replicas of both notches were taken because the likelihood of initiation was equal for both sides.

#### 4.2.4 The Replicating Technique

An appropriately sized piece of 0.034mm thick acetate sheet was dipped for about one second in some acetone and placed on the specimen top surface, making sure that no air bubbles were trapped beneath it. The softened replicating sheet lay flat on the specimen surface and after approximately two minutes the acetone evaporated, leaving a stiff 'mirror image' replica of the specimen

microstructure and any surface cracks present. The replica was peeled from the specimen surface and stuck face up on a microscope slide for later inspection. Sputter coating of the replicas with a thin film of gold was found to improve reflectivity, and thus aid identification and measurement of cracks.

#### 4.3 LONG CRACK EXPERIMENTS

Long crack fatigue tests on the AR (as-received) and the A (aligned) structures were carried out using a Mayes closed loop servohydraulic testing machine. The machine was operated under constant amplitude sinusoidal loading with a frequency of 33Hz and a load ratio (R) of 0.1, in laboratory air. Single edge notched (SEN) specimens conforming to BS 5447:1977 were used. Crack length was monitored via a direct current potential drop technique and tests were started at an initial  $\Delta K$  of approximately  $15\text{MNm}^{-3/2}$ . This was reduced in 5-10% decrements each time the crack had grown through a distance approximately four times the size of the plastic zone size corresponding to the previous  $\Delta K$  level. When no discernible crack growth had occurred in  $10^8$  cycles the value of  $\Delta K$  was equated to the threshold value  $\Delta K_{th}$ . The load was then increased to grow the crack out from threshold. The long crack specimen design is shown in Appendix 1.

#### 4.4 TENSILE TESTING

A limited number of tensile tests were carried out on the two coarse grained structures (CGA and CGB). Standard Hounsfield tensile specimens were prepared by machining them from the ends of four point bend specimens which had been tested. Care was taken to

machine the tensile specimens from the plane of the four point bend specimen neutral axis, so that they would be unaffected by the stress history of the four point bend specimens.

#### 4.5 METALLOGRAPHIC TECHNIQUES

Several techniques were used in preparing specimens for examination (normally on a microscopic scale).

##### 4.5.1 Preparation For Examination Of Microstructure

Specimens were prepared for microscopic examination by grinding on progressively finer grades of silicon carbide paper down to 4000 grit. Mechanical polishing was then carried out using either a suspension of alumina in water or a suspension of 1  $\mu\text{m}$  diamond paste in alcohol. Etching to show up the microstructure was done using Kroll's reagent for approximately 30 seconds.

##### 4.5.2 Preparation For Macro-examination Techniques

The surface to be examined was ground down to a coarse finish (approx. 240 grit). Etching was performed by swabbing the specimen surface for several minutes with a solution of approximately 40vol% nitric acid and 10vol% hydrofluoric acid (40%) in water.

##### 4.5.3 Sectioning Techniques

Sectioning of fracture surfaces was performed in several stages. Firstly the fracture surface was electroplated for approximately 2 minutes in a Watts nickel bath at a temperature around 40°C using a current density of about 50A/m<sup>2</sup> and a nickel

anode. This gave a tenacious layer of nickel 1-2 $\mu$ m thick. The specimens were then electrolessly nickel plated in a bath of Nifoss 2000 at 80°C for several hours.

The actual sectioning of the fracture surface was carried out using a hacksaw, the nickel plate protecting the fracture surface from mechanical damage. The section could then be mounted and prepared in the usual way for microexamination.

#### 4.5.4 Crack Shape Measurement

Two methods were used to determine crack geometry; a crack face oxidation technique and a crack sectioning technique. Both of these techniques involved measurements on previously tested specimens containing fatigue cracks.

##### 4.5.4.1 The Crack Face Oxidation Technique -

Specimens were loaded in three point bend to the test mean load, to open the crack. The specimen was then heated, under load, to approximately 600°C for 1 hour, to oxidise the specimen surface and the crack faces. The interference effects due to the thickness of the oxide film gave a dark brown or purple colour. Therefore when the specimen was broken open after cooling down, the fatigue region on the fracture surface was clearly distinguishable by its colour. The 'top surface' fatigue crack length,  $2a$ , and the depth,  $c$ , at the midpoint of the fatigue region were then measured to determine crack shape. The oxide film could not be detected with the scanning electron microscope and therefore these fracture surfaces were examined using a stereo optical microscope.

#### 4.5.4.2 The Crack Sectioning Technique -

The sectioning technique involved progressive removal of material from the specimen top surface. At various intervals the specimen was repolished mechanically and etched to show up the cracks. Length and position of the cracks could be monitored accurately by measuring the distance of each crack tip from one edge of the specimen. In this way a picture of the crack geometry could be built up by plotting crack length against depth of material removed, i.e. depth below the original specimen top surface. This method was more time-consuming than the crack face oxidation technique but was especially useful when more than one crack was present in a specimen, as well as giving useful three-dimensional information about the microstructure surrounding each crack.

#### 4.6 MICROSCOPY

Measurement of surface crack length was carried out using a Reichert optical bench microscope with an eyepiece graticule. Crack lengths were measured either side of the initiation site so that the behaviour of each individual crack tip with regards to the local microstructure could be monitored more closely. Crack lengths were always measured perpendicular to the applied stress direction. If necessary total surface crack length could be used in calculations by simply adding the lengths of the two individual crack 'tips' together. Micrographs of replicas and specimen top surfaces were taken using a Nikon UFX-II optical microscope.

Fracture surfaces and top surfaces of specimens were examined using a Jeol 35C scanning electron microscope at various magnifications, using an accelerating voltage of 25KV.

Transmission electron microscopy was carried out on thin foils using a Phillips 301 TEM. The foils were prepared by jet polishing in a solution of 5% perchloric acid in ethanol at a temperature of 0°C and a potential of 30V.

Table 4.1 Microstructural dimensions for the four conditions of Ti65s.

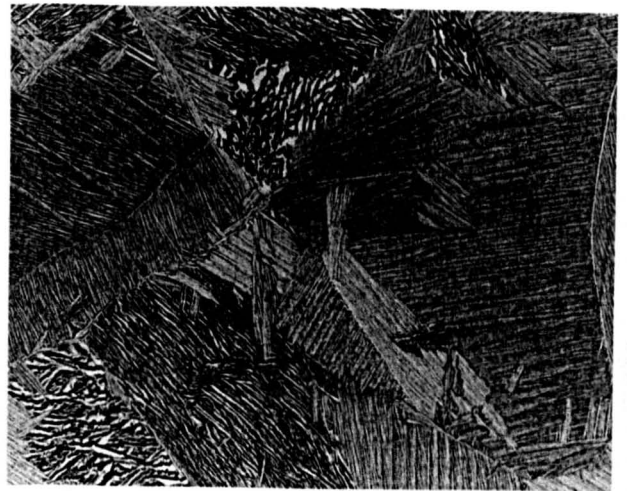
Condition	Ave. prior $\beta$ -grain size / mm	Ave. $\alpha$ -colony size / mm
AR	1.55	0.40
A	1.65	0.25
CGB	9.50	--
CGA	9.20	0.95

Dimensions determined using the mean linear intercept method.



200 $\mu$ m

a



200 $\mu$ m

b

c

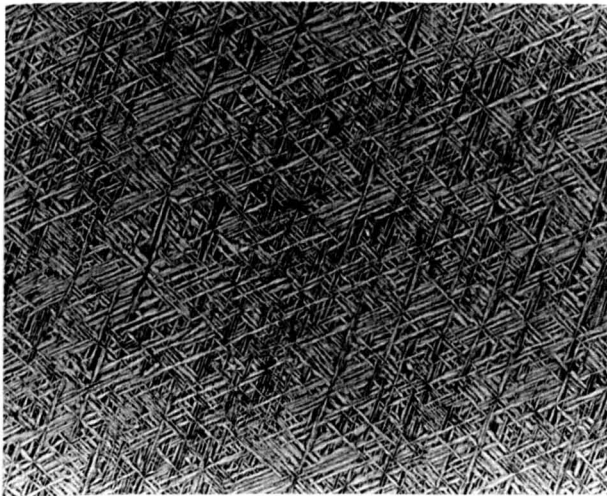


2mm

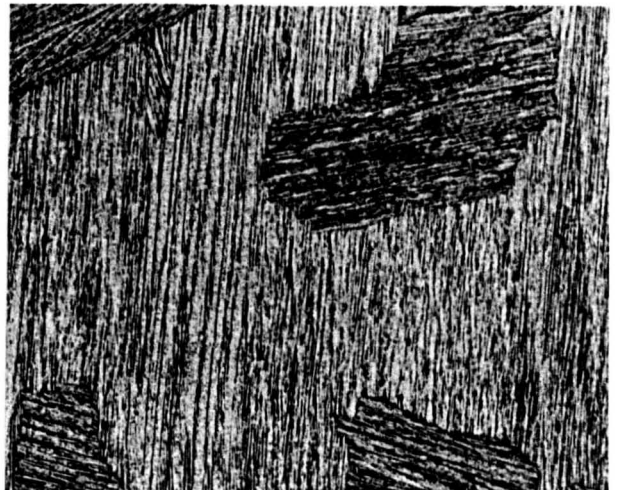
d



2mm



100 $\mu$ m



100 $\mu$ m

Fig.4.1 The four microstructural conditions studied in Ti65s: a) as-received microstructure, b) aligned microstructure, c) coarse grain basketweave microstructure, d) coarse grain aligned microstructure

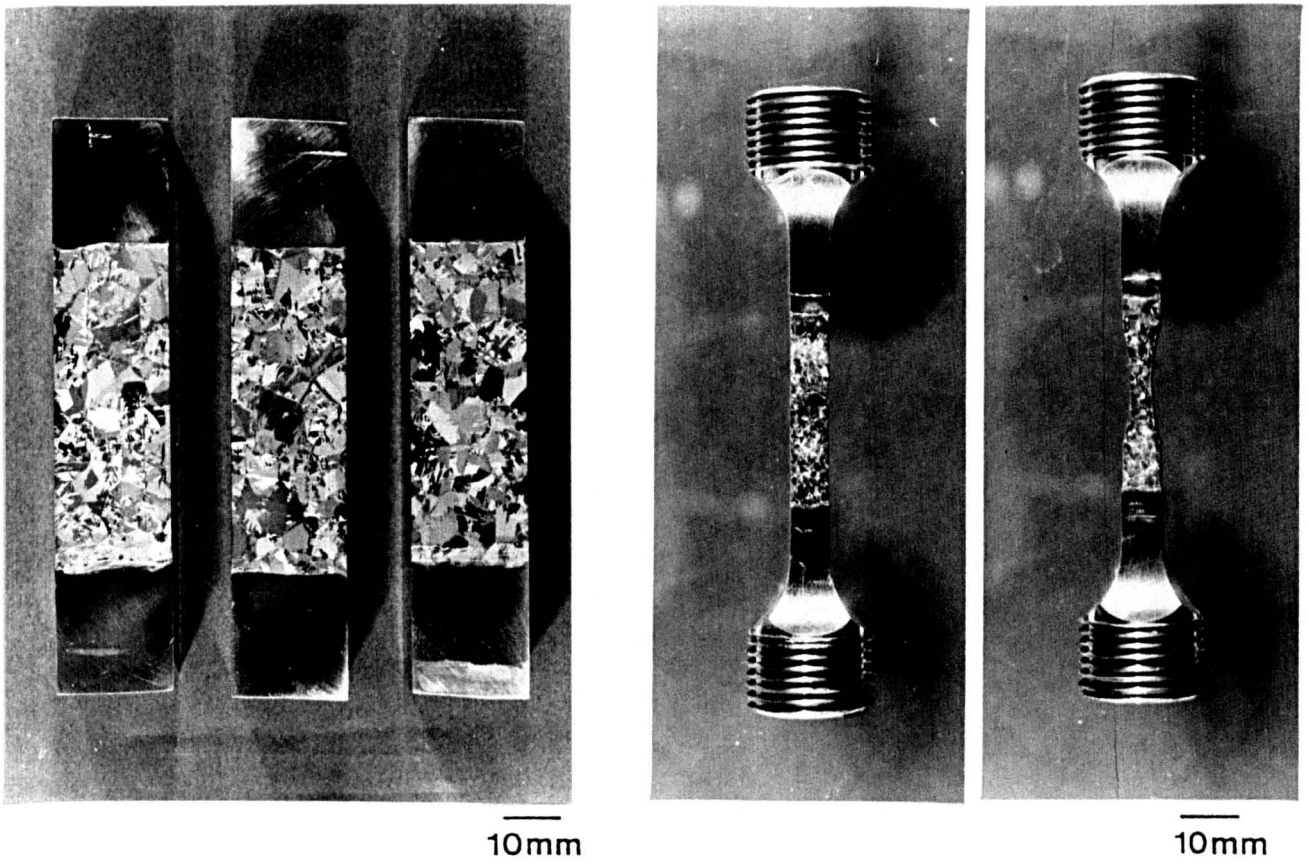


Fig.4.2 Examples of four point bend and uniaxial tension specimens after preparation and prior to testing.

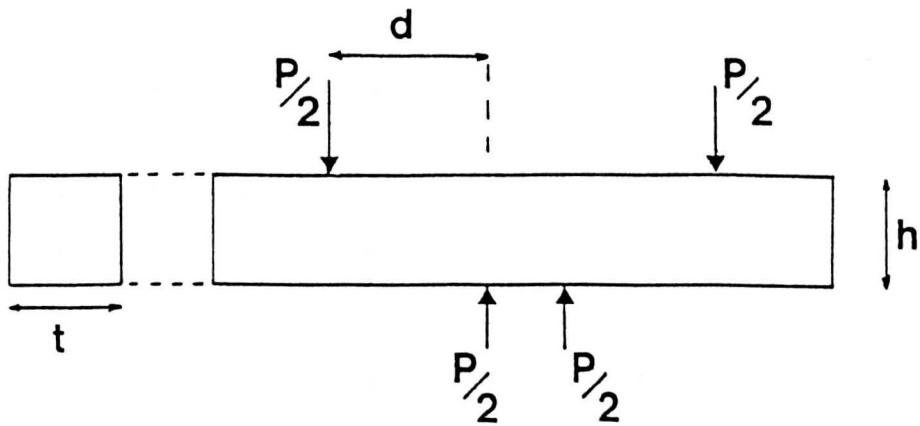


Fig.4.3 Rig configuration and test parameters for four point bend testing.

CHAPTER 5  
TREATMENT OF EXPERIMENTAL SHORT CRACK DATA

5.1 INTRODUCTION

A computer model was used to analyse data obtained from short crack tests. The data were obtained in the form of surface length from initiation site to crack tip,  $a_i$ , where  $i=1$  or  $2$ , versus number of cycles,  $N$ . The crack lengths  $a_1$  and  $a_2$  were not equal to half the total surface crack length,  $2a$ ; it will be seen later that this is an important point when calculating stress intensities. The assumed short crack geometry is shown in Fig.5.1.

5.2 FACILITIES WITHIN THE COMPUTER MODEL

5.2.1 Crack Length Versus Number Of Cycles

Firstly, the model plotted crack length  $a_i$  versus number of cycles  $N$ . This is a useful guide to growth rate behaviour, but this method of comparing material behaviour can be used only when specimen geometry, crack geometry and stress range are consistent. This is the reason why the unifying parameter of stress intensity is used normally when comparing data. A facility was also available to use total surface crack length  $2a$ .

## 5.2.2 Calculation Of Stress Intensity

### 5.2.2.1 Stress Intensity Solutions -

The main purpose of the model was to calculate stress intensities for the short cracks studied and to plot these on a graph of crack growth rate,  $da/dN$ , versus alternating stress intensity range,  $\Delta K$ . Three solutions were used for calculating stress intensities for a semi-elliptical crack in a rectangular-section specimen subjected to pure bending. An additional solution was used to calculate stress intensities for a semi-elliptical crack in a uniaxial tension specimen, with a notch stress concentration ratio  $K_t=1.03$ . Crack shape was assumed to be semi-circular for all cracks studied. The solutions used for the bend specimens were: 1) the Shah and Kobayashi solution for the deepest point of a crack [146-148], 2) the Pickard solution for the deepest point of a crack [149] and 3) the Pickard solution for surface crack tips [149]. Since crack behaviour was actually monitored by measuring the surface crack length, via replicas, solution 3) was favoured. Stress intensities at each individual surface crack tip were calculated.

A comparison of the three solutions is shown in Fig.5.2 using identical data from a test on the A structure. The solutions by Shah and Kobayashi and by Pickard for the stress intensity at the deepest point of a crack show good agreement. The main point to be noted is that, for the plots of  $\Delta K$  at the deepest point of the crack,  $\Delta K$  does not reach values as high as that for the Pickard-surface solution. This can be explained by plotting  $\Delta K$  versus crack length  $a$  and versus crack depth  $c$ , shown in Fig.5.3. As the crack tip approaches the neutral axis of the bend specimen,

$\Delta K$  increases to a maximum point corresponding to  $\Delta K=32\text{MNm}^{-3/2}$ , which occurs at a depth of 2.8mm, some distance away from the neutral axis.

#### 5.2.2.2 An 'Adjusted' Stress Intensity Plot -

From determinations of crack geometry by the crack face oxidation method, it became clear that although  $a_1$  and  $a_2$  on the specimen surface may vary considerably, the overall crack shape remains approximately symmetrical. Therefore the stress intensity at each surface crack tip of a particular crack is due not to the lengths  $a_1$  or  $a_2$ , but to half the total surface crack length,  $a$ . This is illustrated in Fig.5.4. As a result of this, growth rates of each crack tip were plotted against 'adjusted' stress intensity ranges. In fact, the usefulness of the values  $a_1$  and  $a_2$  extends only as far as being a means of measuring the growth increments of each crack tip.

#### 5.2.3 Calculation Of Growth Rates

The standard method of calculating growth rates from values of  $a_i$  and  $N$  was to calculate the gradient between two  $a_i, N$  points. Since this represented an average growth rate between the two points the calculated growth rate was assumed to correspond to the average crack length between the two points. This is illustrated in Fig.5.5.

In order to try to reduce growth rate scatter and make comparisons easier, a facility was added which calculated growth rates between every third  $a$  vs.  $N$  point. The plot of these growth rates against  $\Delta K$  can be thought of as inherent 'background' growth

rate behaviour. This 'Three Point Method', proposed by Kendall and King [150], is shown in Fig.5.6. A comparison between computer plots using the standard method and the 'Three Point Method' is shown in Fig.5.7.

### 5.3 SUMMARY

One of the intentions of this chapter was to illustrate, at least in part, that the evaluation of stress intensities and crack growth rates for short cracks is not as straightforward as it may first appear. There are one or two factors inherent in the physical nature of short cracks which can make the interpretation and utilisation of data difficult. The first of these, which has already been discussed in section 3.2, is that short cracks are three-dimensional and so, regardless of whether  $\Delta K$  is calculated at the surface or at the deepest point, crack geometry must be taken into account. Since a crack cannot be monitored below the surface, assumptions about its crack geometry must be made. Secondly the amount of 'real' scatter inherent in short crack data makes it difficult for straightforward comparisons to be made, as will be seen later.

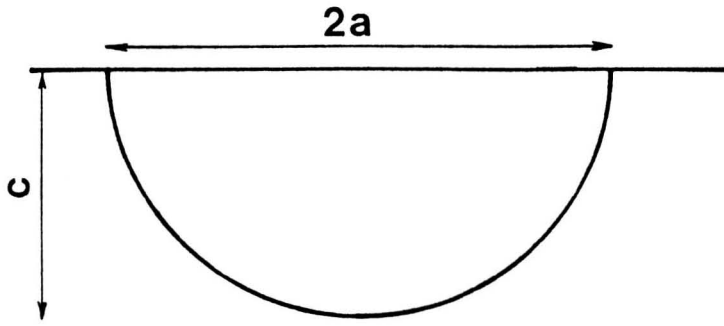


Fig.5.1 Assumed short crack geometry.

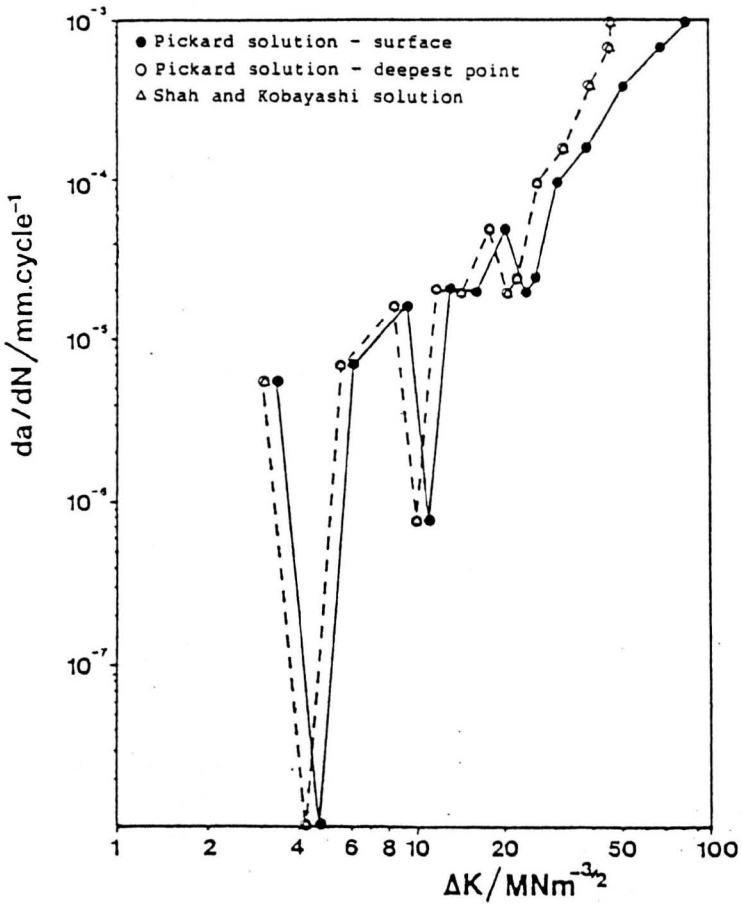


Fig.5.2 Comparison of three stress intensity solutions considered for short thumbnail cracks in smooth four point bend specimens.

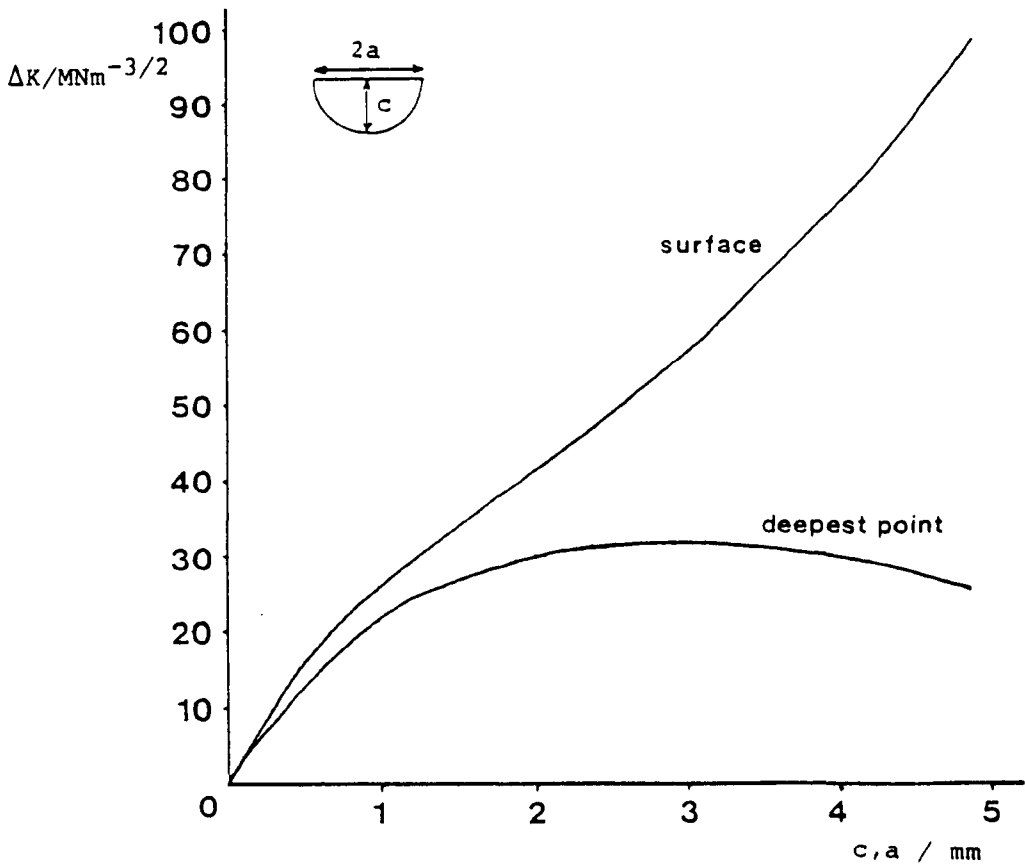


Fig.5.3 Plot of  $\Delta K$  versus half surface crack length,  $a$ , and crack depth,  $c$ , in four point bend, for a square section specimen 10mmx10mm, max. stress 850MPa,  $R=0.1$ .

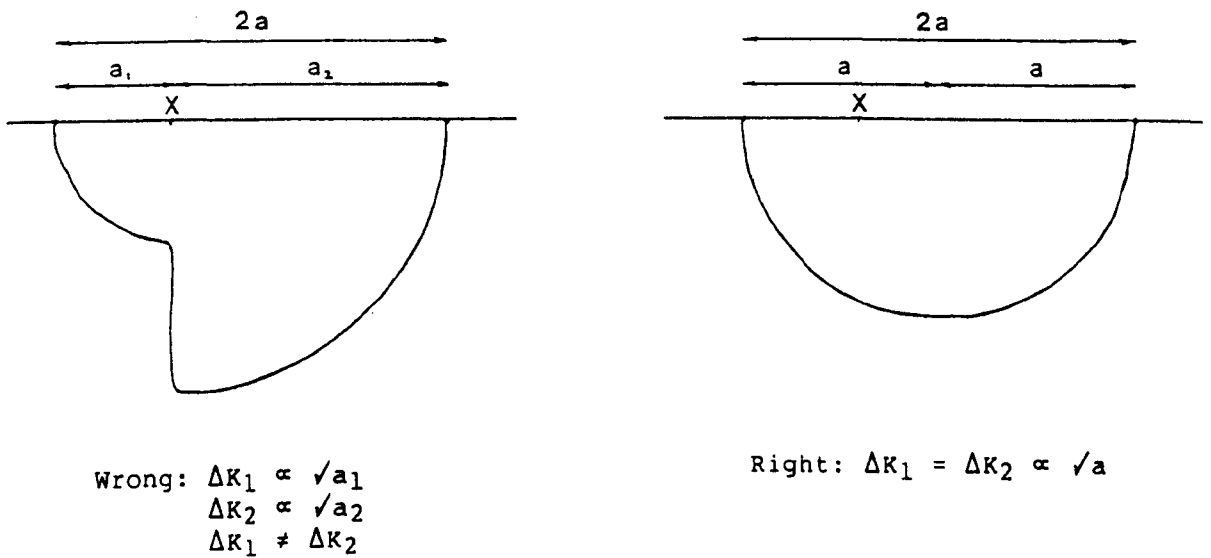


Fig.5.4 Assumptions made about subsurface crack geometry.

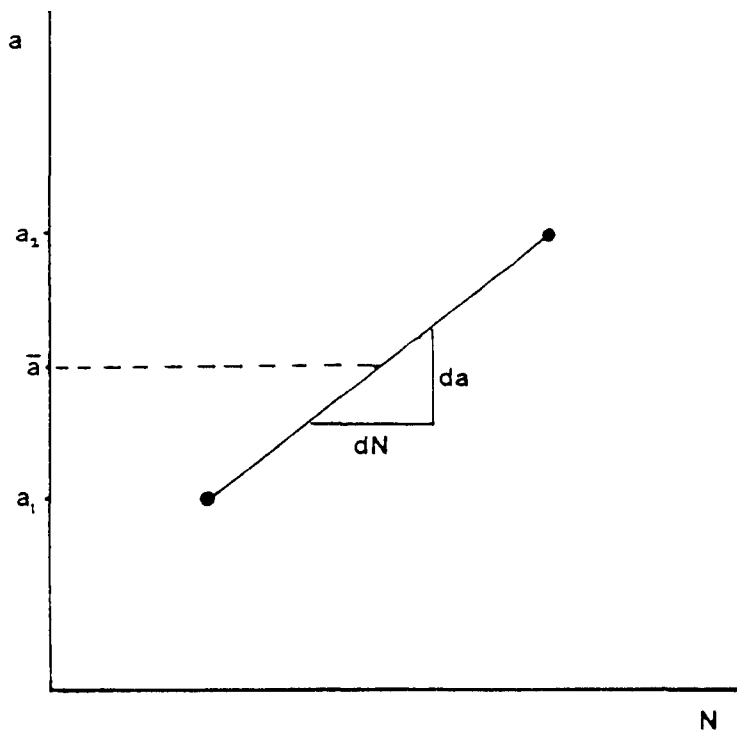


Fig.5.5 Standard method for calculating crack growth rate  $da/dN$ .

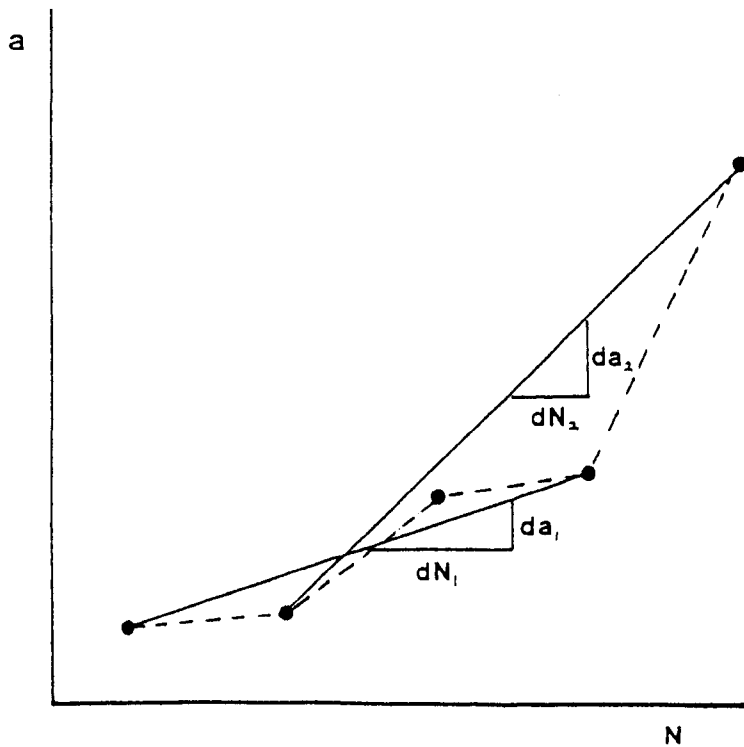


Fig.5.6 'Three Point Method' for calculating crack growth rate  $da/dN$  [150].

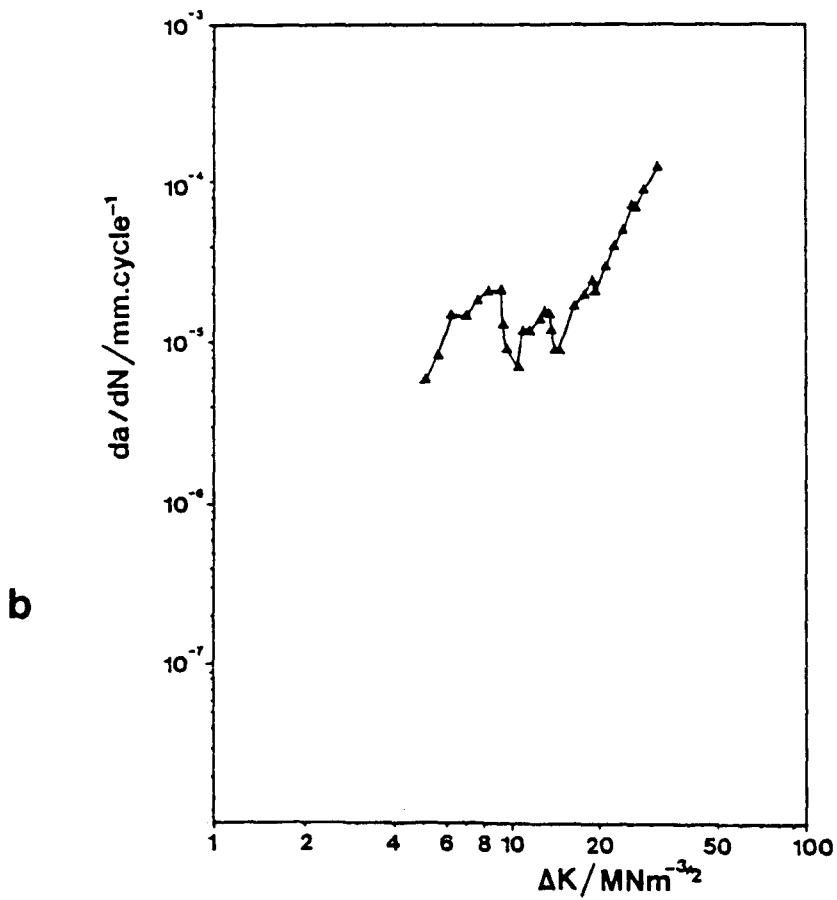
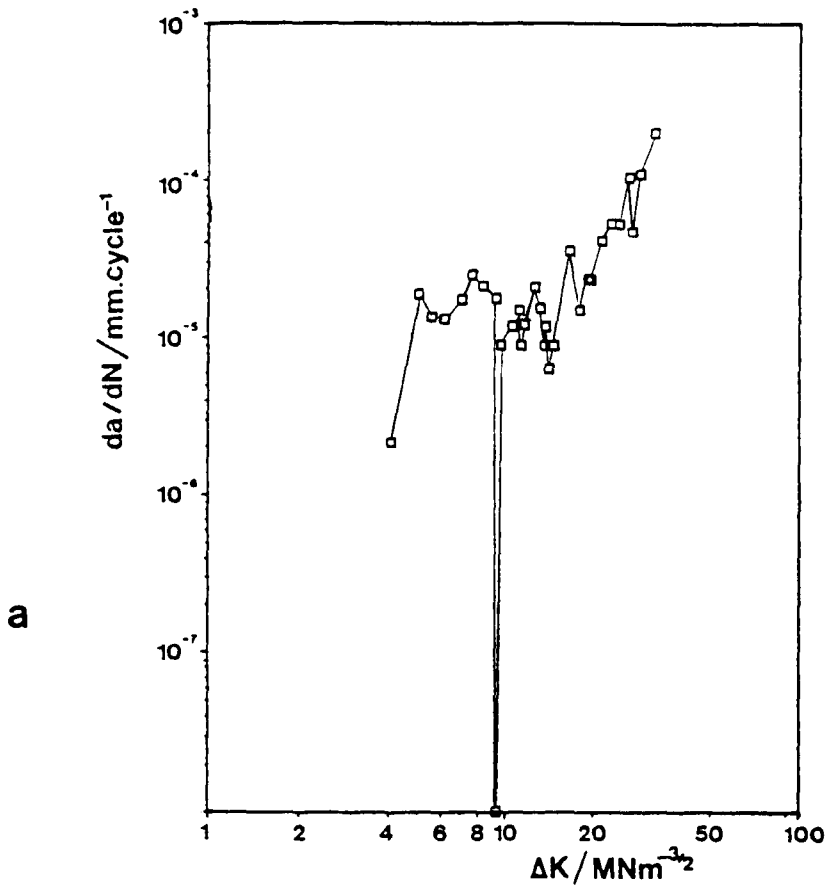


Fig.5.7 Comparison of crack growth rate data using a) the standard method and b) the 'Three Point Method'.

## CHAPTER 6

### MECHANICAL EFFECTS

#### 6.1 INTRODUCTION

This chapter deals mainly with variables imposed by the nature of the different tests carried out. Comparisons of crack growth behaviour are made using plots of crack growth rate  $da/dN$  vs.  $\Delta K$  in the form of scatter bands of data obtained from several cracks. Where the 'Three Point Method' has been used to generate data, this fact will be indicated.

#### 6.2 CRACK SHAPE MEASUREMENTS

##### 6.2.1 Results

Measurements of crack shape by the oxidation method were carried out on cracks of varying size in the as-received (AR) microstructure and the coarse grain basketweave (CGB) structure. Micrographs showing examples of cracks sampled in the AR structure are shown in Fig.6.1.

Determination of crack shape by a crack sectioning technique was performed on a coarse grain aligned (CGA) specimen containing three cracks. Schematics of the three cracks determined from sectioning of the CGA specimen are shown in Fig.6.2.

The figures show that the crack shapes were by no means perfectly semi-circular or semi-elliptical, but in order to determine  $c/a$  ratios they were approximated to semi-elliptical cracks.

A plot of  $c/a$  ratio vs. crack depth  $c$  from all the crack shape determinations is shown in Fig.6.3. All crack shape measurements were made on a plane perpendicular to the stress axis.

#### 6.2.2 Discussion

An interesting aspect of the crack shape in the CGB structure was that disproportionate amounts of crack growth occurred either side of the initiation site due to microstructural factors. This resulted in the initiation site not lying at the centre of the crack, but in spite of this, the crack shape was still approximately symmetrical. The fracture surface with oxidised fatigue region is shown in Fig.6.4. This confirms the validity of the approach used to calculate stress intensities for individual crack tips, discussed in section 5.2.2.2.

The data reported here shows many similarities to earlier work [59-62], particularly that of Bolingbroke and King [59]. Their results from work on  $\beta$ -processed IMI318 are reproduced in Fig.6.5. These results show widely varying  $c/a$  ratios, between

0.75 and 2.5, up to crack depths of about 0.6mm, while above crack depths of 0.6mm  $c/a$  values fell between 0.8 and 1.0. In both this work and that of Bolingbroke and King, the large variations in values of  $c/a$  at shorter crack depths corresponded to growth almost entirely on one slip plane within an  $\alpha$ -colony.

A plot of  $\Delta K$  vs.  $a$  for both large and small bend specimen geometries, shown in Fig.6.6, partly explains the changing crack shapes. The curves show reasonable agreement up to a values of about 0.75mm, but above  $a=0.75$ mm the curves show considerable divergence. The difference between  $\Delta K$  at the surface and  $\Delta K$  at the deepest point continues to increase, so one might expect to see the  $c/a$  ratio decreasing with increasing crack length above  $a=0.75$ mm. In reality, as both Fig.6.3 and Fig.6.5 show,  $c/a$  ratios remain fairly constant above  $a=0.75$ mm. In addition, the  $\Delta K$  vs.  $a$  plot implies that below  $a=0.75$ mm, crack shapes should be roughly semi-circular, i.e.  $c/a=1.0$ , because  $\Delta K$  at the surface is approximately equal to  $\Delta K$  at the deepest point. This is clearly not the case, which suggests that there is a strong microstructural effect at these crack lengths.

The results serve to highlight the difficulties of characterising short crack growth accurately, when it is impossible to monitor the crack subsurface. The assumption that cracks are semi-elliptical is an approximation, as Figs.6.1-6.2 show. In addition to this, attempts to use a varying  $c/a$  ratio in stress intensity solutions would be impractical, as each individual crack would not necessarily follow the same pattern in terms of change in crack shape. Although there seems to be a fairly clear trend as illustrated in Fig.6.3, at the shorter crack

lengths there is a large amount of scatter, so it could be argued that the trend line is not really valid.

### 6.3 EFFECT OF SHORT CRACK SPECIMEN DESIGN

#### 6.3.1 Results

While a large number of tests were carried out on the AR structure using small bend specimens, only a small number of tests were carried out using uniaxial tension specimens. These tests were carried out at maximum stresses of 850MPa, under the same laboratory conditions as the four point bend tests.

Initiation was found to occur at the specimen surface in all the uniaxial tension tests and initiation behaviour appeared to be similar to that observed in the four point bend tests. Stress intensities for the uniaxial tension specimens were determined using the Shah and Kobayashi solution for a plane semi-circular surface crack in a slab subjected to a uniform uniaxial tensile stress (c.f. section 5.2.2.1). Crack growth rate  $da/dN$  vs. stress intensity range  $\Delta K$  data are shown in Fig.6.7, compared with the scatter band for the as-received material in the small specimen four point bend tests. For consistency, the four point bend results used here have been determined using the Pickard stress intensity solution for the deepest point of a semi-circular surface crack in a bar subjected to pure bending. From the comparison of growth rate data it appears that growth rates in the uniaxial tension specimens tended to be slightly higher than those in the four point bend specimens. After testing, the uniaxial tension specimen fracture surfaces were examined and fatigue crack shapes were found to be approximately semi-circular ( $c/a=1$ ).

## 6.3.2 Discussion

### 6.3.2.1 Propagation -

Although not thoroughly conclusive, the initial tests on the uniaxial tension specimens suggest that specimen design may have an effect on growth rate. In this case the tension specimens seem to show faster growth rates than in the four point bend tests. It should be pointed out, however, that the data obtained from the uniaxial tension tests were rather limited in quantity. Initiation always occurred at the surface of the uniaxial specimens, so a similar high stress surface area to that of the bend specimens was sampled.

One factor which might affect crack growth data is crack shape. In the four point bend tests and the uniaxial tension tests a semi-circular crack shape was assumed. A second plot of  $\Delta K$  vs.  $a$  for the uniaxial specimens and the small bend specimens is shown in Fig.6.8. only one curve is shown for the uniaxial tension specimens, because  $\Delta K$  at the surface is identical to  $\Delta K$  at the deepest point, due to the uniform stress field throughout the specimen cross section. Therefore, for the uniaxial tension specimens crack shape should be semi-circular for all crack lengths. As section 6.2 shows, this was not the case for cracks in the bend specimens. The largest difference in growth rates between the two specimen designs were seen at  $\Delta K$  values between  $10\text{MNm}^{-3/2}$  and  $20\text{MNm}^{-3/2}$ . On the plot of  $\Delta K$  vs.  $a$  in Fig.6.8 the curves are very similar below  $\Delta K=20\text{MNm}^{-3/2}$ , so it is unlikely that crack shape is an important factor here.

A second factor which may be important is the existence of compressive residual stresses in the top surface layer of the bend specimens. The maximum stresses used for the tests were between 800 and 900MPa, which is close to the 0.2% proof stress of the Ti65s in the AR condition (900MPa). Fig.6.9a shows the residual stress distribution in a beam after loading such that the surface layers have yielded, i.e.  $\sigma_{\max} > \sigma_y$ . This model assumes that the material has a discrete yield point and that the yield stresses are identical in tension and compression. Ti65s does not have a discrete yield point, so some plastic yielding is likely to occur at the surface below the 0.2% proof stress. Therefore, there might have been a small compressive residual stress in the surface of the bend specimens, similar to that shown schematically in Fig.6.9b. In the uniaxial tension specimens, although maximum stresses were the same proportion of the 0.2% proof stress, any deformation would have occurred in equal amounts throughout the specimen due to the uniform stress field, so there should have been no residual stresses generated by incompatible relaxation in different parts of the specimen. Therefore, the presence of compressive residual stresses in the bend specimens would have the effect of reducing the effective applied stress, thus reducing the stress intensity experienced by the cracks. This could account for the lower growth rates in the bend specimens.

#### 6.3.2.2 Test Life -

A comparison between Rolls-Royce S-N data and those for the four point bend and uniaxial tension tests carried out in this work can be seen in Fig.6.10. The data from this report, mostly for a maximum stress of 850MPa, lie to the right of the

Rolls-Royce data band, showing longer fatigue lives. It should be noted that the Rolls-Royce data band has been generated using uniaxial tension specimens, whereas the majority of the data in this report is from four point bend tests. However the uniaxial tension specimen data still lie to the right of the Rolls-Royce data band, i.e. the specimens have longer fatigue lives.

It is clear that, as well as specimen design apparently having a small effect on growth rate, it can have a large effect on fatigue life. Fig.6.10 shows that fatigue lives for the four point bend specimens tended to be longer than those of the uniaxial tension specimens, especially those tested by Rolls-Royce. This behaviour could be explained by a 'sampling volume' effect associated with the coarse grain size of the  $\beta$  heat treated Ti65S. In the uniaxial tension specimens the whole of the specimen gauge length experiences the same maximum stress, whereas in the bend specimens only the outermost layer of the top surface experiences the maximum fibre stress. Thus if no suitably oriented grain is within this region then it may take a lot longer to initiate a crack than in the tension tests, due to the greater volume of highly stressed material in the latter, hence the fatigue life would be longer. An inconsistency in the sampling volume argument is that initiation in the short crack uniaxial tension specimens occurred at the surface. This suggests that the volume of material involved in the initiation of cracks is actually fairly similar to that in the bend specimens.

The Rolls-Royce uniaxial tension S-N specimens were 4.5mm diameter, so they were similar in cross-sectional area to the short crack uniaxial tension specimens, yet the uniaxial tension

specimens still showed longer fatigue lives than the Rolls-Royce specimens. The more likely cause of the difference in fatigue lives is that the Rolls-Royce S-N specimens had a machined finish whereas all specimens in this work had a smooth finish. Therefore, the Rolls-Royce S-N specimens probably initiated cracks relatively quickly from machining marks on specimen surfaces, leading to a consistently short initiation life and hence a shorter overall fatigue life.

Another possible factor is a variation in grain size and platelet morphology, depending on where the specimens originated from (e.g. which part of a compressor disc forging). Finally, it should be remembered that the work carried out on the smooth uniaxial tension short crack specimens was by no means comprehensive.

#### 6.4 EFFECT OF BEND SPECIMEN SIZE

##### 6.4.1 Results

Tests on large four point bend short crack specimens ( $17 \times 17 \text{mm}^2$ ) of the AR structure were carried out at both high and low stress. In one of the high stress tests, four separate cracks initiated in one specimen. A comparison of  $da/dN$  vs.  $\Delta K$  data for the two different specimen sizes can be seen in Fig.6.11. The scatter bands show good agreement with each other. Initiation lives,  $N_i$ , for the larger bend specimens were more consistent and generally lower than those for the small bend specimens. Values for  $N_i$  in the small specimen tests ranged from 20000 to 790000 cycles with an average of 250000, while those for the large bend specimens ranged from 16000 to 30000 cycles with an average of

24000.  $N_i$  was defined as the number of cycles to initiate a crack with total surface crack length  $2a$  equal to about  $50\mu\text{m}$ . The total specimen lives  $N_f$  of the large four point bend specimens are included on the S-N plot in Fig.6.10. Fig.6.12 shows a comparison of  $\sigma$  vs.  $N$  data from the large bend specimen tests with those from the small bend specimen tests. The data for both specimen sizes show good agreement.

#### 6.4.2 Discussion

##### 6.4.2.1 Initiation -

The sampling volume theory is supported by the results from the tests on the larger bend specimens. Compared to the smaller bend specimens, these had an area subjected to the maximum stress which was 1.7 times the size of that in the small specimen tests. Hence, there was a greater chance of finding a suitably oriented region of microstructure for initiation and subsequent crack growth. In spite of this, only one of the large bend specimen tests saw more than one crack initiated. This can be related to the unusually coarse nature of this type of microstructure, leading to the infrequent occurrence of 'ideal' initiation sites.

##### 6.4.2.2 Propagation -

The agreement between the growth rate data for the large specimen size and those for the smaller specimen size was as expected, consistent with similar microstructure and stress levels for both sizes of specimen. The only thing that might have produced a disagreement between the two sets of data would be incorrect use of the stress intensity solutions. It is important

with different specimen sizes to use a surface stress intensity solution because, as Fig.6.8 shows, there are substantial differences between the plots both in terms of position on the crack front and specimen size, although up to  $a=1\text{mm}$  there is very little difference. Therefore stress intensity at the position being monitored, i.e. the surface crack tip, must be used to avoid any discrepancies. The comparison of  $a$  vs.  $N$  data for the large and small specimens shows that fatigue crack propagation life is insensitive to specimen size.

As a result of these findings large specimens (17mmx17mm) were used in subsequent tests, so that cracks would initiate more consistently and earlier in the test life. In the case of the coarse grained microstructures CGA and CGB, some specimens were 20mm wide. Specimen size has a lot more importance when dealing with such coarse structures, typical of  $\beta$ -processed titanium alloys, than for most other alloys. The main problem that arises is one of taking a representative sample of the alloy microstructure.

## 6.5 EFFECT OF STRESS LEVEL

### 6.5.1 Results

One feature of the low stress tests ( $\sigma_{\text{max}}=400-500\text{MPa}$ ) which was not apparent in the high stress tests ( $\sigma_{\text{max}}=800-900\text{MPa}$ ) was the presence of a large number of microcracks ahead of the crack tip at late stages of crack propagation lives, at crack lengths greater than about 4.5mm. An example of these microcracks is shown in Fig.6.13.

A comparison of growth rate data for the high and low stress levels, generated using the 'Three Point Method', is shown in Fig.6.14. There is no clear difference between the two sets of data. An example of a growth rate plot for one of the low stress tests is shown in Fig.6.15a. The plot shows a large amount of scatter corresponding to arrests at microstructural features such as grain boundaries. The frequency of these growth rate minima and the resultant scatter in the growth rate data was greater in the low stress tests than in the high stress tests, an example of which is shown in Fig.6.15b.

#### 6.5.2 Discussion

The appearance of microcracks ahead of the crack tip during the late stages of the crack propagation lives in the low stress tests can be explained in terms of plasticity. In the high stress tests, the applied stress was close to the yield stress of the material. Therefore the stress gradient between deforming material at the crack tip and material in the bulk of the specimen was small. In the low stress tests, where the applied stress was only approximately half the material yield stress, the stress gradient between deforming material and material in the bulk of the specimen was high. The very localised plasticity in the low stress tests therefore lead to multiple cracking within the plastic zone. Both the LEFM model and the Dugdale model [151,152] for plastic zone size would predict this sort of behaviour in terms of monotonic, maximum plastic zone size,  $r_{pmax}$ . The Dugdale model is different from the LEFM model in that it takes into account that the stress conditions are close to the yield point of the material. Reverse plastic zone size is still  $\Delta K$  controlled, and

therefore should have been the same at both stress levels. It is likely that in the low stress tests when the microcracks were seen, there could well have been some static mode behaviour, corresponding to the final failure region of the crack growth. Static mode behaviour is more likely to be  $K_{max}$  controlled (e.g.[15]), thus reinforcing the above argument.

The amount of scatter in growth rate data for low stress tests is a common feature of short crack behaviour. There are two possible reasons for the greater amount of scatter in the low stress tests than in the high stress tests. Firstly, at high stress levels the microstructural barriers are simply not sufficient to counteract the large driving force at the crack tip. The driving force argument is not a very convincing one in this case, because if this were true, then overall growth rates at low stresses would be lower than those at high stresses for equivalent  $\Delta K$  values. This is clearly not the case, as the comparison of growth rate data shows in Fig.6.14. Another explanation is that the increased scatter is more to do with replicating intervals. If replicating intervals are the same, in terms of actual number of cycles, in a low stress and a high stress test, then each interval in the low stress test will be a smaller portion of the overall propagation life than is the case in the high stress test. Perhaps if the replicating intervals in the high stress test were reduced to similar proportions of the propagation life, the resultant scatter would be similar. To test this theory the data in Fig.6.15a were re-analysed so that replicating intervals were approximately the same proportions of propagation lives for both high and low stress levels. The results of this are shown in Fig.6.16, where the amount of scatter has been greatly reduced and

the high stress and low stress plots are similar in character.

Perhaps the most striking thing to notice from these results is the fact that the K parameter seems to be consistent both at low and high stress levels.

## 6.6 INTERACTION BETWEEN CRACKS - EFFECT OF PLASTIC ZONE SIZE

### 6.6.1 Results

In the majority of the tests carried out only one crack was found to initiate per specimen. In three tests however, more than one crack initiated. There was no consistency in terms of microstructural condition; the three tests concerned were on the AR, A and CGA structures.

In a test on the A structure, three cracks were found to be present. Two of these cracks initiated in close proximity to each other (1180 $\mu$ m apart) and during the later stages of growth, growth rates lower than normal were seen. In the tests in the AR and CGA structures, cracks initiated much further away from each other. Fig.6.17 shows a replica of the two cracks in the A specimen 'overlapping'. The da/dN vs.  $\Delta K$  plots for the two crack tips which interacted are shown in Fig.6.18. Decreases in crack growth rate occurred when  $a_1=0.5$ mm and  $a_2=1.2$ mm (corresponding to  $\Delta K$ s of approximately  $23\text{MNm}^{-3/2}$  and  $30\text{MNm}^{-3/2}$  respectively).

### 6.6.2 Discussion

It is possible that crack growth was affected by the plastic zones surrounding each crack tip, so to determine whether this may have been the case, it is necessary to calculate the plastic zone

sizes for the two crack tips. The crack growth rates of the the two cracks started to decrease at N=88-90000 cycles, so, ideally, this is when the combined size of the two plastic zones should be approximately equal to the distance between the crack tips. The simple LEFM approximation for plastic zone size under conditions of plane stress is:

$$r_y = \frac{1}{2\pi} \left( \frac{K}{\sigma_y} \right)^2 \quad (6.1)$$

where  $r_y$  is plastic zone size,  $K$  is stress intensity and  $\sigma_y$  is yield stress.

Equation 6.2, taken from Dugdale's model [45,46], is possibly a more suitable description of conditions at the crack tip in these smooth bend specimens.

$$\rho = a[\sec(\pi\sigma/2\sigma_y) - 1] \quad (6.2)$$

where  $\rho$  is plastic zone size,  $\sigma$  is applied stress and  $\sigma_y$  is the yield stress of the material.

With the test conditions actually used the values for plastic zone size are much higher using Equation 6.2. Fig.6.19a shows a plot of plastic zone size, calculated from each equation, and distance between crack tips vs. number of cycles,  $N$ . It can be seen from this that, according to Eqn.6.1, the plastic zones of the two cracks do not meet and thus there is no strong interaction to cause a decrease in growth rates. However, from Eqn.6.2 the plastic zones for the two cracks are large enough to interact before there is any retardation of growth rates. This information

suggests that, in this particular situation the simple LEFM approach underestimates the plastic zone size, while the Dugdale equation seems to overestimate the plastic zone size. Cyclic plastic zone sizes,  $r_p^c$  and  $\rho^c$ , can be calculated for the LEFM case using equation 6.3 and for the Dugdale case using equation 6.4. The Dugdale equation in this case has been modified using the same assumptions as LEFM uses, i.e. fully reversed yielding, therefore doubling the  $\sigma_y$  term.

$$r_y^c = \frac{1}{2\pi} \left( \frac{\Delta K}{2\sigma_y} \right)^2 \quad (6.3)$$

$$\rho^c = a[\sec(\pi\Delta\sigma/4\sigma_y) - 1] \quad (6.4)$$

The resultant plots for combined cyclic plastic zone sizes are shown in Fig.19b. In this case the combined reverse plastic zone sizes calculated using the Dugdale model are fairly close to the crack tip separation distance but are slightly too small (200-300 $\mu$ m difference) to account for the reduction in growth rates. This suggests that the behaviour observed was probably influenced by the maximum plastic zone size, although neither of the solutions seems to describe the behaviour adequately.

It seems unlikely that microstructure caused the retardation in crack growth, especially in the case of crack 1 where the path was across a colony of aligned  $\alpha$ -platelets along the basal plane, which would have been expected to show a high crack growth rate.

Work has been carried out by Kishimoto et al [153] and Soboyejo et al [154] on the interaction and coalescence of twin coplanar semi-elliptical fatigue cracks, which were grown from thumbnail starter cracks in a bend specimen. The authors reported that the cracks grew almost independently before contact, which would seem to contradict the results observed here. In their experiments, however, stress levels were low, so that plastic zone sizes would have been correspondingly small. Therefore, if plasticity causes the interactions between cracks, very little interaction between the coplanar cracks would be expected.

## 6.7 SUMMARY

In this chapter, several important aspects of fatigue experimentation have been addressed. Firstly, there are problems in making assumptions about crack shape. The large amount of scatter seen at crack depths up to about 0.6mm means that it is difficult to allow for changing crack shape in stress intensity calculations.

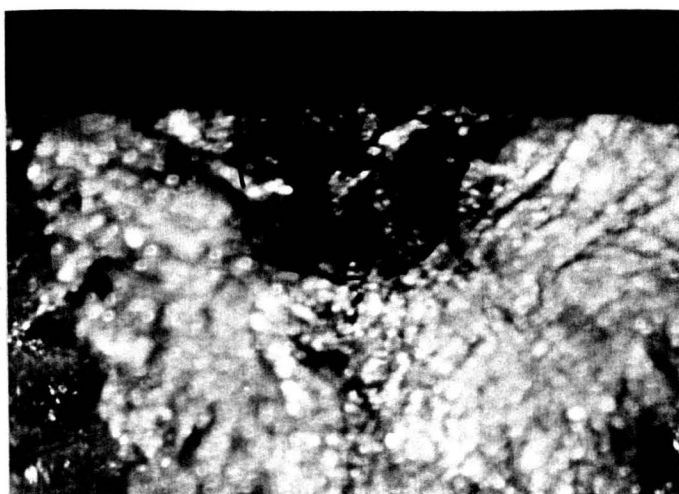
Secondly, variations in both specimen size and design have been considered. The results suggest that specimen design might be important at higher stress levels, where residual stresses caused by yielding may affect the growth of cracks in bend specimens. However, the agreement in the bend specimen data at both high and low stresses is not consistent with the residual stress theory. It seems that the discrepancies between the uniaxial tension specimens and the bend specimens are largely inexplicable. Two important aspects to consider in terms of specimen size, are that testing was considerably easier if the large specimen size was

used, due to greater predictability of specimen life. A positive practical aspect of this is that time spent using the testing machine was not wasted. More importantly, a larger specimen size resulted in a much more representative sample of, in this case, a particularly coarse microstructure.

The agreement between data at high and low stress levels is particularly interesting, because, strictly speaking, the  $K$  parameter should not really be valid for the case of short cracks at stresses close to the yield point. Yet the results presented here seem to show that the  $K$  parameter is useful because of the consistency in growth rates between high and low stress levels. Having said this, the incidence of 'interaction' between the two crack tips in the A specimen suggests that there was a greater amount of plasticity ahead of the crack tip than LEFM would predict, if indeed plasticity was responsible for the reductions in crack growth rates observed.



200μm



200μm



200μm

Fig.6.1 Examples of crack shapes measured in the AR structure using the crack face oxidation technique.

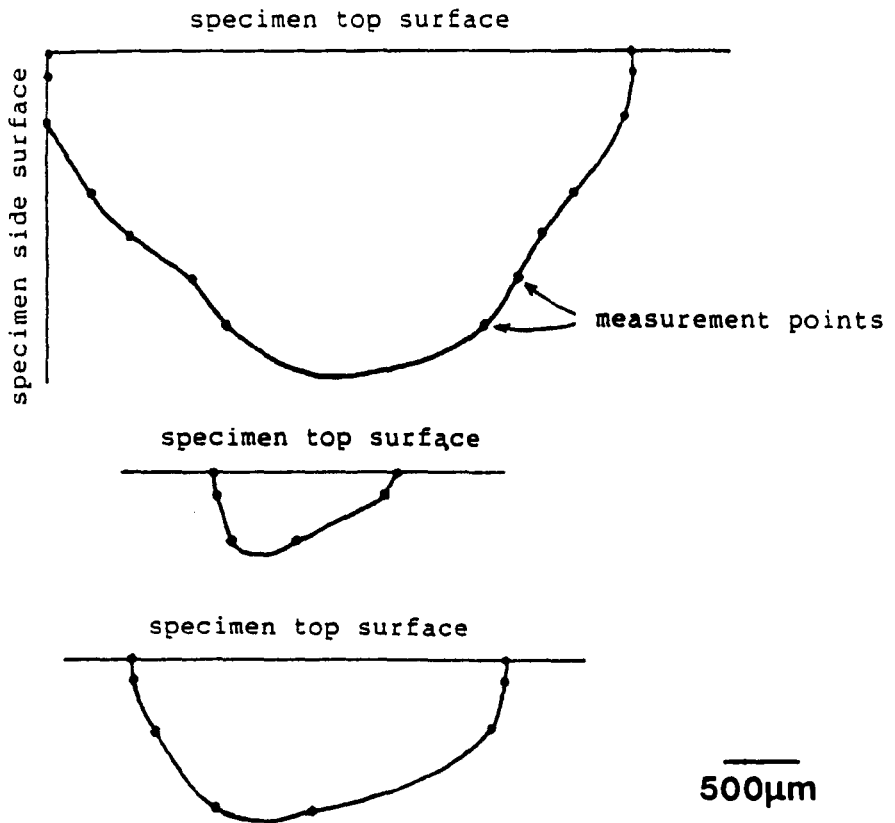


Fig.6.2 Schematic shapes of cracks in the CGA structure determined using a sectioning technique.

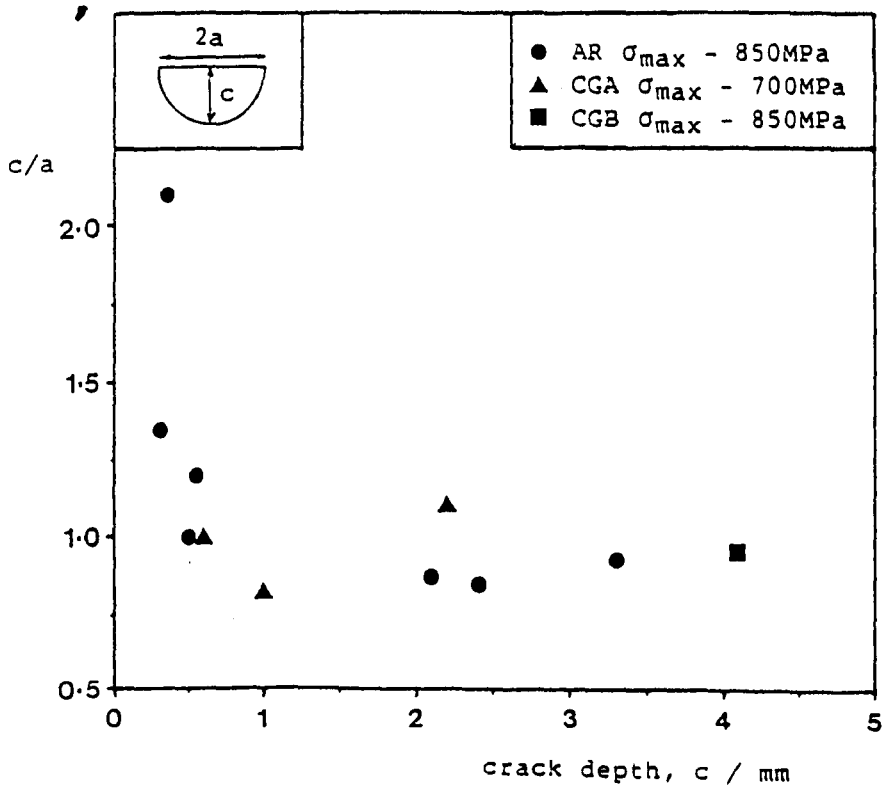
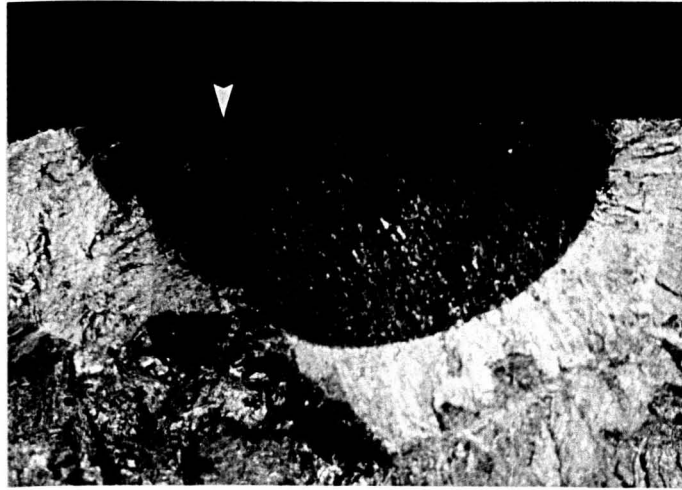


Fig.6.3 Plot of  $c/a$  ratio vs. crack depth  $c$  from all the crack shape determinations carried out.



2mm

Fig.6.4 Example of oxidised crack in the CGB structure (initiation site arrowed).

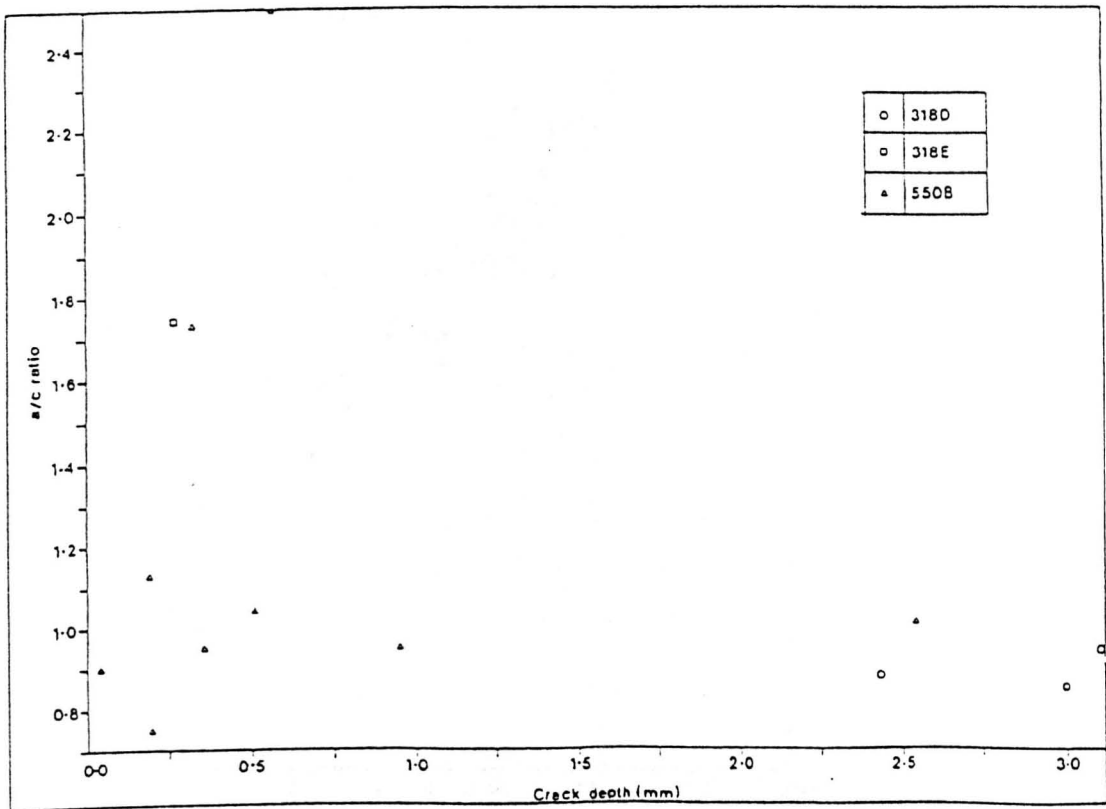


Fig.6.5 Plot of  $c/a$  vs. crack depth  $c$  produced by Bolingbroke and King [59].

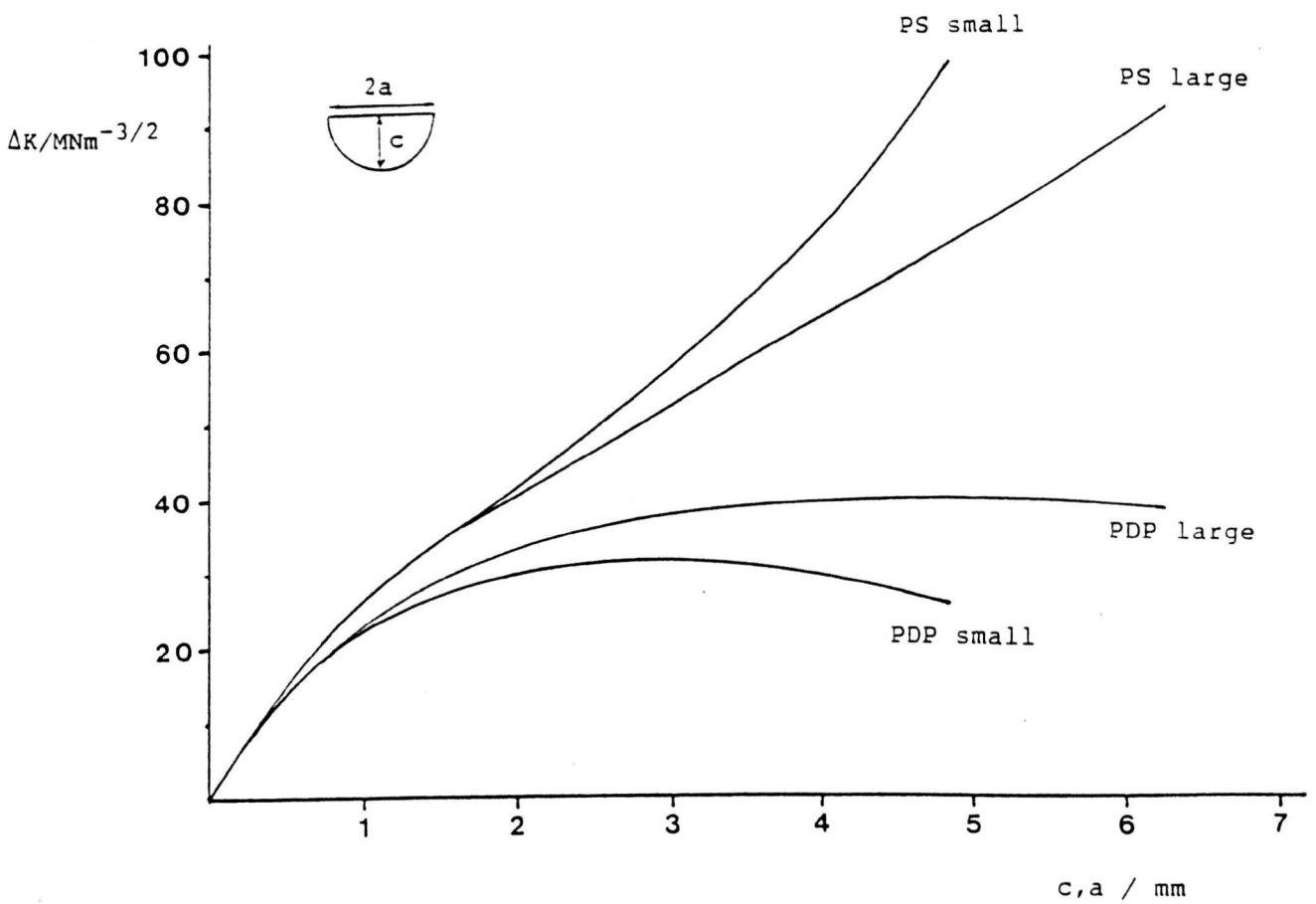


Fig.6.6 Plot of  $\Delta K$  vs.  $a$  for both large (17mmx17mm) and small (10mmx10mm) bend specimens, using the Pickard solution for surface (PS) and deepest points (PDP). Max. stress 850MPa, R=0.1.

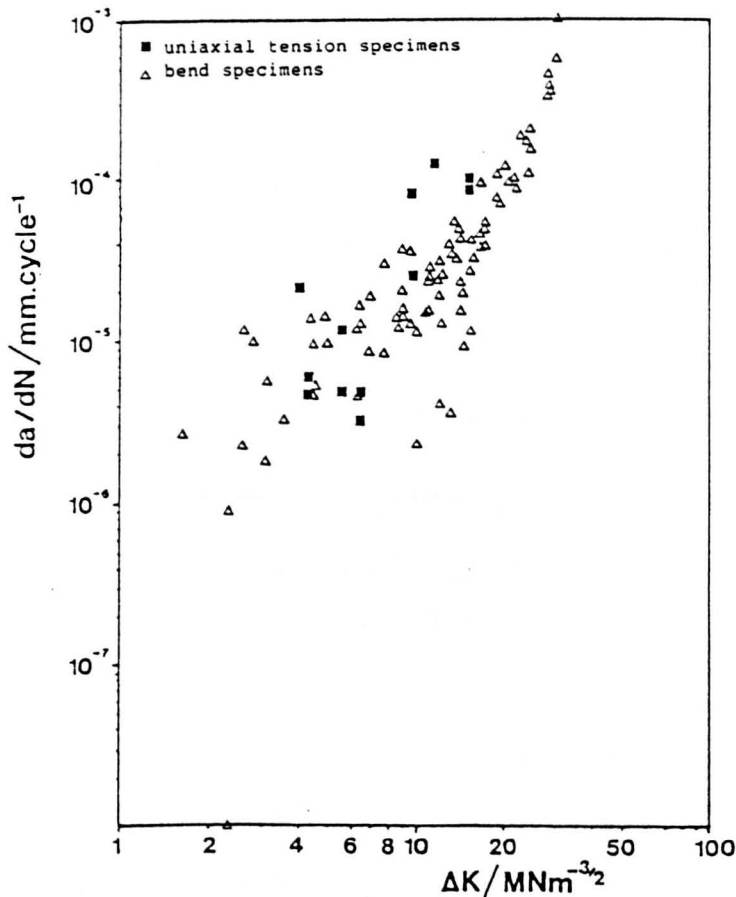


Fig.6.7 Comparison between  $da/dN$  vs.  $\Delta K$  plots for the four point bend specimen and for the uniaxial tension specimen geometries in the AR structure, using Shah and Kobayashi solutions. Max. stress 800-900MPa, R=0.1. Bend specimen data from 5 cracks, tension specimen data from 2 cracks.

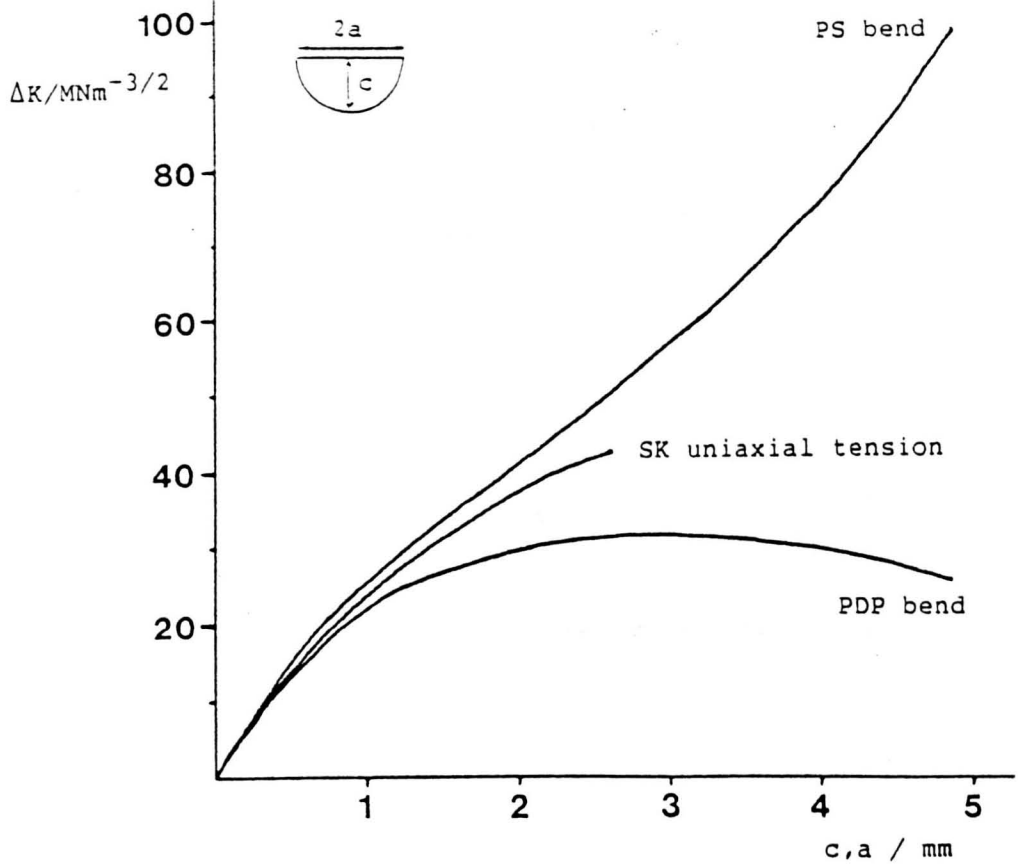


Fig.6.8 Plot of  $\Delta K$  vs.  $a$  for small bend specimens and uniaxial tension specimens.

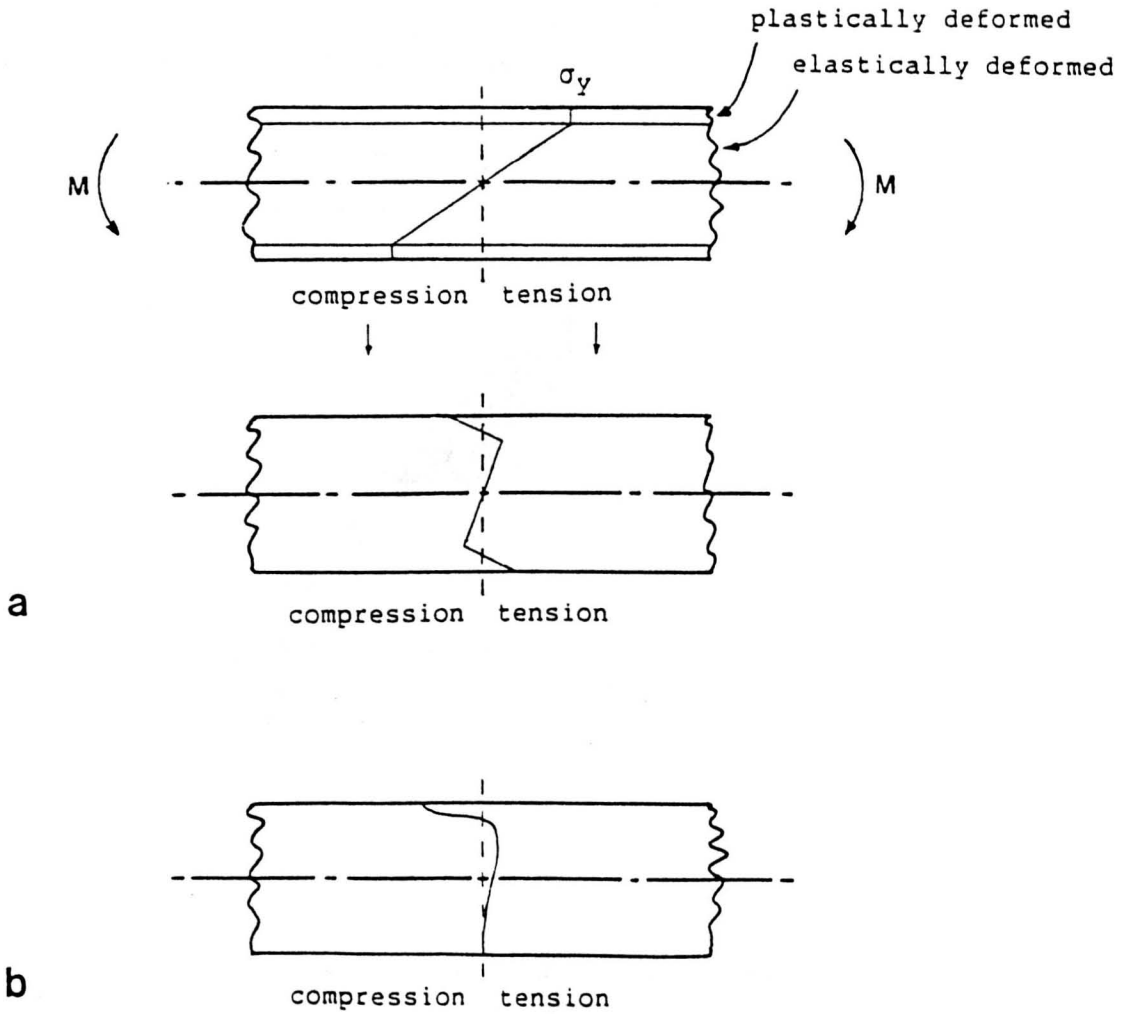


Fig.6.9 Residual stress distributions in bend specimens a) for an elastic-perfectly plastic material and b) for Ti65s.

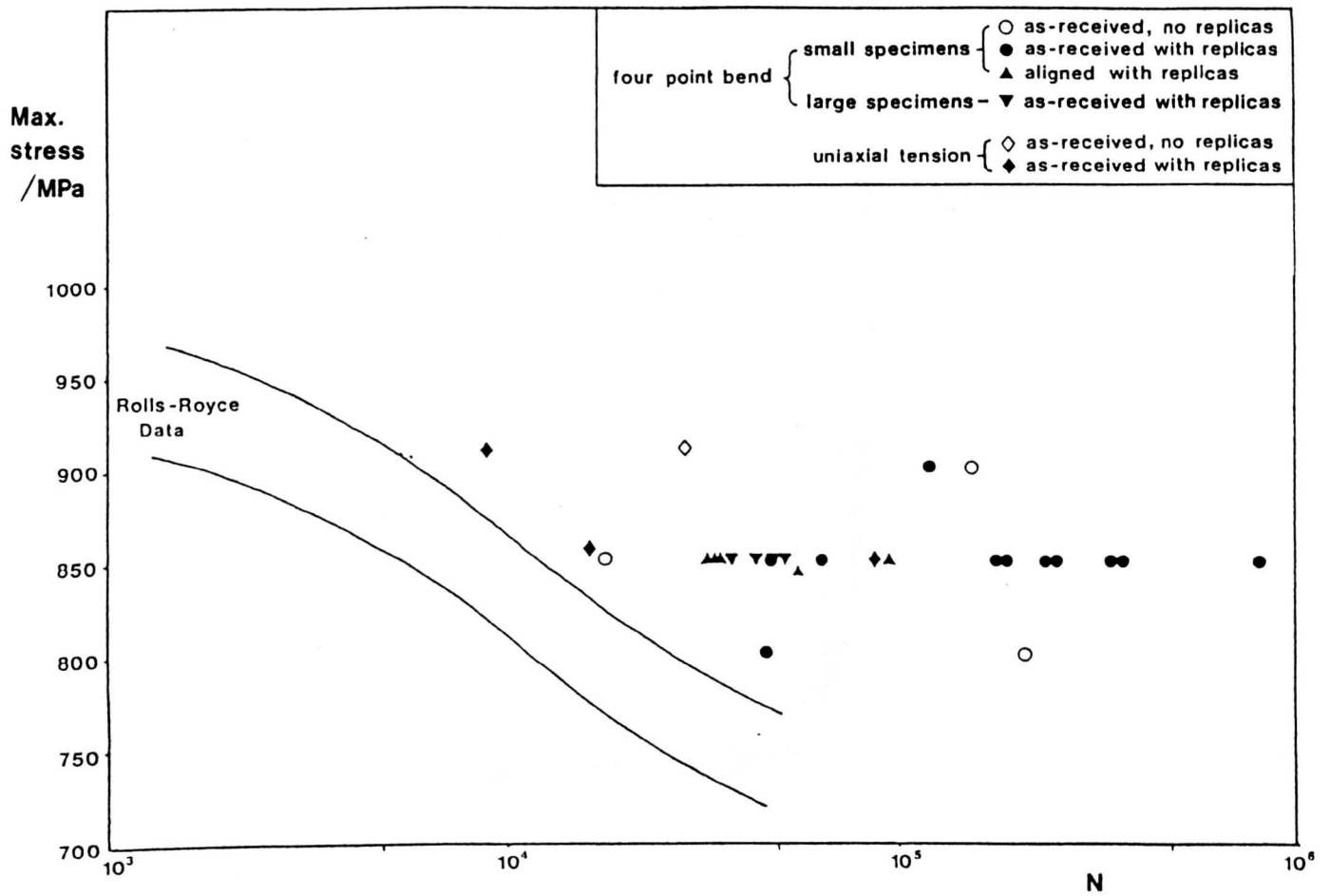


Fig.6.10 Plot of S-N data from four point bend and uniaxial tension tests carried out on the AR and A structures, and Rolls-Royce data band for the AR structure.

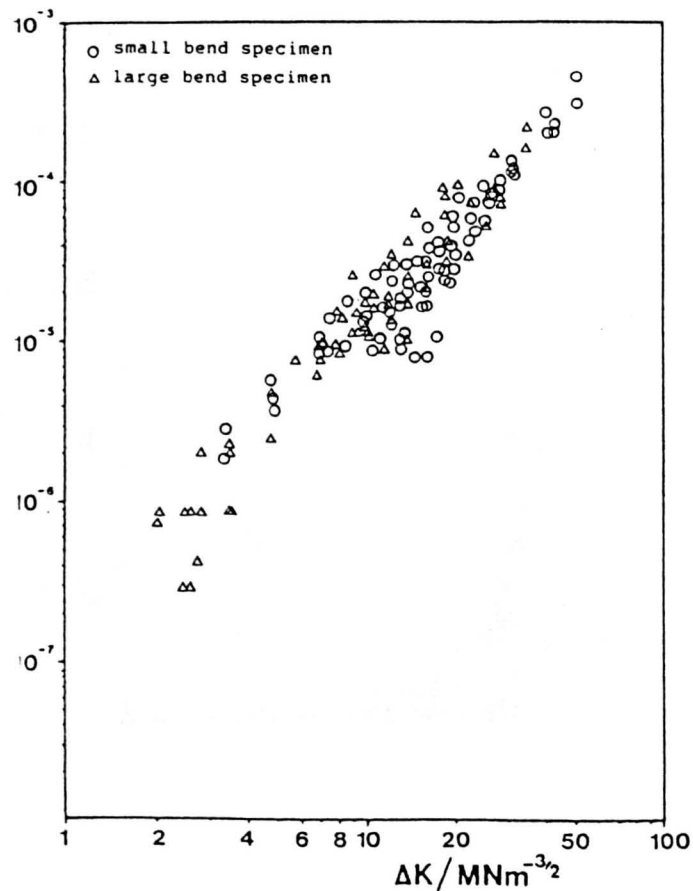
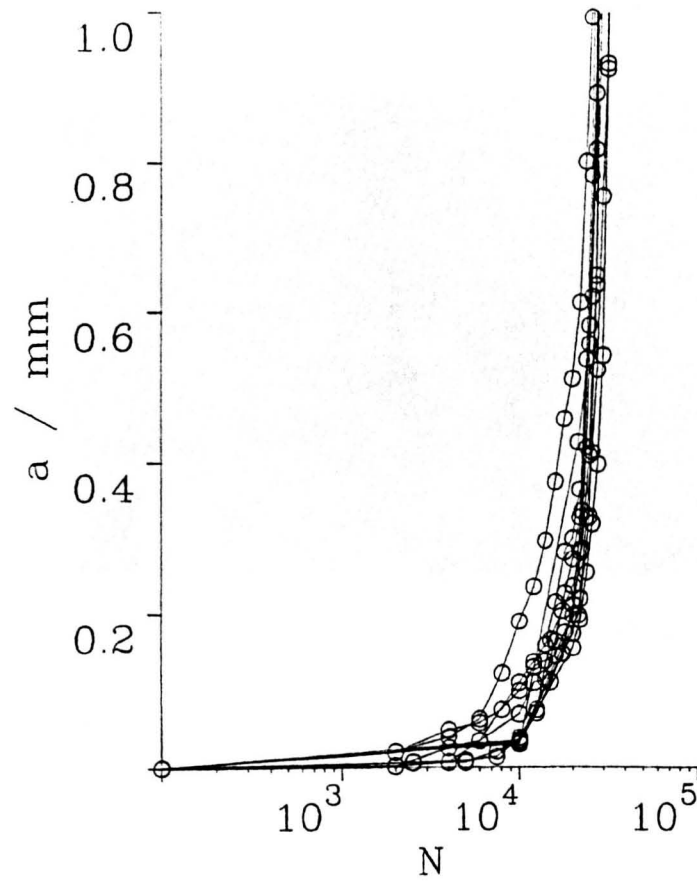
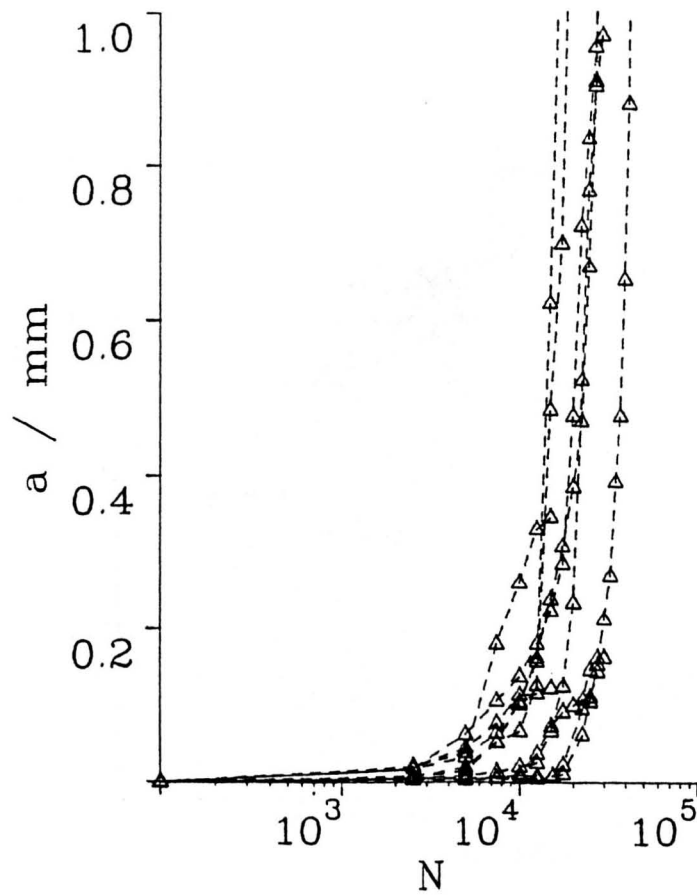


Fig.6.11 Comparison between  $da/dN$  vs.  $\Delta K$  scatter bands for small and large bend specimens. Max. stress 850MPa,  $R=0.1$ . Small specimen data from 5 cracks, large specimen data from 5 cracks.



a



b

Fig.6.12 Comparison of  $a$  vs.  $N$  data for small (a) and large (b) bend specimens.  $N$  is the number of cycles from first crack detection.

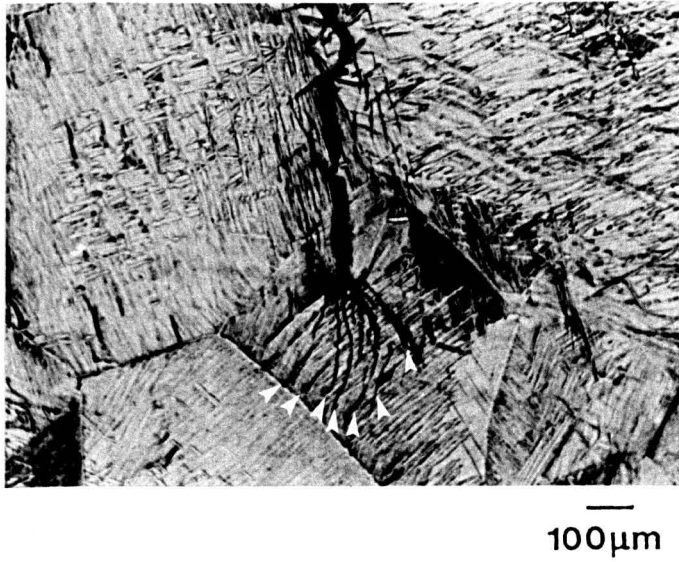


Fig.6.13 Microcracks (arrowed) ahead of a crack tip in a low stress test.

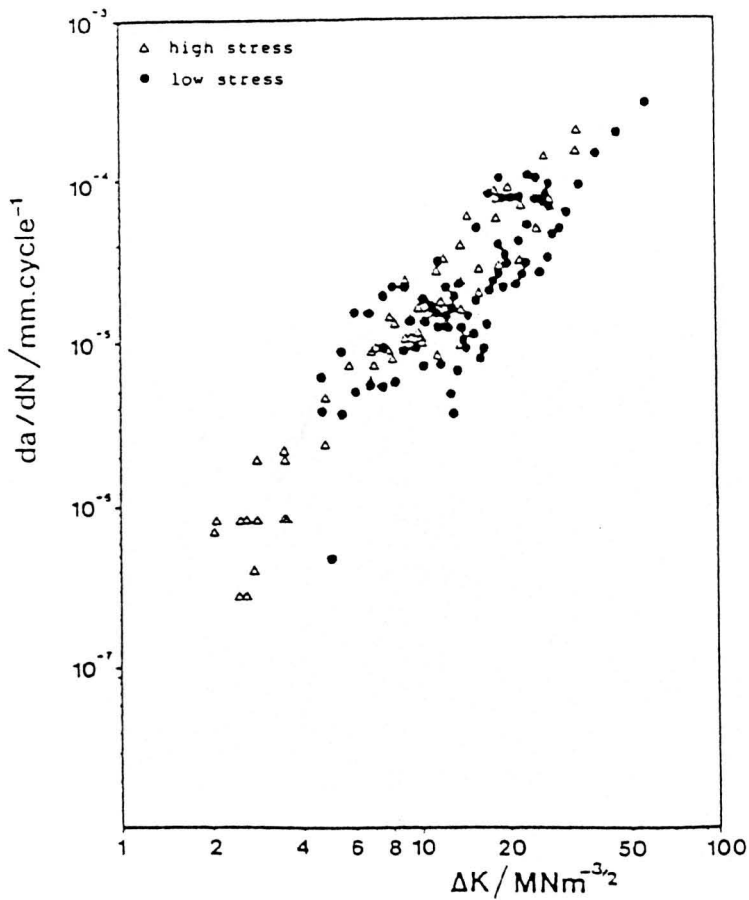
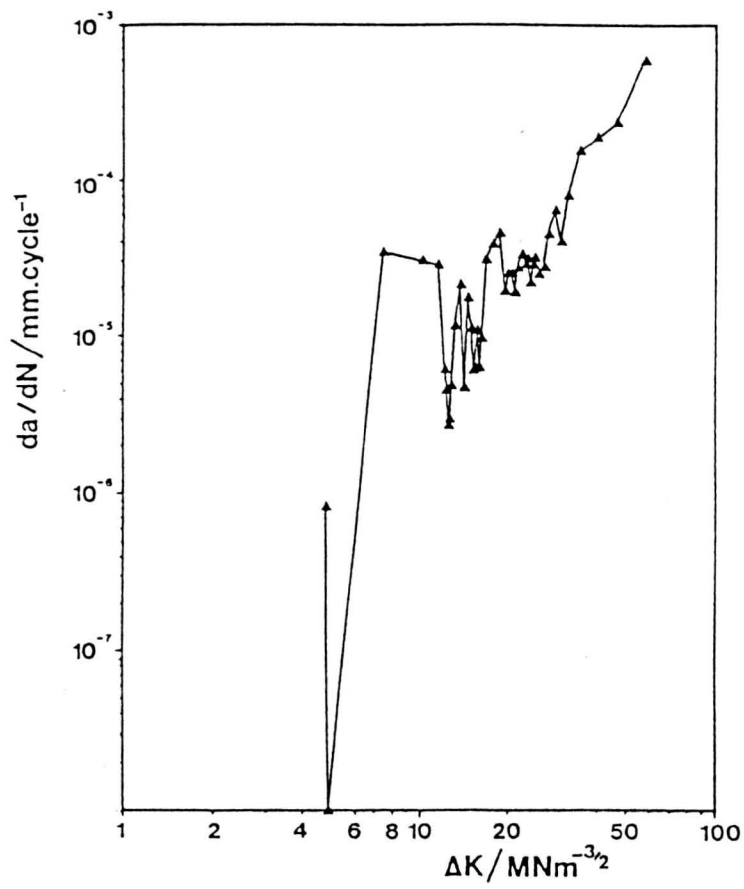
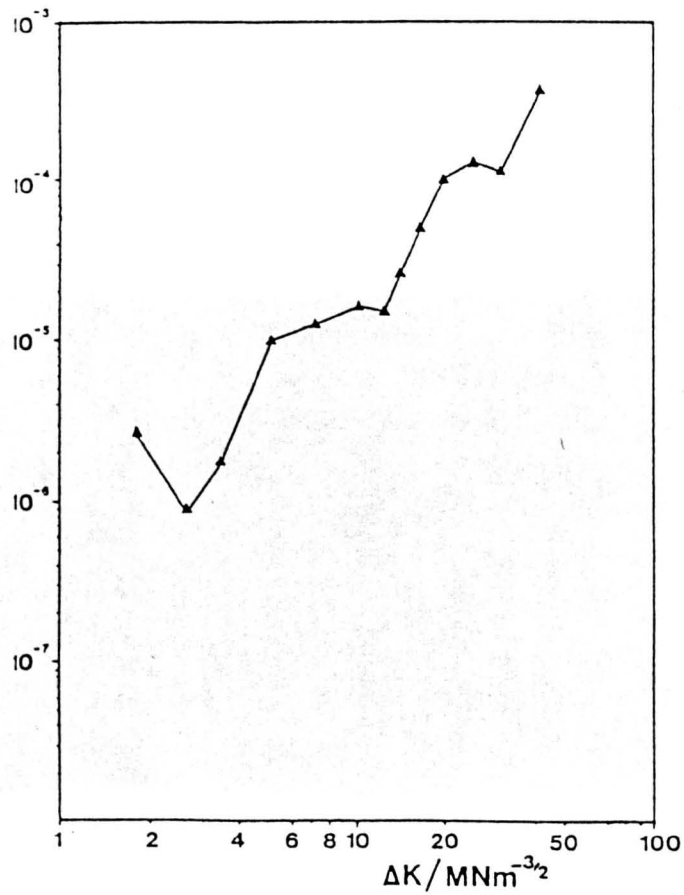


Fig.6.14 Comparison of growth rate data for four point bend tests at high (max. stress = 850MPa) and low (max. stress = 400-500MPa) stresses. High stress data taken from 5 cracks, low stress data taken from 2 cracks.



**a**



**b**

Fig.6.15 Examples of growth rate plots for a) a low stress test and b) a high stress test.

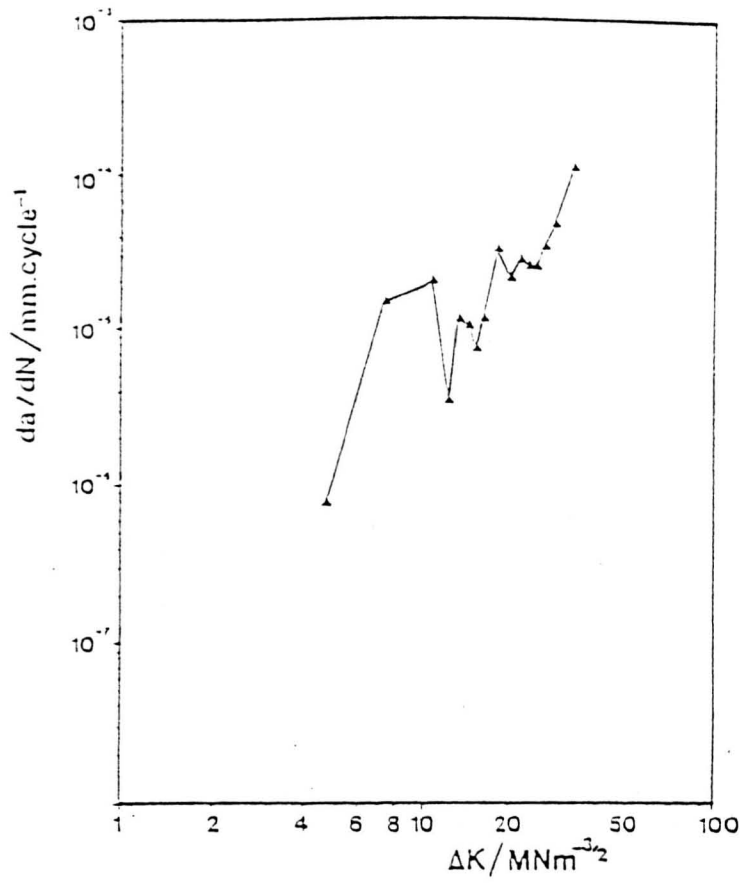


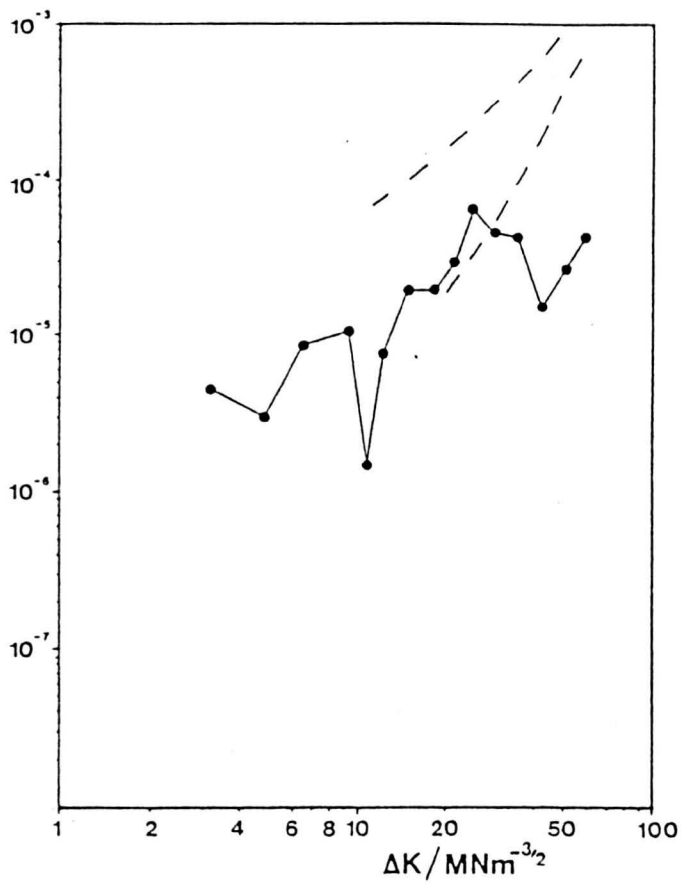
Fig.6.16 Low stress growth rate data from Fig.6.15a after re-analysing at similar intervals to high stress tests.



100  $\mu\text{m}$

Fig.6.17 Micrograph showing interaction between two cracks in A specimen test.

1



2

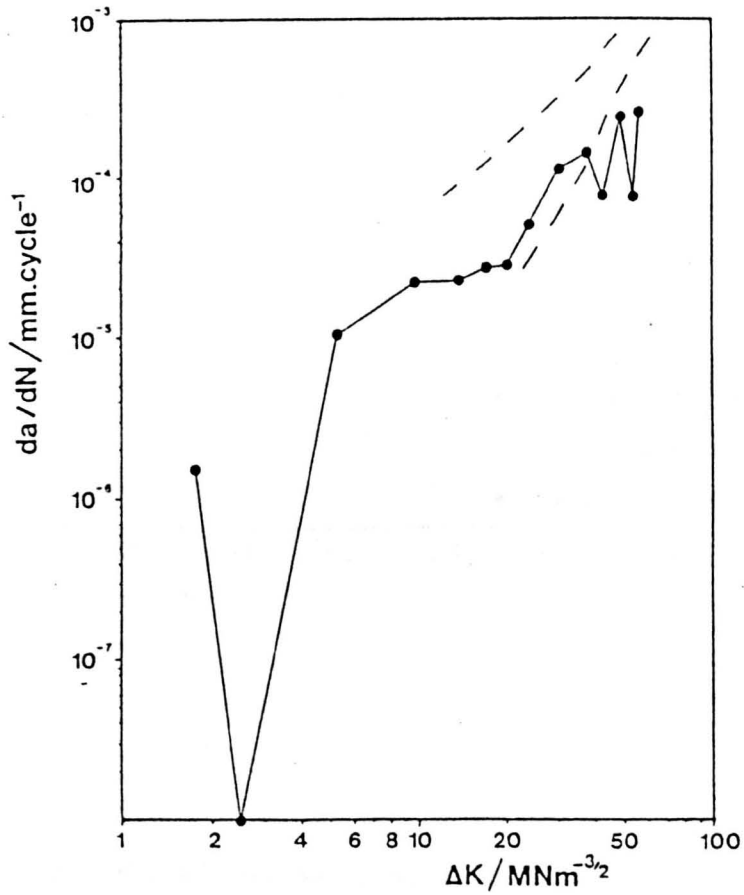


Fig.6.18  $da/dN$  vs.  $\Delta K$  plots for two cracks which interacted (Fig.6.17) with the latter part of the main growth rate scatter band for the A structure superimposed.

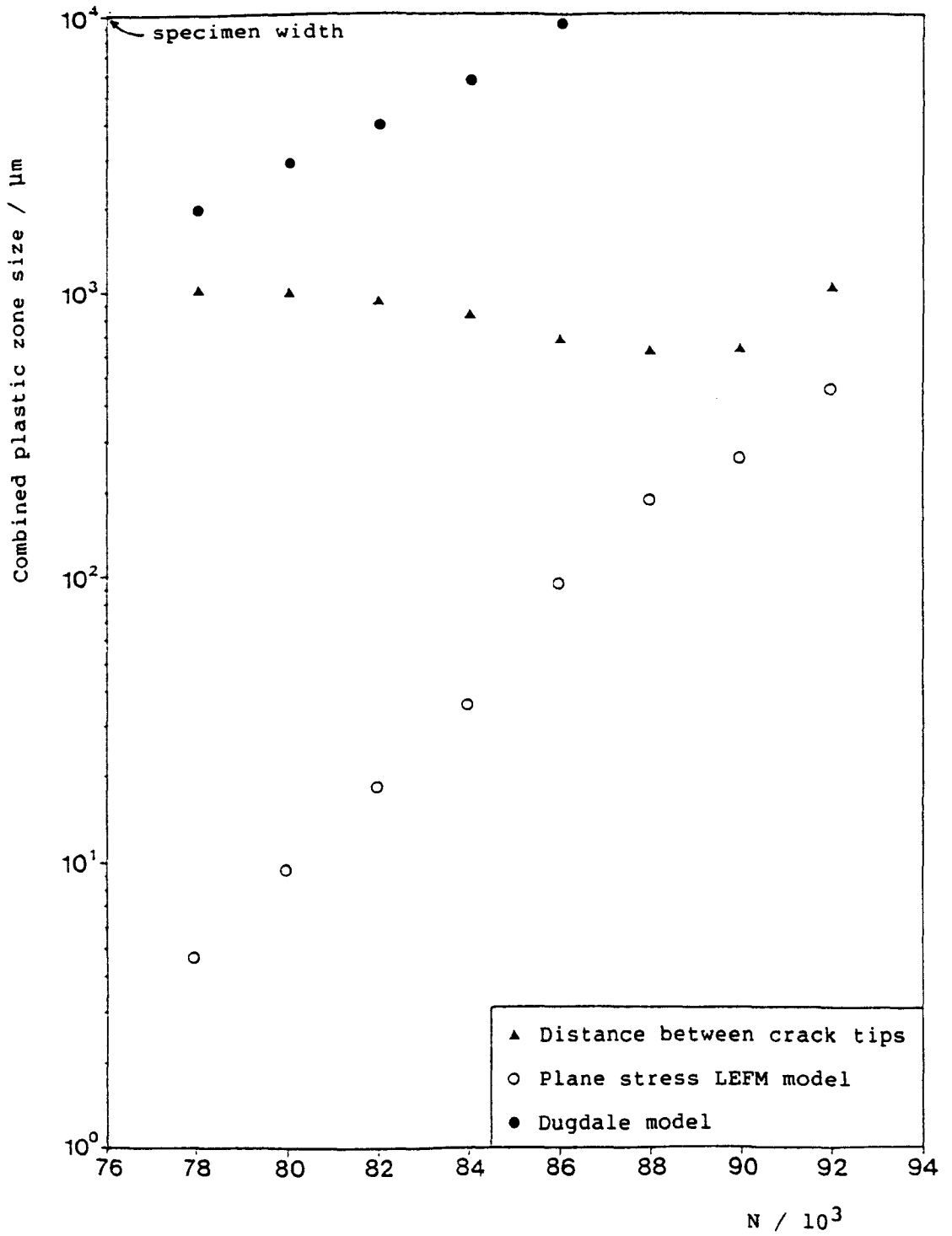


Fig.6.19a Plot of combined maximum plastic zone sizes and distance between crack tips vs. number of cycles  $N$ , for the interacting cracks in Fig.6.17, using both LEFM and Dugdale solutions.

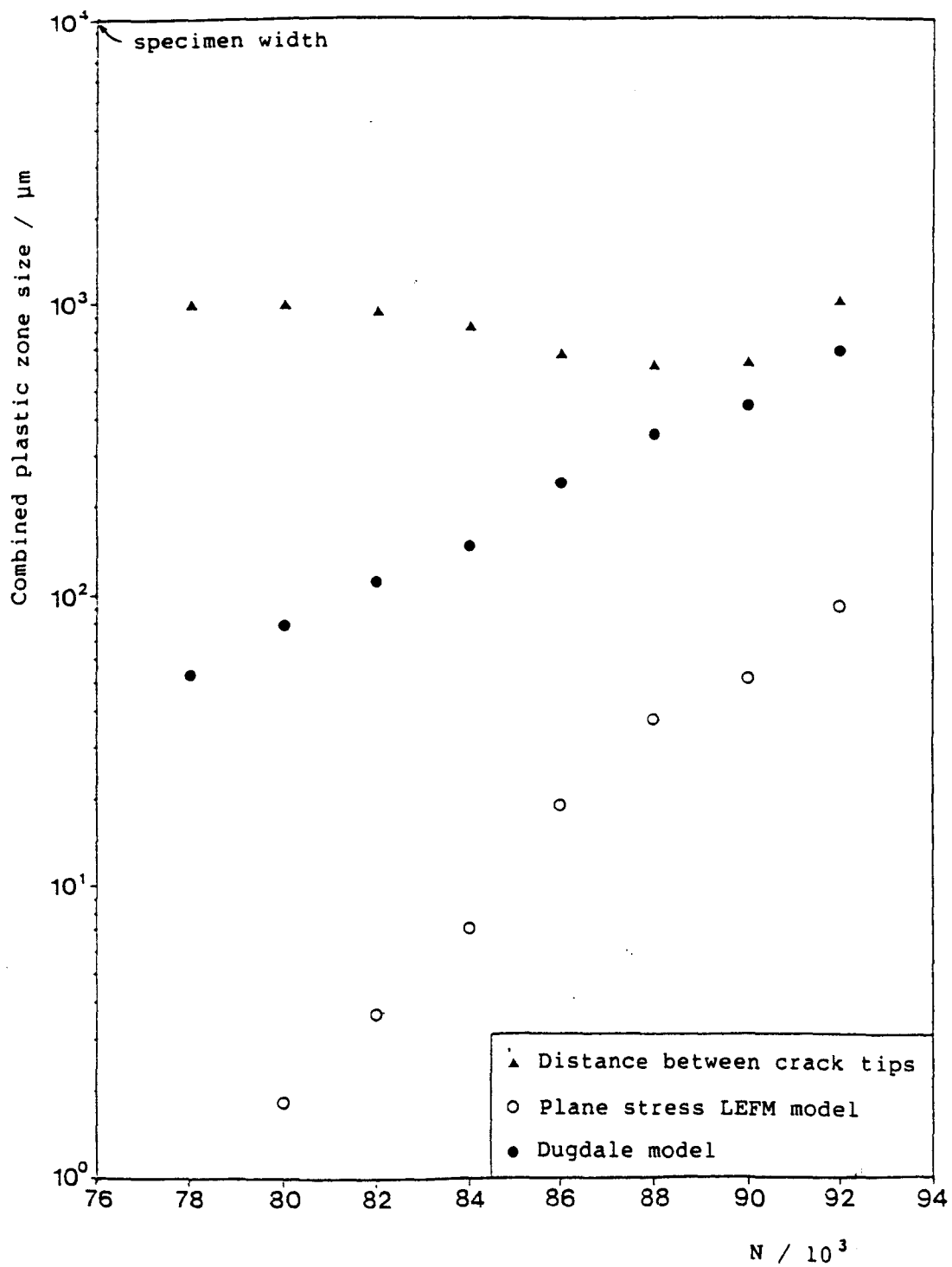


Fig.6.19b Plot of combined cyclic plastic zone sizes and distance between crack tips vs. number of cycles  $N$ , for the interacting cracks, using both LEFM and Dugdale solutions.

CHAPTER 7  
MICROSTRUCTURAL EFFECTS

7.1 BEHAVIOUR OF THE AS-RECEIVED (AR) MICROSTRUCTURE

7.1.1 Results

7.1.1.1 Initiation -

Initiation of cracks usually occurred late on in the life of the specimens, from slip bands in small regions or 'bundles' of  $\alpha$ -platelets. These slip bands formed only a relatively short number of cycles before cracks initiated from them, although deep, long slip bands appeared on the specimen surface within the first 10% of specimen life. Examples of the deep long slip bands are shown in Fig.7.1.

One incidence of initiation from the deep long slip bands was observed in a test on an AR specimen, as Fig.7.2 shows. In this case a crack initiated from a series of slip bands lying very close together across a prior  $\beta$ -grain. The crack appeared to grow very rapidly over a period of approximately 8000 cycles. This was the interval between replicas taken at this stage, the earlier one showing no signs of a crack being present and the latter one showing a crack with surface length of approximately 5mm. Assuming

that initiation occurred immediately after the earlier replica (170000 cycles) was taken, it can be seen clearly that the overall average growth rate in this test was considerably faster, as cracks in other tests took approximately 25000 cycles to reach a similar crack length. On inspection of the fracture surface, there was no evidence of subsurface initiation and growth.

In specimens of the AR material, degree of platelet alignment was often seen to vary across the width of the specimen top surface, depending on where the specimen had been machined from the disc forging. This is illustrated in Fig.7.3, where two regions of microstructure from the top surface of an AR specimen are shown. In the cases where this variation did occur, initiation tended to take place in the regions of more aligned platelets (7.3a). In addition, there were always variations in degree of alignment which provided suitable sites for crack initiation.

#### 7.1.1.2 Propagation -

Crack paths were tortuous with occasional crack branching, propagating across  $\alpha$ -platelets and occasionally along  $\alpha$ -platelet interfaces and prior  $\beta$ -grain boundaries. Propagation in the  $\alpha$ -platelets was mainly along or close to the basal plane directions, but there was also evidence of propagation which was not close to the basal plane directions, suggesting that there was some propagation along pyramidal and prismatic planes. Crack arrest was observed at the first  $\alpha$ -platelet 'bundle' boundary, corresponding to the first change in crystallographic orientation presented to the crack tip. In the tests at low stresses, arrest was observed at  $\alpha$ -colony and prior  $\beta$ -grain boundaries as well. In

the high stress tests, by the time cracks had reached a length of the order of the  $\alpha$ -colony size, no retardation was seen at  $\alpha$ -colony boundaries or prior  $\beta$ -grain boundaries, although cracks were occasionally retarded as they crossed  $\alpha$ -colonies, suggesting that there may have been some interaction with these microstructural barriers below the top surface. Fig.7.4 shows a crack in the late stages of fatigue life on the top surface of an as-received specimen removed from the test rig before failure.

Fig.7.5 shows a typical plot of  $da/dN$  vs.  $\Delta K$  and micrographs of early stages of crack growth for a crack in an AR specimen. The plot shows large variations in growth rate during the initial stages of growth as the crack tips experienced variations in microstructure.

#### 7.1.1.3 Fractography -

An SEM micrograph, typical of the fracture surface region around initiation sites for the AR structure, is shown in Fig.7.6. Generally the fracture surfaces consisted of one or two smooth facets immediately surrounding the initiation sites (Fig.7.7), corresponding to Stage I crack growth, and then somewhat rougher facets reflecting Stage II type growth across colonies of basketweave  $\alpha$ -platelets. Striations were evident near the edge of the fatigue region, corresponding to the late stages of fatigue crack growth (Fig.7.8) The initiation facets were generally at much larger angles to the normal to the applied stress direction than the facets associated with the later stages of growth.

## 7.1.2 Discussion

### 7.1.2.1 Initiation And Early Growth -

Initiation in the AR structure always occurred from slip bands, mainly because there were no defects or inclusions in the material from which short cracks could initiate. Two types of slip band initiation were seen; that from small slip bands in  $\alpha$ -platelet bundles and the isolated incident of initiation from the group of deep long slip bands. The deep long slip bands, which were a regular occurrence during testing, could be mistaken for very fine cracks under a normal optical microscope, but they were shown quite clearly to be slip bands when examined in a laser scanning optical microscope with the facility of 'off-centre' illumination.

Occurrence of initiation late on in the life of specimens agrees with the work of Bolingbroke [88] on IMI318 in the  $\beta$ -heat treated condition. Deep long slip bands were also found to occur within the first 10% of specimen life in the IMI318, but initiation tended to occur in grain boundary  $\alpha$  allotriomorphs, which was not the case in the AR structure.

It is not clear why initiation did not take place more often from the deep long slip bands which were present at a much earlier stage than the small slip bands. One explanation for this type of behaviour might be that slip occurs preferentially in large, favourably oriented surface colonies, early on in the test life. These large surface colonies then work harden until slip is no longer favourable. Subsequent to the hardening of the large surface colonies, slip can now occur with relative ease in the

smaller surface colonies. In the smallest of these it may be that the intersections of the slip bands with the surface colony boundaries are close enough for dislocation pile-ups at either end to interfere with each other. It is interesting to note the apparently conflicting results from the literature. Short crack experiments have tended to show initiation from small packets of  $\alpha$ -platelets [88], whereas long crack and LCF experiments have given rise to claims of initiation on long slip bands across large  $\alpha$ -colonies (e.g. [29,30]).

#### 7.1.2.2 Initiation From Long Slip Bands -

Initiation from the group of long slip bands was an isolated incident but still important, as it had the effect of reducing the crack propagation life. The most likely reason for the higher overall growth rate is that, at the moment when the crack initiated it grew 'instantaneously' to a length of around 100 $\mu$ m due to 'decohesion' along slip planes, i.e. a piece of the material between two of the slip bands may have become detached from the bulk material, thus forming a particularly wide crack. As the smallest growth rates in all the tests were generally seen when crack depth was of the order of a few  $\mu$ m and the crack in this particular test started off at a length of the order of 100 $\mu$ m, the overall average crack growth rate for the test would be greater than that normally seen. In fact, inspection of a vs. N plots for the AR structure shows that the number of cycles for half crack length a to reach 100 $\mu$ m represents approximately half of the total propagation life. Even though this was a case of initiation from deep long slip bands, it took a whole group of them, closely spaced, to initiate a crack. Groups of slip bands

like the one seen in this test were not observed in any other test. Initiation did not take place until late in life, relative to the formation of the deep slip bands, so it is still difficult to explain why, when there was a region of intense slip present, initiation did not take place earlier.

## 7.2 EFFECT OF $\alpha$ -PLATELET MORPHOLOGY

### 7.2.1 Results

This section will deal mainly with those results obtained from tests on the A structure, which were all carried out at high stress on small four point bend specimens.

A typical plot of  $da/dN$  vs.  $\Delta K$  for the A structure is shown in Fig.7.9, along with micrographs showing the early stages of growth. Initiation behaviour in the A structure was similar to that for the AR structure. Cracks tended to initiate from slip bands across small  $\alpha$ -platelet 'bundles'. There was no evidence of crack initiation from slip bands across grain boundary  $\alpha$  in this structure.

Propagation was arrested by the first change in crystallographic direction corresponding to change in platelet orientation and, as the crack increased in length, less retardation occurred.

Fracture surfaces in the A structure (e.g. Fig.7.10) showed a good deal of similarity with the AR structure. Again, smooth, high-angle facets were present at initiation sites, followed by facets corresponding to Stage II type growth which were smoother than the facets in the AR specimens.

## 7.2.2 Discussion

### 7.2.2.1 Initiation -

Consistency of initiation behaviour between the AR and A structures is a good indication of the presence of aligned  $\alpha$  regions in the AR structure. If these were not present, it might have been significantly more difficult for initiation to occur in the AR structure. This is illustrated again by looking at the fracture surfaces for the two materials. The presence of smooth facets at initiation sites in both structures, plus the similarity of these facets with the Stage II facets in the A structure, both suggest strongly that regions of aligned  $\alpha$  played an important role in initiating cracks in the AR structure.

### 7.2.2.2 Propagation -

In order to determine whether platelet alignment had a significant effect on short crack behaviour in Ti65s it is necessary to compare both the  $a$  vs.  $N$  data and the  $da/dN$  vs.  $\Delta K$  data for the AR and A structures.

#### 7.2.2.2.1 $a$ Vs. $N$ Data -

Plots of  $a$  vs.  $N$  for the AR and A structures are shown in Fig.7.11. In the AR structure the plots fall close together and propagation lives are around 28000 cycles (Fig.7.11a). The plots in the A structure cover a much wider range from about 12000 to 27000 cycles (Fig.7.11b).

Four of the  $a$  vs.  $N$  plots for the A structure show substantially shorter propagation lives than the rest, due to fast early growth rates. The cracks whose behaviour these plots describe are shown in Fig.7.12. The first crack initiated on a small slip band across an  $\alpha$ -colony and grew quickly in a Stage I mode across the whole colony (Fig.7.12a). The second crack initiated from slip bands along a prior  $\beta$ - grain boundary (Fig.7.12b). It seems possible that these slip bands extended to the surface from the colony to the left of the grain boundary in the figure.

The growth rate data points generated by these two cracks are shown highlighted in the  $da/dN$  vs.  $\Delta K$  scatter band for the A structure in Fig.7.13.

#### 7.2.2.2.2 $da/dN$ Vs. $\Delta K$ Data -

A comparison of  $da/dN$  vs.  $\Delta K$  scatter bands is shown in Fig.7.14. The 'Three Point Method' was used to obtain the data (see section 5.2.3). The scatter bands coincide at  $\Delta K$  values up to about  $26\text{MNm}^{-3/2}$ . Above this value, the A structure shows higher growth rates than the AR structure for equivalent  $\Delta K$ s, although the scatter bands still overlap. Maximum growth rates in the A scatter band are approximately twice the magnitude of those in the AR scatter band.

If a scale of crack length is used along the 'x' axis, this difference in behaviour can be related to the size of the microstructural features in the two structures. The transition value corresponds to a value for  $a$  of  $600\mu\text{m}$ . The data reflects the similarity of microstructural character at the initiation sites in

the two structures. It has already been established that aligned platelets were the favoured initiation site in the AR structure. Therefore, during the early stages of short crack growth, cracks in both the A and AR structures were experiencing basically the same microstructure. At values of a greater than  $600\mu\text{m}$ , cracks growing through the AR structure, having already grown across at least one colony, were likely to encounter some basketweave  $\alpha$ . Cracks growing through the A structure would still be growing through aligned  $\alpha$ . Crack growth is more difficult through basketweave  $\alpha$  because the orientations of platelets encountered by the crack tip would be changing continually.

### 7.3 EFFECT OF PRIOR $\beta$ -GRAIN SIZE

#### 7.3.1 Results

Tensile results for the CGA and CGB structures are given in Table 7.1. Considerable scatter in results was observed, due to the coarseness of the microstructures compared to the size of the tensile specimens.

In order to determine the effect of prior  $\beta$ -grain size on short fatigue crack behaviour, the behaviour of cracks in the CGA and CGB structures will be compared with that of cracks in the A and AR structures. The grain and colony sizes for the different microstructures are given in Table 4.1. Prior  $\beta$ -grain sizes were approximately 5 times larger in the coarse grain structures than in the small grain structures. Colony size in the CGA structure was approximately 3.5 times the colony size in the A structure.

#### 7.3.1.1 Initiation -

Initiation behaviour in the coarse grain structures, CGA and CGB, was similar to that observed in the A and AR structures.

#### 7.3.1.2 Propagation -

The CGA and CGB structures, as well as giving information on the effect of altering prior  $\beta$ -grain size, also offered valuable information as models of extremes of platelet morphology. This could be observed without interference from as many grain boundary interactions as in the AR and A structures. Figs.7.15a and b and Figs.7.15b and c show typical crack paths through the CGA and CGB structures respectively. Figs.7.16a and b show  $da/dN$  vs.  $\Delta K$  data from several cracks in the CGA and CGB structures respectively.

A comparison between  $da/dN$  vs.  $\Delta K$  scatter bands, generated using the 'Three Point Method', for the CGA and the A structure is shown in Fig.7.17. The points have been generated using similar replicating intervals for consistency. The CGA scatter band shows crack growth rates above those for the A structure, between  $\Delta K$  values of  $10\text{MNm}^{-3/2}$  and  $30\text{MNm}^{-3/2}$ . The maximum growth rates differ by a factor of approximately 2 between the scatter bands in this region. Above a  $\Delta K$  value of  $30\text{MNm}^{-3/2}$ , the CGA data merges with the scatter band for the A data.

The difference in crack growth behaviour between the CGA and CGB structures was substantial, as can be seen by comparing the  $da/dN$  vs.  $\Delta K$  data (Fig.7.18). Examples of fatigue regions of fracture surfaces for the two structures, shown in Fig.7.19, also show quite a difference in character. The CGA fracture surface

consists of large essentially smooth facets. The CGB fracture surface, does not consist of large, highly angular facets like the CGA structure, but is generally much rougher on a microstructural scale. The growth rates for the CGB structure are well below those for the CGA structure, but are also below those for the AR and A structures.

Growth rate data generated by Brown and Hicks [104] from tests on corner crack specimens of a coarse-grained, aligned structure in IMI685, are shown in Fig.7.20, along with the CGA data. The heat treatment given to the IMI685 was similar to that given to the CGA structure, except that grain size was smaller in the IMI685. Brown and Hicks separated their data into four parts. These were crystallographic crack growth, crack growth causing colony boundary separation, crack growth causing  $\alpha/\beta$  interface separation and non-crystallographic crack growth. The data obtained by Brown and Hicks show growth rates up to three times higher than the CGA data at equivalent  $\Delta K$  values, but these higher growth rates correspond only to the crystallographic portion of the Brown and Hicks data.

### 7.3.2 Discussion

The difference in growth rates between the CGA and other structural conditions is related to the overall coarseness of the CGA structure. The very large colonies of aligned  $\alpha$ -platelets provide easy crack paths with few changes in crystallographic direction during crack growth. The platelets are more aligned than in the AR structure and there are fewer colony and grain boundaries to retard crack growth than in both the AR and A

structures.

The merging of the growth rate data at longer crack lengths ( $\Delta K > 30 \text{ MNm}^{-3/2}$ ,  $a > 1 \text{ mm}$ ) could be explained by the presence of closure. The large Stage I type facets, at a large angle to the stress axis normal, produced by crack growth through the CGA structure may promote closure more readily than is the case in the other microstructural conditions. The greater amount of closure in the CGA structure reduces the effective crack driving force and therefore crack growth rates are reduced.

The reason for the CGB structure showing such good fatigue crack propagation resistance is undoubtedly because of platelet morphology. The platelet morphology in the CGB structure was entirely basketweave in nature. There were no regions of aligned platelets such as those in the AR structure and therefore there were no 'easy' initiation sites or propagation paths for cracks to follow. As mentioned earlier in this section, the CGB structure represented the opposite extreme to the CGA structure, and as such can be regarded as being the ideal structure for fatigue crack propagation resistance in terms of platelet morphology.

The much higher growth rates obtained by Brown and Hicks over those of the CGA structure are, at first sight, not easy to understand. However, an explanation may lie in the different nature of the short crack tests used to obtain the two sets of data. The corner crack specimen tests used by Brown and Hicks grew cracks from small slits artificially introduced into one edge of the specimen. The corner crack specimen design is shown in Fig.7.21. The slits were introduced into those large aligned colonies which appeared to be the most suitably oriented for fast,

crystallographic crack growth. In the four point bend specimen tests used in this work, initiation was from a smooth surface and so tended to follow the pattern of initiation behaviour described earlier for the AR and A structures. Since the initiation process was random, then initiation sites were not necessarily surrounded by the ideally oriented aligned colonies, which seemed to give Brown and Hicks such high growth rates. Another explanation might lie in the difference in testing frequencies used. The corner crack specimen testing of Brown and Hicks was carried out at a frequency of 0.25Hz, whereas the testing in this work was carried out at a frequency of 10Hz. Since this particular microstructural condition is known to be susceptible to dwell effects, it is conceivable that such a large difference in frequency could lead to differences in growth rate data.

#### 7.4 COMPARISON OF SHORT CRACK DATA WITH LONG CRACK DATA

##### 7.4.1 Results

Long crack test results for the AR and A structures are shown in Fig.7.22, in the form of  $da/dN$  vs.  $\Delta K$  plots. Values of  $\Delta K$  at threshold were  $10.5\text{MNm}^{-3/2}$  for the AR structure and  $8.0\text{MNm}^{-3/2}$  for the A structure. When compared with the short crack results for the two microstructural conditions, the short crack growth rates are greater at equivalent  $\Delta K$ s until the sets of data begin to merge at a  $\Delta K$  value of approximately  $30\text{MNm}^{-3/2}$  for the AR structure (see Fig.7.23a). and approximately  $25\text{MNm}^{-3/2}$  for the A structure (see Fig.7.23b).

#### 7.4.2 Discussion

The differences between the short crack and long crack data are typical of short crack behaviour and can be partially explained by the nature of the two types of test. In the short crack tests carried out in this report crack initiation and early growth took place at the weakest point in the region of the microstructure which was experiencing the maximum tensile stress. In long crack tests, where a through notch is used to initiate cracks 'artificially', a much larger amount of microstructure is sampled so any individual microstructural effects are averaged out. In other words there is a microstructural continuum. It is difficult to quantify this effect in terms of how much crack growth would be affected.

The next question is whether the LEFM approach is appropriate when looking at short crack behaviour. In the tests carried out the applied stresses were close to the yield point of the material and so there would be substantially more plasticity in the specimen than the amount of local plasticity on which the LEFM argument is based, so for short crack tests, the use of  $K$  may not be a good way to describe conditions at the crack tip. The LEFM approach is also based on continuum mechanics, but in the short crack regime where crack growth is affected by the local microstructure, non-continuum crack growth is taking place.

One other factor which should be taken into account is the effect of closure: in the long crack tests roughness-induced closure occurred which would have the effect of reducing the crack growth rate, whereas in the short crack tests there was no evidence of closure when the cracks were physically short. There

was some evidence of closure when examining cracks on the top surfaces of four point bend specimens, but the cracks had a top surface crack length of around 4-5mm, i.e. outside the physically or microstructurally short crack regime for the AR and the A structures.

Lankford suggested that in most cases short crack data merges with long crack data when cyclic plastic zone size is equal to microstructural unit size [45,50,97]. The long crack and short crack data for the AR structure merge when cyclic plastic zone size is approximately 45 $\mu\text{m}$ , and for the A structure when the cyclic plastic zone size is approximately 30 $\mu\text{m}$ . These are considerably less than the colony sizes (400 $\mu\text{m}$  in the AR structure, 250 $\mu\text{m}$  in the A structure), so if Lankford's criterion were to make any sense it would suggest that platelet size is also an important microstructural dimension. The fact that the CGB data merges with the long crack data at a lower  $\Delta K$  value than the AR structure (about  $20\text{MNm}^{-3/2}$  as opposed to  $30\text{MNm}^{-3/2}$ ) may be caused by an increased influence of platelet size due to the entirely basketweave nature of the CGB structure. Interestingly enough, the Dugdale model as used in equation 6.4 gives reversed plastic zone sizes of 340 $\mu\text{m}$  and 205 $\mu\text{m}$  for the AR and A structures, respectively, which comes much closer to satisfying the condition.

Taylor noticed that most experimental studies showed merging of short crack data with long crack data when crack size was approximately 10 times the microstructural unit size [95]. In this case, the data merges when  $a=1250\mu\text{m}$  for the AR structure and when  $a=750\mu\text{m}$  for the A structure, which is only about 3 times the  $\alpha$ -colony size in both cases, so Taylor's criterion does not seem

to hold particularly well either. The complicated nature of the microstructures studied here may be rather less amenable to the above types of quantitative condition than other alloy microstructures.

Work has been done by Hicks, Jeal and Beevers [31] to generate fatigue crack growth rate data for IMI685 in a random basketweave structure corresponding closely to the AR condition. The  $\Delta K_{eff}$  parameter is a measure of the stress intensity range which takes into account the contribution of closure. Their data were obtained from standard long crack laboratory specimens. These data are shown in Fig.7.24, compared with the short crack  $da/dN$  vs.  $\Delta K$  data for the AR structure. The  $da/dN$  vs.  $\Delta K_{eff}$  data still show a substantial threshold value of  $4-5MNm^{-3/2}$ , which was thought to be due to crack branching and regarded as an intrinsic threshold. The  $\Delta K_{eff}$  data merges with the short crack data at a  $\Delta K$  (or  $\Delta K_{eff}$ ) value of approximately  $10MNm^{-3/2}$ . This is much lower than the value of  $20MNm^{-3/2}$  for the standard long crack data. So, the short crack and long crack data show much better agreement when allowing for closure, but the short crack data still show no threshold value at the low nominal  $\Delta K$  values examined here.

## 7.5 A CASE STUDY IN IMI685

### 7.5.1 Introduction

During the course of this research an opportunity to test an IMI685 cheese presented itself. The cheese was forged from an ingot slice, which had been taken from an ingot suspected of containing defects. It was subsequently heat treated in the same way as the AR structure, i.e. given a  $\beta$ -processing treatment.

Several macroslices were taken from the cheese and four point bend specimens were then machined from these. One of the macroslices is shown in Fig.7.25.

#### 7.5.2 Results

Propagation behaviour showed no difference from that of the Ti65s-AR structure. Anomalous initiation behaviour was observed however. In one of the IMI685 specimens initiation occurred subsurface, at a position corresponding to an estimated applied stress of 770MPa, when the maximum top surface stress was 850MPa. The specimen was removed from the testing machine when close to failure after 45000 cycles and subsequently broken in two.

On inspection of the fracture surface the initiation site was found to be a region containing a number of pores which were approximately 10 $\mu$ m in size. SEM micrographs of these pores are shown in Fig.7.26. It was noted that some of these pores were highly faceted, while others showed curved surfaces, and also that some of them were aligned in a direction roughly parallel to the original central axis of the ingot from which the cheese was taken. The position of the porous region in relation to the macroslice is shown in Fig.7.27.

Sectioning of the fracture surface showed the microstructure of the region to be a fairly good basketweave structure. Qualitative analysis using an energy-dispersive X-ray technique showed there to be lower levels of aluminium and zirconium in the pores themselves. The analyses are shown in Fig.7.28.

A further series of tests were carried out on specimens machined from a macro-slice taken further from the centre of the cheese. The position of the slice is shown in Fig.7.29, along with a macrograph of the slice. The tests were carried out at a maximum stress of 450MPa, which approximates to the sort of stress level components might experience in service. No cracks initiated in these tests.

### 7.5.3 Discussion

#### 7.5.3.1 Possible Causes Of The Porosity -

LIMA analysis was carried out (at Loughborough University) on material taken from the same ingot as, and in close proximity to, the cheese studied in this report. The results of the LIMA analysis showed traces of chlorine in and around the pores. The likely origin of the chlorine contamination is the halide reduction process used to extract titanium from its ore. It is possible that subsequent ingot production could have failed to break up the porous region perhaps due to the occurrence of 'drop-in' (c.f. section 2.2.1). It has been suggested [155] that the very regular 'hexagonal' shape of some of the pores may have been caused by chemical reaction with the chlorine at high temperatures during processing, setting up a 'material transfer' process within the pores. This process would be capable of modifying the metal-pore interface in such a way.

The possibility of chloride contamination may or may not have a direct bearing on this particular case study, but at present there is insufficient evidence to be conclusive. Certainly there was no clear evidence of embrittlement on the facets around the

pores, which seemed like typical Stage I fatigue facets for this material. One might have expected chloride contamination to produce embrittled regions around the pores.

#### 7.5.3.2 Consequences -

The occurrence of initiation from porosity in the IMI685 is similar to the findings of Eylon and Hall [30] who discovered similar defects when carrying out LCF tests on IMI685 (c.f. section 3.2.5.1). A group of pores in close proximity to each other represents a serious hazard, of much greater concern than isolated pores. A straightforward calculation can be done to show whether the  $\Delta K_{th}$  value predicts that the pores would grow at a maximum stress of 770MPa and also at a service stress of 450MPa, assuming the pores to be spherical.

Treating a spherical pore as a penny-shaped crack, equation 7.1 can be used, relating crack size to stress intensity [156].

$$K = 2\sigma\sqrt{\frac{a}{\pi}} \quad (7.1)$$

For this particular calculation, the equation can be rewritten:

$$\Delta K_{th} = 2(1 - R)\sigma_{max}\sqrt{\frac{a}{\pi}} \quad (7.2)$$

where R is the stress ratio,  $\sigma_{max}$  is the maximum stress and  $\Delta K_{th}$  is the threshold stress intensity range. This equation rearranges to give an expression for  $a_{th}$ , the value of half-defect size below

which the defect will not propagate under the given conditions:

$$a_{th} = \pi \left( \frac{\Delta K_{th}}{2(1-R)\sigma_{max}} \right)^2 \quad (7.3)$$

Equation (7.3) was used to calculate  $a_{th}$  for maximum stresses of 770MPa and 450MPa, at a stress ratio R of 0.1, using both the nominal and effective threshold stress intensity ranges for IMI685 ( $12.0\text{MNm}^{-3/2}$  and  $4.5\text{MNm}^{-3/2}$  respectively [31]). The results are shown in Table 7.1. The calculations predict that defects of the size found in the IMI685 cheese, having an a value of approximately  $5\mu\text{m}$ , will not propagate at either the service stress, or the actual stress that these pores experienced, even using the effective threshold stress intensity range,  $\Delta K_{(eff)th}$ . Therefore long crack data does not explain the behaviour. For a pore of size  $a=5\mu\text{m}$  to be able to propagate,  $\Delta K_{th}$  values below  $1.75\text{MNm}^{-3/2}$  and  $1.0\text{MNm}^{-3/2}$  are required for maximum stresses of 770MPa and 450MPa respectively. Short crack growth was seen to occur at these values of  $\Delta K$  in the AR structure at high stresses, although this was not the case in the low stress tests. However, insufficient testing was carried out at low stresses to say that short crack growth would definitely not occur at the  $\Delta K_{th}$  value of  $1\text{MNm}^{-3/2}$  mentioned above. In addition to this, a pore diameter of  $10\mu\text{m}$  was only an average size; one or two of the pores were between 15 and  $20\mu\text{m}$  in diameter.

By fitting a Paris Law equation to the short crack data for the AR structure, further calculations can be performed to estimate the lives of both the particular specimen in which the pores were found and a component in service if it did contain any pores. Fig.7.32 shows the AR scatter band for short crack data

with a straight line fitted through it of the form:

$$\frac{da}{dN} = C.\Delta K^m \quad (7.4)$$

where  $C=1.5 \times 10^{-10}$  and  $m=2$ . Integration of equation 7.4 between the limits of initial pore size and crack size at failure gives equation 7.5, from which a value of  $N_f$ , number of cycles to failure, can be calculated.

$$N_f = \frac{\pi}{4.86 \times 10^{-10} (\sigma_{\max})^2} [\ln. a]_{a_0}^{a_f} \quad (7.5)$$

In the test, the specimen was removed from the testing machine after 45000 cycles, when a crack of size  $a=700\mu\text{m}$  had been detected outside the region of maximum stress. Assuming again that a pore approximates to a penny-shaped crack (equation 7.1) and that the stress field is a uniform one, the number of cycles for the pore to grow to a crack of size  $a=700\mu\text{m}$  is predicted to be 54000 cycles. This is somewhat higher than the actual number of cycles, which suggests that other pores might have been involved.

One way of dealing with initiation from a group of pores is to assume the simple situation of a group of four coplanar pores,  $50\mu\text{m}$  apart as shown in Fig.7.31a. The number of cycles  $N_1$  for the four defects each to grow to a size  $a_2$ , where  $a_2=25\mu\text{m}$ , can be calculated, assuming that all four defects start to grow at the same time and grow at the same rate (Fig.7.31b). It is then assumed that these four cracks coalesce instantaneously to form a penny-shaped crack of size  $A_1$ , where  $A_1=60\mu\text{m}$  (Fig.7.31c). The number of cycles  $N_2$  for the crack to grow from size  $A_1$  to size

$A_2=700\mu\text{m}$  (Fig.7.33d) can also be calculated. The model predicts that  $N_1=17550$  cycles and  $N_2=26790$  cycles. This gives a total of  $N=44340$ , which is remarkably close to the actual number of cycles, 45000.

The model could also be applied to a full sized component. At a maximum stress equal to 450MPa and using a value for fracture toughness equal to  $90\text{MNm}^{-3/2}$  [157], crack size at failure becomes  $a_f=30\text{mm}$ . For growth from one pore, number of cycles to failure  $N_f=278000$  cycles. For growth from four pores, using the same model as before, and with the same distances between pores,  $N_f=250000$ . This is a 10% reduction in component life (assuming there is no initiation stage). In fact, altering the distances between pores has little effect on the magnitude of the life reduction. For a greater number of pores, the reduction in life would be more dramatic. There were certainly more than four pores present in the four point bend specimen, but it is likely that local crystallographic orientation around each pore would prevent some of them from growing.

The negative results from the tests carried out at a maximum stress of 450MPa do not mean that the calculations are wrong. There may not have been any pores in these specimens. The question of 'sampling volume', discussed in Chapter 6, has some relevance here. In a four point bend specimen, only a small portion of the total specimen volume experiences stresses approaching the maximum stress so the chances of finding any porosity are actually quite slim. A uniaxial tension type specimen may actually be a better design to use in this sort of situation, in terms of detecting subsurface porosity.

## 7.6 SUMMARY

In this chapter, the effects of microstructural variation on short crack behaviour have been presented and discussed. In such microstructures initiation behaviour seems to be fairly consistent. With regard to propagation behaviour, both  $\alpha$ -platelet morphology and prior  $\beta$ -grain size have an effect,  $\alpha$ -platelet morphology being the most dominant factor. This was illustrated by the lower growth rates in the CGB structure than in the AR structure, despite the much larger prior  $\beta$ -grain size in the AR structure.

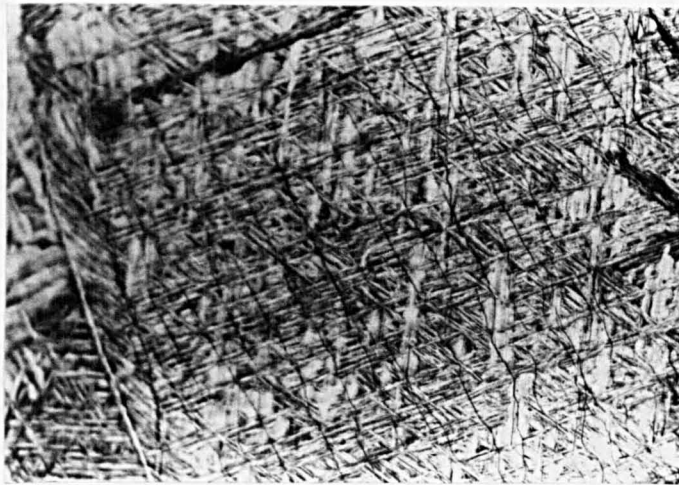
For design purposes, a Paris Law equation can be fitted to the AR  $da/dN$  vs.  $\Delta K$  data to describe short crack growth in a fully heat treated component. The worst possible scenario in a component would be to have a region of porosity in which the microstructure consisted of coarse grains of aligned  $\alpha$ -platelets. In this case it may be sensible to use the data obtained by Hicks and Brown [104], as this shows the highest growth rates of all. If, however, the porosity occurs close to the centre of a compressor disc then there are two possibilities. Either the material containing the pores is removed on machining of the bore, or the porosity would be sufficiently close to the bore surface so that the microstructure would be associated with a fast cooling rate and the porosity would not coincide with a very 'weak', coarse-grained region of microstructure.

Table 7.1 Tensile properties of CGA and CGB conditions.

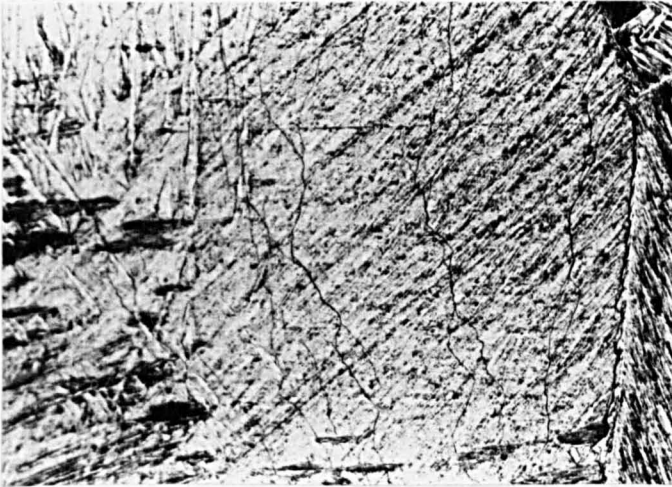
	UTS / MPa	0.2% proof stress / MPa	% elongation
CGA	810-880	690-780	7-10
CGB	920-995	865-945	4-6

Table 7.2 Threshold defect sizes for different maximum stresses, using the parameters  $\Delta K$  and  $\Delta K_{eff}$ , in IMI685.

Max. stress / MPa	$\Delta K$ value used / $\text{MNm}^{-3/2}$	value of $a_{th}$ / $\mu\text{m}$
770	12.1	239
770	4.5	33
450	12.1	701
450	4.5	97



50 $\mu$ m



50 $\mu$ m

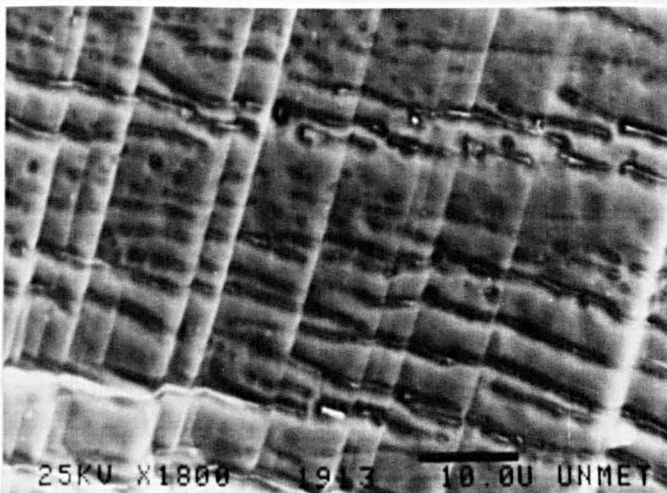
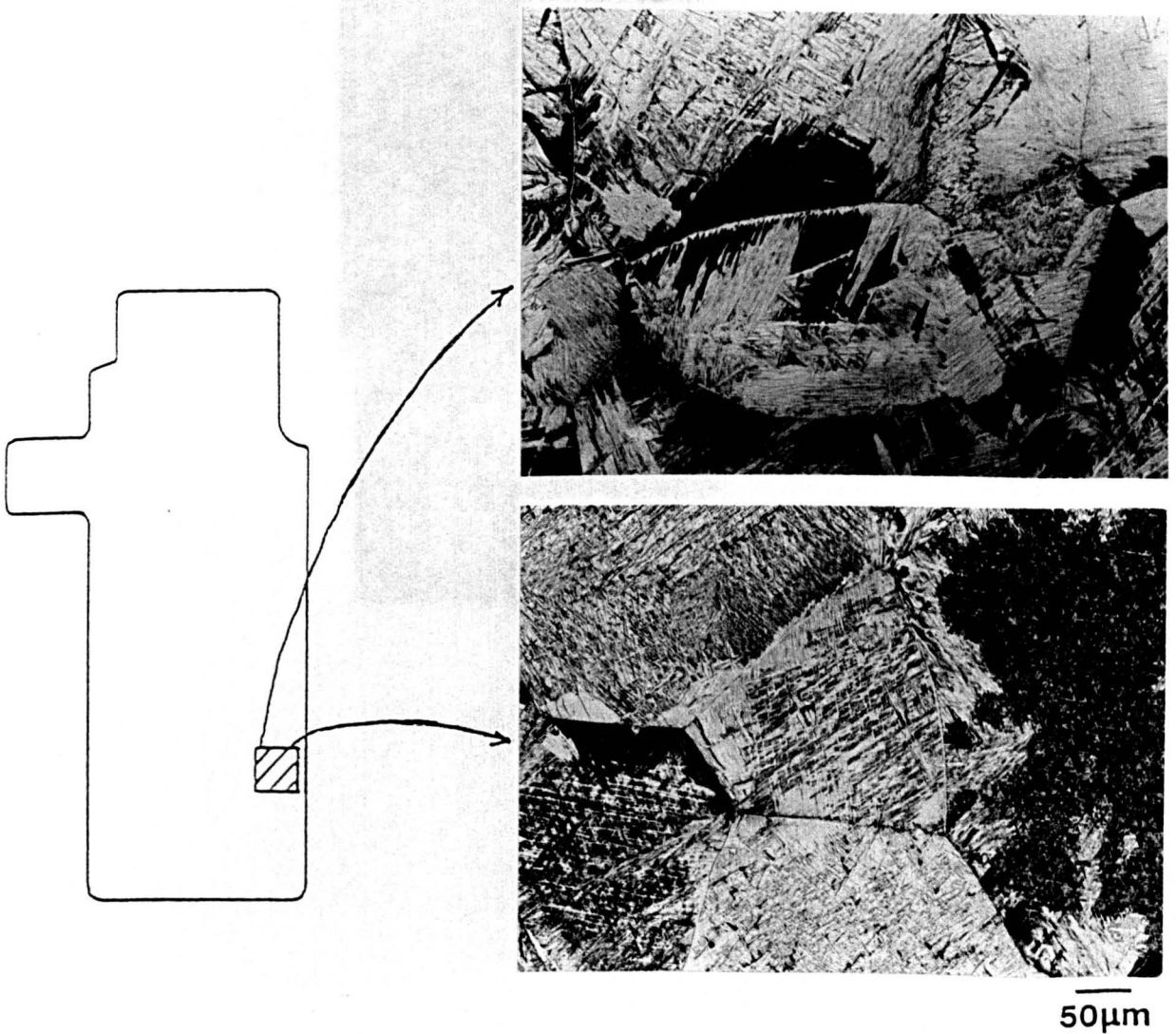


Fig.7.1 Examples of long deep slip bands observed during testing.



100 $\mu$ m

Fig.7.2 Incidence of initiation from group of deep long slip bands in AR specimen (initiation area marked).



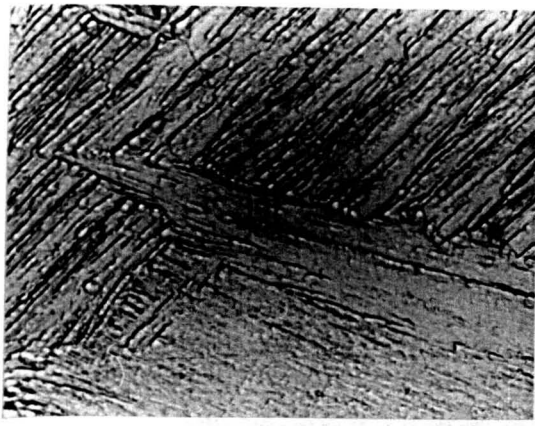
50 $\mu$ m

Fig.7.3 Variation of AR microstructure with position in disc forging.



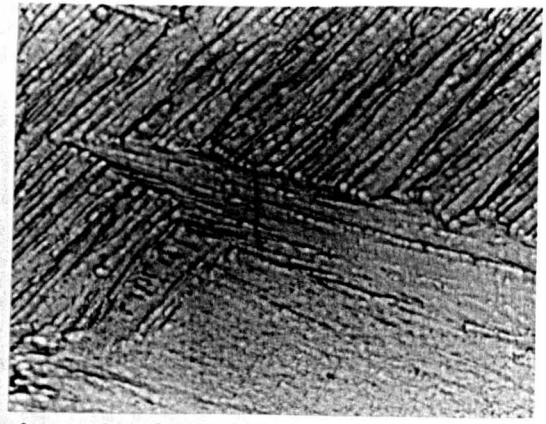
500 $\mu$ m

Fig.7.4 Crack in AR structure in late stages of fatigue life.



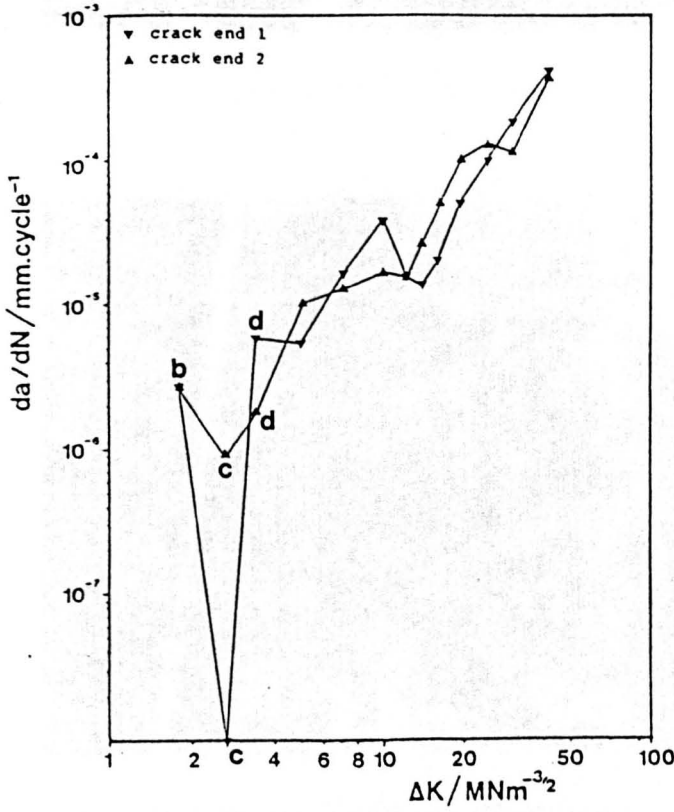
a N=205000

10µm

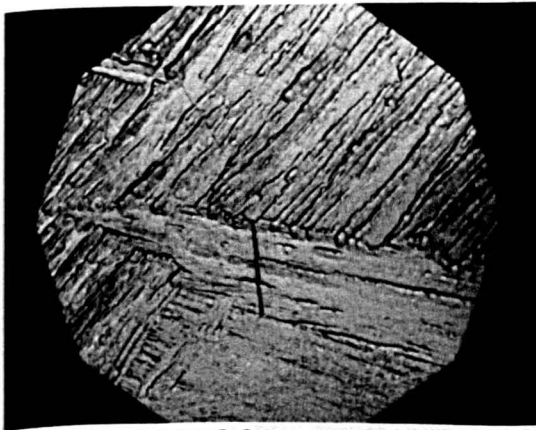


b N=207500

10µm

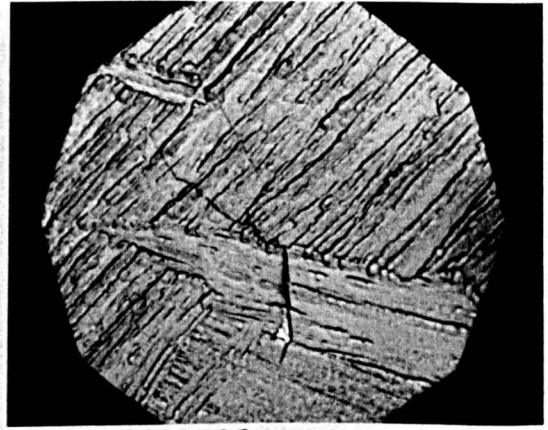


← σ<sub>app</sub> →



c N=210000

10µm



d N=212500

10µm

Fig.7.5 Typical plot of  $da/dN$  vs.  $\Delta K$  and micrographs of early stages of fatigue life in the AR structure. Max. stress = 850MPa,  $R=0.1$ .

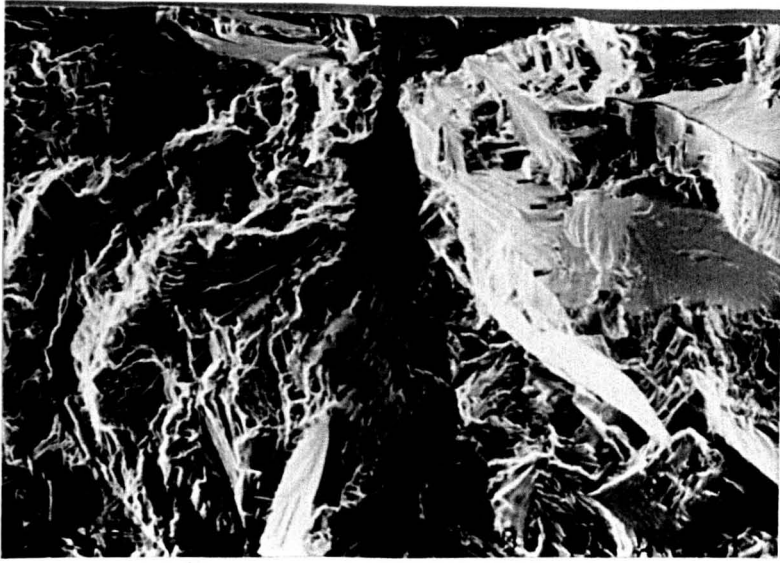


Fig.7.6 Typical AR fracture surface (initiation site marked).

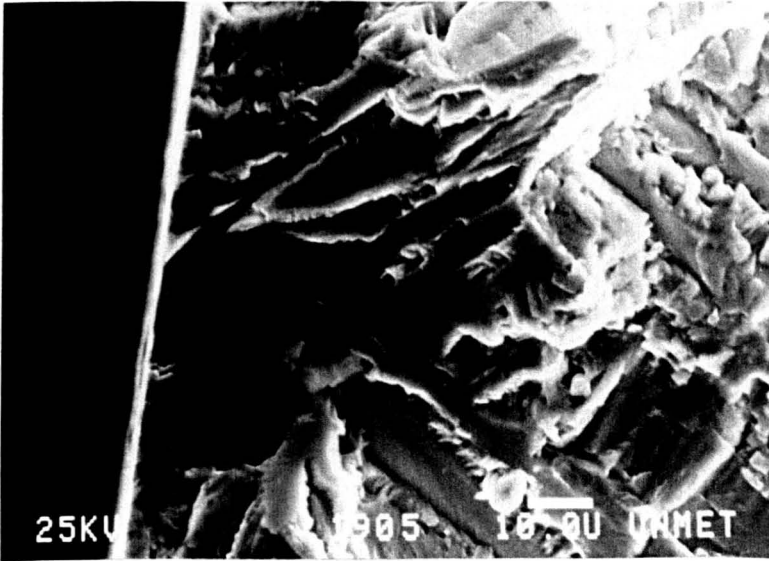


Fig.7.7 Example of initiation facet in AR structure.

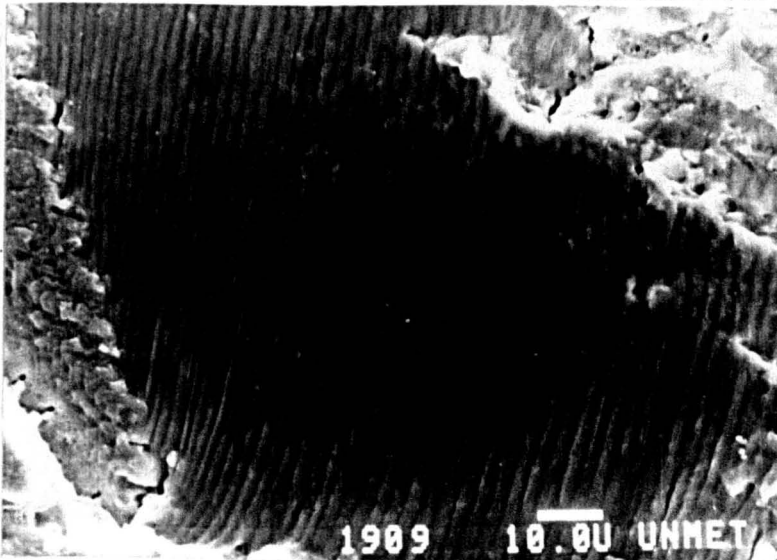
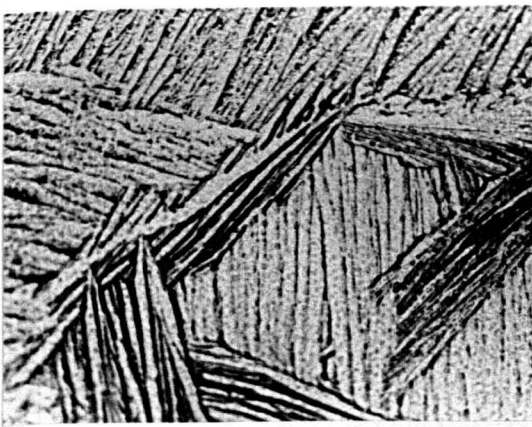
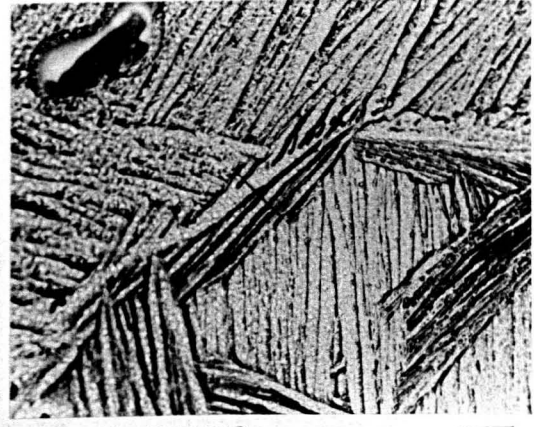


Fig.7.8 Example of striations on the fracture surface of an AR specimen.



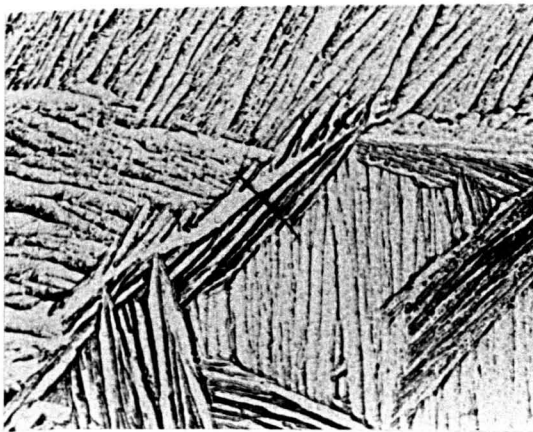
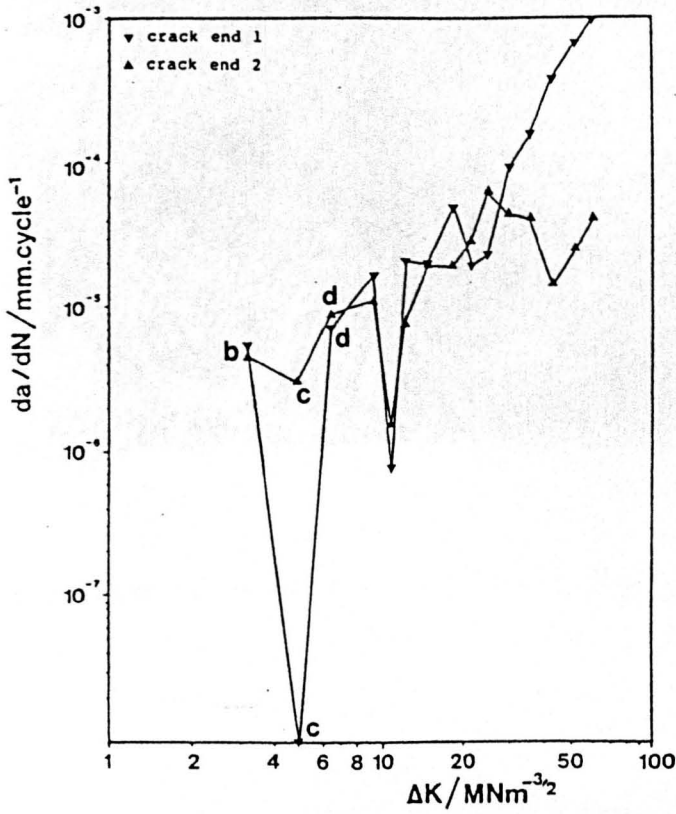
a N=66000

10μm



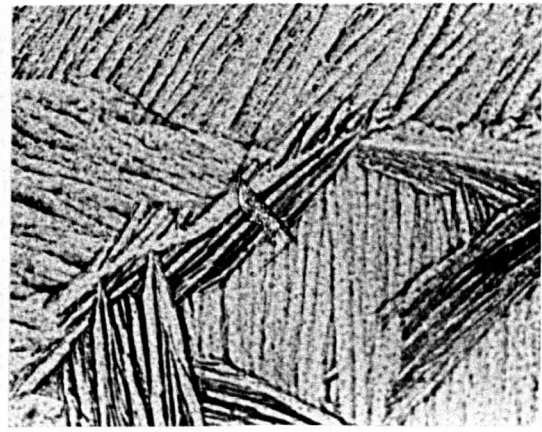
b N=68000

10μm



c N=70000

10μm



d N=72000

10μm

Fig.7.9 Typical plot of  $da/dN$  vs.  $\Delta K$  along with micrographs of early crack growth in the A structure. Max. stress = 850MPa,  $R=0.1$ .



Fig.7.10 Typical fracture surface for the A structure (initiation site marked).

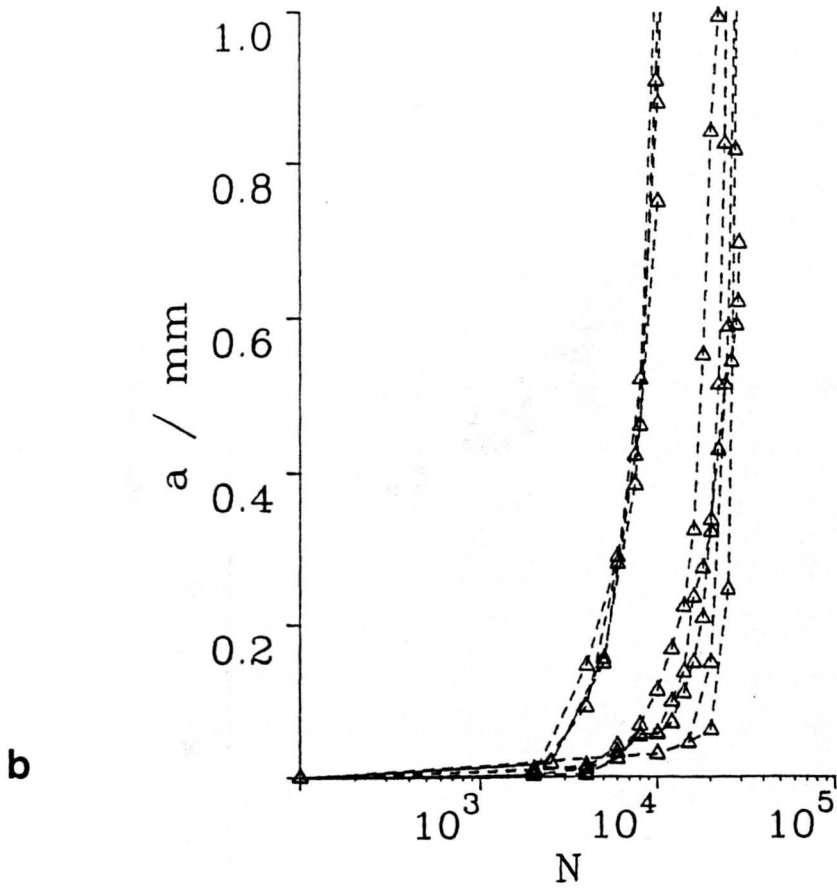
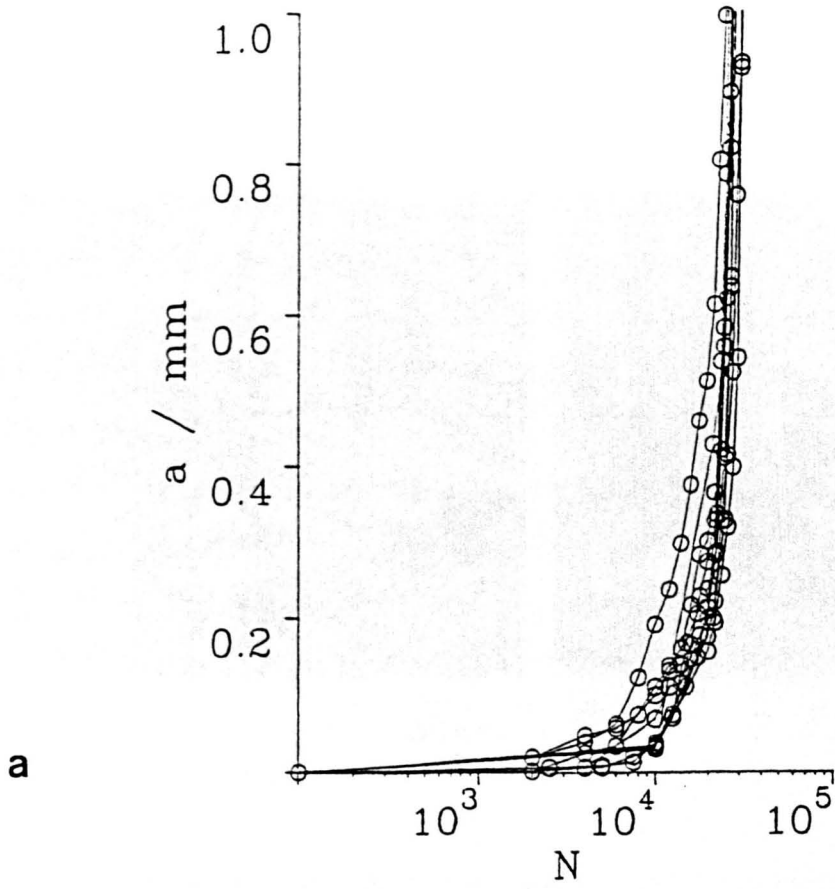


Fig.7.11 Plots of  $a$  vs.  $N$ : a) for the AR structure and b) for the A structure.  $N$  is the number of cycles from first crack detection.

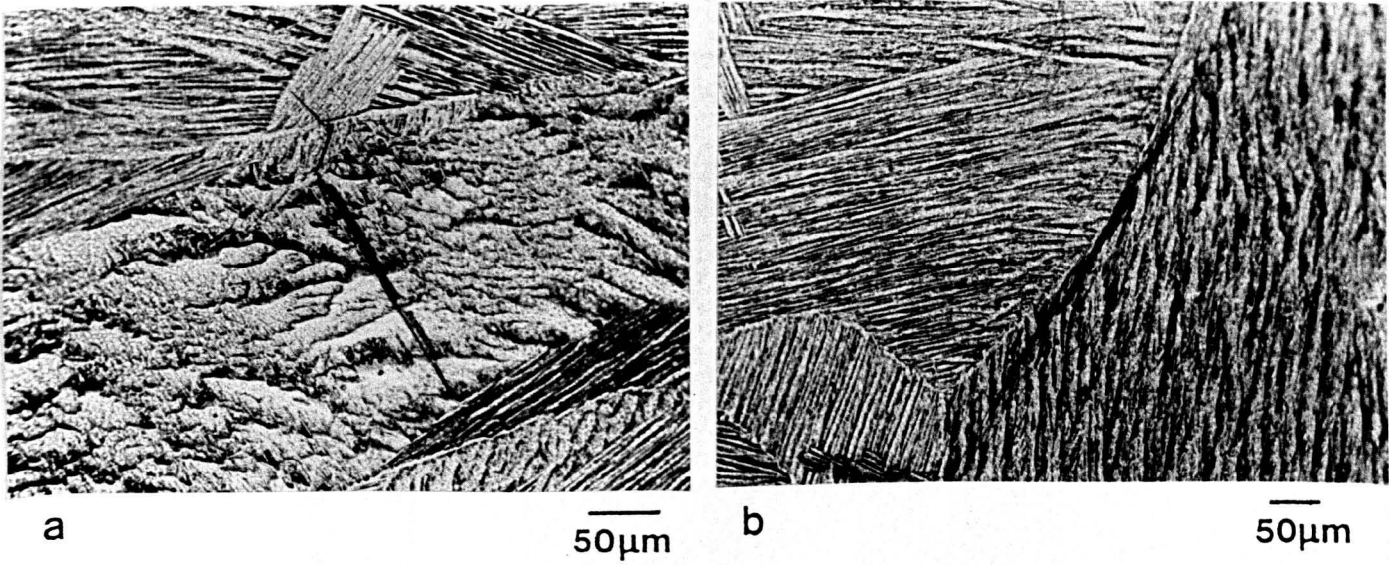


Fig.7.12a and b Cracks in the A structure which showed lower than normal crack propagation lives.

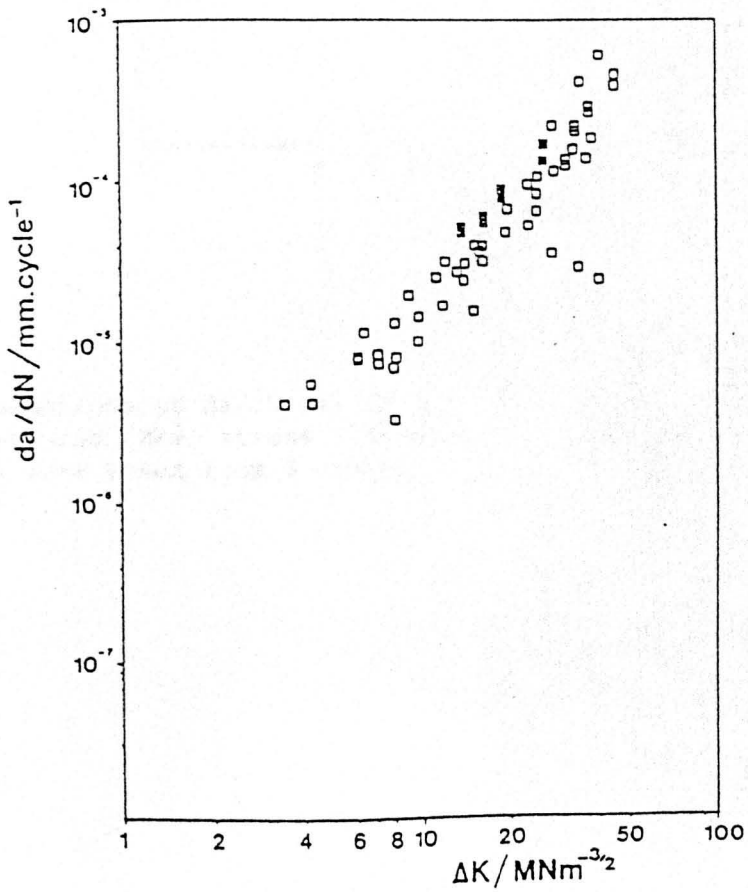


Fig.7.13 Growth rate data points generated by the two cracks in Fig.7.12, highlighted in the A scatter band.

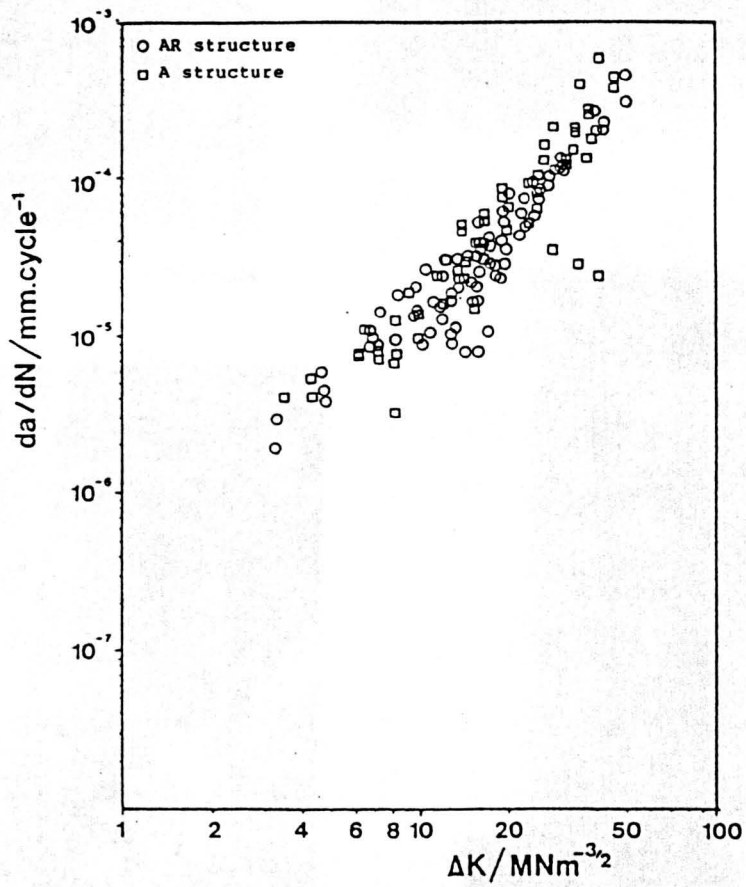
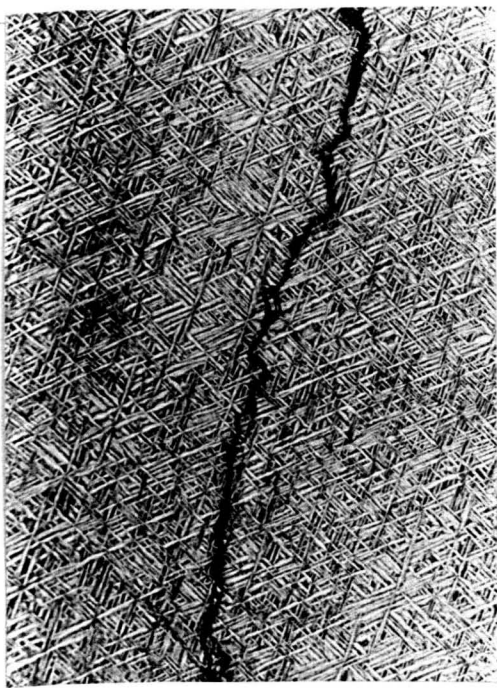
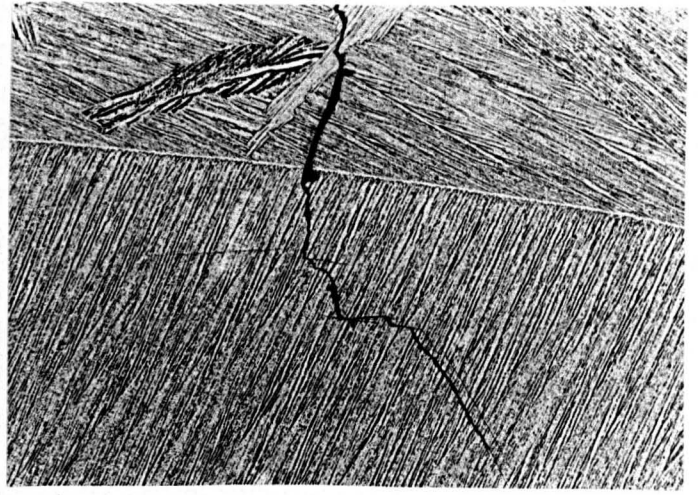


Fig.7.14 Comparison of  $da/dN$  vs.  $\Delta K$  scatter bands for the AR and A structures. Max. stress = 850MPa,  $R=0.1$ . AR data taken from 5 cracks, A data taken from 5 cracks.



a

100 $\mu$ m



b

100 $\mu$ m



c

400 $\mu$ m



d

400 $\mu$ m

Fig.7.15 a,b Typical micro crack paths for the CGB and CGA structures respectively, and c,d typical macro crack paths for the CGB and CGA structures respectively.

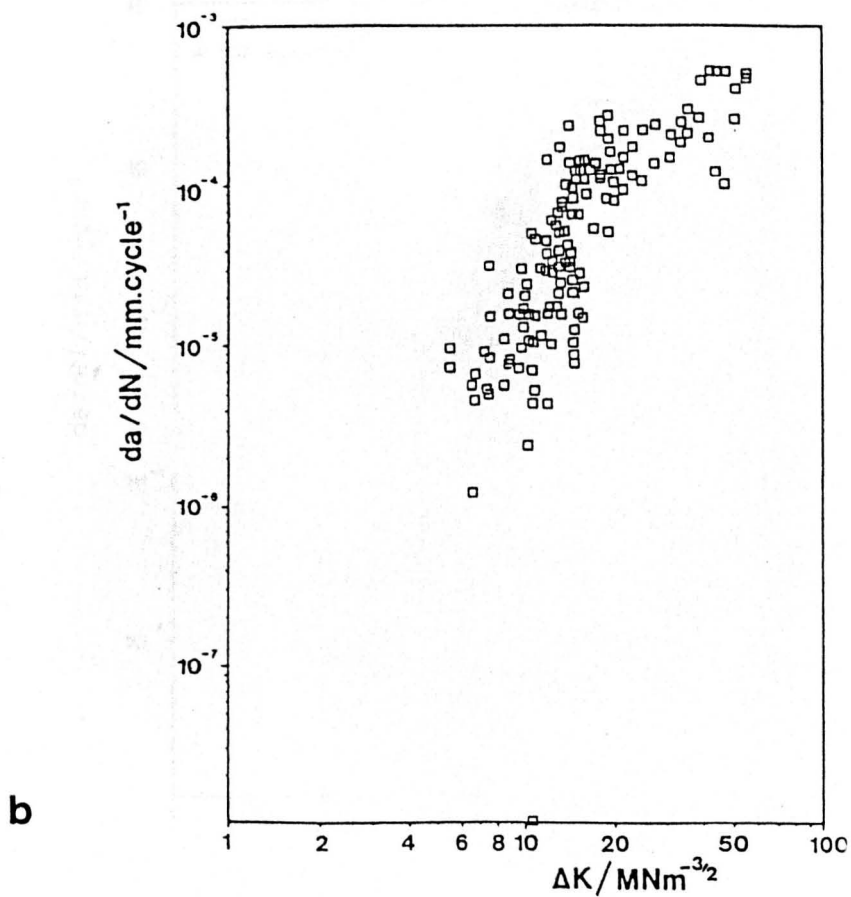
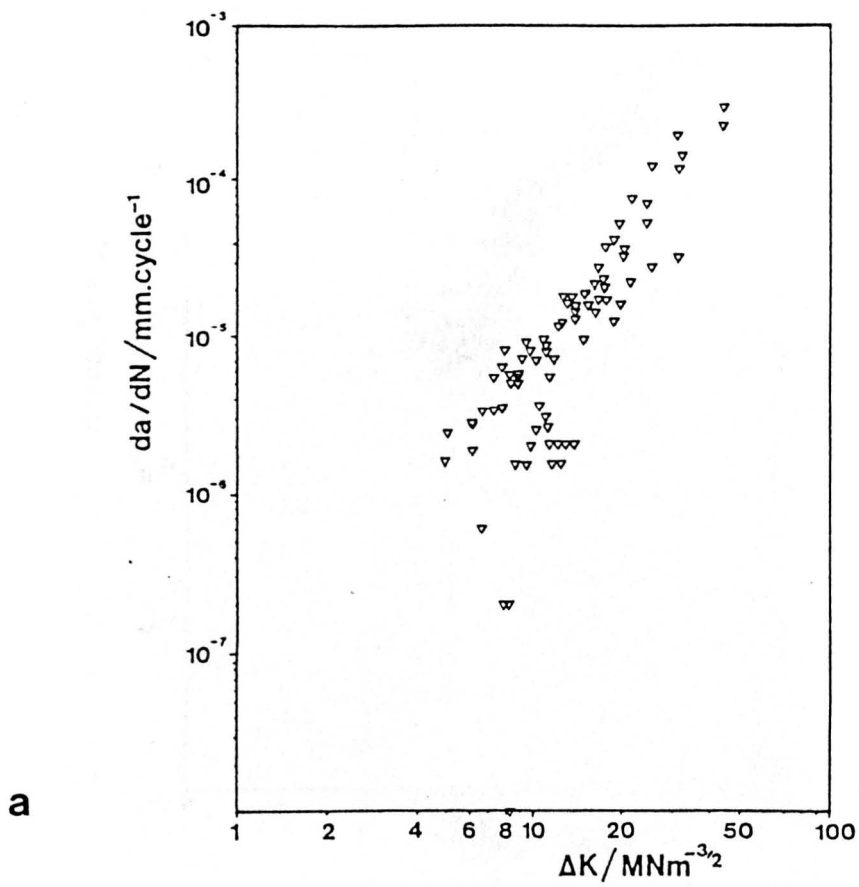


Fig.7.16  $da/dN$  vs.  $\Delta K$  scatter bands for the coarse grain structures: a) CGB scatter band (2 cracks, max. stress = 450 and 850MPa,  $R=0.1$ ), b) CGA scatter band (5 cracks, max. stress = 450-700MPa,  $R=0.1$ )

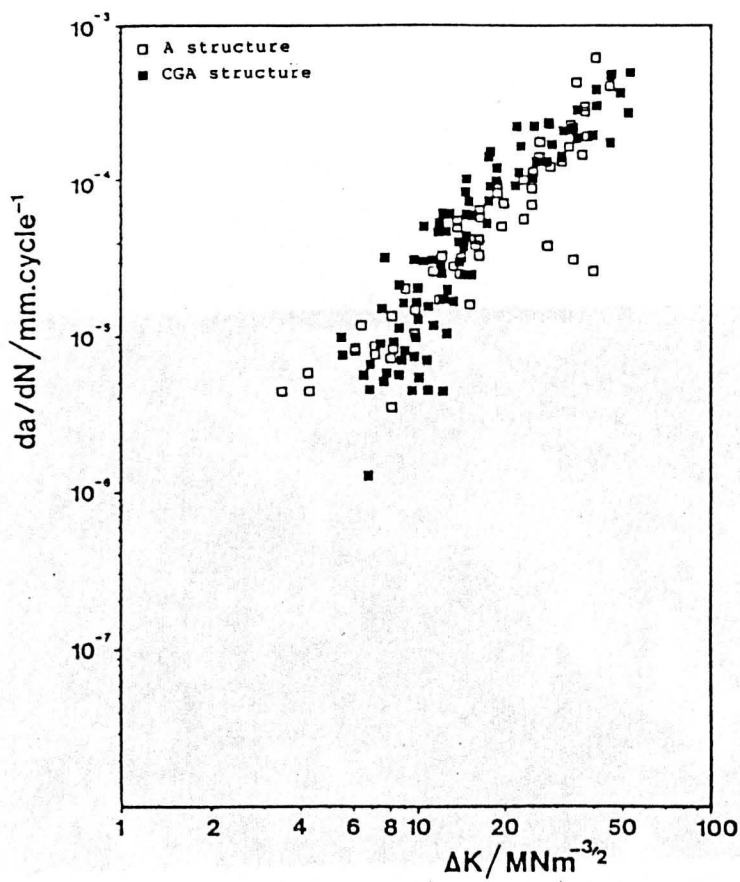


Fig.7.17 Comparison between CGA and A growth rate scatter bands.

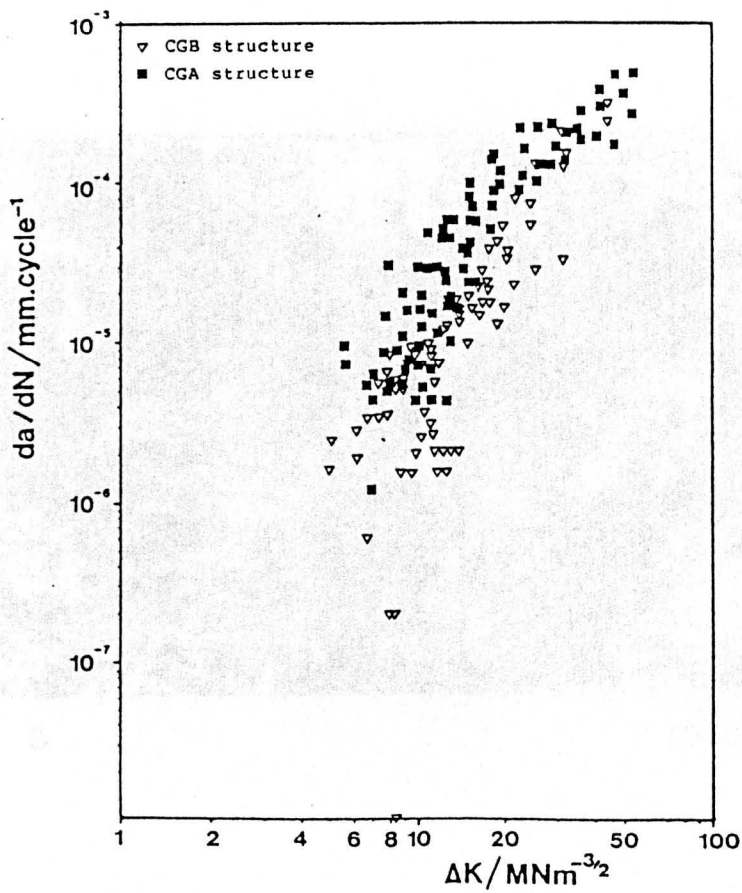


Fig.7.18 Comparison between CGA and CGB growth rate scatter bands.

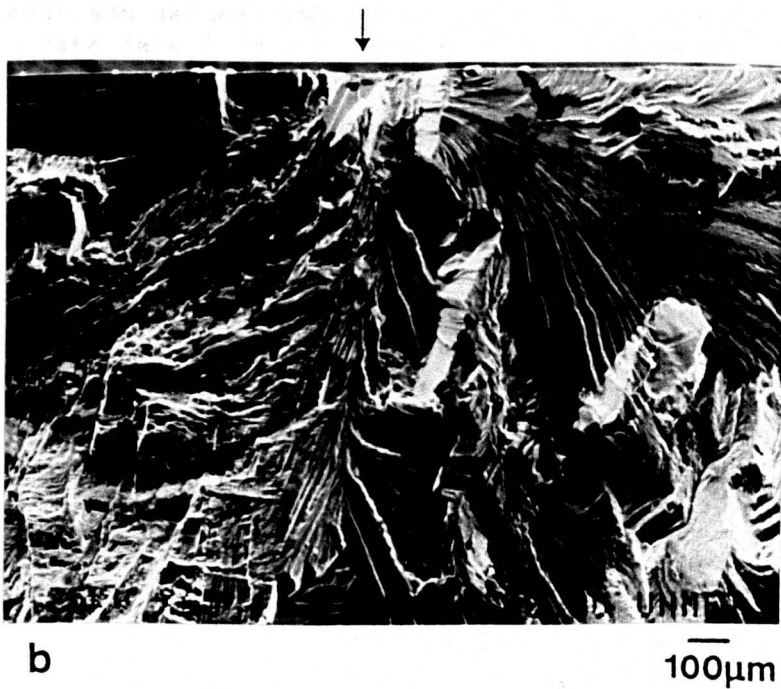
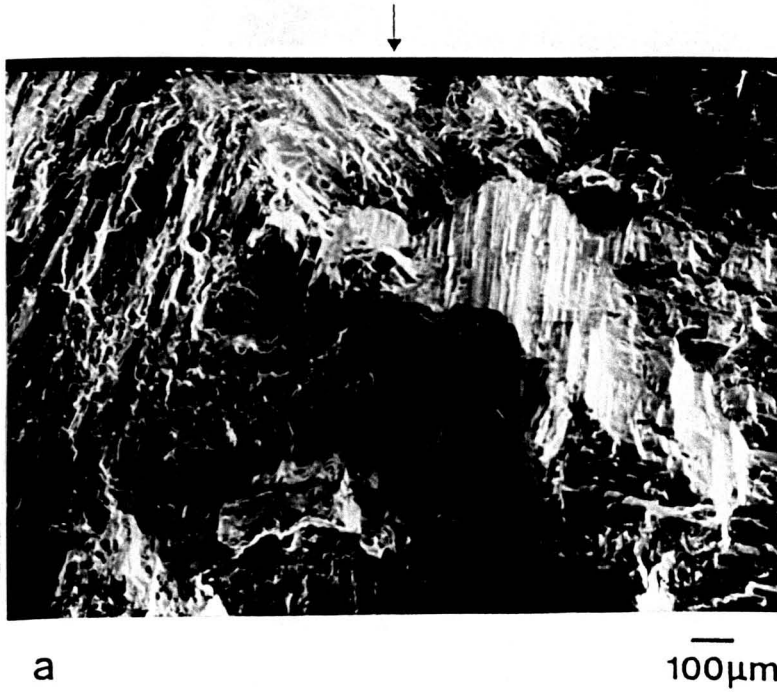


Fig.7.19 Fatigue fracture surfaces in a) the CGB and b) CGA structures (initiation sites marked).

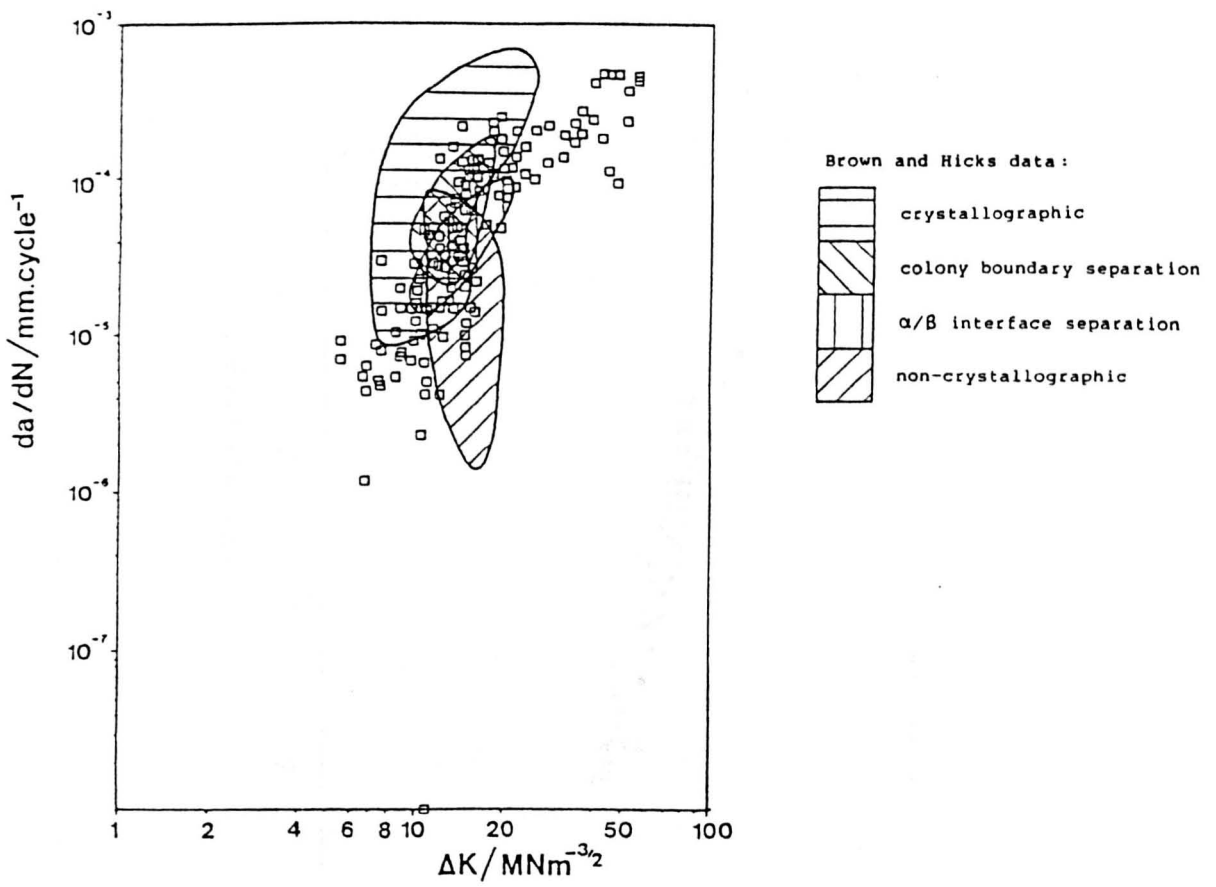


Fig.7.20 Comparison between CGA growth rate data and Brown and Hicks growth rate data from ref. [104].

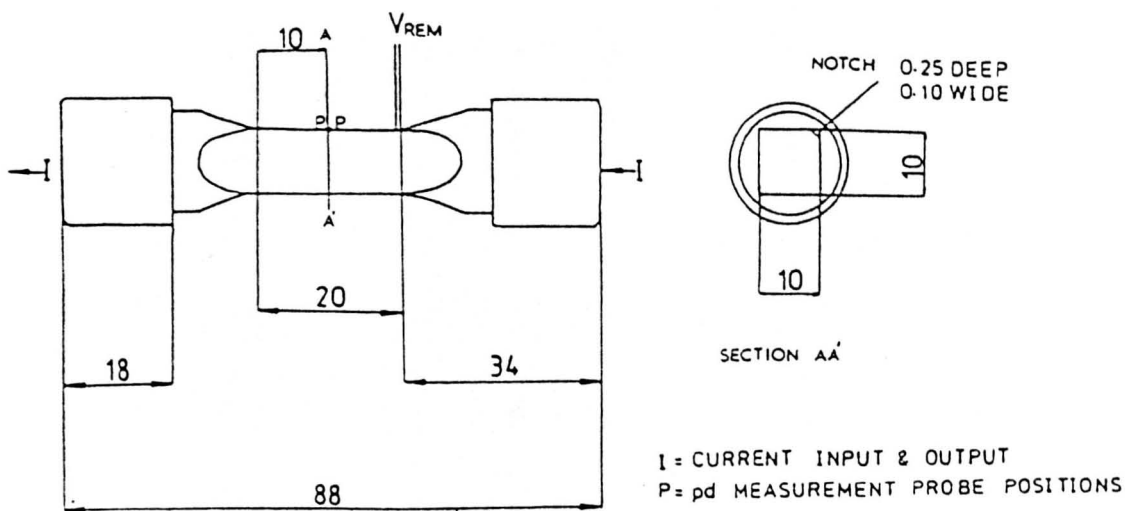


Fig.7.21 Rolls-Royce corner crack specimen design used by Brown and Hicks [104].

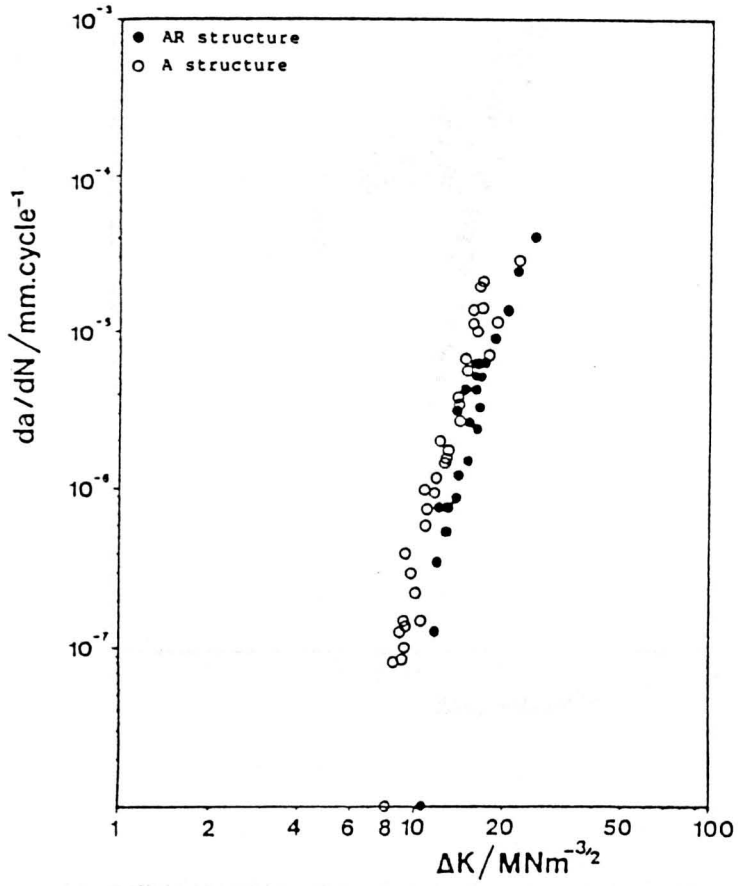
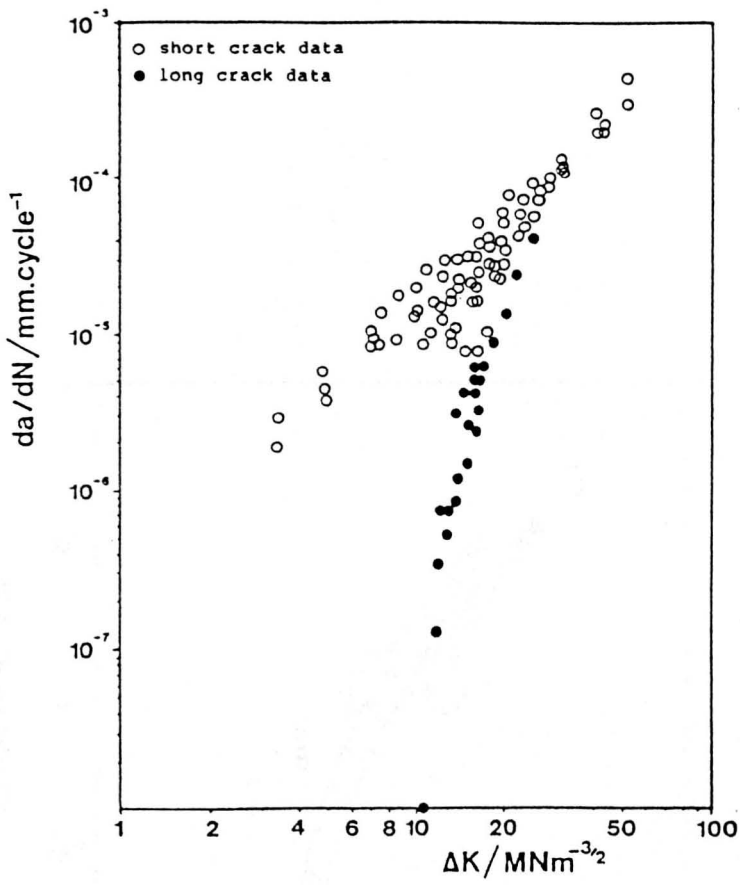


Fig.7.22 Long crack growth rate data for the AR and A structures (R=0.1).

a



b

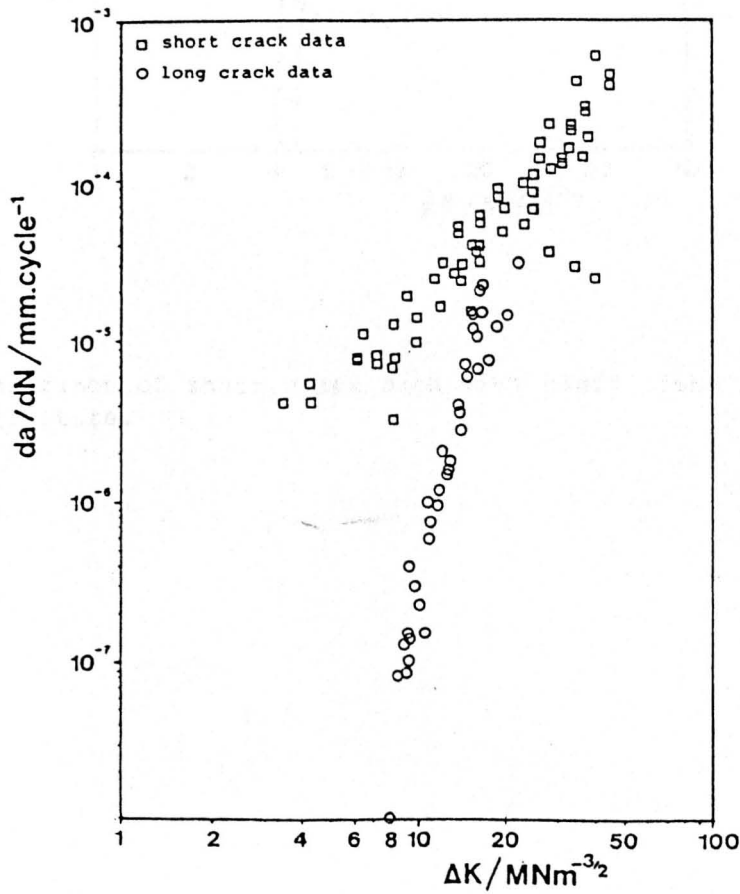


Fig.7.23 Comparison of long crack data with short crack data: a) in the AR structure and b) in the A structure.

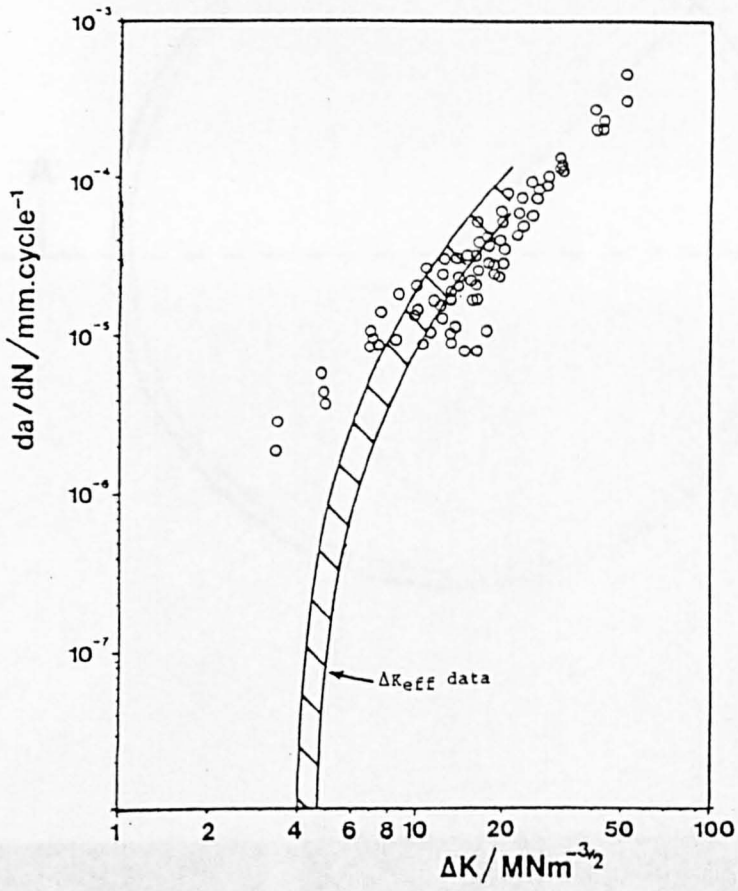
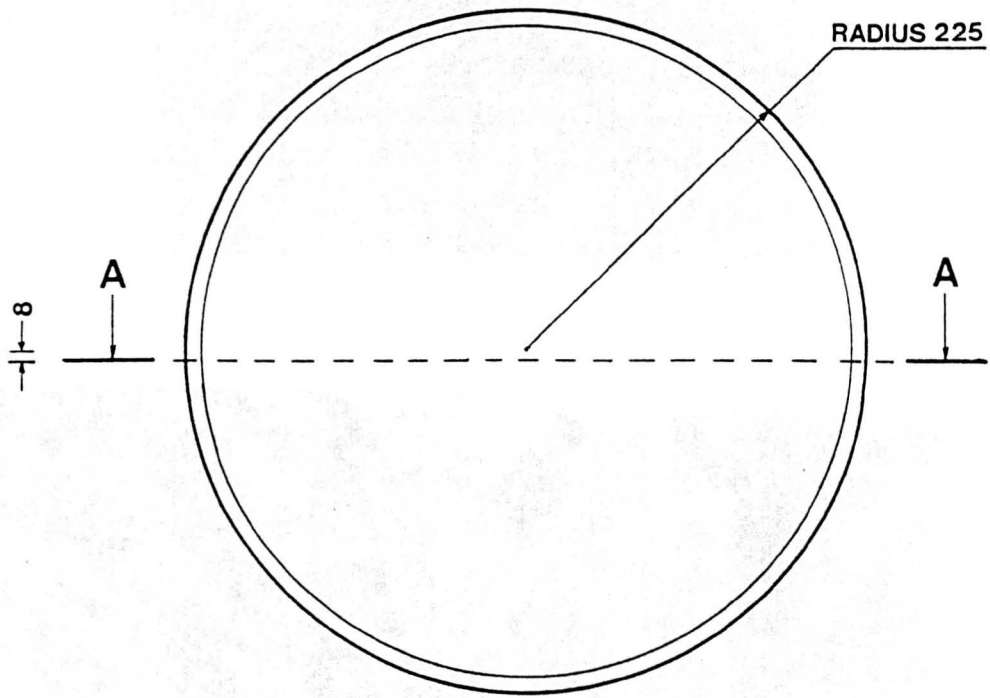
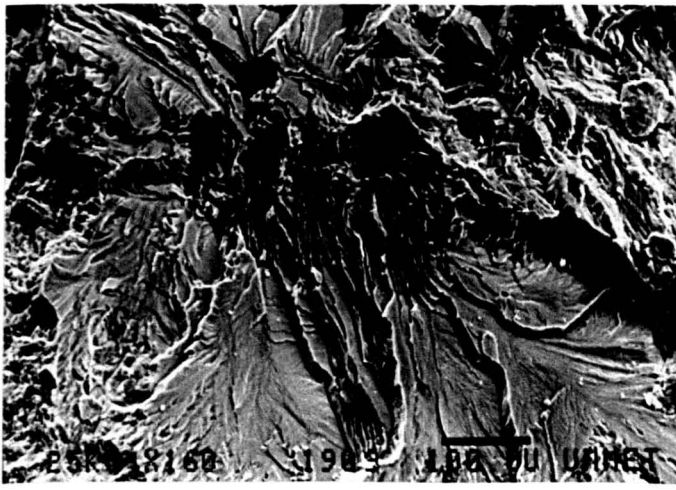


Fig.7.24 Comparison of short crack data with  $\Delta K_{\text{eff}}$  data [31] in the AR structure.

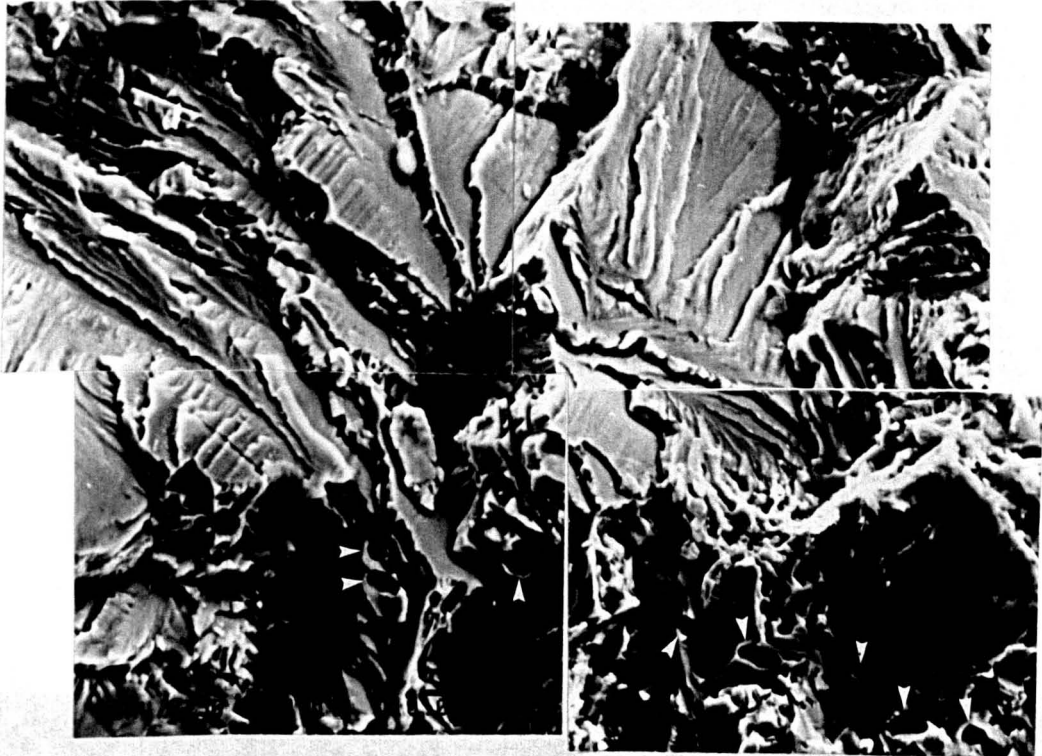


50mm

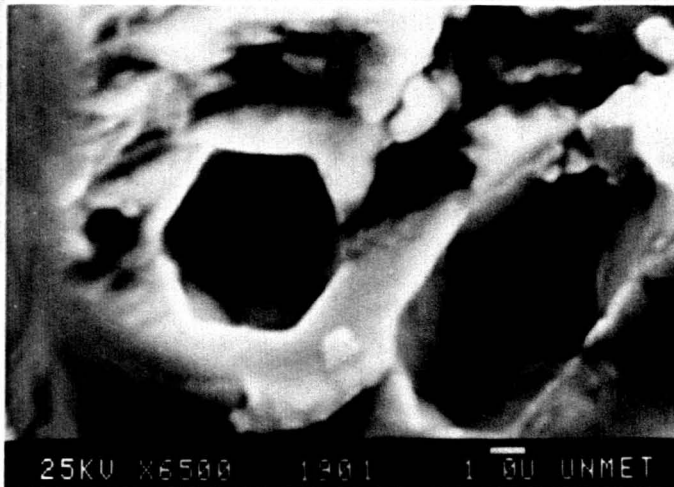
Fig.7.25 Macroslice taken through IMI685 cheese, on section AA (all dimensions in mm).



a

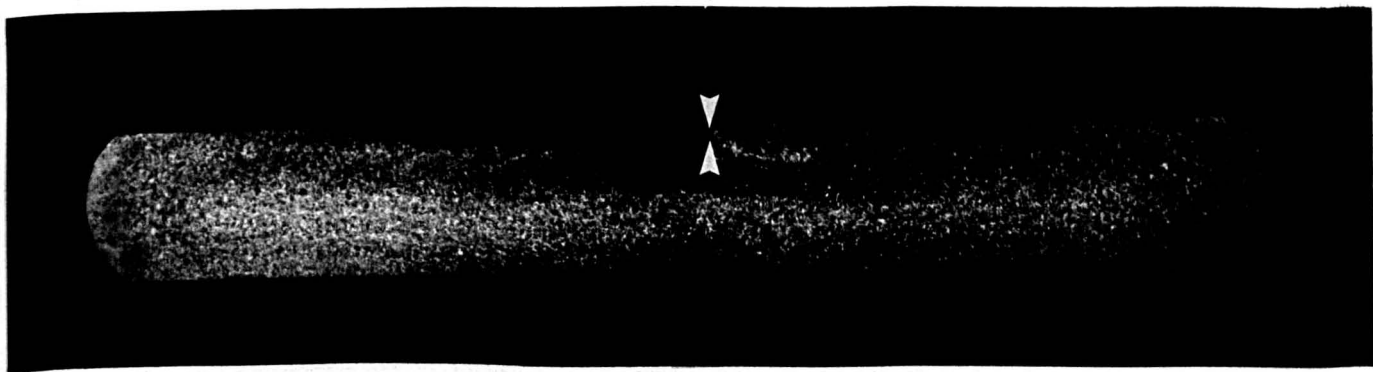
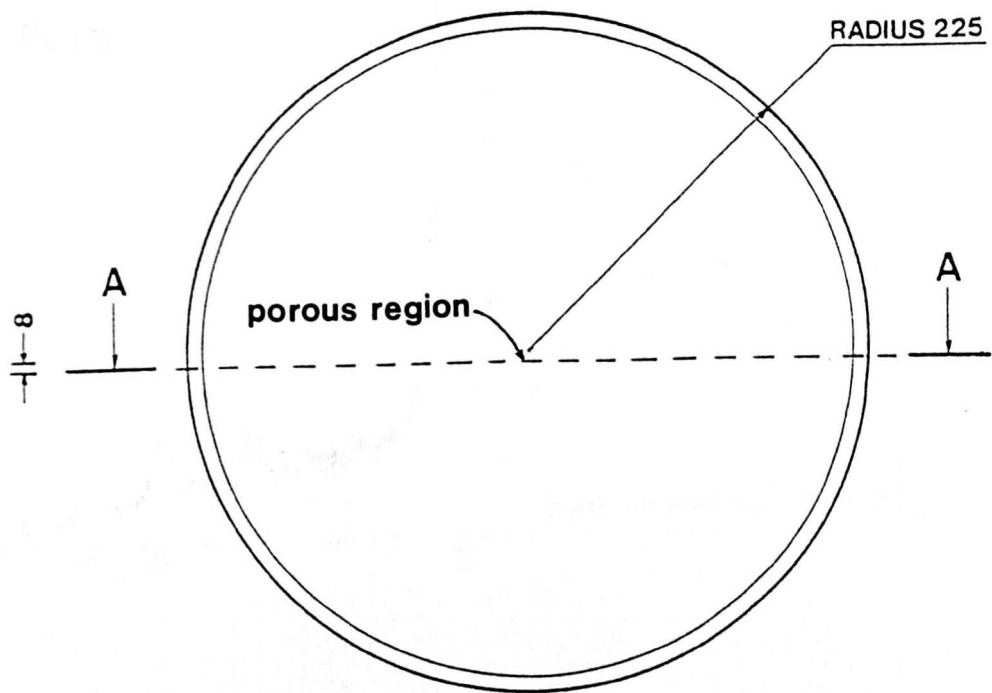


b



c

Fig.7.26 SEM micrographs of group of subsurface pores: a) general view of fracture surface, b) detail of porous region (pores arrowed), c) detail of two of the pores showing faceted nature.



50mm

Fig.7.27 Position of porous region with respect to original macroslice.

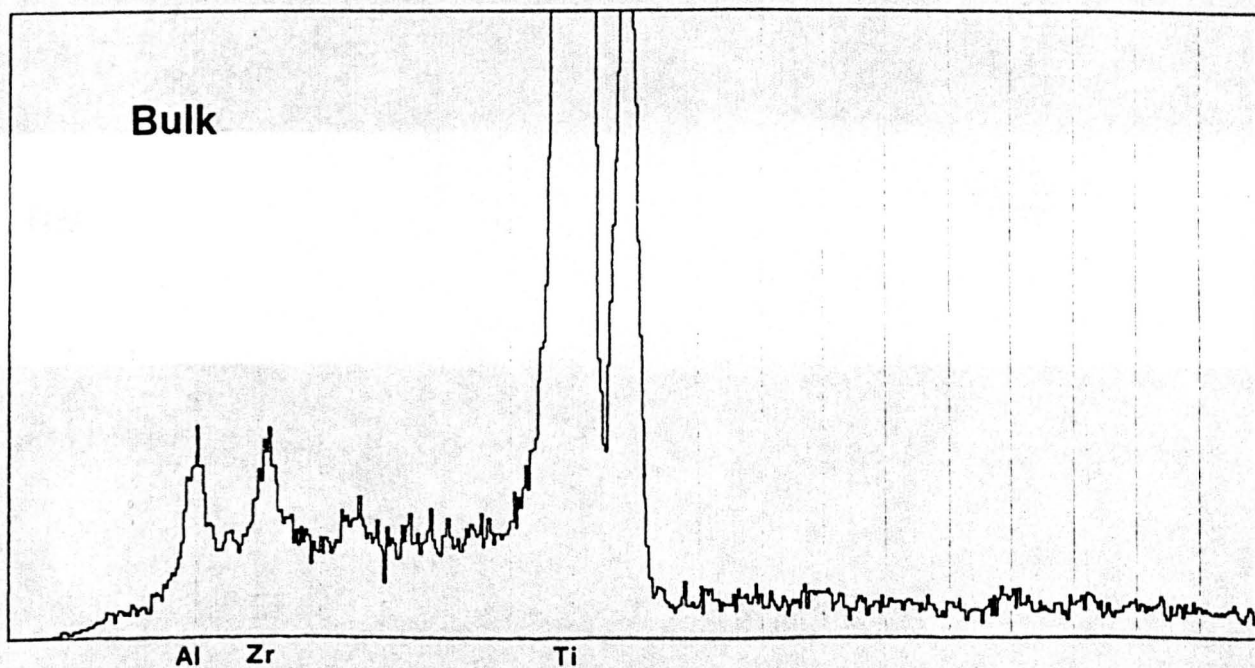
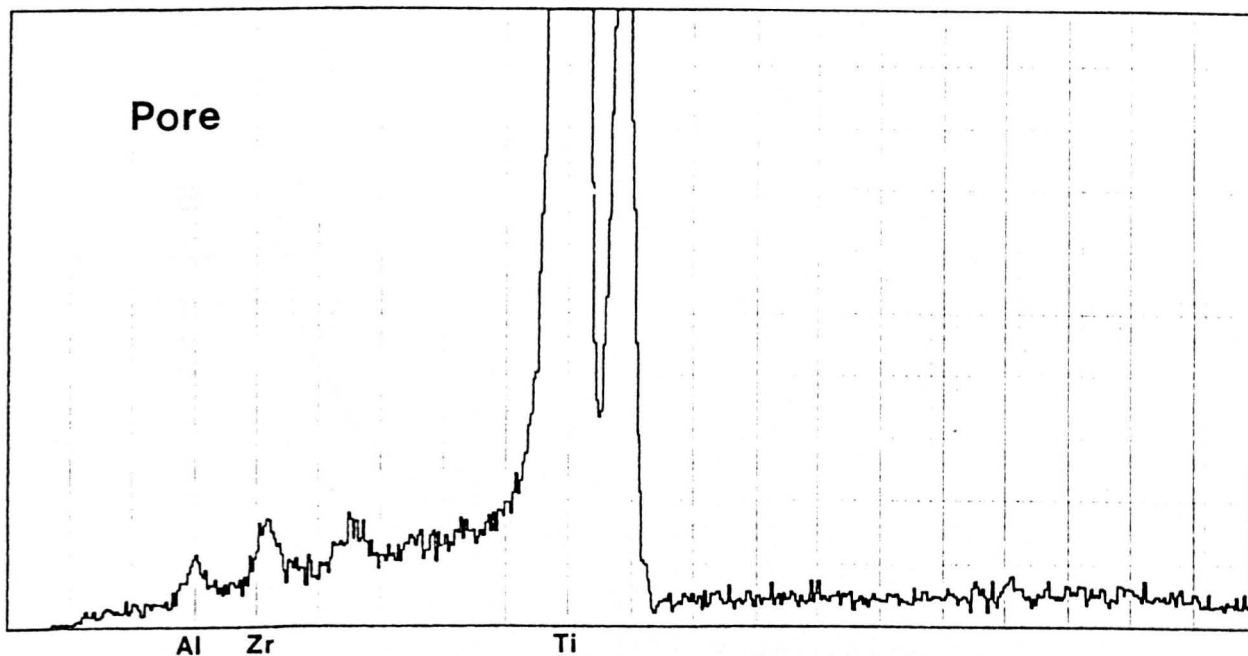
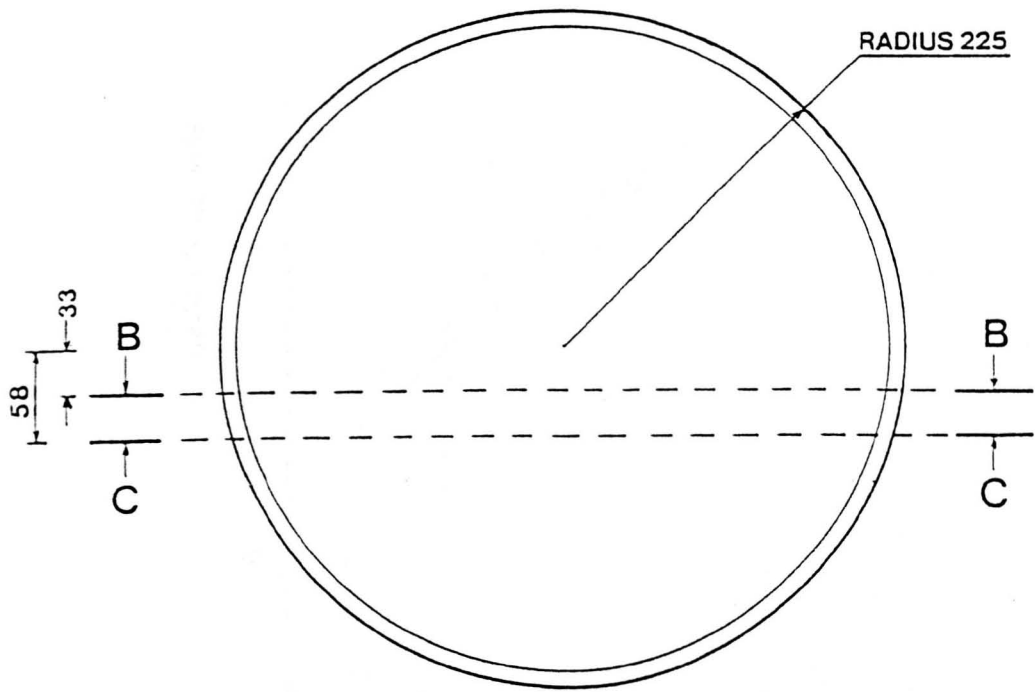
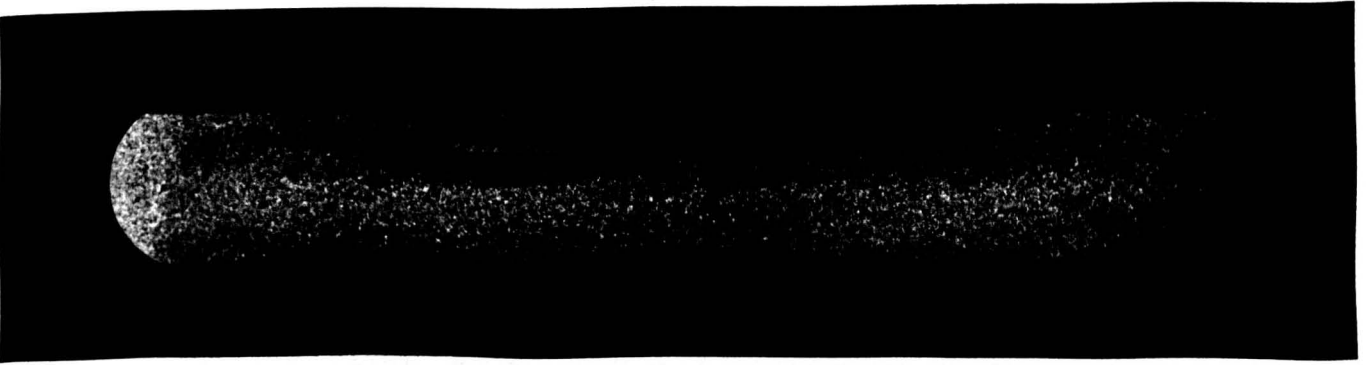


Fig.7.28 Qualitative X-ray analyses for a pore and the bulk material, showing a reduced level of aluminium and zirconium in the pore.



BB

50mm



CC

50mm

Fig.7.29 Position of second macroslice in IMI685 cheese, on sections BB and CC (all dimensions in mm).

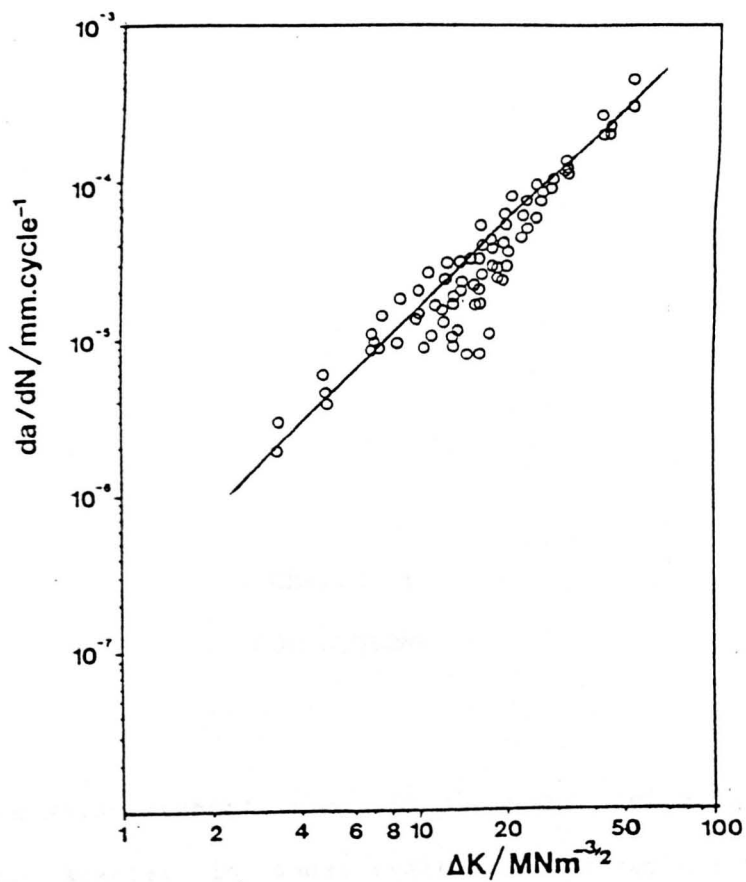


Fig.7.30 Straight line fit through AR short crack growth rate scatter band to obtain Paris Law equation.

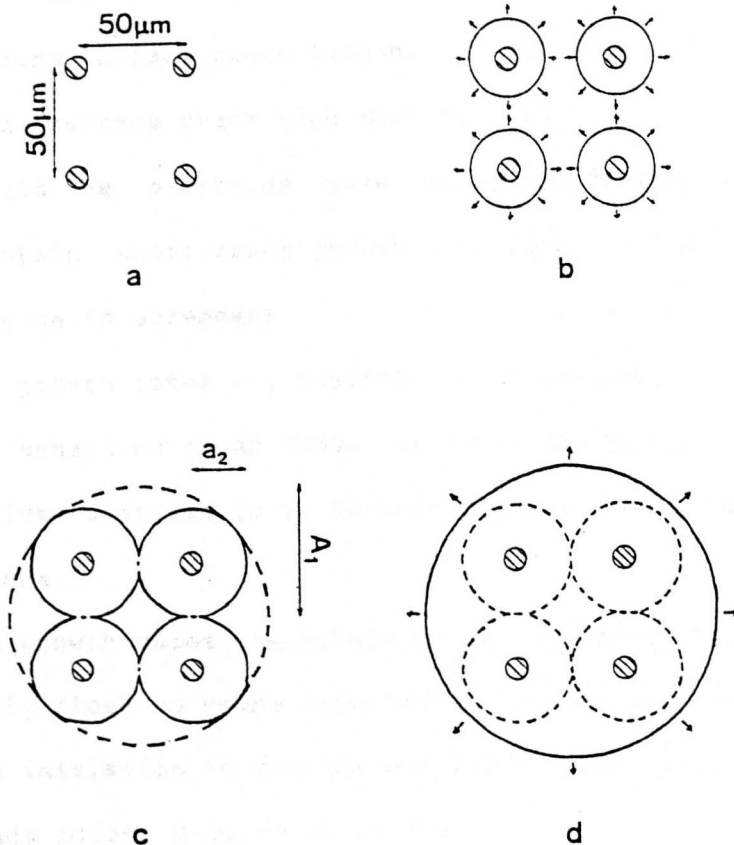


Fig.7.31 Simple two-dimensional model for crack growth from a group of four coplanar spherical pores: a) arrangement of pores, b) growth of cracks from individual pores, c) coalescence of cracks at individual crack sizes,  $a_2$ , to form larger crack of size  $A_1$ , d) growth of larger crack to failure.

## CHAPTER 8

### CONCLUSIONS

- 1) The 'Three Point Method' is an effective and valid method of reducing the scatter in short crack data, to facilitate easier comparison between sets of data.
- 2) c/a ratios for short cracks in  $\beta$ -processed titanium alloys show a large amount of scatter up to crack depth values of approximately 0.75mm.
- 3) When monitoring surface crack length, a solution for stress intensity at the surface crack tips must be used.
- 4) Caution should be exercised when using different specimen designs to obtain short crack growth rate data, as the data may not necessarily be in agreement.
- 5) Short crack growth rates are insensitive to specimen size.
- 6) Short crack behaviour in AR Ti65s, as described by  $\Delta K$ , appears to be insensitive to stress level between maximum stress levels of 450MPa and 900MPa.
- 7) Short crack growth rates are likely to be affected if cracks are sufficiently close to cause interaction between plastic zones.
- 8) Short crack initiation in  $\beta$ -processed Ti65s tends to occur from small slip bands across  $\alpha$ -platelet bundles.
- 9) In the AR and A structures, short cracks grow faster than long

cracks at equivalent  $\Delta K$ 's up to  $\Delta K$  values of  $30\text{MNm}^{-3/2}$  for the AR structure and  $25\text{MNm}^{-3/2}$  for the A structure.

10) The difference between short and long crack growth rate data can be substantially reduced by describing the long crack data in terms of  $\Delta K_{\text{eff}}$ .

11) The four microstructural conditions studied in Ti65s show decreasing short crack growth rates at equivalent  $\Delta K$ s in the order: CGA>A>AR>CGB.

12) Short crack results predict the growth of cracks from pores of size  $a=5\mu\text{m}$ , whereas long crack results do not. The presence of these pores significantly reduces fatigue crack propagation life, due to coalescence of pore-initiated cracks.

13) A Paris Law equation can be used to describe short crack growth behaviour in the disc microstructure (AR structure). The equation is:

$$\frac{da}{dN} = 1.5 \times 10^{-10} \Delta K^2$$

## CHAPTER 9

### FURTHER WORK

1) It would be useful to study short crack behaviour in a small grained basketweave condition in Ti65s, i.e. a microstructure which does not show the variations in cooling rate which are inevitable in such a large component as a compressor disc. This would show how much of an effect grain size has for a basketweave structure, where it appears the  $\alpha$ -platelets themselves could be the dominant microstructural features.

2) A more comprehensive study of slip behaviour in  $\beta$ -processed microstructures is necessary in order to understand why initiation of short cracks does not tend to occur on deep long slip bands even though they have been observed to form early on in the life of a specimen.

3) Another question of interest to Rolls-Royce in terms of quality control, which remains unanswered, is whether isolated coarse grains are a serious problem. Since  $\beta$ -processed microstructures tend to be rather complicated, it may be easier to carry out initial investigations using a model microstructure, where grain size is the only variable. Such a microstructure can be obtained with nickel alloys.

4) The question of specimen design needs to be looked into

further, to clarify whether a uniaxial tension specimen design consistently gives higher short crack growth rates than smooth four point bend specimens.

5) Further work on determination of crack shape in  $\beta$ -processed titanium alloys would be useful. If a definite trend can be found and described reasonably accurately in a quantitative manner, then errors in calculation of crack driving forces would be reduced.

6) The effect of R ratio on short crack behaviour has not really been studied in any detail. This kind of study may help to explain discrepancies between the behaviour of short cracks and long cracks. This could be coupled with the study of threshold behaviour in  $\beta$ -processed alloys. Short crack threshold characteristics of Ti65s would have particular relevance to the case study of the porosity in the IMI685 cheese.

7) Experimental determination of plastic zone sizes of short and long cracks in a  $\beta$ -processed alloy such as Ti65s may go some way to explaining the differences observed between short and long crack behaviour.

8) The effect of dwell on short crack behaviour is a subject which has so far not been given much attention. It would be interesting to see how the influence of dwell periods on short crack behaviour compared with their influence on long crack behaviour. This is particularly relevant since most short crack experiments are monitored using a replication method, which can involve subjecting specimens to test mean load or maximum load for several minutes.

9) Finally, methods of artificial initiation of short cracks may need to be investigated in more detail. One of the problems is being able to make a starter notch sufficiently small so that a crack initiating from it would still be well within the short

crack regime. Electro-discharge-machining (EDM) was used in this work in an attempt to initiate short cracks artificially from pits less than 100 $\mu$ m in diameter, but the attempts were unsuccessful.

## REFERENCES

- 1) **R.O.Ritchie, S.Suresh**  
Met. Trans. A, vol.13A (1982), p.937.
- 2) **A.J.A.Mom, M.D.Raizenne**  
AGARD (NATO), CP-393 (Oct 1985), 9.1-9.9.
- 3) **M.A.Hicks, R.H.Jeal, C.J.Beevers**  
Fat. Eng. Mat. Struct., vol.6, no.1 (1983), p.51.
- 4) **M.E.Fine, R.O.Ritchie**  
'Fatigue and Microstructure', ASM Materials Science Seminar, St. Louis (1978), p.245.
- 5) **P.E.Irving, C.J.Beevers**  
Met. Trans., vol.5A, (Feb 1974), p.391.
- 6) **C.W.Brown, J.E.King, M.A.Hicks**  
Met. Sci., vol.18 (1984), p.374.
- 7) **J.A.Ruppen, A.J.McEvily**  
Fat. Eng. Mat. Struct., vol.2, (1979), p.63.
- 8) **W.Elber**  
Eng. Fract. Mech., vol.2, no.1 (1970), p.37.
- 9) **S.Suresh, R.O.Ritchie**  
'The Propagation of Short Fatigue Cracks', Univ. of California, Report no. UCB/RP/83/1014, (1983).
- 10) **R.O.Ritchie, S.Suresh**  
'Mechanics and Physics of the Growth of Small Cracks', Univ. of California, Report no. UCB/RP/82/A1001, (1982).
- 11) **R.O.Ritchie, W.Yu**  
'Small Fatigue Cracks' (proc. conf., ed. R.O.Ritchie, J.Lankford), The Metallurgical Society (1986), p.167.
- 12) **P.C.Paris, F.Erdogan**  
J. Basic Eng. (Trans ASME-D), vol.85 (1963), p.528.
- 13) **A.R.Rosenfield**  
Eng. Fract. Mech vol.9 (1977), p.509.
- 14) **G.R.Yoder, L.A.Cooley, T.W.Crooker**  
Eng. Fract. Mech vol.11 (1979) p.805.
- 15) **J.L.Robinson, C.J.Beevers**  
Metal. Sci. J., vol.7 (1973), p.153.
- 16) **N.Walker, C.J.Beevers**  
Fat. Eng. Mat. Struct., vol.1 (1979), p.135.
- 17) **P.E.Irving, C.J.Beevers**  
Mat. Sci. Eng., vol.14 (1974), p.229.

- 18) **T.W.Crooker, D.J.Krause**  
Report of NRL Progress, no.1, (1972), p.18.
- 19) **A.Yuen, S.W.Hopkins, G.R.Leverant, C.A.Rau**  
Met. Trans., vol.5 (1974), p.1833.
- 20) **G.R.Yoder, L.A.Cooley, T.W.Crooker**  
Eng. Fract. Mech., vol.17, no.2, (1983), p.185.
- 21) **M.Katcher, M.Kaplan**  
'Fracture Toughness and Slow Stable Cracking', ASTM STP 559 (1974), p.264.
- 22) **J.C.Chesnutt, J.A.Wert**  
'Fatigue Crack Growth Threshold Concepts' (proc. conf.), The Metallurgical Society / AIME (1984), p.83.
- 23) **G.R.Yoder, D.Eylon**  
Met. Trans. A, vol.10A, (1979), p.1808.
- 24) **W.G.Burgers**  
Physica, vol.1, (1934), p.561.
- 25) **J.C.Williams**  
'Titanium Science and Technology', (ed. R.I.Jaffee, H.M.Burte), vol.3, Plenum Press, New York (1973), p.1433.
- 26) **D.Schechtman, D.Eylon**  
Met. Trans. A, vol.9A (1978), p.1018.
- 27) **G.R.Yoder, L.A.Cooley, T.W.Crooker**  
Met. Trans. A, vol.8A (1977), p.1737.
- 28) **D.Eylon, J.A.Hall, C.M.Pierce, D.L.Ruckle**  
Met. Trans. A, vol.7A (1976), p.1817.
- 29) **P.J.Postans, R.H.Jeal**  
'Forging and Properties of Aerospace Materials', (proc. conf.), The Metals Society, London, U.K., (1977), p.192.
- 30) **D.Eylon, J.A.Hall**  
Met. Trans. A, vol.8A (1977), p.981.
- 31) **M.Hicks, R.H.Jeal, C.J.Beevers**  
Fat. Eng. Mat. Struct., vol.6, no.1 (1983), p.51.
- 32) **W.J.Plumbridge, M.Stanley**  
Int. J. Fatigue, vol.8, no.4, (1986), p.209.
- 33) **M.Peters, K.Welpmann, H.Doker**  
'Titanium Science and Technology' (proc. conf., ed. G.Lutjering, U.Zwicker, W.Bunk), D.G.M. (1984), p.226.
- 34) **J.T.Ryder, D.E.Pettit, W.E.Krupp, D.W.Hoepfner**  
'Final Report on Evaluation of Mechanical Property Characteristics of IMI685', Lockheed-California Company, Rye Canyon Laboratory (Oct. 1973).

- 35) **N.G.Paton, R.A.Spurling**  
'Hydride Habit Planes in Titanium-Aluminium Alloys', Science Centre, Rockwell International, Thousand Oaks, California.
- 36) **W.J.Evans, C.R.Gostelow**  
Met. Trans. A, vol.10A (1979), p.1837.
- 37) **W.J.Evans**  
Scripta Metallurgica, vol.21 (1987), p.469.
- 38) **J.E.Hack, G.R.Leverant**  
Met. Trans. A, vol.13A (1982), p.1729.
- 39) **J.M.Clarke**  
J. Strain Analysis, vol.4 (1969), p.95.
- 40) **W.J.Plumbridge**  
Fat. Eng. Mat. Struct., vol.10, no.5, (1987), p.385.
- 41) **Z.Song, D.W.Hoepfner**  
Int. J. Fatigue, vol.10, no.4, (1988), p.211.
- 42) **S.Pearson**  
Eng. Fract. Mech., vol.7 (1975), p.235.
- 43) **A.C.Pickard, C.W.Brown, M.A.Hicks**  
'Advances in Life Prediction Methods', (proc. conf., ed. D.A.Woodford, J.R.Whitehead), ASME Book no. H00255 (1983), p.173.
- 44) **C.W.Brown, J.E.King** 'Small Fatigue Cracks' (proc. conf., ed. R.O.Ritchie, J.Lankford), The Metallurgical Society (1986), p.73.
- 45) **J.Lankford, S.J.Hudak Jr.**  
Int. J. Fat., vol.9, no.2 (1987), p.87.
- 46) **K.J.Miller**  
Fat. Fract. Eng. Mat. Struct., vol.10, no.1 (1987), p.75.
- 47) **K.J.Miller**  
Fat. Fract. Eng. Mat. Struct., vol.10, no.2 (1987), p.93.
- 48) **B.N.Leis, A.T.Hopper, J.Ahmad, D.Broek, M.F.Kanninen**  
Eng. Fract. Mech., vol.23, no.5, (1986), p.883.
- 49) **K.Tanaka**  
JSME Int. J., vol.30, no.259, (1987), p.1.
- 50) **J.Lankford, D.L.Davidson**  
'Small Fatigue Cracks' (proc. conf., ed. R.O.Ritchie, J.Lankford), The Metallurgical Society (1986), p.51.
- 51) **R.O.Ritchie, J.Lankford**  
'Small Fatigue Cracks' (proc. conf., ed. R.O.Ritchie, J.Lankford), The Metallurgical Society (1986), p.1.

- 52) S.J.Hudak Jr.  
Trans. ASME, J. Eng. Mat. Tech., vol.103, (1981), p.26.
- 53) J.R.Rice  
J. Appl. Mech., (1968), p.379.
- 54) N.E.Dowling, J.A.Begley  
ASTM STP 590 (1976), p.82.
- 55) M.F.Kanninen, J.Ahmad, B.N.Leis  
ASME AMD 47 (1981), p.81.
- 56) B.N.Leis, A.Zahoor  
ASTM STP 700 (1980), p.65.
- 57) N.E.Dowling  
ASTM STP 637 (1977), p.97.
- 58) B.N.Leis, T.P.Forte  
ASTM STP 743 (1981), p.100.
- 59) R.K.Bolinbroke, J.E.King  
'Fatigue 87', (proc. conf., ed. R.O.Ritchie, E.A.Starke, Jr.),  
EMAS, U.K. (1987), vol.1 p.281.
- 60) T.Hoshide, T.Yamada, S.Fujimura, T.Hayashi  
Eng. Fract. Mech., vol.21, (1985), p.85.
- 61) K.Tokaji, T.Ogana, Y.Harada, Z.Ando  
Fat. Fract. Eng. Mat. Struct., vol.9 (1986), p.1.
- 62) L.Wagner, J.K.Gregory, A.Gysler, G.Lutjering  
'Small Fatigue Cracks' (proc. conf., ed. R.O.Ritchie, J.Lankford),  
The Metallurgical Society (1986), p.117.
- 63) A.Pineau  
'Small Fatigue Cracks' (proc. conf., ed. R.O.Ritchie, J.Lankford),  
The Metallurgical Society (1986), p.191.
- 64) H.Mughrabi  
Z. Metallk., vol.66 (1975), p.719.
- 65) K.J.Miller  
'Fundamentals of Deformation and Fracture', Eshelby Memorial  
Symposium, Sheffield, U.K. (April 1984).
- 66) B.T.Ma, C.Laird  
'Small Fatigue Cracks' (proc. conf., ed. R.O.Ritchie, J.Lankford),  
The Metallurgical Society (1986), p.9.
- 67) P.Neumann, A.Tonnessen  
'Small Fatigue Cracks' (proc. conf., ed. R.O.Ritchie, J.Lankford),  
The Metallurgical Society (1986), p.41.
- 68) R.W.Suhr  
'The Behaviour of Short Fatigue Cracks' (proc. conf., ed.  
K.J.Miller, E.R.de los Rios), Mechanical Engineering Publications,  
London (1986), p.69.

- 69) **R.N.Wilson, R.W.Gardiner, D.M.Turley**  
'Fatigue of Engineering Materials and Structures' (proc. conf.),  
Mechanical Engineering Publications, London (1986), vol.2, p.407.
- 70) **W.P.Koster, M.Field**  
Proc. Nth. American Metalworking Res. Conf. (1973), vol.2, p.167.
- 71) **S.Jeelani, K.Ramakrishnan**  
J. Mat. Sci., vol.20 (1985), p.3245.
- 72) **G.R.Leverant, B.S.Langer, A.Yuen, S.W.Hopkins**  
Met. Trans. A, vol.10A (1979), p.251.
- 73) **T.Takemoto, K.L.Jing, T.Tsakalakos, S.Weissmann,  
I.R.Dramer**  
Met. Trans. A, vol.14A (1983), p.127.
- 74) **S.Usami**  
'Small Fatigue Cracks' (proc. conf., ed. R.O.Ritchie, J.Lankford),  
The Metallurgical Society (1986), p.559.
- 75) **R.Marissen, M.Peters, K.Schulte, K.-H.Trautmann, H.Nowack**  
'Titanium Science and Technology' (proc. conf., ed. G.Lutjering,  
U.Zwicker, W.Bunk), D.G.M. (1984), p.2289.
- 76) **N.D.R.Goddard**  
Ph.D. Thesis, Department of Materials, Imperial College of Science  
and Technology, London (July 1988).
- 77) **R.O.Ritchie, W.Yu, A.F.Blom, D.K.Holm**  
Fat. Fract. Eng. Mat. Struct., vol.10, no.5 (1987), p.343.
- 78) **O.N.Romaniv, V.N.Siminkovich, A.N.Tkach**  
'Fatigue Thresholds' (proc. conf., ed. J.Backlund, A.F.Blom,  
C.J.Beevers), EMAS, p.799.
- 79) **J.L.Kendall, M.N.James, J.F.Knott**  
'The Behaviour of Short Fatigue Cracks' (proc. conf., ed.  
K.J.Miller, E.R.de los Rios), Mechanical Engineering Publications,  
London (1986), p.241.
- 80) **I.W.Hussey, J.Byrne, T.V.Duggan**  
'The Behaviour of Short Fatigue Cracks' (proc. conf., ed.  
K.J.Miller, E.R.de los Rios), Mechanical Engineering Publications,  
London (1986), p.337.
- 81) **S.L.Breat, F.Mundry, A.Pineau**  
Fat. Eng. Mat. Struct., vol.6 (1983), p.349.
- 82) **M.N.James, J.F.Knott**  
Fat. Fract. Eng. Mat. Struct., vol.8, no.2 (1985), p.177.
- 83) **A.Zeghloul, J.Petit**  
Fat. Fract. Eng. Mat. Struct., vol.8, no.4 (1985), p.341.
- 84) **J.Byrne**  
'Fatigue 87', (proc. conf., ed. R.O.Ritchie, E.A.Starke, Jr.),  
EMAS, U.K. (1987), vol.1, p.195.

- 85) **N.S.Iyyer, N.E.Dowling**  
'Small Fatigue Cracks' (proc. conf., ed. R.O.Ritchie, J.Lankford),  
The Metallurgical Society (1986), p.213.
- 86) **K.Yamada, M.G.Kim, T.Kunio**  
'The Behaviour of Short Fatigue Cracks' (proc. conf., ed.  
K.J.Miller, E.R.de los Rios), Mechanical Engineering Publications,  
London (1986), p.337.
- 87) **K.Takao, H.Nisitani**  
'Fatigue 84' (proc. conf., ed. C.J.Beevers), EMAS, U.K. (1984),  
vol.2, p.827.
- 88) **R.K.Bolingbroke, J.E.Ring**  
'Small Fatigue Cracks' (proc. conf., ed. R.O.Ritchie, J.Lankford),  
The Metallurgical Society (1986), p.213.
- 89) **A.W.Funkenbusch, L.F.Coffin**  
Met. Trans. A, vol.9A, no.8 (1978), p.1159.
- 90) **J.Ruppen, P.Bhowal, D.Eylon, A.J.McEvily**  
ASTM STP 675 (1979), p.47.
- 91) **H.Kitagawa, S.Takahashi**  
Proc. 2nd Int. Conf. on Mechanical Behaviour of Materials, Boston  
(1976), p.627.
- 92) **M.H.El Haddad, N.E.Dowling, T.H.Topper, K.N.Smith**  
Int. J. Fract., vol.15, no.5 (1979).
- 94) **M.W.Brown**  
'The Behaviour of Short Fatigue Cracks' (proc. conf., ed.  
K.J.Miller, E.R.de los Rios), Mechanical Engineering Publications,  
London (1986), p.423.
- 95) **D.Taylor**  
Fat. Eng. Mat. Struct., vol.5, no.4 (1982), p.305.
- 96) **D.Taylor**  
'The Behaviour of Short Fatigue Cracks' (proc. conf., ed.  
K.J.Miller, E.R.de los Rios), Mechanical Engineering Publications,  
London (1986), p.479.
- 97) **J.Lankford**  
Fat. Fract. Eng. Mat. Struct., vol.8, no.2 (1985), p.161.
- 98) **E.Affeldt, V.Gerold**  
'Advances in Fracture Research' (proc. conf., ed. D.Francois),  
Pergamon (1984), p.1579.
- 99) **W.L.Morris, M.R.James, O.Buck**  
Met. Trans. A, vol.12A (1981), p.57.
- 100) **K.Tanaka, Y.Nakai, M.Yamashita**  
Int. J. Fract., vol.17 (1981), p.519.

- 101) **S.Suresh**  
University of California, Report no. UCB/RP/83/A1011 (Feb. 1983).
- 102) **M.R.James, W.L.Morris**  
'Small Fatigue Cracks' (proc. conf., ed. R.O.Ritchie, J.Lankford),  
The Metallurgical Society (1986), p.145.
- 103) **C.Gerdes, A.Gysler, G.Lutjering**  
'Fatigue Crack Growth Threshold Concepts' (proc. conf.), The  
Metallurgical Society / AIME (1984), p.465.
- 104) **C.W.Brown, M.A.Hicks**  
Fat. Eng. Mat. Struct., vol.6, no.1 (1983), p.67.
- 105) **M.A.Hicks, C.Howland, C.W.Brown**  
'The Metallurgy of Light Alloys' (proc. conf.), The Institution of  
Metallurgists (1983), p.252.
- 106) **C.W.Brown, D.Taylor**  
'Fatigue Crack Growth Threshold Concepts' (proc. conf., ed.  
D.L.Davidson, S.Suresh), AIME, Philadelphia, (1984), p.433.
- 107) **E.R.de los Rios, Z.Tang, K.J.Miller**  
Fat. Eng. Mat. Struct., vol.7 (1984), p.97.
- 108) **E.R.de los Rios, H.J.Mohamed, K.J.Miller**  
Fat. Fract. Eng. Mat. Struct., vol.8 (1985), p.49.
- 109) **T.Kunio, K.Yamada**  
ASTM STP 675 (1979), p.342.
- 110) **J.K.Shang, J.-L.Tzou, R.O.Ritchie**  
Met. Trans. A, vol.18A (1987), p.1613.
- 111) **D.F.Socie, C.T.Hua, D.W.Worthern**  
Fat. Fract. Eng. Mat. Struct., vol.10, no.1 (1987), p.1.
- 112) **A.Zeghloul, J.Petit**  
'Small Fatigue Cracks' (proc. conf., ed. R.O.Ritchie, J.Lankford),  
The Metallurgical Society (1986), p.225.
- 113) **V.M.Radakrishnan, Y.Mutoh**  
'The Behaviour of Short Fatigue Cracks' (proc. conf., ed.  
K.J.Miller, E.R.de los Rios), Mechanical Engineering Publications,  
London (1986), p.87.
- 114) **B.Weiss, R.Stickler, A.Fathulla**  
'Small Fatigue Cracks' (proc. conf., ed. R.O.Ritchie, J.Lankford),  
The Metallurgical Society (1986), p.471.
- 115) **V.Bicego**  
'Fatigue 87', (proc. conf., ed. R.O.Ritchie, E.A.Starke, Jr.),  
EMAS, U.K. (1987), vol.1, p.231.
- 116) **K.Tokaji, T.Ogawa, S.Osako, Y.Harada**  
'Fatigue 87', (proc. conf., ed. R.O.Ritchie, E.A.Starke, Jr.),  
EMAS, U.K. (1987), vol.1, p.313.

- 117) **Y.Murakami, K.Matsuda**  
'Fatigue 87', (proc. conf., ed. R.O.Ritchie, E.A.Starke, Jr.), EMAS, U.K. (1987), vol.1, p.333.
- 118) **Y.Verreman, J.-P.Bailon, J.Masounave**  
'Fatigue 87', (proc. conf., ed. R.O.Ritchie, E.A.Starke, Jr.), EMAS, U.K. (1987), vol.1, p.371.
- 119) **B.N.Cox, W.J.Pardee, W.L.Morris**  
Fat. Fract. Eng. Mat. Struct., vol.9, no.6 (1987), p.435.
- 120) **R.K.Bolingbroke, J.E.King**  
'The Behaviour of Short Fatigue Cracks' (proc. conf., ed. K.J.Miller, E.R.de los Rios), Mechanical Engineering Publications, London (1986), p.101.
- 121) **D.L.Davidson, J.Lankford**  
'Small Fatigue Cracks' (proc. conf., ed. R.O.Ritchie, J.Lankford), The Metallurgical Society (1986), p.455.
- 122) **B.P.D.O'Connor, A.Plumtree**  
'Fatigue 87', (proc. conf., ed. R.O.Ritchie, E.A.Starke, Jr.), EMAS, U.K. (1987), vol.1, p.145.
- 123) **K.T.Venkateswara Rao, W.Yu, R.O.Ritchie**  
'Fatigue 87', (proc. conf., ed. R.O.Ritchie, E.A.Starke, Jr.), EMAS, U.K. (1987), vol.1, p.291.
- 124) **X.Su, W.N.Sharpe, Jr.**  
'Fatigue 87', (proc. conf., ed. R.O.Ritchie, E.A.Starke, Jr.), EMAS, U.K. (1987), vol.1, p.343.
- 125) **J.Lankford, D.L.Davidson**  
'Fatigue Crack Growth Threshold Concepts' (proc. conf.), The Metallurgical Society / AIME (1984), p.447.
- 126) **W.L.Morris, M.R.James**  
'Fatigue Crack Growth Threshold Concepts' (proc. conf.), The Metallurgical Society / AIME (1984), p.479.
- 127) **T.Hoshide, D.F.Socie**  
Eng. Fract. Mech., vol.26, no.6 (1987), p.841.
- 128) **J.F.McCarver, R.O.Ritchie**  
Mat. Sci. Eng., vol.55 (1982), p.63.
- 129) **M.A.Hicks, C.W.Brown**  
'Fatigue 84' (proc. conf., ed. C.J.Beevers) EMAS, U.K. (1984), vol.3, p.1337.
- 130) **J.K.Gregory**  
'Fatigue 87', (proc. conf., ed. R.O.Ritchie, E.A.Starke, Jr.), EMAS, U.K. (1987), vol.1, p.303.
- 131) **R.P.Gangloff**  
'Localised Crack Chemistry and Mechanics in Environmentally Assisted Cracking' (proc. conf., ed. R.P.Gangloff), AIME (1984).

- 132) **J.Lankford**  
Eng. Fract. Mech., vol.9 (1977), p.617.
- 133) **T.Yokobori, H.Kuribayashi, M.Kawagishi, N.Takeuchi**  
Reports of the Research Institute for Strength and Fracture of Materials, Tokohu Univ., Japan, vol.7 (1971), p.1.
- 134) **J.Lankford, T.S.Cook, G.P.Sheldon**  
Int. J. Fract., vol.17 (1981), p.143.
- 135) **M.R.James, W.Morris**  
Met. Trans. A, vol.14A (1983), p.153.
- 136) **W.L.Morris**  
Met. Trans., vol.8A (1977), p.1079.
- 137) **P.Newman, C.J.Beevers**  
'Small Fatigue Cracks' (proc. conf., ed. R.O.Ritchie, J.Lankford), The Metallurgical Society (1986), p.97.
- 138) **J.M.Larsen, T.Nicholas, A.W.Thompson, J.C.Williams**  
'Small Fatigue Cracks' (proc. conf., ed. R.O.Ritchie, J.Lankford), The Metallurgical Society (1986), p.499.
- 139) **J.M.Larsen**  
AGARD (NATO) CP393-14 (1985).
- 140) **J.K.Gregory, A.Gysler, G.Lutjering**  
'Fatigue 84' (proc. conf., ed. C.J.Beevers), EMAS, U.K. (1984), p.847.
- 141) **H.R.Gray**  
NASA Technical Note TN D6498, Washington (1971).
- 142) **M.R.Winstone, M.J.Weaver**  
'The Metallurgy of Light Alloys' (proc. conf.), The Institution of Metallurgists (1983), p.282.
- 143) **D.Sinigaglia, G.Taccani, B.Vincentini**  
Corr. Sci., vol.18 (1978), p.781.
- 144) **R.P.Wei**  
'Fatigue of Engineering Materials and Structures' (proc. conf.), Mechanical Engineering Publications, London (1986), vol.2, p.339.
- 145) **D.Taylor**  
'A Probabilistic Approach to the Behaviour of Short Fatigue Cracks', Department of Mechanical and Manufacturing Engineering, Trinity College, Dublin, Departmental report (1982).
- 146) **D.P.Rooke, C.J.Cartwright**  
'A Compendium of Stress Intensity Factors', HMSO, London (1976).
- 147) **R.C.Shah, A.S.Kobayashi**  
ASTM STP 513, vol.3 (1972).

- 148) **R.C.Shah, A.S.Kobayashi**  
Int. J. Fract. Mech., vol.9 (1973), p.133.
- 149) **A.C.Pickard**  
'Application of 3D Finite Element Methods to Fracture Mechanics and Fatigue Life Predictions', EMAS, U.K. (1986).
- 150) **J.M.Kendall, J.E.King**  
Int. J. Fatigue, vol.10, no.3 (1988), p.163.
- 151) **G.R.Irwin**  
9th International Congress on Applied Mechanics, vol.8, Paper 101 (II), Univ. of Brussels (1957), p.245.
- 152) **D.S.Dugdale**  
J. Mech. Phys. Solids, vol.8 (1960), p.100.
- 153) **K.Kishimoto, W.O.Soboyejo, R.A.Smith, J.F.Knott**  
Int. J. Fatigue, vol.11, no.2 (1989), p.91.
- 154) **W.O.Soboyejo, K.Kishimoto, R.A.Smith, J.F.Knott**  
Fat. Fract. Eng. Mat. Struct., vol.12, no.3 (1989), p.167.
- 155) **J.R.Moon**  
Private communication, University of Nottingham, Dept. of Metallurgy and Materials Science (March 1989).
- 156) **J.F.Knott**  
'Fundamentals of Fracture Mechanics', Butterworths, London (1973).
- 157) **I.W.Hall, C.Hammond**  
Mat. Sci. Eng., vol.32 (1978), p.241.

## ACKNOWLEDGEMENTS

First and foremost, I would like to express my sincere thanks to Dr.J.E.King for her assistance and supervision throughout this project. Thanks are also due to the staff, technical staff and postgraduate students in the Department of Metallurgy and Materials Science, Nottingham University, especially to Dr.J.R.Moon and Mr.K.Dinsdale for their advice and assistance and Dr.P.A.Brook for help with computing matters.

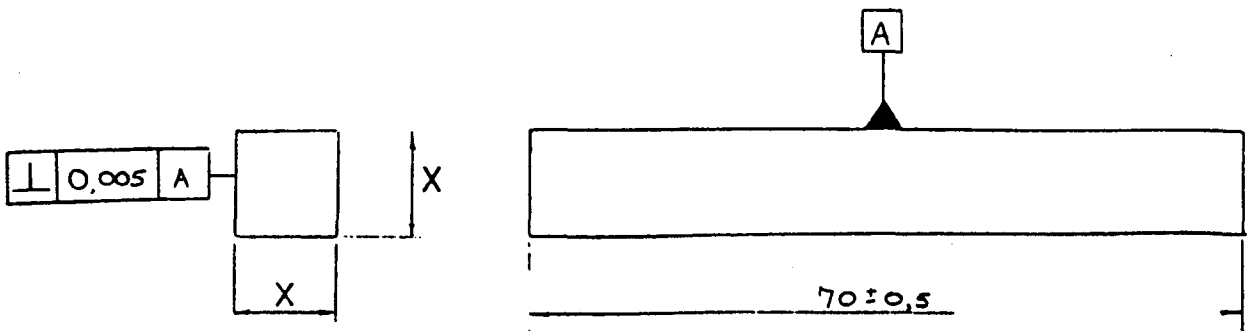
My thanks also go to SERC and Rolls-Royce plc for financial support, to Dr.M.Cope at Rolls-Royce plc, Derby, for some helpful discussions.

Finally, I would like to thank my family and friends, who have made the last four years so enjoyable.

APPENDIX A  
SHORT AND LONG CRACK SPECIMEN DESIGNS

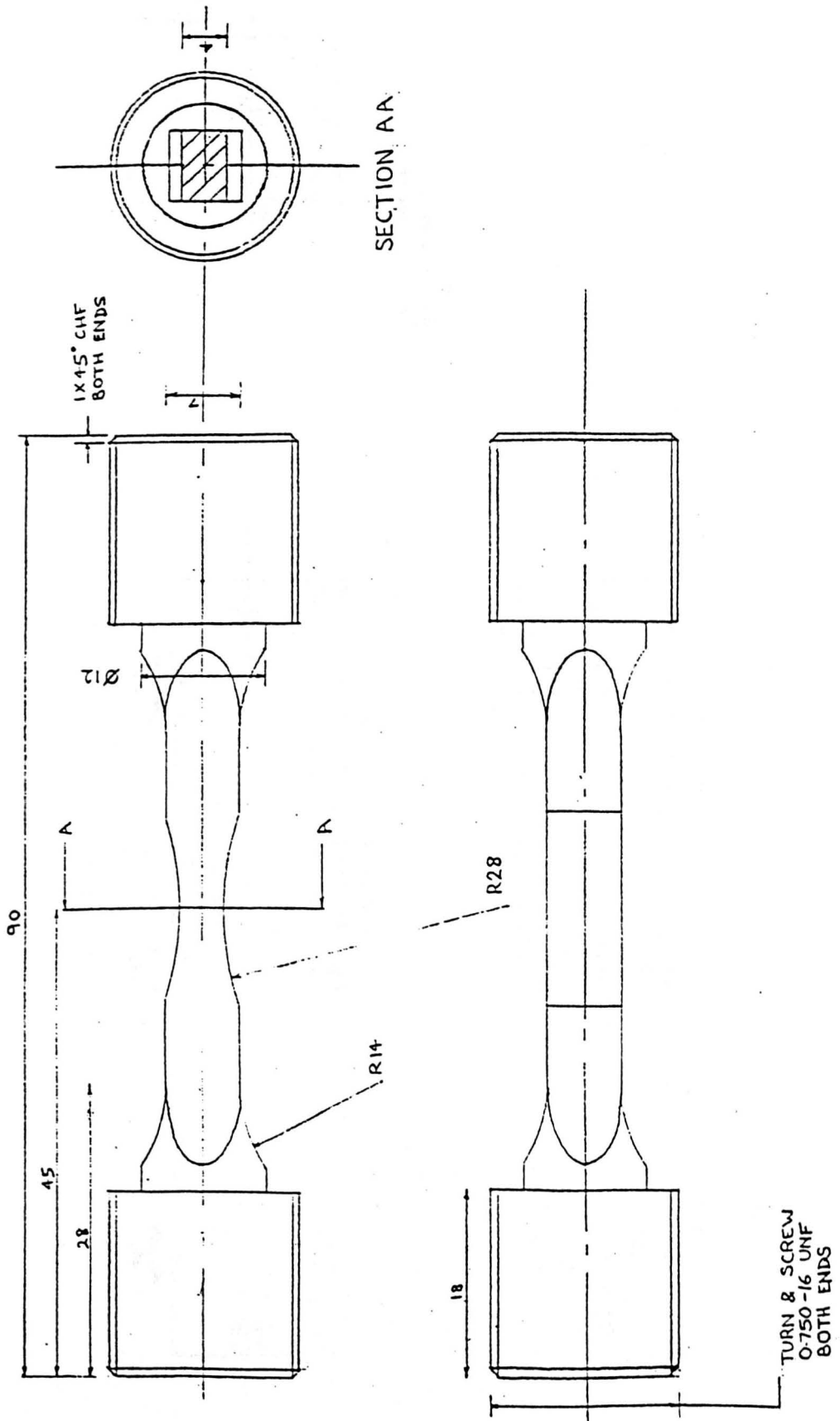
Four point bend short crack specimen design (dimensions in mm).

3<sup>RD</sup> ANGLE PROJECTION



Dimension X to be specified

Uniaxial tension short crack specimen design (dimensions in mm).



SEN long crack specimen design (dimensions in mm).

